Ausschuss Geodäsie (DGK)

der Bayerischen Akademie der Wissenschaften

Reihe C **Dissertationen** **Heft Nr. 959**

Yannick Breva

On the Observation Quality of Robot-based GNSS Antenna Calibration for Determining Codephase Corrections

München 2025

Verlag der Bayerischen Akademie der Wissenschaften, München

ISSN 0065-5325 **ISBN 978-3-7696-5371-7**

DGK Ausschuss Geodäsie (DGK)
der Bayerischen Akademie der Wissenschaften

Reihe C Dissertationen Heft Nr. 959

On the Observation Quality of Robot-based GNSS Antenna Calibration for Determining Codephase Corrections

Von der Fakultät für Bauingenieurwesen und Geodäsie
der Gottfried Wilhelm Leibniz Universität Hannover
zur Erlangung des akademischen Grades
Doktor-Ingenieur (Dr.-Ing.)
genehmigte Dissertation

von

Yannick Breva, M. Sc.

Geboren am 20.12.1991 in Celle

München 2025

Verlag der Bayerischen Akademie der Wissenschaften, München

ISSN 0065-5325 ISBN 978-3-7696-5371-7

Adresse des Ausschusses Geodäsie (DGK)
der Bayerischen Akademie der Wissenschaften:

Ausschuss Geodäsie (DGK) der Bayerischen Akademie der Wissenschaften

Alfons-Goppel-Straße 11 ● D – 80 539 München

Telefon +49 – 89 – 23 031 1113 ● Telefax +49 – 89 – 23 031 - 1283 / - 1100
e-mail post@dgk.badw.de ● http://www.dgk.badw.de

Prüfungskommission:

Vorsitzender:	apl. Prof. Dr. techn. Franz Rottensteiner
Referent:	Prof. Dr.-Ing. Steffen Schön
Korreferenten:	Assistant Prof. Dipl.-Ing. Dr. techn. Gregor Möller (Technische Universität Wien)
	PD Dr.-Ing. Hamza Alkhatib

Tag der mündlichen Prüfung: 13.03.2025

:

Diese Dissertation ist auf dem Server des Ausschusses Geodäsie (DGK)
der Bayerischen Akademie der Wissenschaften, München unter <http://dgk.badw.de/>
sowie unter Wissenschaftliche Arbeiten der Fachrichtung Geodäsie und Geoinformatik
der Leibniz Universität Hannover (ISSN 0174-1454), Nr. 407,
unter <https://repo.uni-hannover.de/handle/123456789/19198>, Hannover 2025 elektronisch publiziert

ISSN 0065-5325 ISBN 978-3-7696-5371-7

Abstract

Global Navigation Satellite System (GNSS) signals are received at the electric phase center of GNSS antennas, which varies based on the direction of the incoming signals. In highly precise GNSS applications, phase center corrections (PCC) for carrierphase signals must be taken into account. Additionally, codephase center corrections (CPC) for codephase signals exist, which become more important in aeronautic navigation or in code- and carrierphase linear combinations. Both, CPC and PCC, describe the difference between the actual receiving point of the signal at the antenna and the antenna reference point (ARP), which is the last point of the antenna that can be mechanically accessed for height measurements. The challenge of estimating multi-GNSS multi-frequency CPC with a robot in the field lies in the high observation noise relative to the pattern magnitude itself. This thesis focuses on reducing the observation noise of codephase signals while preserving the important pattern information within the observations during an absolute robot-based antenna calibration, in order to improve the repeatability and accuracy of the estimated CPC. A Monte-Carlo simulation is performed to study the impact of observation noise on the estimated CPC. The simulation shows that white noise and signal strength dependent noise with a standard deviation of the same magnitude as the pattern's peak-to-peak value results in a degradation of 15 % to 25 % for various comparison metrics. The weighted average standard deviation of the actual observables ranges from 0.476 m to 0.620 m for the analysed GNSS antennas, which is nearly equivalent to the magnitude of the pattern's peak-to-peak values. To reduce the noise, the receiver tracking loop parameters are adjusted based on an experiment using a software receiver during a calibration. The best performance is achieved with a delay lock loop (DLL) bandwidth of 0.5 Hz, using a loop filter order of 1 in a carrier aided DLL. This acquired knowledge is adapted to hardware receivers, significantly improving the weighted average standard deviation of the observables by 42 % resulting in a more repeatable and accurate CPC compared to using the manufacturer's default receiver settings. Additionally, multipath effects during calibration are thoroughly investigated, with the balustrade and the astronomical domes in the robot's surrounding identified as the most significant sources of multipath effects. The studies demonstrate that using time-differenced observations in combination with a dynamic elevation mask and multipath maps can effectively eliminate almost all multipath affected observations. Furthermore, the time differenced multipath linear combination (ΔMPLC) is introduced as an input for the estimation approach, resulting in reduced observation noise compared to the time differenced receiver-to-receiver single differences (ΔSD) approach, as one differencing step is avoided. The estimated CPC, using ΔMPLC, with optimized receiver settings shows similar repeatability. Additionally, applying CPC in a single point positioning (SPP) leads to a 70 % improvement in the estimated Up component compared to when no CPC is applied. In the observation domain, by calculating SD, the long-period trend can be reliably represented by the estimated CPC.

Keywords Absolute GNSS Antenna Calibration, Codephase Center Correction, Group Delay Variations, Observation Quality, GNSS Receiver

Zusammenfassung

Globale Navigation Satellitensignale (GNSS) Signale werden am elektrischen Phasenzentrum der GNSS-Antennen empfangen, das sich je nach Richtung der eintreffenden Signale verändert. In präzisen GNSS-Anwendungen müssen Phasenzentrumskorrekturen (PCC) für Trägerphasensignale berücksichtigt werden. Außerdem existieren Codephasenzentrumkorrekturen (CPC) für Codephasensignale, die in der Luftfahrtnavigation oder bei Code- und Trägerphasen-Linearkombinationen immer wichtiger werden. Sowohl CPC als auch PCC beschreiben den Versatz zwischen dem tatsächlichen Empfangspunkt des Signals an der Antenne und dem Antennenreferenzpunkt (ARP). Die Herausforderung bei der Schätzung von multi-GNSS multi-Frequenz CPC mittels eines Roboters liegt im hohen Beobachtungsrauschen im Vergleich zum Pattern selbst. Der Fokus dieser Arbeit liegt in der Reduzierung des Beobachtungsrauschens von Codephasensignalen, während die wichtigen Patterninformation in den Signalen während einer absoluten, roboterbasierten Antennenkalibrierung erhalten bleiben, um die Wiederholbarkeit und Genauigkeit der geschätzten CPC zu verbessern. Eine Monte-Carlo-Simulation wird durchgeführt, um die Auswirkungen des Beobachtungsrauschens auf die geschätzten CPC zu untersuchen. Die Simulation zeigt, dass weißes und signalstärkebedingtes Rauschen mit einer Standardabweichung in der Größenordnung des Patterns zu einer Verschlechterung von 15 % bis 25 % bei verschiedenen Vergleichsmetriken führt. Die gewichtete, durchschnittliche Standardabweichung der tatsächlichen Beobachtungen liegt für die analysierten GNSS-Antennen zwischen 0,476 m und 0,62 m, was nahezu der Größenordnung der Pattern entspricht. Um das Rauschen zu reduzieren, werden die Tracking-Schleifen der GNSS-Empfänger, basierend auf einem Experiment mit einem Softwareempfänger während einer Kalibrierung, optimiert. Die besten Ergebnisse werden mit einer Delay Lock Loop (DLL)-Bandbreite von 0.5 Hz erzielt, unter Verwendung einer Filterschleifenordnung von 1 bei einer trägerphasenunterstützten DLL. Die Optimierung der Empfänger führt zu einer Verbesserung der gewichteten, durchschnittlichen Standardabweichung der Beobachtungen von 42 % und zu einem wiederholbareren und genaueren CPC im Vergleich zur Nutzung der standardmäßigen Empfängereinstellungen des Herstellers. Zusätzlich wird eine Mehrwegeanalyse durchgeführt, wobei die Balustrade und die astronomischen Kuppeln in der Roboterumgebung als kritische Objekte identifiziert wurden. Die Studien zeigen, dass die Nutzung von zeitlich differenzierten Beobachtungen in Kombination mit einer dynamischen Elevationsmaske und Mehrwegkarten fast alle von Mehrwegen betroffenen Beobachtungen effektiv eliminieren kann. Darüber hinaus wird die zeitlich differenzierte Mehrwege-Linearkombination (ΔMPLC) als Beobachtungen für die Schätzung eingeführt, was im Vergleich zum zeitlich differenzierten Einfachdifferenz (ΔSD)-Ansatz zu reduziertem Beobachtungsrauschen führt, da ein Differenzierungsschritt vermieden wird. Die mit ΔMPLC geschätzten CPC mit optimierten Empfängereinstellungen weisen eine ähnliche Wiederholbarkeit auf. Werden die CPC in einem Single-Point Positioning (SPP) angebracht, führt das zu einer Verbesserung der geschätzten Up-Komponente um 70 %, verglichen mit der Anwendung ohne CPC. Im Beobachtungsraum kann durch Berechnung von SD der langperiodische Trend zuverlässig durch die geschätzten CPC dargestellt werden.

Schlagwörter Absolute GNSS-Antennen Kalibrierung, Codephasenzentrumskorrekturen, Group Delay Variations, Beobachtungsqualität, GNSS-Empfänger

Contents

1 Introduction

Global Navigation Satellite System (GNSS) signals are received at the electric phase center of GNSS antennas, which varies depending on the direction of the incoming signals. This receiving point does not have a mechanical reference for coordinate measurements, but it must be known in order to accurately estimate a position in highly precise GNSS applications. Therefore, PCC for carrierphase and codephase center corrections (CPC), also known as group delay variations (GDV), for codephase signals must be taken into account. These describe the offset between the antenna reference point (ARP), which is a well-defined and mechanically accessible component of the antenna, and the electromagnetic phase center of the antenna.

PCC and CPC can be estimated either with real GNSS signals using a robot in the field or by using synthetically generated GNSS signals in an anechoic chamber. While the calibration of PCC has been well studied over the past 40 years and is carried out by several institutions today, such as ETH Zürich (Willi, 2019), National Geodetic Survey (NGS) (Bilich et al., 2018), Wuhan University (Zhou et al., 2023), Geo++ company (Wübbena et al., 2019) and the Institut für Erdmessung (IfE) (Kröger et al., 2021), the development of methods to estimate CPC primarily began in the last decade. Especially in aeronautic navigation, CPC is becoming increasingly important. GNSS antennas must be designed to ensure that specific limits of the CPC, as defined in RTCA DO-301 (Hegarty et al., 2015), are not exceeded. Therefore, it is crucial to accurately estimate CPC. For example, Caizzone et al. (2022) uses an anechoic chamber for this purpose. Since synthetically generated GNSS signals are used, these signals do not exhibit observation noise. In contrast, when using a robot in the field to estimate CPC, the codephase observables are affected by relatively high noise.

The antenna calibration group at IfE extended its multi-GNSS, multi-frequency absolute antenna calibration approach to estimate CPC (Kersten, 2014) and is in the process of ongoing optimization. However, the challenge lies in managing the relatively high observation noise of the codephase observables compared to the desired pattern information within these signals. This high observation noise reduces the repeatability and accuracy of the CPC calibration. Initial investigations into reducing the noise have been conducted by Breva et al. (2022) and Breva et al. (2024).

The main goal of this thesis is to understand the observation noise in the codephase signals of various receivers during the antenna calibration of different GNSS antennas and to develop strategies to reduce this noise while preserving the important CPC pattern information in the codephase observables. To achieve this, various experiments, simulations, and analyses have been conducted in this thesis, which is structured as follows:

Chapter 2 gives an overview about the theoretical basics, which are required for the analyses carried out in this thesis. A description about the GNSS signals, antennas and receivers are provided, with a strong focus on receiver tracking loops and tracking errors due to their significance in estimating CPC. Additionally, an overview about the GNSS error budget, different linear combinations and observation differences are given.

Beginning with the development and current research on antenna correction values, including their definition and comparison strategies, Chapter 3 primarily focuses on the detailed description of the robot-based absolute multi-GNSS multi-frequency antenna calibration algorithm at IfE. The calibration robot and its mathematical model, as well as the antenna coordinate system and elevation masks, are described. Furthermore, the time differenced multipath linear combination is introduced for use as an input in the estimation process. Additionally, the estimation process is briefly outlined.

Observation noise is a crucial factor for estimating CPC consistently and accurately. Chapter 4 performs a comprehensive study of the impact of observation noise on the estimated CPC, based on a Monte-Carlo simulation. Furthermore, detailed investigations of real observation noise within the robot based-antenna calibration have been carried out for different GNSS receivers and antennas. To this end, a digital receiver twin has been developed to enhance the tracking loop parameter for reducing the observation noise, based on a study performed with a software receiver.

Chapter 5 focuses on the environment of the calibration robot, which can cause multipath effects on the antenna to be calibrated. Thus, a digital model of the robot surrounding is generated. This model is either used for generating multipath maps or to find critical structures on the measurement rooftop, which degrade the GNSS satellite signals by multipath or diffraction effects.

The acquired knowledge of the previous chapters is used in Chapter 6 to estimate CPC pattern with different methods for eliminating problematic observations and by optimizing the GNSS receiver tracking loops. Additionally, the time differenced multipath linear combination is used as estimation inputs. Furthermore, a signal strength dependent weighting scheme is analysed. To this end, the estimated CPC are validated with CPC, estimated in an anechoic chamber, and in the observation and positioning domain.

The results achieved in this work are summarized in Chapter 7. Additionally, an outlook for future work is provided, with a discussion of the current challenges.

2

GNSS Antennas, Receivers and Observations

This chapter describes the fundamentals of GNSS signals and their way through the antenna and the receiver processing chain. In Section 2.1 the radio frequency (RF) signal is described and its modulation with different techniques to transmit the required information towards the Earth. The signals can be received by different kind of antennas, presented in Section 2.2. Afterwards, Section 2.3 describes the processing steps in the GNSS receiver. At the end, a usable high-end GNSS observation in terms of receiver independent exchange format (RINEX) data is available. To use them in different applications, several error sources need to be taken into account, as explained in Section 2.4. Additionally, different strategies for eliminating particular effects using linear combinations or observation differences are presented.

2.1 GNSS Signals

Global Navigation Satellite System (GNSS) signals are electromagnetic waves transmitted from GNSS satellites, which are orbiting the Earth at an altitude of approximately, 20000 km on an elliptic trajectory (eccentricity < 0.02). Thus, the signal travel time is 60-80 ms. These signals are generated by the onboard atomic clocks/oscillators. They consist of one or more radio frequency (RF) carriers, located in the L-band, which can be described as:

$$RF(t) = a(t) \cdot \cos\left(2\pi f(t)t + \theta(t)\right) \tag{2.1}$$

with its amplitude $a(t)$, its frequency $f(t)$ and a phase offset $\theta(t)$ at epoch t. By modifying one of these parameters, the RF carrier can be modulated.

Depending on the parameter to be modulated, it is called frequency modulation, amplitude modulation or phase modulation. This is necessary to transmit information from the GNSS satellite to the GNSS receiver, like satellite almanacs, clock errors, satellite health, atmospheric parameters, etc. One commonly used modulation technique for transmitting the navigation data and code from the satellite to the receiver is called binary phase shift keying (BPSK).

Binary Phase Shift Keying

BPSK is a phase modulation, where $\theta(t)$ can either be 0 deg or 180 deg. The transmitter switches between those two phase states after a defined interval T_b, where $T_b = 1/R_b$, with R_b as the data rate in bits per second. This time series is called data waveform or navigation data waveform with two different states: -1 and 1. It should be noted that data bits only have two states, namely 0 and 1. Therefore, the k^{th} data bit d_k to be transmitted has to be mapped either with [0,1] $\rightarrow$ [-1,1] or [0,1] $\rightarrow$ [1,-1]. The data waveform $d(t)$ can be described mathematically with (Kaplan and Hegarty, 2017):

$$d(t) = \sum_{k=-\infty}^{\infty} d_k p(t - kT_b), \tag{2.2}$$

where $p(t)$ is a rectangular pulse:

$$p(t) = \begin{cases} 1, & 0 \leq t < T_b \\ 0, & \text{elsewhere.} \end{cases} \tag{2.3}$$

The navigation data $d(t)$ is used to transmit information such as satellite locations. To access precise ranging information, $d(t)$ is further modulated with a spreading or pseudo random noise (PRN) waveform $c(t)$, which also employs a rectangular pulse shape. The product of $d(t)$ and $c(t)$ is then multiplied with the unmodulated RF carrier. This modulation is called discret sequence spread spectrum (DSSS) modulation and is used for nearly all GNSS signals:

$$\mathrm{DSSS}(t) = d(t) \cdot c(t) \cdot RF(t). \tag{2.4}$$

The PRN waveform $c(t)$ is deterministic, enabling the use of different unique satellite codes to distinguish between incoming GNSS signals, for example. This technique is called code division multiple access (CDMA) and is used e.g. in Global Positioning System (GPS), Galileo, Beidou (BDS) and for the newer satellite generations from GLObalnaja NAwigazionnaja Sputnikowaja Sistema (GLONASS), namely K, K1 and M satellites (Teunissen and Montenbruck, 2017). Older GLONASS satellite generations using the frequency division multiple access (FDMA) technique, in which every satellite is sending its information on a slightly different frequency ($\Delta f_{L1} = 0.5625$ MHz, $\Delta f_{L2} = 0.4375$ MHz) located around the L1 (1602 MHz-1615.5 MHz) and L2 (1246 MHz-1256.5 MHz) center frequencies.

Besides the CDMA technique, the PRN waveform has a higher chip rate and, consequently, a wider bandwidth than the navigation data waveform, which allows this information to be used for positioning. This waveform is also known as ranging code, PRN code or pseudorandom sequence. The PRN code chips has a certain time duration (chip period). The codephase of the signal is defined as the independent time parameter of the PRN code in units of chips.

Two binary DSSS signals can be combined to transmit more information on one single carrier wave. This approach is called quadrature phase shift keying (QPSK), which divides the signal $s(t)$ into a cosine part, the inphase $s_I(t)$, and a sinus part, the quadrature phase $s_Q(t)$:

$$s(t) = s_I(t)\cos(2\pi f_c t) - s_Q(t) sin(2\pi f_c t), \tag{2.5}$$

with f_c being the frequency of the carrier. Obviously, $s_I(t)$ and $s_Q(t)$ have a relative phase shift of 90 deg. When more than two DSSS should be combined, more complicated techniques are required, like subcarriers.

Binary Offset Carrier

Binary offset carrier signals were mainly developed for military purposes (Betz, 2001). Nowadays, most of the new GNSS signals are modulated with a binary offset carrier (BOC) modulation to ensure spectral separation between various non-interoperable signals from different GNSS systems and to enhance synchronization performance (Teunissen and Montenbruck, 2017). BOC signals reduce the chance of interference between different GNSS signals in the same frequency band, which benefits the coexistence of these signals. The rectangular pulse, which is used for the PRN waveform $c(t)$, is replaced with the following chip waveform $sc(t)$ (Misra and Enge, 2006):

$$sc(t) = \sum_{m=0}^{M-1} (-1)^m p\left(\frac{t - mT_S}{T_S}\right), \tag{2.6}$$

where M defines the number of subchips with a duration of $T_S = T_C/M$. T_C stands for the chip period. The resulting binary subcarrier waveform $sc(t)$ is either in sine or cosines phase to the PRN waveform. The product of $d(t)$, $c(t)$, $sc(t)$ and $RF(t)$ defines the BOC signal:

$$\mathrm{BOC}(t) = d(t) \cdot c(t) \cdot sc(t) \cdot RF(t). \tag{2.7}$$

BOC signals are typically denoted as $\mathrm{BOC}(\alpha, \beta)$, where α defines the ratio between the subcarrier frequency and a reference frequency, which is for example 1.023 MHz for GPS and Galileo signals, and β defines the ratio between the PRN code frequency and the reference frequency. The number of subchips can be calculated by $M{=}2\alpha/\beta$. DSSS signals, e.g. coarse-acquisition (C/A) signals, have one prominent main lobe in the power spectral density (PSD). Because of the sine or cosine behaviour of the subcarrier, the spectrum of the signal is divided into two main lobes, thus, the BOC modulation is also called as split-spectrum modulation (Teunissen and Montenbruck, 2017). The position of the two main lobes depends on α: the larger α is chosen, the further the loops shifted apart. Over the years, the BOC modulation has been extended e.g. as composite BOC, multiplexed BOC, time-multiplexed BOC and AltBOC. The idea is to modulate several binary signal components or, in other words, more information on one common carrier frequency, similar to the QPSK. However, these techniques are not discussed here.

2.2 GNSS Antennas

Components

The analog RF GNSS signals are received at the GNSS antenna. At this stage, a first filtering and amplifying is done when using an active antenna. Active GNSS antennas already incorporate a filter, typically a band pass filter (BPF), as well as an low noise amplifier (LNA), enabling direct signal modification. A BPF is used to reduce the noise contained in the very weak GNSS signal, typically followed by an LNA to amplify the GNSS signal without additionally amplifying the noise. When using a passive antenna, the analog RF signal go through an antenna cable first and is then filtered and amplified at the preamplifier stage in the receiver's front-end.

Types

Several companies offer GNSS antennas in a variety of types, designs, and price ranges. Commonly used antenna types are microstrip patch or helix antennas, however, other designs such as pinwheel, quadrifilar or spiral antennas exist (Maqsood et al., 2017). Microstrip patch antennas have a simple design, consisting of a metallic patch placed above a conductive ground plane, separated by a dielectric substrate. The patch acts as the radiating element and is specifically designed to resonate at a particular frequency. The ground plane is essential for the antenna's effective operation. Multiple patch antennas can be stacked together to enable a multiband operation.

An example of this technique are choke ring antennas, like the Leica AR.25 R3, which is mostly used in the analysis of this thesis. These antennas use a Dorne-Margolin antenna element, a dual-feed-microstrip patch antenna (Bedford et al., 2009). It is positioned above several metallic curved plates arranged in a circular pattern, with either uniform height (forming a 2D choke ring) or varying heights (forming a 3D choke ring). The spacing between the plates is arranged in such a way to prevent the arrival of ground-reflected GNSS signals at the antenna element. Choke ring antennas are usually classified as high-grade geodetic antennas. A mass market patch antenna is for example the ANN-MB1 from the Ublox company. It cannot receive L2 signals like high-grade geodetic antennas can, and typically lacks additional components to mitigate multipath effects. Thus, the antenna can be installed on a ground plate to avoid reflected signals, which is done in the experiments and investigations in this thesis. Besides, the pinwheel design allows a good multipath mitigation capability by being compact and lightweight (Maqsood et al., 2017). This design is used by the Novatel company, especially for the NOV703GGG.R2 antenna, which is investigated in this contribution. More information and detailed description of the different design techniques can be found in Rao et al. (2013) and is not discussed here.

Axial Ratio

Independent of which antenna design is being chosen, its axial ratio should not exceed 3 dB at the antenna's zenith direction (Rao et al., 2013; Maqsood et al., 2017). The axial ratio defines the relation between the major and minor semi axis of the antenna's polarization ellipse. A ratio of 1 (0 dB) represent a circular polarization behaviour of the antenna. Other ratios signify elliptical polarization, with a negative ratio indicating left-handed polarization and a positive ratio indicating right-handed polarization. GNSS satellites transmit the GNSS signals as right-handed circularily polarized (RHCP) signals, because a linear polarization would be distorted by travelling through the ionosphere (Faraday rotation). In an ideal scenario, the polarization of the receiving antenna and the transmitting satellite antenna would match perfectly. However, achieving this

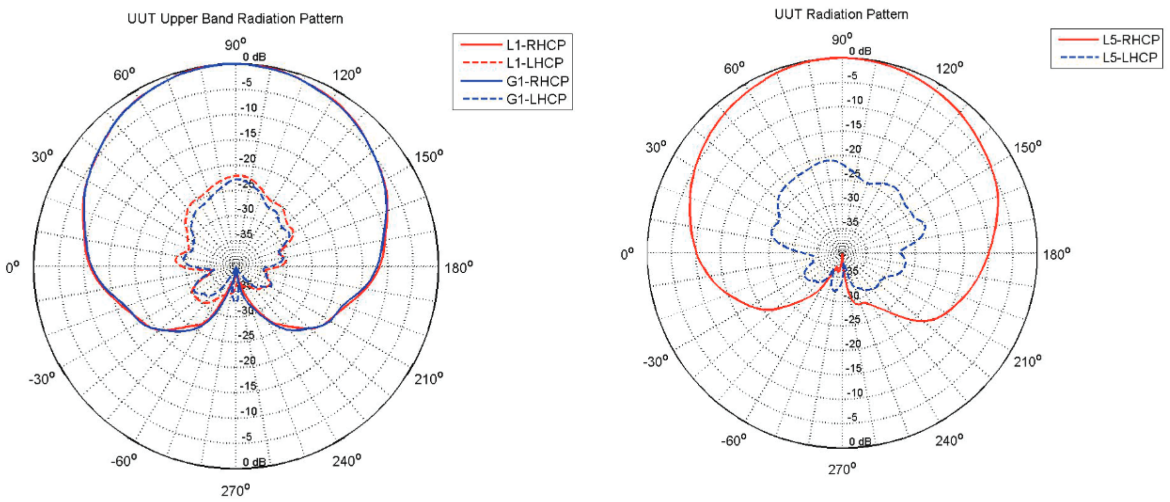

Figure 2.1: Radiation pattern from the NOV703GGG.R2 antenna for GPS (L) and GLONASS (G) on L1 carrier frequency (left) and GPS on L5 carrier frequency (right) (Novatel, 2011).

in the design of a receiving antenna is challenging due to various design trade-offs and constraints.

Polarization

In general, the antenna should be able to receive RHCP signals and suppress left-handed circularily polarized (LHCP) signals. When GNSS signals are reflected on surfaces with an angle of incidence smaller than the Brewster angle, its polarization changes from a RHCP to LHCP. Usually, this polarization is not wanted, so antennas are designed in a way, that LHCP signals are mitigated. Figure 2.1 shows a radiation pattern of the NOV703GGG.R2 antenna for RHCP and LHCP signal components for GPS and GLONASS for the L1 carrier frequency and for GPS L5 carrier frequency. It is visible, that the LHCP behaviour is relatively small compared to the RHCP.

This can also be expressed by the cross-polar discrimation indicator (XPD) (Rao et al., 2013):

$$XPD(e, \alpha) = \left(\frac{E_R(e, \alpha)}{E_L(e, \alpha)} \right), \tag{2.8}$$

where E_R, E_L denote the radiated electric field for RHCP and LHCP signals, respectively. This ratio describes the capability of the antenna to suppress LHCP signals. The higher the ratio, the better the multipath rejection. The XPD depends on the elevation e and azimuth α of the incoming GNSS signals in the antenna frame, as Equation 2.8 suggests and Figure 2.1 visually presents. It is highest at the antenna's zenith and decreases with elevation. Since multipath effects are usually received at low elevations, a higher XPD is also achieved at low elevations to mitigate these signals.

Gain

Another antenna characteristic parameter is the antenna gain. It describes the signal reception behaviour of RHCP and LHCP signals relative to an isotropic antenna. This ratio is typically given in dBic, where i denotes the ratio to an isotropic antenna and c denotes a circular polarization radiation. Typically, the antenna gain is highest at zenith and decreases with the elevation. For example, the NOV703GGG.R2 antenna (Figure 2.1) has an antenna gain of +5.0 dBic at zenith for the L1 signals and +3.0 dBic for L2 and L5 signals and decreases by 12–13 dB towards the horizon (Novatel, 2011).

2.3 GNSS Receiver Internal Processing Steps

After the GNSS signals are received at the antenna, they are processed by a GNSS receiver, which is the focus of this section. The fundamental internal processing steps within the receivers are outlined, beginning with the receiver's front-end in Section 2.3.1, where the noise temperature and noise figure are discussed. Additionally, the intermediate frequency (IF) is introduced. The IF feeds into the receiver's signal processing, which is described in Section 2.3.2. An overview of the key components is provided. To this end, a detailed description on the receiver's tracking loops is given in Section 2.3.3, because of its significance in this thesis.

2.3.1 Receiver Front-End

The front-end is the first part of each GNSS receiver. It is directly connected to an active or passive GNSS antenna (cf. Section 2.2) via cable. Its main task is to amplify and down convert the received analog RF signals to a lower frequency in a way, that they can be used in the digital signal processing part later. The target digital frequency is called IF. Typically, one front-end is used for each GNSS signal center frequency or closely spaced group of frequencies (Kaplan and Hegarty, 2017). Consequently, more front-ends are required for multi-GNSS multi-frequency processing, at which each of them are designed for its specific L-band frequency with unique components, like different band pass filter (BPF) or local oscillator (LO) frequencies. A typical receiver front-end can consists of a preamplifier and a down conversion scheme with an automatic gain control (AGC) and an analog-to-digital conversion (ADC) as exemplary shown in Fig. 2.2.

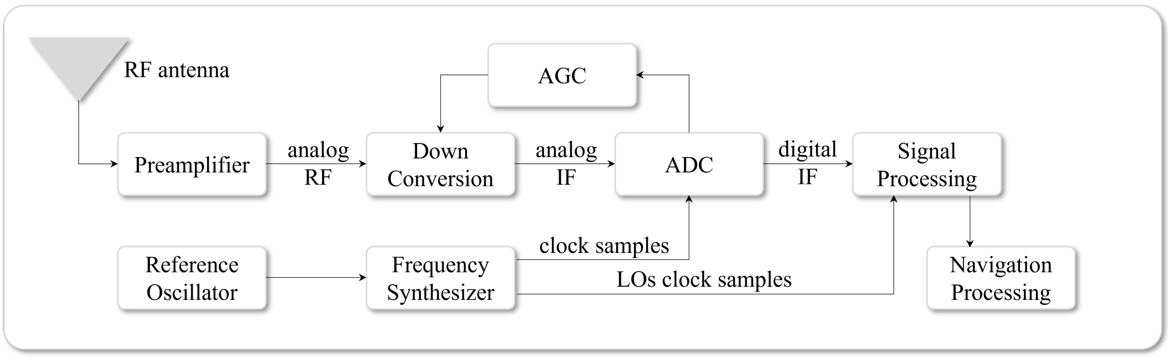

Figure 2.2: Principal components of a GNSS receiver based on Häberling (2016).

Noise Power and Noise Temperature

After the analog RF signal is received by the GNSS antenna, whether it is active or passive, the signal is filtered and amplified several times at the receiver's front-end by using different pairs of BPF and LNA with individual settings, like bandwidth, gains, etc. This depends mostly on the receiver manufacturer and the receiver plan, as well as on the GNSS signal frequency. The ideal output would be a strong and noisefree signal, which can be down-converted to a common IF.

Unfortunately, this is not realizable in reality, because every signal at the receiver competes with noise. Noise can occur in different ways, like coloured noise or in a random walk process. For understanding noise within a GNSS receiver, the noise N_0 is considered as white noise here. It can excellently be used for modelling natural noise, which is received along with GNSS signals, because it is assumed to has a constant PSD across the GNSS band frequencies:

$$PSD = N_0 \text{ [W/Hz]}. \tag{2.9}$$

The noise power P_N can be calculated by

$$P_N = B_{(1,2),N} N_0 \text{ [W]}, \tag{2.10}$$

using the noise equivalent-bandwidth B_N (Misra and Enge, 2006). When the noise power of a filter under test would pass through an ideal filter, its bandwidth is defined as B_N. The subscripts 1 and 2 in Equation 2.10 represent either filters with a one-sided bandwidth, like low pass filter (LPF), or filters with a two-sided bandwidth, like BPF. Typically, the noise PSD is set into a relation with the signal power C defining the well known ratio C/N_0. In Equation 2.10, the noise power P_N is related to the PSD, but it can also be set into a relation with an equivalent noise temperature T_{eq} $[K]$ by writing the PSD as a function of T_{eq} and k:

$$N_0 = kT_{eq} \text{ [W/Hz]}, \tag{2.11}$$

at which the Boltzmann's constant is defined as $k = 1.38 \cdot 10^{-23}$ [J/K]. Inserting Equation 2.11 into 2.10 leads to

$$P_N = kT_{eq}B_N \text{ [W]}. \tag{2.12}$$

It should be noted, that the equivalent noise temperature is not the physical temperature of the devices. It is the temperature of a noise power source, like an LNA, that would generate the same noise power as the physical temperature would do. From here, by using the term *noise temperature*, the equivalent noise temperature is meant.

Noise Figure

In general, any GNSS receiver component generates a thermal noise with a noise temperature of T_{com}, when the physical temperature is above absolute zero (0 K). When a GNSS signal passes through a receiver component, the input signal-to-noise ratio $C/N_{0,in}$ and the output ratio $C/N_{0,out}$ differs, due to added noise from the component.

This ratio is defined as the noise figure F (Misra and Enge, 2006):

$$\begin{aligned} F(T_{in}) &= \frac{C/N_{0,in}}{C/N_{0,out}} = \frac{CGk(T_{in} - T_{com})}{GCkT_{in}} \\ &= 1 + \frac{T_{com}}{T_{in}} \geq 1 \\ T_{com} &= F(T_{in} - 1)T_{in} \text{ [K]}. \end{aligned} \tag{2.13}$$

The noise temperature T_{in} represents the temperature of the signal, which feeds the GNSS receiver component, whereat T_{com} is the noise temperature generate by the component itself. The C/N_0 ratios can also be expressed by the power gain G. In general, T_{in} must be known to get the correct relation between the noise figure and the noise temperature of a receiver component, however, the receiver manufacturers can not provide a value for T_{in}, because it highly depends on the application. Therefore, specifications about the noise figure of different components are based on room temperature T_0 with 290 K. Rewriting Equation 2.13 leads to

$$\begin{aligned} F(T_0) &= 1 + \frac{T_{com}}{T_0} \geq 1 \\ T_{com} &= F(T_0 - 1)T_0 \text{ [K]}. \end{aligned} \tag{2.14}$$

As Equation 2.13 and 2.14 show, the noise figure can only be 1 or greater. A GNSS receiver component adds noise to the signal, when the noise figure is greater than 1, otherwise no additional noise is added.

Typically, a GNSS receiver contains several and different components. There are components like LNAs that amplify the signal within the system, but there are also components like antenna cables or connectors where the signal power decreases. These components are called *passive*, therefore their power gain G is less than one. After Tsui (1995) and Vizemuller (1995) the noise figure of passive components is equal to the power loss L and the inverse of the power gain:

$$\begin{aligned} F = L &= \frac{1}{G} \geq 1, \\ T_{com} &= \left(\frac{1-G}{G}\right) T_0 \text{ [K]}. \end{aligned} \tag{2.15}$$

With this, the noise temperature of a whole GNSS receiver system T_R can be calculated using the well known *Friis' forumulas*:

$$T_R = T_A + T_{com,1} + \frac{T_{com,2}}{G_1} + \frac{T_{com,3}}{G_1, G_2} + ... \text{ [K]}. \tag{2.16}$$

The temperature T_A defines the noise temperature of the incoming GNSS signal or in other words, from an external noise source, $T_{com,1}$, $T_{com,2}$ and $T_{com,3}$ defines the noise temperature of the different components, whereat G_1 and G_2 indicates their power gain.

The Friis' formula shows, that the noise temperature of a whole system mostly depends on the first GNSS receiver components. For example, when the gain power of the first component G_1 is very large, the impact of the following components lose significance. When G_1 is small and G_2 is large, then the first two components are mostly responsible for the noise temperature of the whole system.

The Friis' formula can also be used to calculate the signal-to-noise ratio $C/N_{0,out}$ after the preamplifier stage (Misra and Enge, 2006):

$$C/N_{0,out} = \frac{C}{k\left(T_A + T_{com,1} + \frac{T_{com,2}}{G_1} + \frac{T_{com,3}}{G_1,G_2} + ...\right)} \tag{2.17}$$

or in [dB-Hz]

$$C/N_{0,out} = P_{R,dB} + G_{R,dB} - L_{R,dB} - 10\log_{10}(kT_A) - F_{R,dB}(T_A) \quad \text{[dB-Hz]}. \tag{2.18}$$

The preamplified analog GNSS signal is now prepared to be down converted to an IF.

Signal represented at Intermediate Frequency Level

The analog RF GNSS signal is usually down converted to an intermediate frequency (IF). The IF has a lower frequency than the RF signal, however, it maintains the same information. This holds true for the Doppler shift Δf, the PRN and signal phase θ. Lowering the frequency benefits the ADC, because it is typically limited by the sampling frequency, the bandwidth of the input signal and the bit resolution (Häberling, 2016). Additionally, a lower frequency can decrease the impact of system and clock jitter on the ADC. In order to down convert the analog RF signal to the defined IF, which is based on the frequency plan of the manufacturer's receiver design, a reference oscillator and a frequency synthesizer is required. The oscillator is the key component in every GNSS receiver. The quality of its performance, especially its short term stability for tracking stability, decide whether the receiver is defined as high end or as low cost. Nowadays, temperature-compensated crystal oscillator (TXCO) or oven-compensated crystal oscillator (OXCO) are generally used in GNSS receivers (Häberling, 2016). The oscillator feeds the frequency synthesizer, which generates clock samples, used in the ADC and the numerical controlled oscillator (NCO) in the signal processing part, and local oscillator (LO). LOs are phase locked to the reference oscillator and necessary for the IF down conversion. The IF signal can be described after Häberling (2016) with

$$s_{IF}(t) + n_{IF}(t) = (s_{RF}(t) + n_{RF}(t)) \cdot LO(t), \tag{2.19}$$

whereat the analog RF signal and its noise is defined by parameter $s_{RF}(t)$ and $n_{RF}(t)$. The IF signal $s_{IF}(t)$ can also be described with

$$\begin{aligned} s_{IF}(t) = & s_I(t)\cos(2\pi(f_{IF} + \Delta f - \delta f)t + \theta) + \\ & s_Q(t)\sin(2\pi(f_{IF} + \Delta f - \delta f)t + \theta). \end{aligned} \tag{2.20}$$

and its noise by

$$\begin{aligned} n_{IF}(t) = & n_I(t)\cos(2\pi(f_{IF} + \Delta f - \delta f)t + \theta) + \\ & n_Q(t)\sin(2\pi(f_{IF} + \Delta f - \delta f)t + \theta) \end{aligned} \tag{2.21}$$

As already described in Section 2.1, a GNSS signal can be divided into a cosine (inphase I) and sinus (quadrature Q) term. Obviously, this is also done for the IF signal with s_I and s_Q. The Doppler shift is defined as Δf, the signal phase as θ and δf stands for the oscillator drift. The intermediate frequency f_{IF} is defined by:

$$\begin{aligned} f_{IF,low} &= f_{RF} - f_{LO} \\ f_{IF,upp} &= f_{RF} + f_{LO} \end{aligned} \tag{2.22}$$

with f_{RF} as the frequency of the GNSS signal and f_{LO} the frequency of the LO. It is clearly visible, that the IF signal contains two sidebands, an upper and a lower one. Since the IF should have a low frequency, the upper sideband is not required, because it has a higher frequency than the RF signal. Therefore, a particular filter is implemented to eliminate the upper sideband, so that f_{IF} is defined as $f_{RF} - f_{LO}$.

Afterwards, the analog IF needs to be converted to a digital IF in order to start the signal processing part. Therefore, an analog-to-digital conversion is used to sample and quantize the analog IF signal. The sampling rate frequency must be at least two times higher than the IF to ensure that all information are maintained (Nyquist theorem). After Häberling (2016) the quantization of the amplitude are affected by two different noise types: the quantization noise caused by the finite amplitude resolution and the clipping noise, which occur when the amplitude is beyond the maximum range of the ADC. The impact of the noise can be decreased, when using a multi-bit ADC. To control the different quantization levels, an AGC is implemented, together with a filter and an amplifier to reduce signal degradations, in a closed loop scenario. After the AGC, usually a variable gain amplifier (VGA) is implemented to arrange the IF in an ideal dynamic range for the ADC. To this end, the analog IF is converted to a digital IF, which can be used for further processing of the signal.

2.3.2 Signal Processing

The main component in each GNSS receiver is the signal processing part. A possible implementation is shown in Figure 2.3. The digital IF feeds the algorithm, which is responsible for two main tasks. First, the signal processing searches for satellite signals in the input data stream (acquisition). This is necessary, because the IF data stream contains a mixture of all satellite signals, frequencies and noise. Secondly, after the acquisition is ensured, the stable tracking of the satellite signals starts acting. At the end, the desired measurements can be extracted, which are the replica code phases and replica carrier Doppler phases. A brief overview of the signal processing and its main components is provided here. However, the primary focus is on the loop filters due to their relevance to this thesis. More details about each component and mathematical descriptions can be found, for example in Häberling (2016), Misra and Enge (2006) or Kaplan and Hegarty (2017).

Overview

The algorithm in Figure 2.3 represent one digital channel, which is responsible for one satellite and one frequency. Consequently, several channels are necessary for multi-GNSS and multi-frequency applications. Each channel consists of two main loops. The delay lock loop (DLL) is used for the code, which demodulates the PRN from the carrier and requires a smaller loop filter bandwidth, due to a noisy code signal (Häberling, 2016). However, it is not accurate enough to ensure a closed loop tracking. Therefore, a phase lock loop (PLL) is used in addition, which estimates and tracks the Doppler shifted signal. PLL can not act without a DLL, because the demodulation of the PRN is necessary beforehand. Both loops consist of three main components: A discriminator, a loop filter and a numerical controlled oscillator (NCO). These components are numerically implemented in the signal processing, why they often called digital. The main tasks of the loops is to align the replica signals, generated by the receiver, to the reference signal (IF). Therefore, the code time delay $\Delta\tau$ between both signals in the DLL and the phase shift $\Delta\theta$ in the PLL needs to be modified, so that these parameters are zero or constant. When this is achieved, the loops are in a locked state. Besides, a frequency lock loop (FLL) is usually implemented, however, it is generally used for the signal acquisition or when the carrier to noise density (C/N_0) is too weak for PLL operations. Here, the frequency shift Δf needs to be modified, in order to get a locked FLL.

Acquisition: Before the loops starts operating, the satellite signal has to be found in the IF data stream. Therefore, the PRN codes and the frequency Doppler are considered to set up a 2-D search space including different pairs of $\{\Delta\tau, \Delta f_D\}$. With particular search algorithms, each pair is statistically tested and compared with a specific threshold (Häberling, 2016). When finding a pair of $\{\Delta\tau, \Delta f_D\}$, which exceed this threshold, the satellite signal is found. Both, $\Delta\tau$ and Δf_D, are used as initial values for the lock loops. Tracking: The primary task of the lock loops is to refine these parameters and continuously track their variations (Misra and Enge, 2006). The acquisition process requires some time to get a first fix, which depends on the availability of ephemeris data in the receiver. Without this information, the time to first fix increase from 30 seconds up to 12.5 minutes, because the whole almanacs have to be acquired (Häberling, 2016).

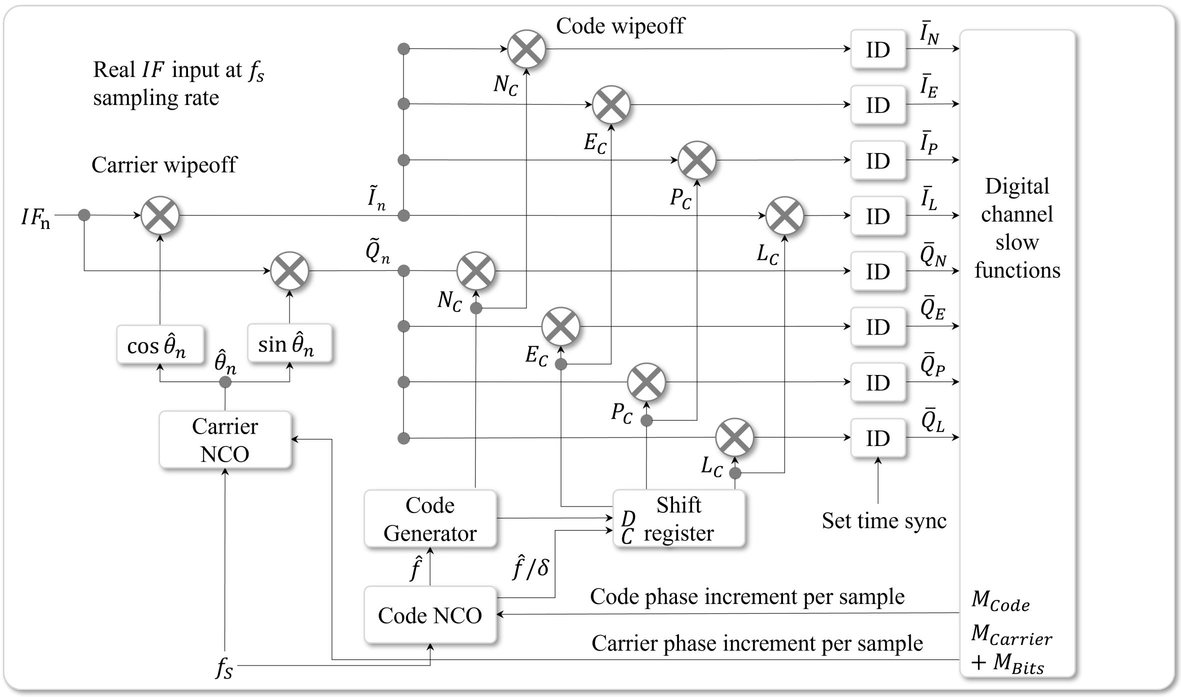

Figure 2.3: Closed loop fast function of a digital channel within GNSS receivers using real IF as input, based on Häberling (2016) and Kaplan and Hegarty (2017).

Closed Loop Fast Functions

In general, the NCO generates the new estimates of the code ($\Delta\tau$) and carrier phase (Δf_D) replica signal based on the outputs of the loop filter. These estimates are processed in the discriminator to align the replica to the reference signal, by either slowing down/speeding up the clock that controls the speed of the replica code generator or by synchronizing the frequency and phase. Each loop uses an individual NCO, namely the code NCO and carrier NCO. The latter is responsible for the baseband down conversation of the IF signal for generating a complex signal, with an inphase ($\tilde{I}$) and a quadrature ($\tilde{Q}$) part. This process is called phase rotation, Doppler removal or carrier wipe-off. When the estimated phase $\hat{\theta}_n$ of the carrier NCO equals the phase of the reference signal, $\tilde{I}$ becomes maximum and $\tilde{Q}$ contains noise only, which corresponds to a phase lock carrier-tracking loop (Kaplan and Hegarty, 2017).

However, remaining code samples are still contained in the signals, which are removed by a following code wipe-off process using particular correlators to combine the outcomes from the carrier wipe-off and the replica code phases. These code phases are generated by the code generator in combination with a shift register. They provide generally three different replica code phases, the early replica code (E_C), prompt (P_C) and late replica (L_C), with a typical shift between them of $\delta = 1/2$ chip. The replica signals are created using the outcomes (frequency $\hat{f}$ and frequency rate $\hat{f}/\delta$) from the code NCO, whereas these outcomes are estimated based on the ADC sampling clock f_S and the code phase increments per sample M_{Code}. In addition, the code generator creates a signal N_C, describing the noise behaviour of the signal, using a 2-chip early replica signal. This parameter is later used in a code noise meter, providing the noise power at the end. The four replica codes are further modified by an integrate and dump process (ID), which generally prepare the data for the discriminator by using different filter techniques, results in $\bar{I_N}$ (noise), $\bar{I_E}$ (early) ,$\bar{I_P}$ (prompt) and $\bar{I_L}$ (late).

Closed Loop Slow Functions

At this point, the so-called slow functions start operating. An overview is given in Figure 2.4. The early and late replica codes are responsible for the code loop discriminator. First, the code envelopes are calculated, considering the inphase and quadrature signal of the replicas. Here, a further ID step can be made, when a carrier aiding of the DLL is possible. Then, the ID process acts as a noncoherent filter, which increases the update rate of the code loop filter. If this is not possible, a noncoherent integration is done (Kaplan and Hegarty, 2017). The early and late envelopes (E and L) are used by the discriminator to align the replica with the reference signal, based on the early and late code phases.

An often used technique is the early-minus-late correlator, where the replica signal is shifted in time by $\Delta\tau$ until the difference between the early and late correlator in the autocorrelation function is zero. A detailed description about this process can be found e.g. in Misra and Enge (2006). Afterwards, the discriminator outcomes are processed in the code loop filter to produce an accurate estimate of the original signal by reducing the noise (Kaplan and Hegarty, 2017).

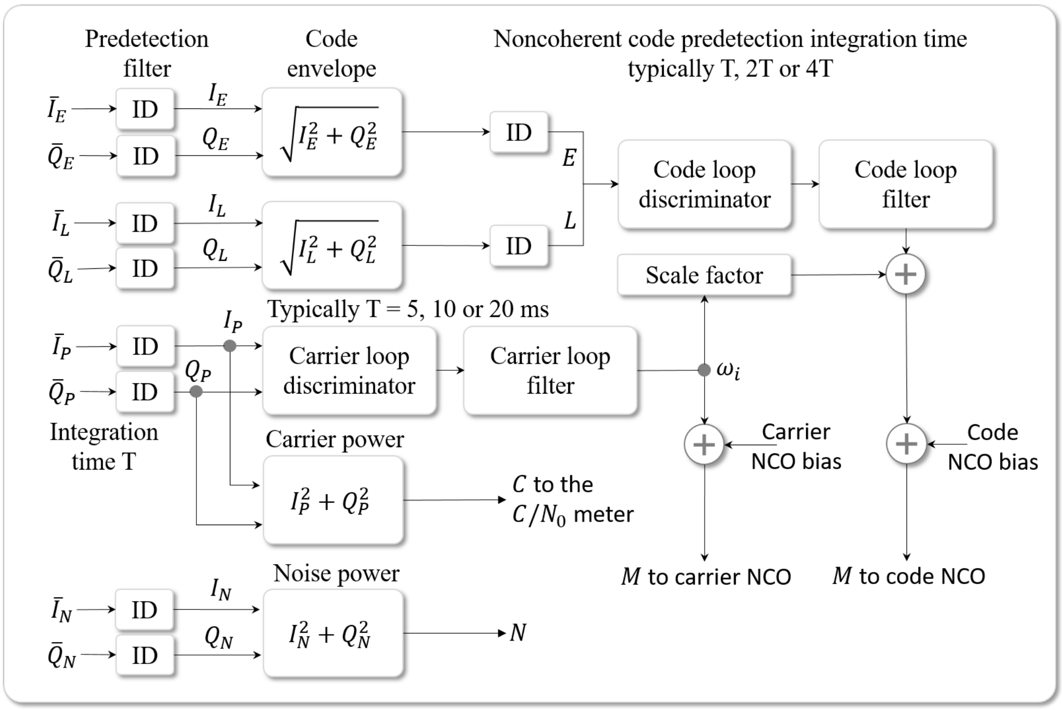

Figure 2.4: Closed loop slow function of a digital channel within GNSS receivers, based on Kaplan and Hegarty (2017).

Loop filters are discussed in the next section in more detail. A specific scale factor has to be considered and multiplied by the carrier loop filter outcome, when using a carrier aided DLL, because the amount of Doppler distinguishes between the code and carrier loop. To this end, a code NCO bias is added to get the code phase increment per sample M_{Code}, which is transmitted back to the code NCO.

A similar process is done for the carrier phase loop, however, the prompt signals I_P and I_Q are used. They are passing the carrier loop discriminator, to estimate the carrier phase error, followed by the carrier loop filter. The loop filter outcome is the Doppler frequency correction sample ω, necessary for the required carrier aiding DLL scale factor and for determining the carrier phase increments per sample $M_{Carrier}$ together with the carrier NCO bias. In addition, the prompt signals are used calculating the carrier power C, which is used in the code noise meter to generate C/N_0 values. The noise signals I_N and Q_N are obviously used for the noise power calculation N.

Closing Remarks Nearly all parts in the signal processing are usually done by the GNSS receiver manufacturer to ensure a stable satellite tracking and a good performance for the user. In general, an average user has no access to this. However, some parts can be modified to may optimize the performance in different GNSS applications, e.g. antenna calibration. Typically, some of the loop filter parameters can be changed, like the bandwidth or the carrier aiding. The amount of modifiable parameters highly depends on the manufacturer.

Table 2.1: Loop filter characteristics after Kaplan and Hegarty (2017). Note: ω_0 can be calculated with the chosen B_N.

Loop order	Noise bandwidth B_n [Hz]	Typical Filter Values	Steady state error
First	$\frac{\omega_0}{4}$	ω_0 $B_n = 0.25\omega_0$	$\frac{dR/dt}{\omega_0}$
Second	$\frac{\omega_0(1+a_2^2)}{4a_2}$	ω_0^2 $a_2\omega_0 = 1.414\omega_0$ $B_n = 0.53\omega_0$	$\frac{d^2R/dt^2}{\omega_0^2}$
Third	$\frac{\omega_0(a_3b_3^2+a_3^2-b_3)}{4(a_3b_3-1)}$	ω_0^3 $a_3\omega_0^2 = 1.1\omega_0^2$ $b_3\omega_0 = 2.4\omega_0$ $B_n = 0.7845\omega_0$	$\frac{d^3R/dt^3}{\omega_0^3}$

2.3.3 Loop Filter and Tracking Errors

Loop filters are responsible for reducing the noise of the discriminator outcomes to ensure an accurate estimate of the original signal (Kaplan and Hegarty, 2017). Many different designs and techniques exist, where each receiver manufacturer implemented its own. However, almost all the designs have two parameters in common that have to be chosen carefully to ensure a stable satellite tracking. These parameters are the loop order and the noise bandwidth B_n. Usually, they can be modified by the user in the manufacturers' receiver firmware. It provides default values for these parameters to ensure a stable receiver performance for many GNSS applications.

In general, the loop order and bandwidth are carefully determined, taking the signal dynamics, the environment, other receiver component, noise and required tracking precision of the signals into account. The noise bandwidth is mostly responsible for the noise behaviour of the signal. Reducing the bandwidth, which is in units of [Hz], results in a less noisy signal. However, it requires a longer predetection integration time T and computation time t_C, which can introduce delays in the closed loop and potentially lead to loop instabilities.

Kaplan and Hegarty (2017) investigate the loop stability by using the Bode analysis in detail. Here, the dimensionless product B_nT is considered for two phase margins: 0 deg and 30 deg. A stable loop tracking is ensured, when the B_nT product is smaller than the 30 deg margin threshold. Even with B_nT products larger than this threshold a stable tracking is possible, however, with an underdamped and distorted response. The loop will lose its lock, when the product is higher than the 0 deg phase margin.

For example, for a third order PLL a stable tracking is ensured, when $B_nT < 0.306$, whereas $B_nT > 0.558$ results in an unlocked loop. These values are valid, when no additional computation time is considered. By considering a computation time equals the predetection integration duration, $t_C = T$, B_nT must be smaller than 0.146 for a stable tracking and looses its locked state when $B_nT > 0.245$. This can be crucial in dynamic GNSS environments, for example in the robot-based antenna calibration, due to frequent changes in the antenna pose.

Typical filter values are presented in Table 2.1. By choosing the filter order and the noise bandwidth, all other required parameters for the loops can be calculated. Please note, that ω_0 can be calculated with the chosen bandwidth. In general, three different filter orders with particular characteristics can be used in DLL, FLL and PLL. The different loop filters for code and carrier lock loops are very similar. They distinguish mostly in the chosen loop order and noise bandwidth.

First order loop filters are mostly used for aided DLLs, because they are sensitive to velocity stress. Thanks to the carrier aiding, the DLL does not have to deal with dynamic stress. Therefore, a narrow bandwidth should be chosen (less than 1 Hz) to reduce the noise (Kaplan and Hegarty, 2017). Second order loops are sensitive to acceleration stress. They can be used in PLLs, when moderate dynamic application are executed. For higher dynamic application, a PLL third loop order should be used, because it is only sensitive to jerk stress. FLLs are generally using a loop filter order, which is one order lower than the PLL.

The remaining loop error (steady state error) can be calculated for each order using the line-of-sight (LOS) range R to the satellite. For example, for a satellite at the horizon, dR/dt is approximately 656 m/s, $d^2R/dt^2 \approx 0.02\,\mathrm{m/s^2}$ and $d^3R/dt^3 \approx 1.3 \cdot 10^{-3}\,\mathrm{m/s^3}$. By assuming a DLL B_n of 1 Hz and a correlator spacing of 1 chip, the natural frequency ω_0 equals 4 Hz for a first loop order ($4B_n = \omega_0$). The steady state error is typically given in units of chips for a DLL, thus, the velocity has to be converted by

$$v = \frac{656\,[\mathrm{m/s}]}{293.05\,[\mathrm{m/chip}]} = 2.24\,[\mathrm{chips/s}], \tag{2.23}$$

resulting in

$$\frac{dR/dt}{\omega_0} = \frac{v}{w_0} = \frac{2.24\,[\mathrm{chips/s}]}{4\,[\mathrm{Hz}]} = 0.56\,[\mathrm{chips}]. \tag{2.24}$$

The steady state error from the second and third order loops is $5.6 \cdot 10^{-3}$ chips and $6 \cdot 10^{-4}$ chips, respectively. Please note that the formulas for calculating ω_0 for the second and third loop order differs (cf. Table 2.1).

For a satellite at higher elevations (77 deg), $dR/dt \approx 89\,\mathrm{m/s}$, $d^2R/dt^2 \approx 0.1\,\mathrm{m/s^2}$ and $d^3R/dt^3 \approx 6 \cdot 10^{-6}\,\mathrm{m/s^3}$, resulting in a steady state error for the first loop order of $8 \cdot 10^{-2}$ chips, for the second order of $3 \cdot 10^{-3}$ chips and for the third order of $3 \cdot 10^{-6}$ chips.

When considering the FLL or PLL, the velocity, the acceleration, and the jerk must be converted into Hz and degrees, respectively. This transformation is detailed in Kaplan and Hegarty (2017).

In addition to the steady-state error of the different loops, several other error sources exist, which degrade the performance of the tracking loops and consequently the performance of the GNSS receiver itself. Kaplan and Hegarty (2017) give an overview about the dominant error sources and establish different rule of thumbs to evaluate tracking error thresholds for DLL, FLL and PLL. When the measurements exceed those thresholds, the loop loses its lock state. A brief overview about these error sources is presented in the following. Unless otherwise noted, all equations used are derived from Kaplan and Hegarty (2017).

Phase Lock Loop Measurement Error

The PLL measurement error can be approximated with

$$
\begin{aligned}
\sigma_{PLL_P} &= \sqrt{\sigma^2_{tPLL_P} + \sigma^2_\nu + \theta^2_A} + \frac{\theta_e}{3} \leq 30\,\mathrm{deg} \\
\sigma_{PLL_D} &= \sqrt{\sigma^2_{tPLL_D} + \sigma^2_\nu + \theta^2_A} + \frac{\theta_e}{3} \leq 15\,\mathrm{deg}
\end{aligned}
\tag{2.25}
$$

where σ_{tPLL_P} and σ_{tPLL_D} are errors, caused by thermal noise, σ_ν indicates errors, which occurring due to vibration-induced oscillator phase noise. Allan deviation oscillator noise is depicted with θ_A and θ_e defines the dynamic stress error. The combination of all error sources (Equation 2.25) should not exceed 30 deg for the pilot channel P (dataless) and 15 deg for the data channel D, otherwise the PLL loses its locked state.

The most dominant error source in PLLs is the thermal noise and can be calculated with

$$
\begin{aligned}
\sigma_{tPLL_P} &= \frac{360}{2\pi}\sqrt{\frac{B_n}{C/N_0}}\ [\mathrm{deg}] \\
\sigma_{tPLL_D} &= \frac{360}{2\pi}\sqrt{\frac{B_n}{C/N_0}\left[1 + \frac{1}{2TC/N_0}\right]}\ [\mathrm{deg}]
\end{aligned}
\tag{2.26}
$$

for both channels. The equations are similar, except the squaring loss part for the data channel. It is visible, that the error gets smaller, when B_n decreases. In addition, a higher C/N_0 of the satellite signal lead also to a better PLL performance. The predetection integration time T has only an impact on the squaring loss in the data channel, thus, a longer integration T leads to better performance.

The error, caused by the vibration-induced oscillator phase, can be approximated with

$$
\sigma_\nu = \frac{360 f_L}{2\pi}\sqrt{\int_{f_{min}}^{max} S^2_\nu(f_m)\frac{P(f_m)}{f^2_m} df_m}\ [\mathrm{deg}]. \tag{2.27}
$$

It has to be taken into account, when the oscillator experiences unexpected vibrations, e.g. in high dynamic applications. Therefore, the L band frequency of the GNSS signal f_L, the oscillator vibration sensitivity S_ν as a function of a random vibration modulation frequency f_m and the power curve $P(f_m)$ of this random vibration have to be considered.

PLL performance is also influenced by the short-term stability of the oscillator, which can be denoted by the Allan variance. With τ being the short-term stability gate of the Allan variance measurements and $\Delta\theta$ the root mean square (RMS) error of the phase discriminator, the Allan deviation $\sigma_A(\tau)$ can be calculated for a second order PLL $\sigma_{A2}(\tau)$ and third order $\sigma_{A3}(\tau)$:

$$
\begin{aligned}
\sigma_{A2}(\tau) &= 2.5\frac{\Delta\theta}{2\pi f_L \tau}, \\
\sigma_{A3}(\tau) &= 2.25\frac{\Delta\theta}{2\pi f_L \tau}.
\end{aligned}
\tag{2.28}
$$

By including $\sigma_{A2}(\tau)$ and $\sigma_{A3}(\tau)$ into Equation 2.29 the Allan deviation oscillator phase noise can be calculated:

$$\begin{aligned}\theta_{A2} &= 144\frac{\sigma_{A2}(\tau) f_L}{B_n} \text{ [deg]},\\ \theta_{A3} &= 160\frac{\sigma_{A3}(\tau) f_L}{B_n} \text{ [deg]}.\end{aligned} \tag{2.29}$$

The last error is caused by dynamic stress and can be derived from the steady-state error formulas in Table 2.1 for second and third loop order:

$$\begin{aligned}\theta_{e2} &= 0.2809\frac{d^2R/dt^2}{B_n^2} \text{ [deg]},\\ \theta_{e3} &= 0.4828\frac{d^3R/dt^3}{B_n^3} \text{ [deg]}.\end{aligned} \tag{2.30}$$

Frequency Lock Loop Measurement Error

In FLLs, the noise caused by oscillator vibrations and short-term stabilities can be neglected because their impact is not significant. Therefore, the 3σ FLL noise needs to be smaller than $1/(4T)$ Hz:

$$3\sigma_{FLL} = 3\sigma_{tFLL} + f_e \leq 1/(4T) \text{ [Hz]}. \tag{2.31}$$

The thermal noise σ_{tFLL} can be approximated with

$$\sigma_{tFLL} = \frac{1}{2\pi T}\sqrt{\frac{4FB_n}{C/N_0}\left[1 + \frac{1}{TC/N_0}\right]} \text{ [Hz]}, \tag{2.32}$$

where $F = 1$ for high C/N_0 values and $F = 2$ for low C/N_0.

The dynamic stress f_e can be approximated with

$$f_e = \frac{1}{360\omega_0^n}\frac{d^{n+1}R}{dt^{n+1}} \text{ [Hz]} \tag{2.33}$$

for the n^{th} loop order. The loop filter natural radian frequency order ω_0^n can be calculated based on B_n as presented in Table 2.1.

Delay Lock Loop Measurement Error

Similar to FLLs, DLLs are mostly influenced by thermal noise σ_{tDLL} and the dynamic stress R_e, when not using a carrier aided DLL. The 3σ noise $3\sigma_{DLL}$ must be below half of the early-late correlator spacing D to ensure a locked DLL:

$$3\sigma_{DLL} = 3\sigma_{tDLL} + R_e \leq D/2 \text{ [chips]}. \tag{2.34}$$

The thermal noise, expressed in units of chips, can be approximated as follows:

$$\sigma_{tDLL} \cong \begin{cases} \sqrt{\frac{B_n}{2C/N_0} D \left[1 + \frac{2}{TC/N_0(2-D)}\right]}, D \geq \frac{\pi R_c}{B_{fe}} \\ \sqrt{\frac{B_n}{2C/N_0} \left(\frac{1}{B_{fe}T_c} + \frac{B_{fe}T_c}{\pi - 1}\left(D - \frac{1}{B_{fe}T_c}\right)^2\right) \left[1 + \frac{2}{TC/N_0(2-D)}\right]}, \frac{R_c}{B_{fe}} < D < \frac{\pi R_c}{B_{fe}} \\ \sqrt{\frac{B_n}{2C/N_0} \left(\frac{1}{B_{fe}T_c}\right) \left[1 + \frac{1}{TC/N_0}\right]}, D \leq \frac{R_c}{B_{fe}} \end{cases} \tag{2.35}$$

The calculation of σ_{tDLL} depends on the double-sided front-end bandwidth B_{fe}, the spreading code rate R_c and the correlator spacing D. The chip period T_C is the reciprocal of R_c. The second part of each equation is considered as the squaring loss. It needs to be considered, when no information about the actual phase shift ($\Delta\theta$, outcome from PLL) is available (noncoherent DLL). When this information is provided by the PLL, the squaring loss is negligible and a coherent DLL is executed. Similar to the PLL thermal noise error, the bandwidth plays the major role for the noise performance. Reducing the bandwidth results in a smaller σ_{tDLL}. Also, a higher predetection integration time and C/N_0 values lead to a better DLL performance. Furthermore, the correlator spacing has an impact on the noise performance. Lowering the spacing decreases the noise, however, code tracking sensitivity to dynamics could get worse.

In case of an unaided DLL, the dynamic stress error has to be taken into account:

$$R_e = \frac{d^n R/dt^n}{\omega_0^n} \text{ [chips]}. \tag{2.36}$$

A carrier aided DLL removes all the dynamic stress on the code loop and R_e gets zero.

Closing Remarks Loop filters are used to ensure an accurate estimate of the original signal by reducing the noise of the discriminator outcomes. The noise bandwidth and the loop order are mainly responsible for the performance of the filter. They must be carefully selected, taking into account the environment, signal dynamics, and other receiver components to achieve a lock loop state. Typically, these parameters can be modified by an average user in the manufactures' software. Other noise influencing parameters, like the predetection integration time or the correlator spacing, are generally not changeable. To this end, the choice of the parameters is a trade-off between a less noisy GNSS signal and a stable tracking. For example, reducing the DLL bandwidth can significantly decrease noise on the codephase. However, if the bandwidth is reduced too much, the DLL may lose its lock state, resulting in the loss of important information in the GNSS signal. Section 4.2.3 will present the default loop settings of various hardware receivers used in this thesis and discuss their performance in the context of antenna calibration.

2.4 Observation Equation and Linear Combination

The previous sections described the GNSS satellite signals, as well as their reception by different types of antennas and processing in GNSS receivers. The outcome of the receivers are the actual pseudorange, carrierphase, signal strengths and Doppler observations of the satellite. This section describes these high-level observables and shows how they can be used in GNSS applications. The main focus lies on the pseudorange measurements. Section 2.4.1 introduces the GNSS observation equation and briefly describes the error sources, which are necessary to be considered in order to obtain an accurate observable for precise GNSS applications. The following Section 2.4.2 presents different differencing techniques to reduce or eliminate errors using one observation type and two stations and one satellite, or vice versa. There exist also techniques to linearly combine different types of observations and frequencies, when using only one station. Such a combination is called linear combination (LC) and is described in Section 2.4.3 for different commonly used LC.

2.4.1 Observations

A GNSS receiver processes the received satellite signals and stores the data in specific formats, defined by the receiver's manufacturer. The manufacturer usually provides a software, to convert the raw data to the common usable receiver independent exchange format (RINEX) (International GNSS Service, 2024). Typically, four different observation types are gathered in these files: The codephase/pseudorange, carrierphase, Doppler and signal strength, which are defined by a four digit character code. For example, 'GC1X' indicates the codephase measurement 'C' on the L1 carrier frequency '1' for the GPS system 'G' with the tracking method 'X'. In this contribution, this character code will be used to distinguish between different GNSS signals.

The codephase C_R^k and carrierphase measurements L_R^k of satellite k can be used for the GNSS positioning of the receiver R, however, they are affected by different error sources, which have to be taken into account to ensure a precise and accurate positioning:

$$\begin{aligned} C_R^k &= \rho_R^k + c\left(\delta t_R - \delta t^k\right) + T_R^k + I_{R,f}^k + MP_R + CPC_R^k + ... + \epsilon\,[\mathrm{m}], \\ L_R^k &= \rho_R^k + c\left(\delta t_R - \delta t^k\right) + T_R^k - I_{R,f}^k + N_f\lambda_f + MP_R + PCC_R^k + ... + \epsilon\,[\mathrm{m}], \end{aligned} \tag{2.37}$$

with the geometric distance between the receiver and the satellite ρ_R^k, the receiver and satellite clock error δt_R and δt^k multiplied by the speed of light c, as well as a delay caused by the troposphere T_R^k and the ionosphere $I_{R,f}^k$, which depends on the signal frequency f. It should be noted here, that the corrections for avoiding ionospheric delay have different signs for codephase and carrierphase. Additionally, for carrierphase measurements the unknown carrierphase ambiguity $N_f\lambda_f$ has to be taken into account. Both observables could be affected by multipath effects MP_R, which is described later in this section in detail.

Satellite signals are received at the electric phase center of the GNSS antenna, a point that lacks mechanical access and varies with the direction of the incoming signal. Therefore, CPC for the codephase measurement and PCC for carrierphase measurement must be considered to link the actual receiving point to the ARP, the well-defined point

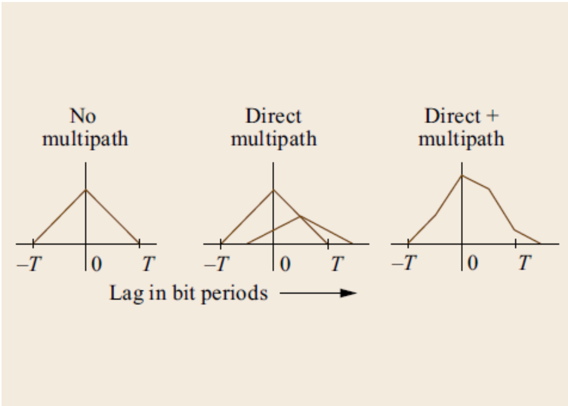

(a) Autocorrelation function

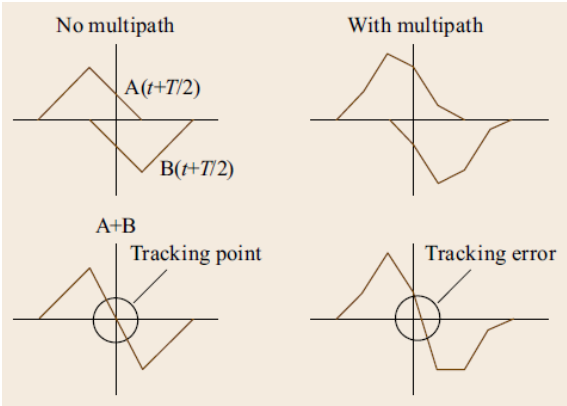

(b) Discriminator function

Figure 2.5: Autocorrelation (a) and discriminator function (b) with and without the presence of multipath (Braasch, 2017).

that is mechanically accesible. Their definitions and a detailed description about these corrections are provided in Section 3.2.

Besides, further error sources exist, indicated by the three dots in the Equation 2.37. Such effects are hardware delays in the receiver D_R and the satellite D^S, differential code biases, when using multi-frequency multi-GNSS applications, relativistic effects Rel_R^k and a phase-wind up (PWU) effect on the carrierphase, due to the satellite rotation around its boresight angle. Furthermore, orbital errors Orb^k occur, leading to variations in satellite coordinates and consequently impacting the geometric distance ρ_R^k. In robot-based antenna calibration, an additional PWU effect arises for the carrierphase measurement due to the robot motion, which must be taken into account. A detailed description of its modelling is provided in Section 3.3.3. All unmodelled effects are gathered in the parameter ϵ.

Thanks to the measuring setup of the robot-based antenna at IfE and the use of differenced observations, almost all error sources are cancelled out or reduced to negligible values (cf. Section 3.3.3). Thus, a detailed description of these errors is omitted in this thesis, but can be found, for example, in Langley et al. (2017).

Multipath

GNSS signals propagate through the atmosphere as electromagnetic waves. Instead of a straight single wave, a whole wavefront is continuously transmitted from satellites towards the Earth. Beside the direct wavefront, also a delayed wavefront can reach the antenna, caused by reflections in the antenna surrounding. The delayed signals induce interferences in the received GNSS signal, which leads to wrong pseudorange measurements.

Figure 2.5 (a) illustrates the presence of multipath effects in the autocorrelation function within a GNSS receiver. Here, a BPSK signal with an infinite bandwidth and a single multipath is shown. The receiver uses this function to shift the replica to the actual GNSS signal to achieve a locked DLL. The time delay in chips correspond to the pseudorange to a particular satellite. More details about this process can be found

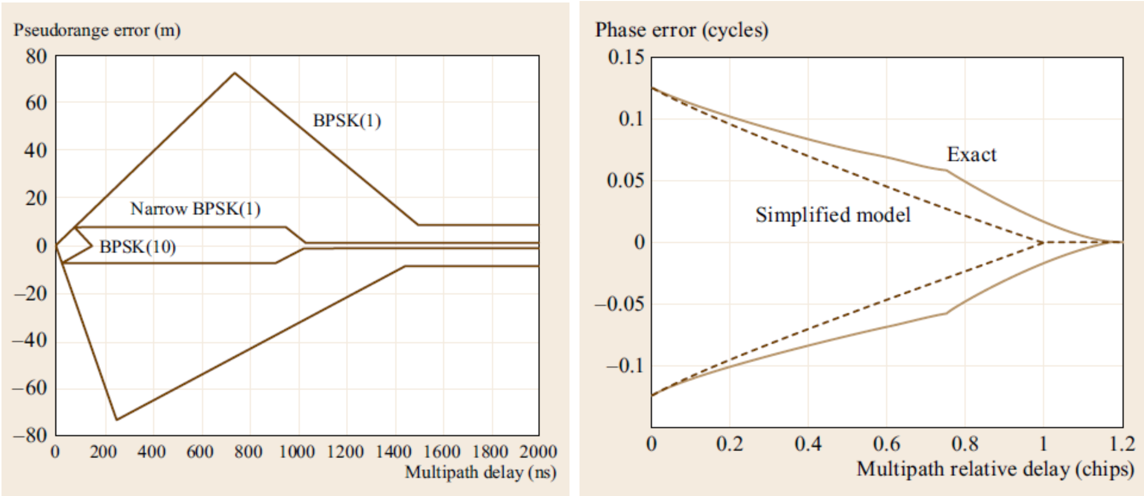

(a) Pseudorange error (b) Phase error

Figure 2.6: Pseudorange error (a) in presence of multipath with half the amplitude of the direct signal. Phase error (b), when using a coherent DLL and a correlator spacing of 1 chip (Braasch, 2017).

in Misra and Enge (2006) and will not be discussed here. The left subfigure (Figure 2.5 (a)) shows the autocorrelation function, when no multipath occurs. A multipath would lead to an additional delayed correlation peak with a smaller magnitude. This is depicted in the middle subfigure of Figure 2.5 (a), however, that does not correspond to reality. The right subfigure (Figure 2.5 (a)) present the actual autocorrelation function in presence of a multipath effect.

Figure 2.5 (b) shows the corresponding discriminator function (early-minus-late) of the example in (a). When no multipath occurs, the discriminator shows two prominent peaks with a zero crossing in between, which corresponds to the peak in the autocorrelation (prompt). A multipath delays this tracking point and leads to a tracking error in chips, which can be converted to a multipath pseudorange error in meter taking the chiplength into account.

An example of the amount of pseudorange errors due to multipath for three different signals is shown in Figure 2.6 (a). Here, the BPSK(1) with a correlator spacing of 1 chip is presented, as well as this signal with a correlator spacing of 0.1 chips (defined as narrow) and a BPSK(10) with a spacing of 1 chip. The magnitude of the multipath signal is assumed to be half of the directed signal. The number in the brackets of the BPSK defines the ratio between the frequency of the spreading code and the reference frequency, which is for example 1.023 MHz for GPS and Galileo signals. It is evident, that the error decreases, when the correlator spacing is reduced. Additionally, a BPSK(10) signal shows the smallest pseudorange error. The two curves of one signal forming an envelope, which defines the maximum and minimum multipath error.

The phase error, caused by multipath, is shown in Figure 2.6 (b). When a reflected signal in addition to a direct signal arrives at the antenna, the carrier tracking loops of a GNSS receiver measures the phase of a composite signal, which is the vector sum of the direct and multipath phasors (cf. Figure 2.7). The phase between the direct (zero by definition) and the composite signal is defined as the carrierphase measurement error θ_C, which corresponds to the phase of the composite received signal. The maximum mul-

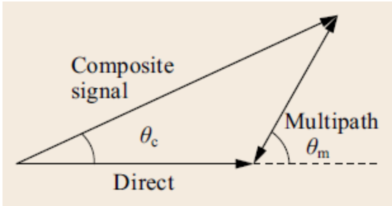

Figure 2.7: Sketch of the phasor diagram with the direct and multipath phasor. Their vector sum defines the composite signal (Braasch, 2017).

tipath error occurs, when the multipath phasor is orthogonal to the composite phasor (Teunissen and Montenbruck, 2017):

$$max(\theta_C) = \arcsin(A_M/A_D), \tag{2.38}$$

with A_M/A_D being the ratio between the amplitude of the multipath and the direct signal. The exact measurements in Figure 2.6 (b) have been computed and validated by Kalyanaraman et al. (2006), whereas the simplified model was developed by Van Nee (1993) and will not be discussed here.

Multipath effects can either occur when the satellite signal is reflected on a surface, resulting in directional or diffuse reflections, or by diffraction.

As the name already reveals, directional reflections are GNSS signal reflections on objects, where their angle of incidence equals their angle of reflection. This holds true for objects with a smooth surface, w.r.t. the GNSS signal wavelength. When the objects have irregularities in their surface, diffuse reflection can occur. Thus, the signal is not reflected at one specific point, as it is for directional reflections, but on many points with different reflection angles. The reflected signals have a random behaviour in terms of their amplitude, phase and polarization and are not so critical when viewed individually, but in total can lead to multipath effects with a receiver noise magnitude (Dilßner, 2007).

Diffraction occurs, when the satellite can be tracked by a receiver, even when the direct satellite LOS is blocked with an object, for example a building. This phenomenon can be explained by the Huygens–Fresnel principle, which says, that every point of a wavefront is the starting point of a new wavefront. To deal with diffraction effects can be very difficult.

In general, reflected signals change their polarization from a RHCP to a LHCP behaviour, when the reflection angle is smaller than the Brewster angle. This can be used in antenna design, where LHCP signals are in general attenuated to reduce the sensitivity to received multipath effects. The polarization of the GNSS signal is in general not changed for diffracted signals, which makes it more difficult for the receiver to distinguish between direct and diffracted signals. Even more challenging are multiple reflections, which often occur in urban areas. The polarization of the GNSS signal can be changed twice or more. This is critical for a receiver, because the reflected and the direct signal can have the same RHCP polarization, thus the antenna can not pre-filter the reflected signal.

GNSS signals are electromagnatic waves that propagate in a cone shape from the satellite towards the Earth. Thus, the reflection on objects are not limited to one specific point, but to a whole area around the antenna. This area is called Fresnel zone and can be estimated by using Fresnel ellipsoids. Fresnel ellipsoids are fictional ellipsoids, where the satellite and the antenna's projection onto the reflector surface are the focal points. The area of intersection between the ellipsoid and the reflector surface is defined as the Fresnel zone with the order of n, which defines the phase difference between direct and reflected signal by $n \cdot \lambda/2$. Most of the GNSS signal's energy is transmitted in the Fresnel ellipsoid with the order $n = 1$, whereat the surface area F of its corresponding Fresnel zone can be approximate by Dilßner (2007) with

$$F \approx \frac{\pi \cdot \lambda \cdot d}{\sin \vartheta}, \tag{2.39}$$

where ϑ defines the angle of incidence and d the distance between reflector surface and antenna. Fresnel zones can be a useful tool to identify critical objects in the surrounding of the antenna.

Another tool to analyse GNSS signals w.r.t. antenna's surrounding was developed by Icking et al. (2020). The authors split the received GNSS signals into two classes, line-of-sight (LOS) and non-line-of-sight (NLOS). The segmentation is based on a 3D CityGML model of Hannover's city with level of detail 2 (three-dimensional buildings with generalized roof shapes and height accuracy of ± 1 m). To do so, direct paths between the satellite and the antenna are considered. When these paths intersect with a building (polygon), the satellite is defined as NLOS, when no intersection occurs, the satellite is defined as LOS. This ray tracing algorithm was extended for diffracted signals by Schaper et al. (2022), for multipath signals by Icking et al. (2022) and validated by Baasch et al. (2022). To this end, the incoming GNSS can be defined as a NLOS, LOS, multipath, blocked or diffracted signal, however, the algorithm can consider only a single reflection by the time of writing this thesis.

2.4.2 Observation Differences

Single Differences

When two stations are used for a specific GNSS application, like real time kinematic (RTK) or antenna calibrations with a robot, the observations of the same type (codephase / carrierphase) and frequency from a particular satellite k of both stations A and B can be combined by subtracting them. This approach is called receiver-to-receiver single differences (SD):

$$SD^k_{A,B} = C^k_A - C^k_B. \tag{2.40}$$

For clarity, the codephase observations $C^k_{A/B}$ are considered, however, the approach for the carrierphase is similar. The benefit of this combination is, that all error sources caused by the satellite are cancelled out. This holds true for the satellite clock error δt^k, hardware delays in the satellite transmitting device D^S and satellite CPC, as well as remaining orbital errors Orb^k, so that:

$$\begin{aligned} SD^k_{A,B} =& \delta\rho^k_{A,B} + c\delta t_{A,B} + \delta T^k_{A,B} - \delta I^k_{A,B} + \delta MP^k_{A,B} \\ &+ \delta CPC_{A,B} + \delta D_R + \delta Rel^k_{A,B} + \epsilon. \end{aligned} \tag{2.41}$$

The δ terms stand for the remaining error sources between the two stations to the satellite k. Their amount depends on the baseline length for the atmospheric effects, the geometric distance and the relativistic effects. For example, for a very short baseline of few meters the impact of the troposphere can be neglected, because the tropospheric effects on both station are almost the same, so that this error is reduced to a negligible value. The larger the distance between the two stations, the higher is the remaining tropospheric effect. The differential hardware delays of the receivers as well as the differential receiver clock error depend on the used receiver, the δCPC on the used antennas and the differential multipath effect on the antenna's environment.

Besides, single differences (SD) can also be calculated between two satellites k and j and one station A, defined as satellite-to-satellite single differences:

$$SD_A^{k,j} = C_A^k - C_A^j. \tag{2.42}$$

The outcome of this combination is complementary to the receiver-to-receiver single differences. Here, all receiver dependent error sources are eliminated, like the receiver clock error δt_A and receiver hardware delays D_R, so that:

$$\begin{aligned} SD_A^{k,j} =& \delta\rho_A^{k,j} + c\delta t^{k,j} + \delta T_A^{k,j} + \delta I_A^{k,j} + \delta MP_A^{k,j} + \delta CPC^{k,j} \\ &+ \delta CPC_A + \delta D^S + \delta Rel_A^{k,j} + \delta Orb^{k,j} + \epsilon. \end{aligned} \tag{2.43}$$

The δ term defines now the remaining error sources between the two satellites k and j to the station A. The amount of the errors depends mostly on the relative position between the station and the two satellites, except the differential CPC and the differential hardware delays of the satellites. Whether the CPC of the station's antenna is cancelled out, depends highly on its pattern behaviour and the position of the two satellites. For example, the CPC can be very similar for satellites with the same elevation, when using an antenna with an azimuthal pattern behaviour. Then the differential CPC can be neglected. With satellites in complete different elevations, the CPC values differ and the corrections must be taken into account.

SD are a great approach to eliminate satellite or receiver dependent error sources, however, by combing two observations the noise is increased by a factor of $\sqrt{2}$.

Double Differences

When receiver- and satellite-dependent error sources need to be eliminated in one combination, double differences (DD) can be used. This approach is commonly used for GNSS networks. It involves subtracting two SD from each other, as follows:

$$\begin{aligned} DD_{A,B}^{k,j} &= SD_A^{k,j} - SD_B^{k,j} \\ &= (C_A^k - C_A^j) - (C_B^k - C_B^j) \end{aligned} \tag{2.44}$$

As a result, the error sources in the observations are significantly reduced. However, a comparatively small component of the geometric distance $\Delta\delta\rho$, the tropospheric effect $\Delta\delta T$, the ionospheric effect $\Delta\delta I$, the multipath effects $\Delta\delta MP$, the relativistic effects $\Delta\delta Rel$ as well as the receivers' $\Delta\delta CPC$ still remain. This leads to

$$\begin{aligned} DD_{A,B}^{k,j} =& \Delta\delta\rho_{A,B}^{k,j} + \Delta\delta T_{A,B}^{k,j} + \Delta\delta I_{A,B}^{k,j} + \Delta\delta MP_{A,B}^{k,j} \\ &+ \Delta\delta Rel_{A,B}^{k,j} + \Delta\delta CPC_{A,B} + \epsilon. \end{aligned} \tag{2.45}$$

Due to another differencing step, compared to the SD, the noise is further increased by a factor of $\sqrt{2}$. Compared to the raw observations (Equation 2.37), the noise is increased by the factor of 2.

Triple Differences

Raw carrierphase GNSS observations can experience cycle slips, which are phase jumps in the carrierphase that are integer multiples of the wavelength. A good example of this is when a satellite moves behind a tree from the antenna's point of view. The received signal becomes intermittent, nevertheless, the receiver continues to attempt tracking the satellite. Once the satellite becomes visible again, the receiver continues tracking, but may lose the correct amount of integer ambiguities between itself and the satellite, due to this interruption. This results in integer phase jumps in the observations. When the signal gap is too long, the receiver loses tracking entirely and starts a new tracking session when the satellite becomes visible again, necessitating the setup of a new initial ambiguity, which comes at the cost of observable satellite time.

Cycle slips can be effectively corrected during post-processing. However, identifying and correcting these jumps within raw GNSS observations can be challenging. Therefore, DD are considered, as cycle slips are highly prominent in these time series. A common technique to identify cycle slips in DD is the use of triple differences (TD). In this method, the DD are time differenced to produce the TD between epooch t_i and t_{i+1}:

$$TD_{A,B}^{k,j}(t_i) = DD_{A,B}^{k,j}(t_{i+1}) - DD_{A,B}^{k,j}(t_i). \tag{2.46}$$

A cycle slip appears as a peak in this time series. Once identified, the peak is used in the DD to correct all subsequent observations by the integer wavelength value of the peak itself. This process is repeated for each peak in the TD sequentially until no more cycle slips are present. The noise of TD increased by a factor of $2\sqrt{2}$ compared to the raw observation.

There are antenna calibration approaches that use TD as input for the estimation process, e.g. Willi (2019). Thanks to the rotating antenna, TD also maintain information about the antenna pattern.

2.4.3 Linear Combinations

Different observation types and frequencies can be combined with linear combinations, usable either for particular GNSS applications or for investigations of specific error sources. This section briefly describes some of the most commonly used combinations like the ionosphere-free LC, code-minus-carrier (CMC) LC, multipath LC and Melbourne-Wübbena (MW) LC. Here, combinations with two frequencies are considered. The following equations are taken from Teunissen and Montenbruck (2017), unless otherwise referenced.

Ionosphere-free LC

The ionosphere-free LC is the most important observable in relative positioning with baseline lengths larger than 10 km. Additionally, it is used for single point positioning approaches like precise point positioning (PPP). Rather than modelling the ionospheric impact, e.g. using the model from Klobuchar (1987), the first order ionospheric term, which includes approximately 99 % of the ionospheric effect on GNSS observations, can be eliminated by using this LC. To do so, observables of two different frequencies f_a and f_b are necessary. Because the ionosphere is a dispersive medium, the refraction of GNSS signals depends on their wavelength. This can be used to combine two codephase or carrierphase observations in different frequency bands f_a and f_b to get the ionosphere free observable C^k_{IF} and L^k_{IF} from satellite k:

$$\begin{aligned} C^k_{IF} &= \frac{f_a^2}{f_a^2 - f_b^2} C^k_a - \frac{f_b^2}{f_a^2 - f_b^2} C^k_b, \\ L^k_{IF} &= \frac{f_a^2}{f_a^2 - f_b^2} L^k_a - \frac{f_b^2}{f_a^2 - f_b^2} L^k_b, \end{aligned} \tag{2.47}$$

with C being the codephase measurement for frequency a and b and L being the carrierphase observation. This linear combination only eliminates the ionospheric influence, however, other error sources are still included in this linear combination and have to be considered in GNSS applications.

This linear combination results in a significant increase in noise. For example, using GPS L1 and L2 observations to calculate the ionosphere free LC, the noise would be increased by a factor of 3, approximately, and 2.6 for a GPS L1/L5 combination or a Galileo E1/E5a combination (Teunissen and Montenbruck, 2017).

Code-Minus-Carrier LC

The CMC LC is a very simple approach to eliminate the non-dispersive parts. As the name implies, the carrierphase observation L_a is subtracted from the codephase observation C_a with the same frequency:

$$CMC^k = C^k_a - L^k_a. \tag{2.48}$$

The ionospheric effect is still included in the CMC-LC, twice, because the ionosphere acts different on carrierphase and codephase observations (cf. Equation 2.37). Beside some other error sources, like multipath or satellite PWU, also the CPC and the PCC of the receiving and transmitting antenna are present.

Multipath LC

The multipath LC ($MPLC$) is a geometry and ionosphere free LC and can be computed using one codephase observation C_a and two carrierphase observations L_a and L_b from satellite k:

$$MPLC^k = C^k_a - L^k_a - 2 \cdot \frac{f_b^2}{f_a^2 - f_b^2} (L^k_a - L^k_b). \tag{2.49}$$

The $MPLC$ still contains some remaining error sources, like the CPC of the receiving antenna, signal biases and receiver noise, as well as the codephase multipath. In addition, differential PCC, differential PWU, differential carrierphase multipath, ambiguities, noise and signal biases between the two carrier frequencies are present (Teunissen and Montenbruck, 2017). This LC is mostly used in single station applications to study the noise behaviour of the receiver or the codephase multipath effect.

One of the main goals of this thesis is to understand the multipath within the antenna calibration and to find concepts to improve the estimation of CPC. One approach is to use this linear combination as input for the estimation process, because CPC information is still present in the $MPLC$. This method is described in Section 3.3.3 in detail.

Melbourne-Wübbena LC

The Melbourne-Wübbena LC was developed by Melbourne (1985) and Wübbena (1985) and is mostly used to detected cycle slips in the carrierphase. It is a combination of a carrierphase wide lane (WL) L_{WL} and a codephase narrow lane (NL) C_{NL}:

$$MW^k = L^k_{WL} - C^k_{NL}. \tag{2.50}$$

The codephase NL can be calculated with

$$C^k_{NL} = \frac{f_a C^k_a + f_b C^k_b}{f_a + f_b}, \tag{2.51}$$

and the carrierphase WL with

$$L^k_{WL} = \frac{f_a L^k_a - f_b L^k_b}{f_a - f_b}. \tag{2.52}$$

The wide lane is characterized by a large wavelength compared to the individual wavelength of GNSS signals, which benefits the integer ambiguity resolution, but at cost of the observation noise. For a GPS L1 and L2 combination, the noise of the carrierphase wide lane is increased by a factor of approximately 5.7, when using the L2 and L5 observation the noise even increase by a factor of approximately 33.2 (Teunissen and Montenbruck, 2017).

To reduce the noise impact, the MW-LC uses a codephase NL. The combination of carrierphase WL and codephase NL leads to an ionosphere and geometry free LC, so that only the WL ambiguity, biases, CPC and PCC of the receiving antenna and multipath effects are present. Kersten (2014) shows that the usage of CPC values can improve the ambiguity resolution in the MW-LC.

3

Absolute multi-GNSS Antenna Calibration at the Institut für Erdmessung

In highly precise GNSS applications, phase center corrections (PCC) have to be taken into account to ensure accurate positioning. GNSS signals are received in the electric phase center, which varies with the direction of the incoming signals. PCC describe the offset between the receiving point on the antenna hemisphere and the antenna reference point (ARP), which is typically the last mechanical component accessible for height measurement. Beside the corrections for carrier phase observations, also corrections for codephase signals exist, so called codephase center corrections (CPC). Both can be estimated using an absolute robot-based antenna calibration approach. This chapter focuses on this process and outlines the important steps involved. Section 3.1 briefly depicts different calibration methods and the current researches on PCC and CPC. In Section 3.2 the definition of these corrections is presented, as well as metrics for comparing the resulting pattern. Section 3.3 outlines the robot-based antenna calibration approach at Institut für Erdmessung, starting with the data acquisition and robot parameters and ends with the estimation approach.

3.1 Development of and Current Research on Antenna Calibration

First investigations about the necessity of phase center variations (PCV) have been published in the 1980s by e.g. Sims (1985). In the following years, two main approaches have been carried out for estimating PCV: The estimation in an anechoic chamber and with real GPS data in a short baseline approach with known point coordinates. Initially, PCV values represented the vertical and horizontal offsets between two antennas (Gurtner et al., 1989). Later, Breuer et al. (1995) and Rothacher et al. (1995) determined elevation-dependent PCV values between the two antennas. Based on these investigations, the relative antenna calibration approach was introduced by Mader and MacKay (1996) and Mader (1999). This approach is described, for example, in Menge (2003). In this setup, two antennas are utilized on a short baseline, with the correction values for one antenna constrained to zero. This allows the PCV determination of the other antenna relative to the first one. First multi-GNSS multi-frequency calibrations have been done by Schmolke et al. (2015). In a recent publication, Marut et al. (2024) use a relative calibration approach to estimate the phase center offset (PCO) of different low-cost GNSS antennas using the Bernese 5.2 software (Dach et al., 2015). The authors estimate the coordinates of the antennas relative to a reference antenna nearby and compare them with the known coordinates of their ARPs. They defined the differences as the antennas' PCO. However, these corrections are only valid for specific pairs of antennas. Thus, absolute corrections values are required.

One approach to estimate absolute antenna correction values involves using an anechoic chamber, where synthetically generated GNSS signals are used to determine these corrections. The first GPS PCV values were published by Schupler (2001). Further developments of this method were carried out, for instance, by Görres et al. (2006) and Zeimetz (2010). The authors determined the PCV of different receiver antennas and compared the results with absolute robot-based PCV values. First multi-GNSS multi-frequency PCV estimate in an anechoic chamber were published by Becker et al. (2010).

In addition to using an anechoic chamber, absolute antenna corrections can also be estimated with a robot in the field. The idea is to rotate and tilt an antenna under test (AUT) around a fixed point in space. By using time-differenced observations between the AUT and a reference in a short-baseline configuration, the PCV of the AUT are maintained, while the PCV of the reference are effectively eliminated. This approach was developed at IfE in close cooperation to the Geo++ company (Wübbena et al., 1996; Seeber et al., 1997; Menge et al., 1998; Wübbena et al., 2000; Böder et al., 2001; Seeber and Böder, 2002) and is described in Section 3.3 in detail. It is more cost-effective than older methods because the antenna rotation enables quicker and more thorough coverage of the antenna's hemisphere (Schmitz et al., 2002). Since 2005, the robot-based antenna calibration is an international standard within the global IGS network (Schmid et al., 2007). Antenna calibration at IfE, using a 5-axis robot, has been further developed and optimized in recent years. The approach has been extended to calibrate multi-GNSS, multi-frequency antenna PCV. Initial results were published by Kröger et al. (2019), Breva et al. (2019a), and Kröger et al. (2021), and further optimization of the approach is ongoing (Kröger et al., 2022; Kröger et al., 2024).

In recent years, more institutions have started using calibration robots to estimate absolute antenna correction values for carrierphase signals. Mader et al. (2012) presented their approach at the NGS using a 2-axis robot, which was later replaced by a 6-axis calibration robot (Bilich et al., 2018). Most other groups also use a 6-axis robot. The antenna group at ETH Zürich employs their 6-axis robot to calibrate all CDMA signals (GPS, Galileo, BDS) in a time differenced double differences approach (Willi et al., 2019; Willi, 2019), which is also utilized by the group at the University of Zagreb in Croatia. Preliminary results have been reported by Tupek et al. (2023). Initial findings from Wuhan University were documented by Hu et al. (2015), and recent developments for GPS and BDS-3 PCC were presented by Zhou et al. (2023). Sutyagin and Tatarnikov (2020) detailed the absolute antenna calibration approach at Topcon Positioning Systems. The group from Geoscience Australia uses a 5-axis robot (Riddell et al., 2015), similar to the robot used at IfE and Geo++.

Since 2022, a ring calibration is carried out, which studies the calibration results of different methods and agencies. Seven facilities using robot-based antenna calibration (IfE, Geo++, Topcon, NGS, ETH Zürich, Wuhan University and Geoscience Australia) and two facilities using an anechoic chamber (Deutsches Zentrum für Luft- und Raumfahrt (DLR), University of Bonn) are participating in this project. Six different antennas have been selected, which are calibrated by the different institutaions, using their particular calibration method and infrastructure. First results have been presented by Kersten et al. (2024a) and Kersten et al. (2024b) on international conferences. This project focuses on the calibration of carrierphase frequencies.

CPC, in literature often referred to GDV, becomes more important in aeronautic navigation. While CPC represents the actual correction that must be included in the observation equation (cf. Equation 2.37), GDV describe the resulting effect. Murphy et al. (2007) have been carried out in a practical experiment that GDV impact the positioning accuracy. However, for a long time, they have not been included in the aircraft position protection level calculations. First analyses on this have been done by Raghuvanshi and van Graas (2016). The RTCA DO-301 (Hegarty et al., 2015) defines limits of the GDV for L1 GNSS antennas. An antenna, which barely meets these requirements, would lead to a 75 cm ranging error for satellites at low elevation (Harris et al., 2017). Further investigation on GDV in aeronautics have been done by Caizzone et al. (2017), Caizzone et al. (2019) and Caizzone et al. (2022), where the authors also investigates multipath and pseudorange errors, caused by GDV. They estimate the receiver antenna GDV, among other antenna parameters like the antenna gain, in an anechoic chamber.

First absolute GDV for geodetic receiver antennas have been published by Wübbena et al. (2008) using a robot in the field. At IfE, Kersten (2014) adopted the calibration approach for estimating PCC to codephase observations and presented CPC values for various patch and geodetic choke ring antennas and showed that CPC can reach up to several decimeters. Considering CPC in code-carrierphase LC can benefit the integer ambiguity resolution. Kersten and Schön (2017) using CPC in the MW-LC and show that integer ambiguity phase jumps can be corrected by taking CPC into account. In recent years, the absolute robot-based antenna calibration algorithm at IfE has been further developed and optimized for estimating multi-GNSS multi-frequency CPC (Breva et al., 2019b). In order to estimate CPC accurately and precisely, the challenge is to deal with the very noisy codephase observable. Breva et al. (2022) applied the empirical mode decomposition (EMD) method on the codephase observable and were able to reduce its noise, which results in an improvement in the CPC estimation repeatability. Another possibility for the noise reduction is the optimization of the GNSS receiver tracking loops. First analysis have been done by Breva et al. (2024) using a software receiver, which allows investigations of tracking loop parameters in post-processing. Investigations based on this are carried out in this thesis. A set of multi-GNSS multi-frequency GDV for different receiver antennas have been published by Wübbena et al. (2019) using a robot in the field.

Beside CPC for receiving GNSS antennas, there exist also CPC for satellite transmitting antennas. First results for satellite GDV were published by Wanninger and Beer (2015) for the second generation of BDS medium Earth and inclined geosynchronous orbiting satellites. The authors used a CMC approach in a global network to estimate relative GDV for these BDS satellites. First relative GDV for GPS satellites have been published by Wanninger et al. (2017) using the same CMC approach. Further, Galileo and GLONASS relative GDV have been calculated by Beer et al. (2019). Thanks to their non-sideral repetition, a global network is not required any more, making the data acquisition easier. After Wübbena et al. (2019) published absolute multi-GNSS multi-frequency GDV for several receiver antennas, Beer et al. (2021) were able to estimate absolute satellite GDV with their CMC approach. Beer (2022) explained the overarching research context of the aforementioned literatures in her dissertation.

3.2 Antenna Correction Values

In high precise GNSS applications, corrections of the used antenna have to be taken into account. There exist corrections for the carrierphase and for the codephase. Their definition is presented in Section 3.2.1. Additionally, different strategies for comparing different sets of antenna correction values are given. To this end, the corrections are provided in the antenna exchange format, which is described in Section 3.2.3.

3.2.1 Definitions

For almost all GNSS applications, it is necessary to know the correct height of the antenna. The height is the distance between the antenna reference point (ARP) and the measured point on the plumb line, e.g. a marked point on the ground. In general, the ARP is the lowermost antenna element with mechanical access for height measurement, usually the bottom of the 5/8" thread, which is used to connect the antenna to a tripod or other devices. However, GNSS signals are not received at the ARP, but at the electric phase center of the antenna. This displacement has to be taken into account, so that the signals are projected onto the ARP to get the correct coordinates. It can be described by phase center corrections (PCC) for carrierphase and codephase center corrections (CPC) for codephase GNSS signals, which are also known as group delay variations (GDV) in the literature (cf. Section 3.1).

According to Rothacher et al. (1995), Wübbena et al. (2000) or Menge (2003) the realization of PCC of a GNSS signal is based on three different conditions:

- Definition/existence of an ARP,
- Determination of a phase center offset (PCO),
- and corresponding phase center variations (PCV).

The PCO describes a three-dimensional offset between the ARP and the mean electric phase center. This point is located at the center of a sphere, which is approximated by the actual phase front of the antenna. The PCO consists of a North, East and Up component in the antenna coordinate system, where the ARP defines the origin. The North axis pointed towards a predefined north marker of the antenna, which is often the antenna cable connector. The Up axis is defined as the direction from the ARP towards the antenna's zenith direction, and the East axis completes the left-handed system.

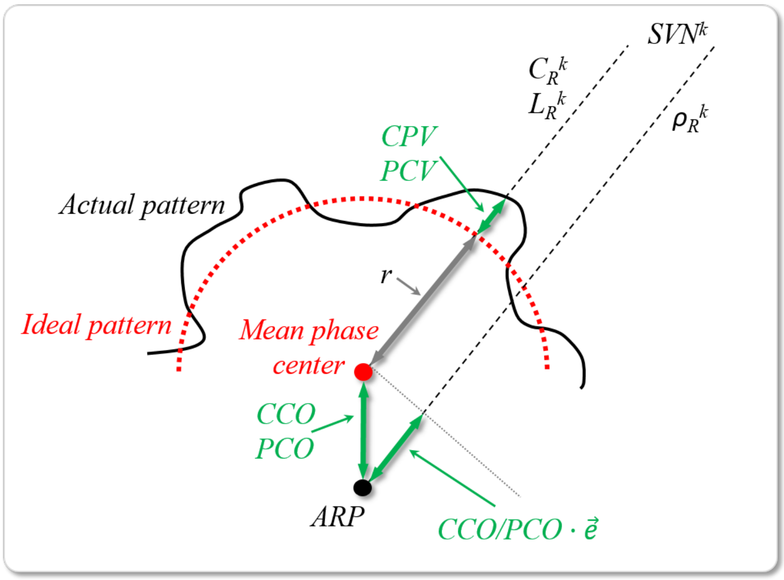

Figure 3.1: Geometric interpretation of CCO/PCO, CPV/PCV and parameter r.

For an ideal isotropic antenna, the PCO would perfectly describe the receiving behaviour of GNSS signals, however, it is not possible to actual build such antennas. Due to different construction elements in the antenna design, the ideal phase front and the actual receiving phase front of the signals differ. These differences are defined as PCV and depend on the direction of the incoming signal. Therefore, the PCC can mathematically be described as:

$$PCC(\alpha^k, z^k) = -PCO \cdot \vec{e}(\alpha^k, z^k) + PCV(\alpha^k, z^k) + r. \tag{3.1}$$

with $PCC(\alpha^k, z^k)$ describing the corrections, which are added in the carrierphase observation equation (Equation 2.37) for a satellite k visible at an azimuth α and zenith angle z. The PCO values are projected onto the LOS vector to the satellite $\vec{e}(\alpha^k, z^k)$.

Besides the $PCV(\alpha^k, z^k)$ also the parameter r is included in the equation. This parameter describes the radius of the ideal isotropic pattern, however, it is difficult to estimate and is not given in the antenna files (cf. Section 3.2.3). Thanks to its constant behaviour, r is absorbed in the estimated receiver clock error and has no impact in positioning applications.

The named definitions are valid for PCC, but can also be used for CPC (Kersten, 2014). Thus, the CPC are divided into a codephase center offset (CCO) and their corresponding codephase center variations (CPV), similar to the PCC (International GNSS Service, 2010):

$$CPC(\alpha^k, z^k) = -CCO \cdot \vec{e}(\alpha^k, z^k) + CPV(\alpha^k, z^k) + r. \tag{3.2}$$

It should be noted, that the CCO and the PCO for the same antenna are not identical.

Figure 3.1 shows a geometrical interpretation of the relation between CCO/PCO, CPV/PCV, ARP as well as the parameter r. In Equation 3.1 and 3.2 the PCO/CCO has a negative sign, which is not directly visible in this figure, or other figures in the literature (Kersten (2014), Kröger et al. (2021), Breva et al. (2022)). To avoid misleading interpretation, a short mathematical interpretation is depicted here. Assuming, that all error sources in the carrierphase measurements L_R^k from a receiver R are corrected, except the geometric distance ρ_R^k and the PCO_R^k, already projected onto LOS of the satellite k, than

$$\begin{aligned} L_R^k &= \rho_R^k - PCO_R^k \\ L_R^k + PCO_R^k &= \rho_R^k. \end{aligned} \tag{3.3}$$

L_R^k are the actual measurements, which are received at the electric phase center of the antenna. The geometric distance ρ_R^k contains the requested receiver coordinates, which is the ARP. This proofs the negative sign of the PCO, respectively CCO, in the calculation of PCC/CPC and the correctness of the graphical representation.

3.2.2 Comparison Strategies

From here onwards, only the PCC will be discussed for clarity, however, it is also valid for CPC. PCV values are always related to a particular PCO. By combing them, with Equation 3.1, PCC can be calculated. Though, one PCC value can be represented by different PCO and PCV combinations (Menge, 2003):

$$\begin{aligned} PCC(\alpha^k, z^k) &= -PCO_1 \cdot \vec{e}(\alpha^k, z^k) + PCV_1(\alpha^k, z^k) \\ &\vdots \\ &= -PCO_n \cdot \vec{e}(\alpha^k, z^k) + PCV_n(\alpha^k, z^k), \end{aligned} \tag{3.4}$$

with n being the number of combination. This allows, e.g. the transformation of different patterns onto a common PCO, for a better comparison. It is also possible to study the impact of different effects on the PCC, like a height offset. The parameter r is not included in Equation 3.4. Because of the challenges in estimating this parameter arising from the time differencing approach in robot-based antenna calibration, and its constant behaviour, PCC values are estimated using a particular datum. This allows the comparison between different pattern. Two common datum definition exist (Kersten et al., 2022):

- The PCV values in zenith directions are set to zero (zero zenith constraint),
- The PCV values over the whole (or partly) antenna hemisphere have a zero mean (zero mean constraint).

The most common approach is the zero zenith constraint, which is used by the majority of absolute antenna PCC in the *NGS20 absolute ANTEX file* (cf. Section 3.2.3). The second datum is often used for calibrations within an anechoic chamber.

When two pattern should be compared, either for calibration repeatability purposes or comparison between different calibration agencies, PCV and PCO values should always be considered together (Kersten et al., 2022). As Equation 3.4 suggests, the same PCC can have a completely different PCO. Therefore, it is not recommended to compare the PCO, only. The best way to compare patterns is to calculate the difference pattern by setting up the *PCC* of the two individual pattern as a grid (usually 73x19 for a 5 degree grid width) using Equation 3.1 (without r) and subtract them from each other:

$$\Delta PCC = PCC_1 - PCC_2. \tag{3.5}$$

The difference pattern (ΔPCC) gives information about differences in PCO, PCV as well as information about different datum definition or constraints. From this pattern, several scalar comparison metrics can be derived:

- Minimum, Maximum difference of ΔPCC,
- Range: $max(\Delta PCC) - min(\Delta PCC)$,
- Spread: $max(\Delta PCC_1) - min(\Delta PCC_1) - (max(\Delta PCC_2) - min(\Delta PCC_2))$,
- Standard deviation and RMS of ΔPCC,
- Correlation coefficients using image similarities (Kröger et al., 2022).

In this thesis, the main focus is on CPC. Therefore, the difference pattern (ΔCPC) of the codephase is considered. The above-mentioned comparison metrics will be analysed and used, except the correlation coefficients from Kröger et al. (2022). More information about these parameters can be found in Schön and Kersten (2013) or Kersten et al. (2022).

3.2.3 ANTEX File

At the time of writing this thesis, the current standard for providing antenna correction values is antenna exchange format (ANTEX) version 1.4. The definition of an *.atx* file was published in 2010 and is based on the work of Rothacher and Mader (2002) and Schmid et al. (2005). It is publicly available on the International GNSS Service (IGS) website and applies to both satellite transmitting antennas and receiver antennas. Each file begins with a header section, which lists the ANTEX version along with the included satellite systems. The systems are indicated by specific letters for each GNSS: GPS (G), GLONASS (R), Galileo (E), BDS (C), Quasi-Zenith Satellite System (QZSS) (J), and Satellite Based Augmentation System (SBAS) (S). If the file contains more than one GNSS, the identifier (M) is used. Alongside some metadata, the calibration method is also listed, indicating either absolute (A) or relative (R) calibration.

```
                                                            START OF ANTENNA
LEIAR25         NONE                                        TYPE / SERIAL NO
ROBOT               Geo++ GmbH              5    03-APR-13 METH / BY / # / DATE
     5.0                                                    DAZI
     0.0  90.0   5.0                                        ZEN1 / ZEN2 / DZEN
     4                                                      # OF FREQUENCIES
IGS20_2233                                                  SINEX CODE
Number of Calibrated Antennas GPS:      005                 COMMENT
Number of Individual Calibrations GPS:  010                 COMMENT
Number of Calibrated Antennas GLO:      005                 COMMENT
Number of Individual Calibrations GLO:  010                 COMMENT
# GLONASS PCV                                               COMMENT
#  derived from Delta PCV per 25.0 MHz                      COMMENT
#  for frequency channel number k=0                         COMMENT
   G01                                                      START OF FREQUENCY
     +1.41     +1.00   +155.34                              NORTH / EAST / UP
   NOAZI   +0.00   +0.16   +0.61   +1.22   +1.82   +2.23   +2.30   +1.98   +1.29   +0.36   -0.63   -1.52   -2.17   -2.48   -2.35   -1.67   -0.26   +2.02   +5.15
     0.0   +0.00   +0.10   +0.52   +1.15   +1.82   +2.33   +2.49   +2.21   +1.52   +0.58   -0.44   -1.33   -1.96   -2.26   -2.18   -1.61   -0.37   +1.74   +4.74
     5.0   +0.00   +0.09   +0.51   +1.14   +1.81   +2.31   +2.46   +2.17   +1.47   +0.51   -0.53   -1.43   -2.08   -2.41   -2.35   -1.82   -0.62   +1.46   +4.47
    10.0   +0.00   +0.09   +0.50   +1.12   +1.79   +2.29   +2.43   +2.13   +1.42   +0.44   -0.61   -1.53   -2.19   -2.54   -2.51   -2.00   -0.83   +1.23   +4.24
    15.0   +0.00   +0.08   +0.49   +1.11   +1.77   +2.27   +2.40   +2.10   +1.38   +0.38   -0.68   -1.61   -2.29   -2.64   -2.63   -2.15   -0.99   +1.06   +4.08
    20.0   +0.00   +0.08   +0.48   +1.10   +1.76   +2.25   +2.38   +2.07   +1.34   +0.34   -0.73   -1.67   -2.35   -2.71   -2.71   -2.23   -1.09   +0.97   +4.01
    25.0   +0.00   +0.08   +0.48   +1.09   +1.75   +2.23   +2.36   +2.05   +1.32   +0.32   -0.75   -1.70   -2.39   -2.75   -2.75   -2.26   -1.10   +0.96   +4.02
    30.0   +0.00   +0.08   +0.47   +1.08   +1.73   +2.22   +2.35   +2.04   +1.31   +0.31   -0.76   -1.70   -2.39   -2.75   -2.74   -2.23   -1.05   +1.04   +4.11
    35.0   +0.00   +0.08   +0.47   +1.08   +1.72   +2.21   +2.34   +2.03   +1.32   +0.32   -0.74   -1.69   -2.37   -2.73   -2.69   -2.15   -0.92   +1.20   +4.27
    40.0   +0.00   +0.07   +0.47   +1.07   +1.72   +2.20   +2.33   +2.04   +1.33   +0.35   -0.71   -1.65   -2.33   -2.67   -2.61   -2.03   -0.75   +1.41   +4.47
    45.0   +0.00   +0.07   +0.46   +1.07   +1.71   +2.19   +2.33   +2.04   +1.34   +0.37   -0.68   -1.61   -2.28   -2.61   -2.51   -1.88   -0.55   +1.64   +4.68
    50.0   +0.00   +0.08   +0.46   +1.06   +1.70   +2.18   +2.32   +2.04   +1.35   +0.40   -0.64   -1.56   -2.23   -2.54   -2.41   -1.73   -0.35   +1.88   +4.89
    55.0   +0.00   +0.08   +0.46   +1.06   +1.70   +2.17   +2.31   +2.03   +1.36   +0.42   -0.61   -1.52   -2.18   -2.48   -2.32   -1.60   -0.16   +2.09   +5.06
```

Figure 3.2: Example of PCC from a receiving antenna (LEIAR25 NONE) is presented (International GNSS Service, 2010)

```
                                                            START OF ANTENNA
BLOCK IIA           G01                 G032      1992-079A TYPE / SERIAL NO
                                             0    29-JAN-17 METH / BY / # / DATE
     0.0                                                    DAZI
     0.0  17.0   1.0                                        ZEN1 / ZEN2 / DZEN
     2                                                      # OF FREQUENCIES
  1992    11    22     0     0    0.0000000                 VALID FROM
  2008    10    16    23    59   59.9999999                 VALID UNTIL
IGS20_2317                                                  SINEX CODE
   G01                                                      START OF FREQUENCY
    279.00      0.00   2253.47                              NORTH / EAST / UP
   NOAZI   -0.80   -0.90   -0.90   -0.80   -0.40    0.20    0.80    1.30    1.40    1.20    0.70    0.00   -0.40   -0.70   -0.90   -0.90   -0.90   -0.90
   G01                                                      END OF FREQUENCY
   G02                                                      START OF FREQUENCY
    279.00      0.00   2253.47                              NORTH / EAST / UP
   NOAZI   -0.80   -0.90   -0.90   -0.80   -0.40    0.20    0.80    1.30    1.40    1.20    0.70    0.00   -0.40   -0.70   -0.90   -0.90   -0.90   -0.90
   G02                                                      END OF FREQUENCY
                                                            END OF ANTENNA
```

Figure 3.3: Example of PCC from the GPS PRN 1 satellite (International GNSS Service, 2010)

The antenna section follows the header descriptions. An example of a receiving antenna is shown in Figure 3.2 and an example of a satellite transmitting antenna is shown in Figure 3.3. Each antenna has its own section, beginning with *START OF ANTENNA* and ending with *END OF ANTENNA*. An additional header for each antenna includes details such as the type and serial number of the antenna, the calibration method, the calibration agency, and the date of the calibration, followed by the grid width definition for the antenna correction values. Typically, a grid width of five degrees is used. In addition to some commentary, the number of calibrated frequencies is provided, which determines the number of subsequent sections, bounded by *START OF FREQUENCY* and *END OF FREQUENCY*. Each frequency is represented by three characters, with the first character indicating the GNSS and the next two characters representing the frequency itself. For instance, G01 refers to the GPS L1 signal.

As previously mentioned in Section 3.2.1, the PCC values are divided into PCO and PCV. The PCO is presented as North, East, and Up components, followed by the PCV. The first column shows only the *NOAZI*, an elevation-dependent PCV. To calculate *NOAZI*, all PCV within a specific elevation bin are typically averaged. For antennas without azimuthal pattern variations, this is sufficient. However, for antennas with significant azimuthal variations, additional information about the PCV in different azimuth directions is necessary. Therefore, the following values represent the PCV in a grid format, beginning with the azimuth angle in the first row. Subsequent rows display values from zenith down to the horizon, from left to right, in steps defined by the grid width. This is the typical representation but depends on the header definitions. All values are expressed in millimeters.

This process is repeated for each calibrated frequency. It is important to note that each entry has a specified character length and position. For example, the antenna type and serial number must be 20 characters long, and the PCO components have fixed positions, among other formatting rules.

A comprehensive collection of correction values for various satellite and receiving antennas is provided by the NGS in the form of the *NGS20 absolute ANTEX file*, which is publicly available on their website. The latest version was released in 2020, compiling calibration results from several agencies. Beginning with some metadata, the file includes PCC values for all GNSS satellites. For GPS and GLONASS satellites, PCO and *NOAZI* PCV values are currently available. Additionally, for Galileo and QZSS, the complete PCV grid is listed. For BDS satellites, only the PCO components are published. Furthermore, the file includes PCC for several receiving antennas. However, these are type mean values for antenna types. A type mean of an antenna is defined as the average result from different antennas of the same type (e.g., LEIAR25.R3 NONE), but with different serial numbers. The differences among these antennas can be quite significant. Therefore, it is recommended to use individual antenna correction values for the specific antenna in highly precise GNSS applications. Different agencies, such as IfE, can calibrate antennas to provide individual antenna patterns. The provided antenna correction values conform to ANTEX standards. If a type mean value suffices for a particular GNSS application, the NGS provides separate *.atx* files for various antennas from different brands on their website.

The ANTEX version 1.4 met the requirements and needs of the geodesy community at that time. However, interest in PCC as well as CPC has increased in recent years, indicating that the standards need updating. For instance, the current version does not address CPC at all. Additionally, accuracy information for the correction values is not considered. They are currently assumed to be perfect. However, uncertainties in the estimation process do exist, affecting the resulting antenna pattern, as Kröger (2025) demonstrates in his work. These uncertainties can arise from various sources such as the robot model, estimation approach, observation noise, robot environment, and more. Given that the current standards do not provide CPC, the estimated CPC in this thesis are incorporated into the current ANTEX version 1.4. The three-character frequency indicator is thus adapted so that the second character is set to 'C' when codephase frequencies are included. For example, the GPS C/A codephase on the L1 frequency is designated as 'GC1' in the ANTEX file.

3.3 Antenna Calibration Algorithm in Detail

At IfE, a robot is used for calibrating GNSS receiver antennas. The robot is installed on a pillar on the laboratory rooftop at the Geodetic Institute Hannover (GIH) building, indicated as MSD7 in Figure 3.4. Additionally, a reference antenna is essential for estimating absolute multi-GNSS multi-frequency PCC and CPC. It is located on pillar MSD8, with both forming a short baseline of approximately eight meters. Precise coordinates with sub millimeter accuracy of the pillar network are available, measured

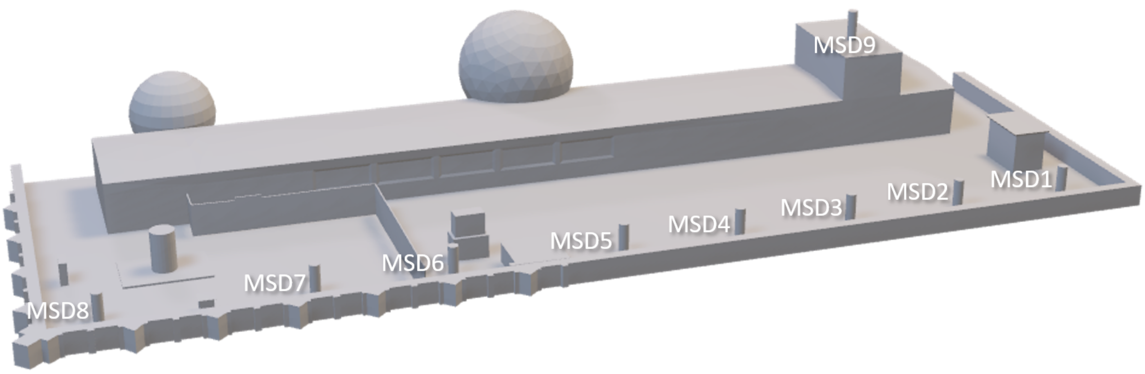

Figure 3.4: 3D model of the laboratory rooftop of the GIH.

in a relative positioning approach by Koppmann (2018). The antenna to be calibrated, referred to as the AUT, is mounted on the robot, which tilts and rotates the AUT around a fixed point in space. This is necessary to preserve the pattern information during the antenna calibration process. Each antenna is connected to a GNSS receiver, with both receivers being of the same brand and type. Additionally, both receivers are linked to an external frequency standard (Rubidium FS725) with a stability of $2 \cdot 10^{-11}$ @1 s. With this, a short-baseline common-clock setup is achieved, which allows forming time differenced receiver-to-receiver single differences (ΔSD). Except the AUT's PWU, differential multipath effects (cf. Section 5.2), unmodelled effects and the pattern information of the AUT, all error sources are either eliminated or reduced to a negligible value. The robot is precisely leveled using a precise leveling device (Zeiss Ni2 with an accuracy of 0.15 mm per 100 m) and oriented towards geographic North. This orientation is achieved by estimating the *north offset* O_N, which represents the angle between the geographic North and the robot's initial tilting direction. Therefore, the robot is first tilted by 90 deg in its initial tilting direction, and then a second time by 90 deg in the direction opposite to its initial tilt. In both robot poses, the geographic coordinates are estimated.

This section outlines the main components of the antenna calibration algorithm at IfE, as depicted in Figure 3.5. Section 3.3.1 focuses on the calibration robot and the calculation and necessity of a robot model. Additionally, it presents the determination of all required module poses, which are necessary either to set up the robot model or to transform the observations into the antenna frame to link the pattern information to the actual position on the antenna hemisphere. This is detailed in Section 3.3.2. To mitigate multipath effects and enhance the quality of the estimation inputs, different obstruction masks can be applied. Afterwards, Section 3.3.3 outlines the actual observations used as estimation inputs for the estimation approach, which is also explained in this section. At the end, PCC and CPC of the AUT are available. Additionally, the calibration algorithm at IfE can be used for further analyses to answer specific research questions and to get more depth into the calibration data.

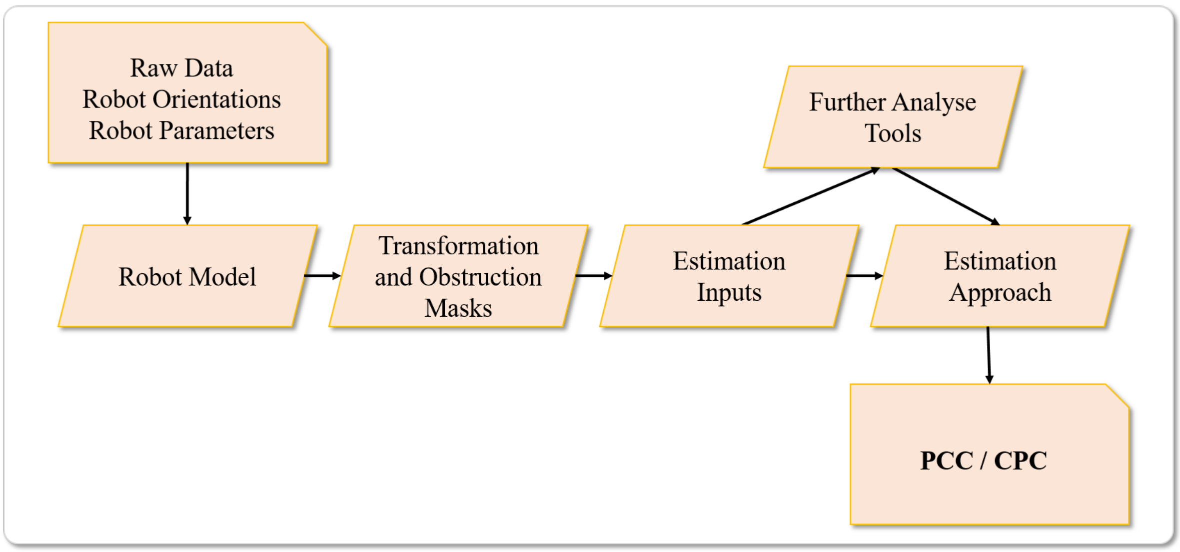

Figure 3.5: Main components of the antenna calibration algorithm at IfE

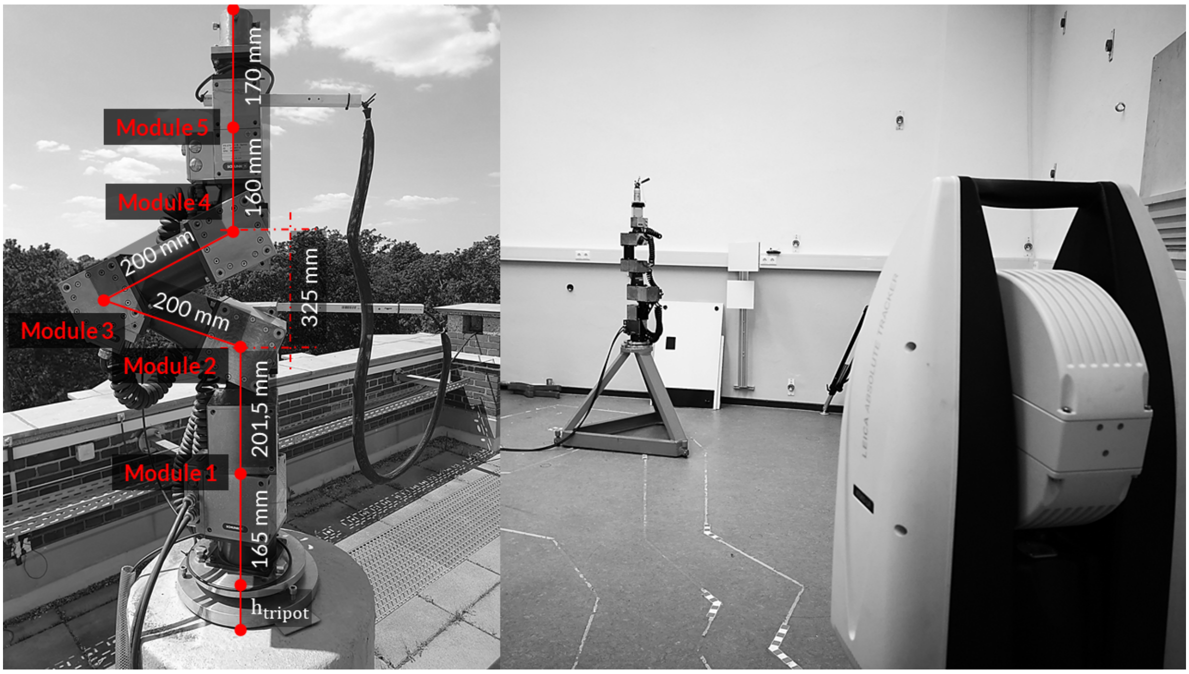

Figure 3.6: Calibration robot mounted on MSD7 with its nominal module lengths in a default calibration position (Left). Calibration of robot within the 3D laboratory from the GIH with a laser tracker in 2022 (Right).

3.3.1 Calibration Robot and its Mathematical Model

The calibration robot has been developed in a close cooperation between the *Institut für Erdmessung* and the *Geo++* company in the framework of a project funded by the Bundesministerium für Bildung, Wissenschaft, Forschung und Technologie (BMBF). Beside the development, Seeber and Böder (2002) used this robot to evolve an approach to estimate absolute antenna PCV. From this point on, the robot had been used many years to calibrate receiver antennas. In 2021, the robot has been replaced by a newer one of the same design. In Fig. 3.6 (left) the robot can be seen on the pillar with its five degrees of freedom, realized by five modules.

The modules can move clockwise and vice versa, whereas module 1 and module 5 are arranged so that the AUT is rotating horizontally. Modules 2, 3 and 4 are responsible for tilting the AUT and are rotating vertically. Each module defined its own three-dimensional left-handed coordinate system. This allows the robot to precisely hold a predefined point in space, hereinafter called fixed point in space (FP), in static robot phases. It is not possible, that the robot can hold this point during motion, due to lack of rotating modules. Accordingly, only observations, where the robot is at rest, can be used for the pattern estimation. One additional module would be necessary to make this possible.

The important lengths of the robot, provided by the manufacturer, are shown in Figure 3.6 (left), whereas the height h_{tripod} of the tripod has to be measured manually. The height of the FP is defined as

$$h_{FP} = h_{tripot} + 165 + 201.5 + 325 + 160 + 170 + h_{Adapt} + d \text{ [mm]}, \tag{3.6}$$

using the adapter height h_{Adapt}, which depends on the type of adapter (typically 7.6 mm) and the parameter d that defines the distance between the adapter and the FP, which is generally the mean value between the GPS L1 and L2 PCO of the AUT. However, small discrepancies of these lengths and also angular offsets between different modules exist, so the robot is not able to tilt and rotate the antenna around the FP exactly, thus, a calibration of the robot itself is needed.

The current set of parameters were estimated on November, 14^{th} 2022. In this process, the robot, equipped with a high precision reflector, is mounted on a solid tripod in the 3D laboratory of the Geodetic Institute Hannover (cf. Figure 3.6 (right)). It moves between 156 different, carefully predefined poses, which are precisely measured with a laser tracker (LT, Leica AT960LR) in two faces. Afterwards, the observations from the LT are used in an adjustment process to estimate the parameter set of the robot model. Leistner (2000) and Menge (2003) have investigated the first so-called theodolite measurement system (TMS) robot model. This approach used 1500 different robot positions to estimate the parameter set, which is very time-consuming and not efficient economically. Therefore, Paffenholz et al. (2007) extend and optimize the TMS robot model by using a LT. This approach significantly reduces the required time by 70%. Based on previous studies and simulations, further optimization has been done by Meiser (2009), which leads to a decrease in required poses of 156. This method is still used to calibrate the IfE antenna calibration robot, which is discussed in the mentioned literature in detail.

The outcome of the robot calibration is a set of 20 different parameters, that define:

- the origin of the laser tracker coordinate system $[m]$: $\boldsymbol{x}_{LT}$,
- the horizontal offset between module 1 and 2 $[m]$: $dX_{1,2}$, $dY_{1,2}$,
- the lengths between the modules 2, 3, 4 and 5 $[m]$: $L_{2,3}$, $L_{3,4}$, $L_{4,5}$,
- the angular offsets between modules 1, 2, 3 and 4 $[deg]$: O_2, O_3, O_4,
- the loading coefficients of modules 2, 3 and 4 $[deg/Nm]$: k_2, k_3, k_4,
- the rotation around the x-axis of module 2, 3 and 4 $[deg]$: ω_2, ω_3, ω_4,
- and the rotation around the z-axis of module 3 and 4 $[deg]$: φ_3, φ_4.

The last parameter O_{M1} completes the set. This parameter specifies the angular offset between the LT coordinate system and the system of module 1. It is estimated within the adjustment process, however, it is not used for the antenna calibration, as well as $\boldsymbol{x}_{LT}$. Based on these parameters, a robot model is set up to correct the received GNSS observations by the displacement between the actual and ideal FP. At the end, the estimated pattern is related to the ideal FP, which is connected to the ARP by the parameter d. Therefore, it is important to project the observations onto the ideal FP in satellite LOS direction at each epoch during the calibration.

The coordinates of the actual FP $\boldsymbol{x}_{FP,actual}$ in the superior pillar coordinate system in every robot resting phase can be calculated after Menge (2003) and Meiser (2009) with

$$\boldsymbol{x}_{FP,actual} = \boldsymbol{x}_1 + \boldsymbol{R}_1 \cdot (\boldsymbol{t}_{2,1} + \boldsymbol{R}_2 \cdot (\boldsymbol{t}_{3,2} + \boldsymbol{R}_3 \cdot (\boldsymbol{t}_{4,3} + \boldsymbol{R}_4 \cdot (\boldsymbol{t}_{5,4} + \boldsymbol{R}_5 \cdot \boldsymbol{t}_{FP,5})))) \,, \quad (3.7)$$

Table 3.1: Composition of rotation angles to set up the rotation matrices of different modules. All parameters are in unit [deg], except the loading coefficients k in $[deg/Nm]$ and the moment of force M in $[Nm]$.

R	φ	ω	κ	k'
$\boldsymbol{R}_1$	$Mod_1 + O_N$	0	0	-
$\boldsymbol{R}_2$	0	ω_2	$Mod_2 + O_2 + k_2'$	$k_2 \cdot M_2$
$\boldsymbol{R}_3$	φ_3	ω_3	$Mod_3 + O_3 + k_3'$	$k_3 \cdot M_3$
$\boldsymbol{R}_4$	φ_4	ω_4	$Mod_4 + O_4 + k_4'$	$k_4 \cdot M_4$
$\boldsymbol{R}_5$	$Mod_5 + O_5$	0	0	-

with $\boldsymbol{x}_1$ being the initial coordinates from module 2:

$$\boldsymbol{x}_1 = \begin{bmatrix} 0 \\ 0 \\ h_{Mod2} \end{bmatrix}, \tag{3.8}$$

and $\boldsymbol{t}$ defines different translation vectors:

$$\boldsymbol{t}_{2,1} = \begin{bmatrix} dX_{1,2} \\ dY_{1,2} \\ z_{shift,u} \end{bmatrix}, \boldsymbol{t}_{3,2} = \begin{bmatrix} 0 \\ 0 \\ L_{2,3} \end{bmatrix}, \boldsymbol{t}_{4,3} = \begin{bmatrix} 0 \\ 0 \\ L_{3,4} \end{bmatrix}, \boldsymbol{t}_{5,4} = \begin{bmatrix} 0 \\ 0 \\ L_{4,5} \end{bmatrix}, \boldsymbol{t}_{FP,5} = \begin{bmatrix} 0 \\ 0 \\ z_{shift,o} \end{bmatrix} \tag{3.9}$$

where $z_{shift,u}$ is the constant distance between module 1 and module 2 (currently 0.195 m) and $z_{shift,o}$ is defined as the difference between module 5 and FP, which is depending on the used antenna:

$$z_{shift,o} = 170 + h_{Adapt} + d \text{ [mm]}. \tag{3.10}$$

The remaining parameters in Equation 3.7 are the different rotation matrices $\boldsymbol{R}$. Each rotation matrix is composed of three individual rotation matrices around all three axes $\boldsymbol{R}_\omega$ (x-axis), $\boldsymbol{R}_\kappa$ (y-axis) and $\boldsymbol{R}_\varphi$ (z-axis):

$$\boldsymbol{R}_\omega = \begin{bmatrix} 1 & 0 & 0 \\ 0 & \cos\omega & -\sin\omega \\ 0 & \sin\omega & \cos\omega \end{bmatrix}, \boldsymbol{R}_\kappa = \begin{bmatrix} \cos\kappa & 0 & \sin\kappa \\ 0 & 1 & 0 \\ -\sin\kappa & 0 & \cos\kappa \end{bmatrix}, \boldsymbol{R}_\varphi = \begin{bmatrix} \cos\varphi & -\sin\varphi & 0 \\ \sin\varphi & \cos\varphi & 0 \\ 0 & 0 & 1 \end{bmatrix}, \tag{3.11}$$

which are combined to set up $\boldsymbol{R}$

$$\boldsymbol{R} = \boldsymbol{R}_\varphi \cdot \boldsymbol{R}_\omega \cdot \boldsymbol{R}_\kappa \tag{3.12}$$

$$\boldsymbol{R} = \begin{bmatrix} \cos\varphi \cdot \cos\kappa - \sin\varphi \cdot \sin\omega \cdot \sin\kappa & -\sin\varphi \cdot \cos\omega & \cos\varphi \cdot \sin\kappa + \sin\varphi \cdot \sin\omega \cdot \cos\kappa \\ \sin\varphi \cdot \cos\kappa + \cos\varphi \cdot \sin\omega \cdot \sin\kappa & \cos\varphi \cdot \cos\omega & \sin\varphi \cdot \sin\kappa - \cos\varphi \cdot \sin\omega \cdot \cos\kappa \\ -\cos\omega \cdot \sin\kappa & \sin\omega & \cos\omega \cdot \cos\kappa \end{bmatrix} \tag{3.13}$$

The matrix $\boldsymbol{R}$ is used for every module coordinate system transformation, however, the input angles differ.

Table 3.1 depicts the composition of each rotation angle. The loading coefficients k and the moment of force M are required to calculate the rotation angle around the y-axis for the vertically rotating modules. A detailed description about the calculation

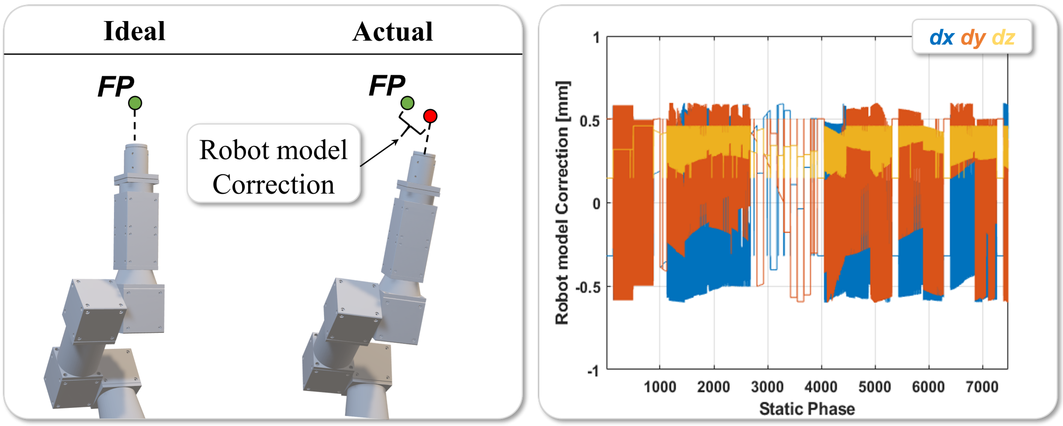

Figure 3.7: Sketch of the displacement between actual FP (red dot) and ideal FP (green dot) within a calibration process (left). Amount of three-dimensional robot model correction (displacement) in millimeters in robot resting phases during a standard antenna calibration (right).

process of the moment of force for the robot can be found in Meiser (2009) and is not discussed in this thesis. The parameters Mod_1 to Mod_5 define the angular position of the modules at the robot resting phases. These angles have to be determined, since they are not provided by the robot software. The calculation will be described later in this section. The angle θ_N describes the offset between the installed robot at its initial position and the North direction.

To determine the coordinates of the ideal FP, Equation 3.7 is utilized without applying additional corrections, considering solely the distances between different module coordinate systems. The coordinates $\boldsymbol{x}_{FP,ideal}$ equal $[0,0,h_{FP} - h_{Mod2}]$, within computational accuracy. By subtracting $\boldsymbol{x}_{FP,ideal}$ from $\boldsymbol{x}_{FP,actual}$ the displacement can be determined.

Figure 3.7 illustrates the necessity of a robot model. The actual FP (red dot) is not fixed during the antenna calibration process, but is varying each epoch. In an ideal case (green dot), the FP is fixed over the whole calibration time. This displacement is the correction, that has to be applied to the GNSS observations to project the actual FP onto the ideal FP. The right part of Figure 3.7 shows the three-dimensional displacement in the pillar coordinate system for a typical robot based antenna calibration. The x-axis shows the amount of robot resting phases and the y-axis presents the amount of displacement in millimeters. It is clearly visible, that the robot can hold the ideal FP within millimeter accuracy. With a relatively high noise in GNSS codephase signals with several decimeters, this displacement has no significant impact on the estimation of CPC.[1] However, for PCC, the robot model needs to be taken into account, because of the small noise in GNSS carrierphase observations.

Even if the GNSS observations are corrected by the robot model, only observations within robot resting phases can be used for the pattern estimation, as the robot cannot maintain the FP during motion. Thus, the observations from the AUT and the reference antenna must align to these phases. After each calibration, the robot software (*GNRTANT, GNSMART, GNNET*) provides a file, called *gnp.ane*, that contains

[1]Even if the displacement of the FP has no significant impact on the CPC estimation, the robot model will still be used in different analysis of this thesis.

information about the robot positions during the calibration. An example of this file is shown in Figure 3.8. Each row contains the data for one resting phase, with the following content:

- Start and end time of static phase [GPS SOW]: Column 1 and 2
- Azimuth and zenith angle of antenna's north marker (NM) [deg]: Column 3 and 4
- Zenith angle of antenna's east marker (EM) [deg]: Column 5
- Corrections of azimuth and zenith angle of antenna's NM and EM calculated with Geo++ software [deg]: Column 6 to 8
- Azimuth of bottom module (a) [deg]: Column 9
- Azimuth of upper module (A) [deg]: Column 10
- Inclination of the system (PCV) [deg]: Column 11.

The duration of these phases is not stable and varies between 0.1 s and several seconds, depending on the calculation time of the robot control software. The robot must wait for the software response to start its motion, which includes information about the module poses for the next resting phase, for example. The detailed workings of this process will not be described in this thesis. An average duration of approximately half a second is realistic.

Based on this data, the antenna calibration algorithm at IfE connects the observations of both stations with the robot resting phases, so that the observations are within these phases. The related parameters of a particular resting phase are used to preprocess the observations by using the robot pose to apply the robot model or to transform the observations into the antenna system (cf. Section 3.3.2). The algorithm allows using different sampling rates, so that more than one observation for a resting phase can be used.

For setting up the rotation matrices for the robot model or for transforming the observations into the antenna frame, the angular pose for each robot resting phase have to be available. As already shown in Figure 3.8, the robot software provides only the angles of module 1 and 5, column 9 (a) and 10 (A), respectively, and the inclination of the whole robot system, indicated with PCV. In order to calculate the rotation matrices

```
gnp.ane
# COM STARTLOG
  207529.529000 207530.589000   0.0000  90.0000  90.0000 0.000011 0.000300 -0.000116 1 # a   0.0 A   0.0 PCV   0.0
  207533.659000 207534.509000 180.0000  90.0000  90.0000 0.000011 0.000300 -0.000116 1 # a   0.0 A-180.0 PCV   0.0
  207535.579000 207536.509000 192.0000  90.0000  90.0000 0.000011 0.000300 -0.000116 1 # a   0.0 A-168.0 PCV   0.0
  207537.589000 207538.519000 204.0000  90.0000  90.0000 0.000011 0.000300 -0.000116 1 # a   0.0 A-156.0 PCV   0.0
  207539.569000 207540.499000 216.0000  90.0000  90.0000 0.000011 0.000300 -0.000116 1 # a   0.0 A-144.0 PCV   0.0
  207541.549000 207542.479000 228.0000  90.0000  90.0000 0.000011 0.000300 -0.000116 1 # a   0.0 A-132.0 PCV   0.0
  207543.540000 207544.460000 240.0000  90.0000  90.0000 0.000011 0.000300 -0.000116 1 # a   0.0 A-120.0 PCV   0.0
  207545.540000 207546.460000 252.0000  90.0000  90.0000 0.000011 0.000300 -0.000116 1 # a   0.0 A-108.0 PCV   0.0
  207547.531000 207548.390000 264.0000  90.0000  90.0000 0.000011 0.000300 -0.000116 1 # a   0.0 A -96.0 PCV   0.0
  207549.450000 207550.370000 276.0000  90.0000  90.0000 0.000011 0.000300 -0.000116 1 # a   0.0 A -84.0 PCV   0.0
  207551.430000 207552.351000 288.0000  90.0000  90.0000 0.000011 0.000300 -0.000116 1 # a   0.0 A -72.0 PCV   0.0
  207553.411000 207554.331000 300.0000  90.0000  90.0000 0.000011 0.000300 -0.000116 1 # a   0.0 A -60.0 PCV   0.0
  207555.381000 207556.311000 312.0000  90.0000  90.0000 0.000011 0.000300 -0.000116 1 # a   0.0 A -48.0 PCV   0.0
  207557.361000 207558.291000 324.0000  90.0000  90.0000 0.000011 0.000300 -0.000116 1 # a   0.0 A -36.0 PCV   0.0
  207559.341000 207560.271000 336.0000  90.0000  90.0000 0.000011 0.000300 -0.000116 1 # a   0.0 A -24.0 PCV   0.0
  207561.321000 207562.251000 348.0000  90.0000  90.0000 0.000011 0.000300 -0.000116 1 # a   0.0 A -12.0 PCV   0.0
  207563.311000 207564.241000   0.0000  90.0000  90.0000 0.000011 0.000300 -0.000116 1 # a   0.0 A   0.0 PCV   0.0
```

Figure 3.8: Example of a *gnp.ane* robot orientation file.

for the robot model, the angular position of the vertical rotating modules are required (cf. Table 3.1). The definition of these angles is listed as follows and also presented in Figure 3.9:

- Angle of module 2, Mod_2, is defined as the angle between the zenith direction and the direction towards module 3.
- Angle of module 3, Mod_3, is defined as the angle between the extended direction from module 2 towards module 3 and the direction from module 3 towards module 4.
- Angle of module 4, Mod_4, is defined as the angle between the extended direction from module 3 towards module 4 and the direction from module 4 towards the FP.

The calculation of these angles is based on simple trigonometry, with the assumption that FP is always fixed and is vertically aligned (zenith direction) with module 2. In addition, the lengths $\mathbf{L}_{M4,FP}$, $\mathbf{L}_{2,3}$ and $\mathbf{L}_{3,4}$ are assumed to be constant. The relation between all parameters can be seen in the right part of Fig. 3.9. In this case, the robot is tilted with a specific inclination z, however, the following calculations also apply to non-tilting scenarios ($z = 0$). In general, the robot position can be divided into two triangles, printed in orange and green in the plot. The orange triangle will be disappeared, when the robot is not in a tilt position. First, the height h in meter of the FP is determined by

$$h = z_{shift,o} + 0.325 \text{ [m]}, \tag{3.14}$$

with $z_{shift,o}$ and the constant value 0.325 m, which describes the vertical distance between module 2 and 3 in non tilting scenarios. Within the calibration process, h is assumed to be constant. With c,

$$c = \sqrt{h^2 + L_{M4,FP}^2 - 2 \cdot h \cdot L_{M4,FP} \cdot \cos z} \text{ [m]} \tag{3.15}$$

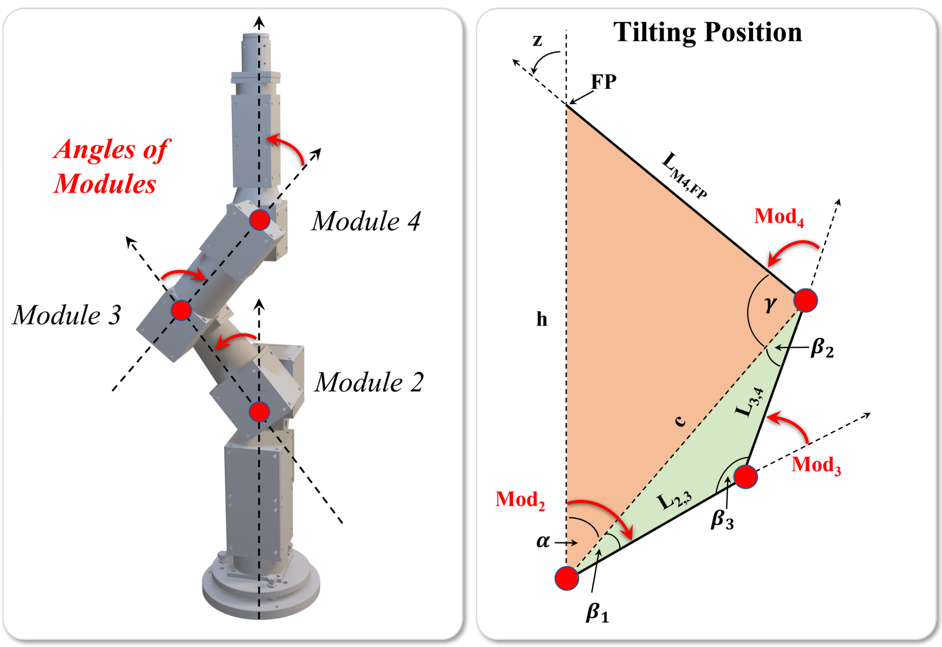

Figure 3.9: Definition of the angular positions of the tilting modules.

and α,

$$\alpha = \arcsin\left(\frac{\sin z \cdot h}{c}\right) \text{ [rad]} \tag{3.16}$$

the angles β_1, β_2 and β_3 can be calculated:

$$\begin{aligned}
\beta_1 &= \arccos\left(\frac{L_{3,4}^2 - (c^2 + L_{2,3}^2)}{-2 \cdot L_{2,3} \cdot c}\right) \text{ [rad]},\\
\beta_2 &= \arccos\left(\frac{L_{2,3}^2 - (c^2 + L_{3,4}^2)}{-2 \cdot L_{3,4} \cdot c}\right) \text{ [rad]},\\
\beta_3 &= \pi - \beta_1 - \beta_2 \text{ [rad]}.
\end{aligned} \tag{3.17}$$

With help of γ,

$$\gamma = \pi - z - \alpha \text{ [rad]}, \tag{3.18}$$

all three modules angles in radians can be calculated

$$\begin{aligned}
Mod_2 &= -(\alpha + \beta_1) \text{ [rad]}\\
Mod_3 &= \pi - \beta_3 \text{ [rad]}\\
Mod_4 &= \pi - \gamma - \beta_2 \text{ [rad]}.
\end{aligned} \tag{3.19}$$

The angle Mod_2 is assumed to be negative, because of the predefined rotation direction of this module, estimated in the robot calibration. These calculations are done for every robot resting phase, based on the inclination of the system.

3.3.2 Antenna Coordinate System and Elevation Masks

The antenna coordinate system is essential to match the GNSS observations to its position on the antenna hemisphere. The origin of this left-handed system is located in the FP, the x-axis is defined as the direction towards the antenna's NM ($North_{ant}$), which is in general the cable connector, the z-axis pointed from the ARP towards the FP (Up_{ant}) and the y-axis completed the left-handed system ($East_{ant}$). Figure 3.10 illustrates the antenna system in relation to the topocentric system in horizontal and tilting scenarios. The transformation from topocentric satellite positions into the antenna frame can be done either by using the orientations for the NM and EM and their respective corrections, or by using the module orientations with their corrections from the robot model (cf. Section 3.3.1). The transformation matrix $\boldsymbol{R}_{topo \to ant}$ equals a three-dimensional rotation matrix around each axis, when using the positions of the NM and EM:

$$\boldsymbol{R}_{topo \to ant} = \begin{bmatrix} 1 & 0 & 0 \\ 0 & \cos el_n & \sin el_n \\ 0 & -\sin el_n & \cos el_n \end{bmatrix} \cdot \begin{bmatrix} \cos el_e & 0 & -\sin el_e \\ 0 & 1 & 0 \\ \sin el_e & 0 & \cos el_e \end{bmatrix} \cdot \begin{bmatrix} \cos azi_n & \sin azi_n & 0 \\ -\sin azi_n & \cos azi_n & 0 \\ 0 & 0 & 1 \end{bmatrix}, \tag{3.20}$$

where

$$\begin{aligned}
el_n &= \frac{\pi}{2} - z_n\\
el_e &= \frac{\pi}{2} - z_e.
\end{aligned} \tag{3.21}$$

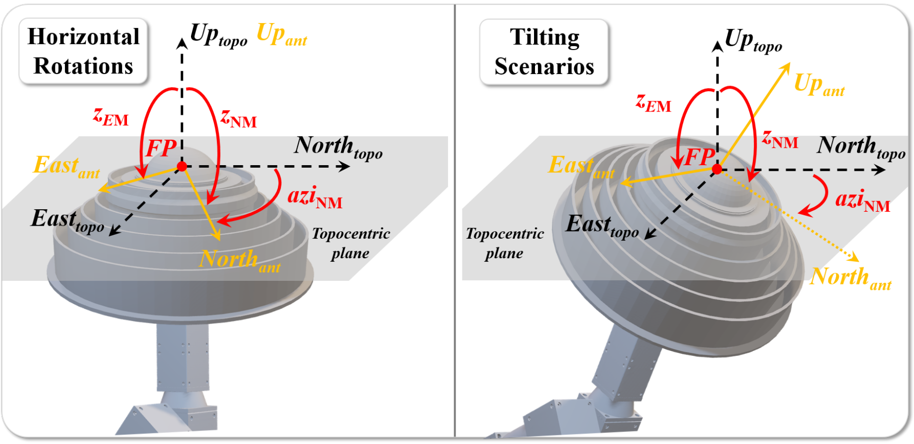

Figure 3.10: Definition of the antenna coordinate system during a calibration in horizontal (left) and tilting (right) scenarios.

Additionally, the corrections of the positions have to be taken into account:

$$\begin{aligned} azi_n &= azi_{NM} + \delta azi_{NM} \\ z_n &= z_{NM} + \delta z_{NM} \\ z_e &= z_{EM} + \delta z_{EM}. \end{aligned} \tag{3.22}$$

When using the poses of the modules, the rotation is as follows:

$$\boldsymbol{R}_{topo \rightarrow ant} = \begin{bmatrix} \cos\alpha_u & \sin\alpha_u & 0 \\ -\sin\alpha_u & \cos\alpha_u & 0 \\ 0 & 0 & 1 \end{bmatrix} \cdot \begin{bmatrix} \cos z_s & 0 & -\sin z_s \\ 0 & 1 & 0 \\ \sin z_s & 0 & \cos z_s \end{bmatrix} \cdot \begin{bmatrix} \cos\alpha_b & \sin\alpha_b & 0 \\ -\sin\alpha_b & \cos\alpha_b & 0 \\ 0 & 0 & 1 \end{bmatrix}, \tag{3.23}$$

with α_b being the azimuth of the bottom module, α_u the orientation angle of the upper module and z_s for the tilting angle of the whole system, at which the angular offsets between the tilting modules (O_2, O_3, O_4) have to be taken into account:

$$z_s = z + O_2 + O_3 + O_4. \tag{3.24}$$

Regardless of which method was used to compose the transformation matrix, it is then used to calculate $\mathbf{e}_{ant}$ by

$$\mathbf{e}_{ant} = \boldsymbol{R}_{topo \rightarrow ant} \cdot \mathbf{e}_{topo}. \tag{3.25}$$

Then, azimuth azi_{ant}^k and elevation el_{ant}^k of satellite k in antenna system can be computed with

$$\begin{aligned} azi_{ant}^k &= \arctan\frac{\mathbf{e}_{ant}(2)}{\mathbf{e}_{ant}(1)}, \\ el_{ant}^k &= \arctan\frac{\mathbf{e}_{ant}(3)}{\sqrt{\mathbf{e}_{ant}(1)^2 + \mathbf{e}_{ant}(2)^2}}. \end{aligned} \tag{3.26}$$

From now on, the GNSS observations can directly be connected to their position on the antenna hemisphere, which is essential to estimate the exact PCC or CPC value. In this thesis, the transformation is based on the module orientations to become more independent of the correction values listed in the *gnp.ane* file and have fully control over the correction values.

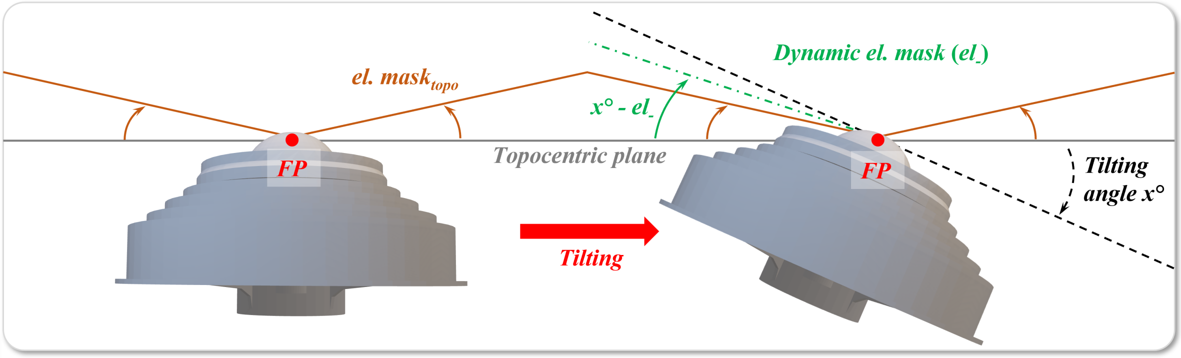

Figure 3.11: Concept of a TEM (orange) and DEM (green), based on Menge (2003).

In tilting scenarios, GNSS signals are received at a different point on the antenna hemisphere, compared to a static case, and experience a different antenna gain. Consequently, they are more vulnerable to multipath, caused by ground reflections. To avoid these signals, obstruction masks can be used to achieve more accurate and precise calibration results. In the IfE antenna calibration algorithm, two different elevation masks are used, which complements each other; a topocentric elevation mask (TEM) and a dynamic elevation mask (DEM). Both of them are presented in Figure 3.11. The TEM, presented in orange, is similar to an elevation masks in a static GNSS measurements. It eliminates all GNSS observations from satellites below a predefined elevation angle. In horizontally robot poses, a TEM is applied with a typical cut-off angle of 10 deg. This mask is extended by a DEM, presented in green, in robot tilting scenarios developed by Menge (2003). The author shows that GNSS antennas can receive signals from below the antenna horizon. By additionally using these signals, the stability of the pattern estimation process with spherical harmonics can be significantly increased. The basic idea is to use satellite signals arriving from the opposite of the tilting direction, up to a negative elevation angle el_- of 5 deg in the antenna system. This negative cut-off still leads to a stable tracking of GPS L1 and L2 signals (Menge, 2003). The DEM begins operating when the sum of the tilting angle $x°$ and el_- exceeds the TEM; otherwise, only the TEM is used.

3.3.3 Observations and Estimation Approach

A commonly used approach to estimate CPC and PCC pattern is to use time differenced receiver-to-receiver single differences (ΔSD) as estimation inputs. They are calculated between the AUT and the reference antenna and between each robot resting phase. The benefit to use this observable is that almost all error sources are cancelled out while preserving the pattern information of the AUT. In general, codephase and carrierphase measurements are affected by different error sources, which have to be corrected to get an accurate position in the end. These effects can be either corrected by models, by using specific measurement configuration or by using different kind of LC.

In the following, the calculation of the codephase and carrierphase ΔSD is stepwise presented, to understand the benefits of using ΔSD for antenna calibration with a robot in the field.

Therefore, Equation 2.37 will be shown here, once again:

$$\begin{aligned} C_R^k &= \rho_R^k + c\left(\delta t_R - \delta t^k\right) + T_R^k + I_{R,f}^k + MP_R + CPC_R^k + ... + \epsilon, \\ L_R^k &= \rho_R^k + c\left(\delta t_R - \delta t^k\right) + T_R^k - I_{R,f}^k + N_f\lambda_f + MP_R + PCC_R^k + ... + \epsilon. \end{aligned} \tag{3.27}$$

The definition of the different elements within the equation was already given in Section 2.4.1 and will not be repeated here. First, receiver-to-receiver single differences are calculated between the AUT, labeled with subscript *Robo*, and the reference station, labeled with subscript *Ref*, to a satellite k:

$$\begin{aligned} SD_C^k &= C_{Ref}^k - C_{Robo}^k, \\ SD_L^k &= L_{Ref}^k - L_{Robo}^k. \end{aligned} \tag{3.28}$$

This eliminates in the first place all satellite specific error sources, like the satellite clock error δt^k, errors in the orbit calculation, satellite specific hardware biases and delays, satellite PWU and satellite CPC and PCC. In the second place, the effects of the troposphere and ionosphere are reduced to a negligible value, because the atmospheric condition between the two stations (8 m baseline) are assumed to be identical. This leads to:

$$\begin{aligned} SD_C^S &= \delta\rho^k + c\delta t_R + \delta MP_R + (CPC_{Ref} - CPC_{Robo}) + \epsilon, \\ SD_L^k &= \delta\rho^k + c\delta t_R + \delta MP_R + N_{f,SD}\lambda_f + PWU_{ROBO} + (PCC_{Ref} - PCC_{Robo}) + \epsilon \end{aligned} \tag{3.29}$$

with the remaining geometric distance $\delta\rho^k$, receiver clock error δt_R and multipath δMP_R between the two stations. Besides, a SD ambiguity $N_{f_S,D}$ for carrierphase observations remains included. Due to the robot motion, the AUT experiences a PWU effect in the carrierphase observable. Thus, the PWU has to be modelled, which is described later in this section. By forming the time difference of the single differences between t_{i+1} and t_i, the final estimation inputs $\Delta\mathrm{SD}(t_{i+1}, t_i)$ can be calculated:

$$\begin{aligned} \Delta SD_C^k(t_{i+1}, t_i) &= \Delta CPC_{Robo}^k(t_{i+1}, t_i) + \Delta\delta MP_R(t_{i+1}, t_i) + \epsilon, \\ \Delta SD_L^k(t_{i+1}, t_i) &= \Delta PCC_{Robo}^k(t_{i+1}, t_i) + \Delta\delta MP_R(t_{i+1}, t_i) + \Delta PWU_{Robo}(t_{i+1}, t_i) + \epsilon \end{aligned} \tag{3.30}$$

By assuming that the receiver-satellite geometry will not be significantly changed between two consecutive epochs, the remaining geometrical part, the carrierphase ambiguities and the CPC_{Ref} / PCC_{Ref} are eliminated or rather reduced to a negligible value. The pattern information from the AUT on the robot are maintained, thanks to the robot motion, or at least the differences in pattern between two consecutive points in time on the antenna hemisphere. The remaining receiver clock error, δt_R, is cancelled out, thanks to an external frequency standard and the time differencing approach. Even with time differencing, differential multipath effects can still be contained in the ΔSD. Thus, obstruction mask are applied to avoid most of the multipath affected observations. A broad analysis of multipath within the antenna calibration is presented in Chapter 5.2. For the general overview about the antenna calibration algorithm, the multipath effects are assumed to be gathered in the noise ϵ.

Phase-Wind Up Effect

The phase-wind up is an effect on the GNSS signal, that leads to an error in the carrierphase measurement by a maximum of one carrier cycle. Wu et al. (1993) identified this effect in the early 1990s, noting a change in the phase when the receiver or transmitter antenna is rotated. The geometric distance between both antennas stays the same, but the phase and thus the carrierphase measurement is increased/descreased due to the rotation. The transmitter antennas of GNSS satellites are pointed towards the Earth, whereat the y-axis points parallel to the solar panels and the x-axis completes this right-handed coordinate system (Teunissen and Montenbruck, 2017). The solar panels of the satellites are always pointed towards the sun to ensure the power supply of the satellites. Consequently, the whole satellite system is rotating around the satellite's bore sight axis during the flight around the Earth and the PWU effect starts to impact the carrierphase observations, because of the RHCP polarization of the electromagnetic GNSS signals. In absolute positioning application, like PPP, this effect has to be taken into account. In the robot-based antenna calibration, the PWU effect, caused by the satellite rotation, is eliminated thanks to the SD approach, however, the moving robot causes a PWU by itself. This influences the carrierphase observations and the resulting PCC, however, this has no impact on the CPC, when using ΔSD as estimation inputs. This thesis proposes to use the ΔMPLC as an input for estimating CPC, which will be introduced later in this section. Within this LC, the differential PWU effect between two carrier frequencies remains, why it has to be taken into account, too.

To model the PWU caused by the robot motion, the calculation process by Beyerle (2008) is adopted to the robot case, which is based on the original approach from Wu et al. (1993). There, the transmitter and the receiver antenna are modelled as crossed dipoles, which consists of an aligned dipole a and a transverse dipole t. Both are orthogonal to each another and only differ in a way, that the signal path to the transverse dipole is phase delayed by $\pi/2$. The boresight direction of the transmitting antenna $\hat{\mathbf{t}}^b$ and the receiver antenna $\hat{\mathbf{r}}^b$ are defined as:

$$\begin{aligned}\hat{\mathbf{t}}^b &= \hat{\mathbf{t}}^a \times \hat{\mathbf{t}}^t,\\ \hat{\mathbf{r}}^b &= \hat{\mathbf{r}}^a \times \hat{\mathbf{r}}^t,\end{aligned} \tag{3.31}$$

which complete the right-handed orthonormal coordinate systems. In case of GNSS, $\hat{\mathbf{t}}^b$ is the unit vector from the satellite towards the Earth center. Because the y-axis is oriented towards the satellite's solar panels, and they are always oriented towards the sun, $\hat{\mathbf{t}}^t$ can be calculated by

$$\hat{\mathbf{t}}^t = \hat{\mathbf{t}}^b \times \mathbf{e}_{sun}. \tag{3.32}$$

$\hat{\mathbf{t}}^a$is then defined by

$$\hat{\mathbf{t}}^a = \hat{\mathbf{t}}^t \times \hat{\mathbf{t}}^b. \tag{3.33}$$

The receiver vectors are defined by:

$$\begin{aligned}\hat{\mathbf{r}}^a_{ant} &= [1,0,0],\\ \hat{\mathbf{r}}^t_{ant} &= [0,-1,0].\end{aligned} \tag{3.34}$$

Both of them have to be transformed into the Earth-centered Earth-fixed (ECEF) coordinate system. Because the receiver antenna is in motion, the two receiver dipoles $\hat{\mathbf{r}}^a_{ant}$ and $\hat{\mathbf{r}}^t_{ant}$ have to be rotated at each epoch into the topocentric system, with the transposed rotation matrix $\mathbf{R}^T_{topo\rightarrow ant}$ described in Section 3.3.2:

$$\begin{aligned}\hat{\mathbf{r}}^a &= \boldsymbol{R}_{topo\rightarrow ECEF}\left(\mathbf{R}^T_{topo\rightarrow ant}\cdot \hat{\mathbf{r}}^a_{ant}\right),\\ \hat{\mathbf{r}}^t &= \boldsymbol{R}_{topo\rightarrow ECEF}\left(\mathbf{R}^T_{topo\rightarrow ant}\cdot \hat{\mathbf{r}}^t_{ant}\right).\end{aligned} \tag{3.35}$$

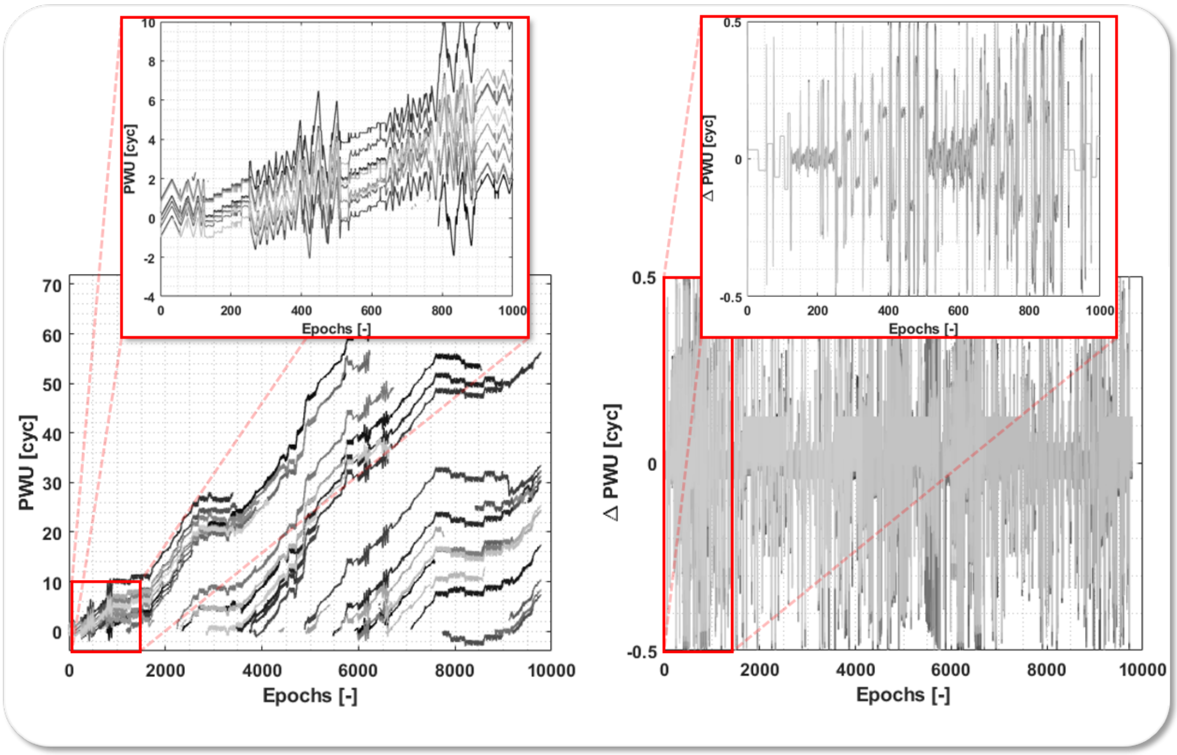

Figure 3.12: The left figures show the PWU caused by the robot motion during the antenna calibration. The right figures show the corresponding time differenced PWU.

The PWU in unit cycle can be calculated after Beyerle (2008) with

$$\mathrm{PWU} = \arctan\left(\frac{\mathbf{T}^t\left(\hat{\mathbf{k}}\right)\cdot\hat{\mathbf{r}}^a + \mathbf{T}^a\left(\hat{\mathbf{k}}\right)\cdot\hat{\mathbf{r}}^t}{\mathbf{T}^a\left(\hat{\mathbf{k}}\right)\cdot\hat{\mathbf{r}}^a + \mathbf{T}^t\left(\hat{\mathbf{k}}\right)\cdot\hat{\mathbf{r}}^t}\right), \tag{3.36}$$

with

$$\begin{aligned}\mathbf{T}^a(\hat{\mathbf{k}}) &= (\hat{\mathbf{k}}\times\hat{\mathbf{t}}^a)\times\hat{\mathbf{k}},\\ \mathbf{T}^t(\hat{\mathbf{k}}) &= (\hat{\mathbf{k}}\times\hat{\mathbf{t}}^t)\times\hat{\mathbf{k}},\end{aligned} \tag{3.37}$$

where $\hat{\mathbf{k}}$ is the unit vector from the satellite to the receiver.

Figure 3.12 shows the PWU effect in a normal calibration operation in the unit of cycles. Here, a time span of about ten hours is considered. The bottom left figure shows the whole time span, whereas the above figure depicts a zoom of the first 1000 epochs. It is visible, that the PWU is clearly not in a range of -0.5 to 0.5 cycle. The effect seems to be drifting away, when the calibration duration increases. The subfigures in the right show the corresponding time differenced PWU, the actual corrections, which are added to the ΔSD. However, by correcting the ΔSD by the ΔPWU, a lot of cycle jumps occur, as depicted in Figure 3.13 (left). To get a good estimation of the antenna pattern, these jumps need to be either deleted, what decrease the amount of usable observations, or corrected, which is visible in the right subfigure of Figure 3.13.

To do so, a function is implemented in the antenna calibration algorithm, which considers the relative motion of the robot and compares them with the relative behaviour of the PWU. When the antenna is rotating clockwise, from the transmitter point of

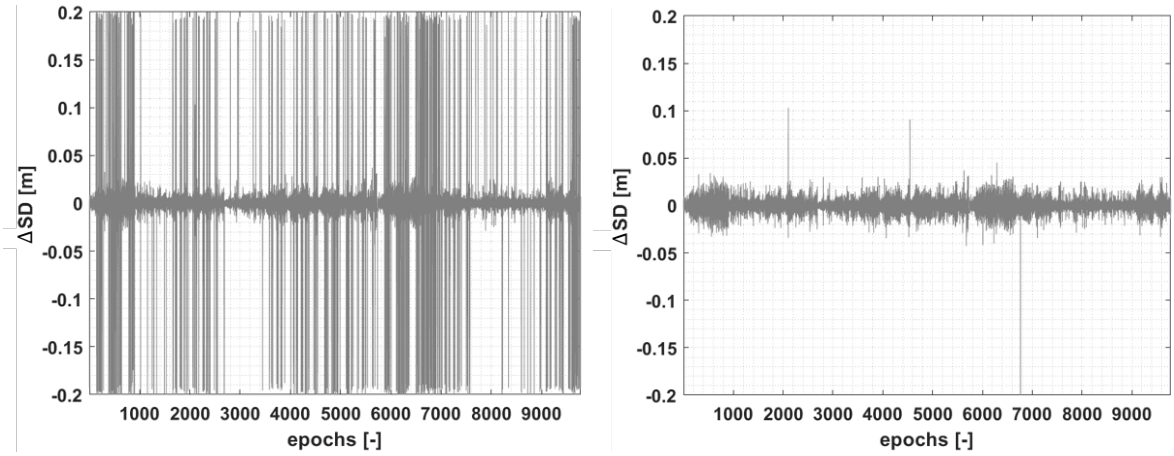

Figure 3.13: ΔSD before the PWU cycle slip fixing (left) and after (right).

view, the PWU value must increase and vice versa, because of the RHCP behaviour of GNSS signals. The relative motion of the rotating AUT can be determined by time differencing the azimuth of antenna's NM. Thus, negative values represent a counterclockwise rotation, while positive values define clockwise rotations. The same is done for the calculated PWU (cf. Equation 3.36). The relative motion of both have to be the same. If this is not the case, a cycle slip occurs which has to be corrected. Figure 3.14 shows the cycle slip corrected PWU and the time differenced PWU as the actual correction to calculate the ΔSD, as seen in Figure 3.13 (right). It should be noted, that the remaining spikes are caused by another error source.

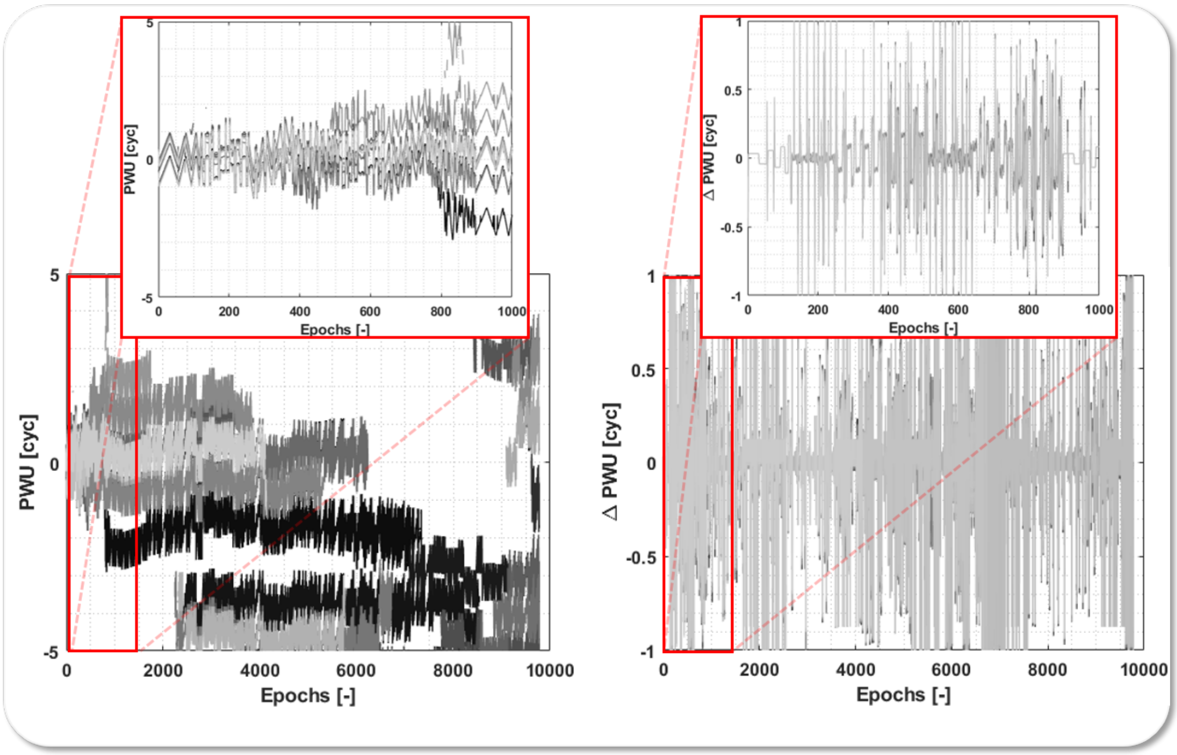

Figure 3.14: The left figures show the PWU caused by the robot motion during the antenna calibration after the cycle slip fixing. The right figures show the corresponding time differenced PWU.

Time differenced Multipath Linear-Combination

Besides the commonly used estimation approach with ΔSD, a new approach is proposed here for estimating CPC. The idea is to use the time differenced multipath linear combination (ΔMPLC) as inputs for the pattern estimation. The benefit of using ΔMPLC is that one differencing step is avoided, so that the noise is decreased by $\sqrt{2}$ compared to the ΔSD approach, because only the robot station is used. The need of a reference antenna is only necessary for controlling the robot motion with the *Geo++* software.

The multipath linear combination (MPLC) has already been introduced in Section 2.4.3. This LC can be calculated using one codephase C_a^k and two carrierphase observations L_a^k and L_b^k to satellite k. By time differencing the MPLC, the ΔMPLC can be achieved. However, beside the CPC information, some effects are remained in the LC. These effects are the time differenced differential PWU $\Delta\delta PWU_{a,b}^k$, caused by the robot motion, and the time differenced differential PCC $\Delta\delta PCC_{a,b}^k$ between the two carrierphase observables and multipath effects. They have to be modelled, estimated or eliminated, so that the ΔMPLC only contain CPC information.

The PCC values of the AUT are estimated for the required frequencies with an initial calibration run. For that purpose, the ΔSD approach is used for estimating the carrierphase pattern. Afterwards, the PCC values are combined to get the remaining effect $\delta PCC_{a,b}^k$ in the MPLC. Thus, Equation 2.49 can be rewritten by using the wavelength λ instead of the frequency:

$$MPLC^k = C_a^k - L_a^k - w \cdot (L_a^k - L_b^k), \tag{3.38}$$

with

$$w = 2 \cdot \frac{\lambda_a^2}{\lambda_a^2 - \lambda_b^2}. \tag{3.39}$$

By replacing the carrierphase observation L_a and L_b in Equation 3.38 by the PCC of the two frequencies, the effect of carrierphase pattern within the LC can be calculated:

$$\delta PCC_{a,b}^k = -PCC_a^k + w \cdot (PCC_a^k - PCC_b^k). \tag{3.40}$$

A similar approach is used for the PWU effect caused by the robot motion:

$$\delta PWU_{a,b}^k = -PWU_a^k + w \cdot (PWU_a^k - PWU_b^k). \tag{3.41}$$

However, the calculation of the PWU needs to be adopted, when combining different frequencies on a metric scale. In general, the PWU is identical for all frequencies in units of cycle. By multiplying the PWU in cycle with the wavelength of the GNSS signal, the PWU is transformed into a metric scale and differs for different frequencies. In the calibration algorithm, the calculated PWU is still ambiguous, as it is visible in Figure 3.14. Thanks to time differencing, the ambiguities are eliminated. A combination of the PWU from two frequencies are only possible on a metric scale. When the ambiguities are not removed, the difference becomes large and wrong. Therefore, the phase cycle ambiguities have to be estimated and subtracted from the PWU time series first, before Equation 3.41 can be used.

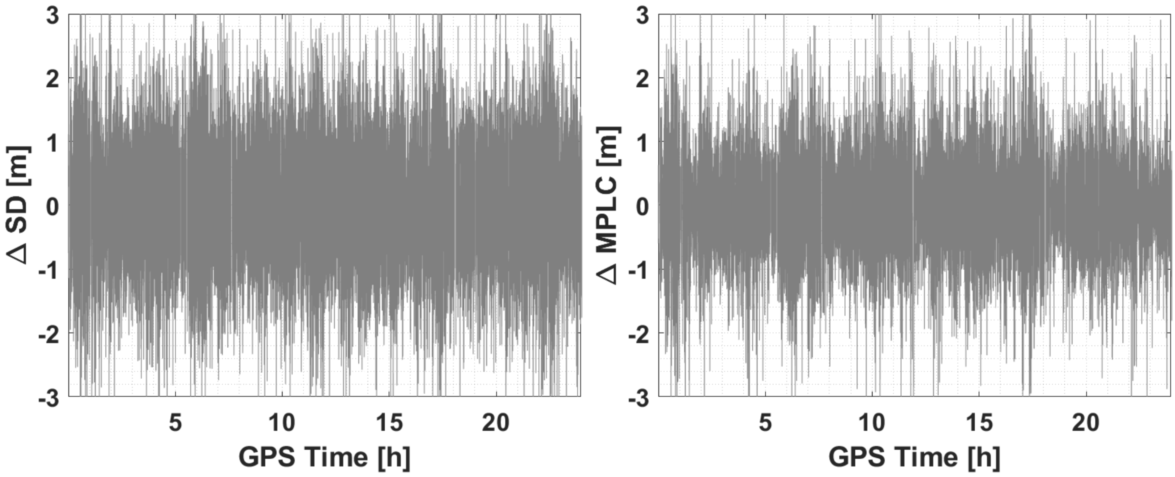

Figure 3.15: ΔSD from a calibration of an u-blox ANN-MB1 NONE (S/N:2133) for the GPS C1 signal (Left) and ΔMPLC of the same calibration (right). All visible satellites are presented by overlapping.

Finally, the calculated MPLC can be corrected by the PWU and the PCC of the carrierphase observations to get $MPLC^k_{est,in}$:

$$MPLC^k_{est,in} = MPLC^k - \delta PCC^k_{a,b} - \delta PWU^k_{a,b}. \tag{3.42}$$

$MPLC^k_{est,in}$ contains the CPC information, multipath effects, noise and unmodelled effects. The final estimation inputs $\Delta MPLC^k_{est,in}$ can be calculated, by time differencing. The multipath effects are assumed to be not contained within the $\Delta MPLC^k_{est,in}$, thanks to special multipath maps provided by the DLR. With these maps, multipath affected observations are eliminated in a preprocessing step. A detailed description about the multipath maps can be found in Chapter 5. Figure 3.15 shows an example of the ΔMPLC (right) compared to the ΔSD (left) for an u-blox ANN-MB1 NONE (S/N:2133) antenna for the GPS C1 signal. The calibration has been carried out on July, 13^{th} 2024 with Javad Delta receivers and use of default receiver settings. All visible satellites are presented in the figure. It is clearly visible, that the overall noise is significantly reduced, when using ΔMPLC observations instead of ΔSD. How the different estimation inputs impact the resulting CPC pattern is presented and discussed in Chapter 6 in detail.

Estimation Approach

The antenna calibration algorithm at IfE is able to estimate CPC and PCC for an arbitrary frequency or GNSS system. The general workflow will be briefly described here, however, there exist several opportunities and analysis techniques to go very deep into the estimation algorithm. Detailed information and analysis of this topic can be found in Kröger (2025), where the author focuses mainly on the carrierphase.

After Kröger et al. (2021), CPC and PCC are usually parametrized with spherical harmonics with a degree (m) and an order (n) of 8. With the fully normalized Legendre function $\tilde{P}_{mn}$, the azimuth α and the zenith angle z of the satellite k, as well as the coefficients a_{mn} and b_{mn}, CPC/PCC can be written as:

$$CPC/PCC(\alpha^k, z^k) = \sum_{m=1}^{m_{max}} \sum_{n=0}^{m} \tilde{P}_{mn}\left(\cos(z^k)\right)\left(a_{mn}\cos(n\alpha^k) + b_{mn}\sin(n\alpha^k)\right). \quad (3.43)$$

In order to get the required CPC/PCC of the antenna, a_{mn} and b_{mn} ($\hat{\boldsymbol{x}}$) have to be estimated with the least squares adjustment first, using ΔSD (or ΔMPLC) as input observations:

$$\hat{\boldsymbol{x}} = (\boldsymbol{A}^T\boldsymbol{P}\boldsymbol{A})^{-1} \cdot \boldsymbol{A}\boldsymbol{P}\Delta\boldsymbol{SD}, \quad (3.44)$$

where $\boldsymbol{A}$ contains the partial derivatives of Equation 3.43 w.r.t. the coefficients. The weight matrix $\boldsymbol{P}$ can be selected as an identity matrix or by weighting the observations by their elevation or their respective signal strength. First, the normal equation matrix $\boldsymbol{N}_k$ for each satellite k is calculated by

$$\boldsymbol{N}_k = \boldsymbol{A}_k^T\boldsymbol{P}\boldsymbol{A}_k, \quad (3.45)$$

with the design matrix $\boldsymbol{A_k}$ for each satellite. Because time differenced observations are used, the design matrix needs to be taken these time differencing into account, thus

$$\boldsymbol{A}_k = \boldsymbol{A}_k(t_{i+1}) - \boldsymbol{A}_k(t_i). \quad (3.46)$$

The normal equation matrices are stacked over the different satellites from one GNSS signal

$$\bar{\boldsymbol{N}} = \sum_{k=1}^{k_{max}} \boldsymbol{N}_k. \quad (3.47)$$

Additionally, the right part of the normal equation system (NES) $\boldsymbol{n}_k$ is stacked, too, with

$$\boldsymbol{n}_k = \boldsymbol{A}_k^T\boldsymbol{P}\Delta\boldsymbol{SD}, \quad (3.48)$$

and

$$\bar{\boldsymbol{n}} = \sum_{k=1}^{k_{max}} \boldsymbol{n}_k. \quad (3.49)$$

$\boldsymbol{N}_k$ is in general poorly conditioned, due to observations in the upper antenna hemisphere, only (Kröger et al., 2021). To improve the condition, different techniques were analysed by Kröger (2025). So far, the whole normal equation matrix $\tilde{\boldsymbol{N}}$ is set up, by extending $\boldsymbol{N}_k$ with a restriction matrix $\mathbf{R}$:

$$\tilde{\boldsymbol{N}} = \begin{bmatrix} \bar{\boldsymbol{N}} & \mathbf{R}^T \\ \mathbf{R} & 0 \end{bmatrix}. \quad (3.50)$$

The right side of the NES also needs to be extended:

$$\tilde{\boldsymbol{n}} = \begin{bmatrix} \bar{\boldsymbol{n}} \\ 0 \end{bmatrix}. \quad (3.51)$$

In $\mathbf{R}$ the coefficients with an odd index sum, e.g. $a_{21}, b_{21}, ...$, are restricted to zero. These coefficients represent the anti-symmetry between the upper and the lower part of the sphere. By using this restriction, the condition number can be improved.

Another approach is proposed by Kröger (2025), who developed a new strategy to improve the condition number and avoid the usage of restrictions. This approach uses hemispherical harmonics. Therefore, Equation 3.43 is modified with the factors k_1 and k_2:

$$CPC/PCC(\alpha^k, z^k) = \sum_{m=1}^{m_{max}} \sum_{n=0}^{m} \tilde{P}_{mn} \left(k_1 \cos(z^k) + k_2\right) \left(a_{mn} \cos(n\alpha^k) + b_{mn} \sin(n\alpha^k)\right). \tag{3.52}$$

These factors have to be estimated in a preprocessing step and allows considering only the upper antenna hemisphere plus a negative elevation angle within the estimation of CPC and PCC. This improves the condition number significantly from approximately 10^{11} to 10^2. Finally, the coefficients a_{mn} and b_{mn} in vector $\hat{\boldsymbol{x}}$ can be estimated by

$$\hat{\boldsymbol{x}} = \tilde{\boldsymbol{N}}^{-1} \cdot \tilde{\boldsymbol{n}}. \tag{3.53}$$

As described in Section 3.2, the antenna patterns following the definitions of the IGS and are listed in ANTEX files. For each frequency, a PCO / CCO and their corresponding PCV / CPV are provided as a grid with a specific width of usually 5 degree. Thus, the estimated coefficients are inserted again in Equation 3.43 to estimate the PCC / CPC values at the grid points $\alpha, z \in$ grid width. From this grid, the PCO / CCO is estimated in a least squares adjustment, together with the parameter r. To get rid of this parameter, a datum is defined. At IfE the PCC / CPC at zenith are restricted to zero. The residuals indicate the PCV / CPV values of the antenna.

The primary focus of this thesis is on optimizing the codephase signals for the estimation process. Thus, the all presented CPC are estimated using the hemispherical harmonic approach with a degree and order of 8. For detailed information about the estimation and their impacts on the results, the work from Kröger et al. (2021), Kröger et al. (2024) and Kröger (2025) is highly recommended here.

4 Observation Noise and its Role for repeatable Antenna Calibrations

Noise impacts every GNSS signal and degrades the derived parameters. Its behaviour depends mostly on the used GNSS receiver, however, also the observation type (codephase or carrierphase) and the GNSS signal frequency play a role. Noise, generated by the receiver, highly depends on the receiver design and the tracking loop parameters. The latter can be modified by an average user to a certain extent, e.g. by setting the tracking loop bandwidth or loop filter order. This chapter focuses on the observation noise of the estimation inputs (ΔSD) and its role in the antenna calibration. Section 4.1 describes a simulation environment, which can be used to analyse the impact of various noise types on the estimated antenna pattern, as presented in Section 4.3. Section 4.2 presents the actual noise behaviour of the observations, when using the manufacture's default receiver settings, for different antennas, frequencies and receivers. Section 4.4 closes this chapter with a software receiver analysis, which allows studying the impact of different loop parameters on the observables. To this end, optimized receiver settings are defined for the antenna calibration approach, that can be transferred to a hardware receiver.

4.1 Simulation Environment

The simulation environment is integrated in the antenna calibration algorithm described in Section 3.3 and allows computing SD, as well as ΔSD, from an existing CPC or PCC pattern based on the actual poses of the calibration robot. It is possible to estimate antenna correction values based on these simulated observations. This simulation approach can either help to crossvalidate the estimation process in a closed loop scenario or to deeply analyse noise behaviour during the calibration and the final corrections. For clarity, the following parts will be described with the codephase terms CPC, CCO and CPV, however, this approach is identical for PCC.

The CCO and CPV values from the requested GNSS frequency are extracted from the considered ANTEX file. Usually, these values are valid for a north orientated antenna in a horizontal pose. However, for calculating simulated time differenced receiver-to-receiver single differences ($\Delta \mathrm{SD}_{sim}$), it is necessary to have the correct relation between the satellite and its receiving point on the antenna hemisphere. The azimuth azi^k_{ant} and

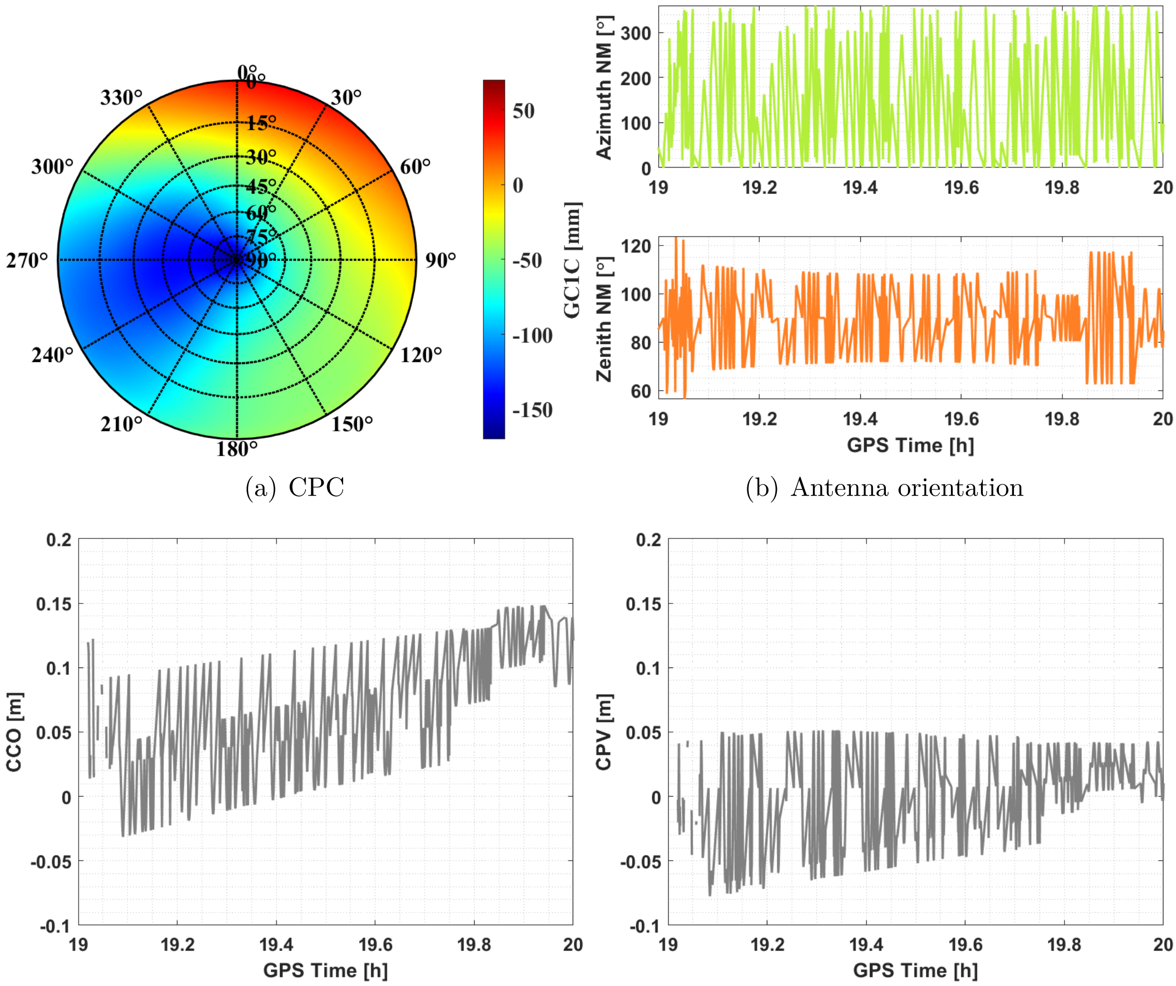

(a) CPC (b) Antenna orientation

(c) CCO (d) CPV

Figure 4.1: Example of the behaviour of GPS C1 CCO (c) and CPV (d) from GPS PRN5 for a LEIAR25.R3 antenna during a robot calibration, based on the pattern presented in (a). The actual AUT pose is presented as a function of zenith angle and azimuth of the antenna's NM (b).

elevation el^k_{ant} of the satellite k in the antenna coordinate system have to be taken into account, due to the robot motion. The CCO is projected onto the LOS of satellite k at each epoch t. For clarity, one epoch is considered in the following equations:

$$CCO^k_{ant} = \begin{bmatrix} \cos azi^k_{ant} \cos el^k_{ant} \\ \sin azi^k_{ant} \cos el^k_{ant} \\ \sin el^k_{ant} \end{bmatrix} \cdot \begin{bmatrix} \mathrm{CCO}_N \\ \mathrm{CCO}_E \\ \mathrm{CCO}_U \end{bmatrix} \tag{4.1}$$

The corresponding CPV values (CPV^k_{ant}) are determined with a bilinear interpolation technique directly from the grid, using the same satellite positions. When using a dynamic elevation mask (cf. Section 3.3.2), satellite elevations below zero may occur within the antenna frame. In general, ANTEX files do not provide corrections values for negative elevations. The values from the horizon (zero degree elevation) are extended (copied) to the used negative elevation angle, which is typically minus five degree, taking the grid width into account. Another approach is to mirror the values from positive elevation to negative elevation, which will be analysed later in this section.

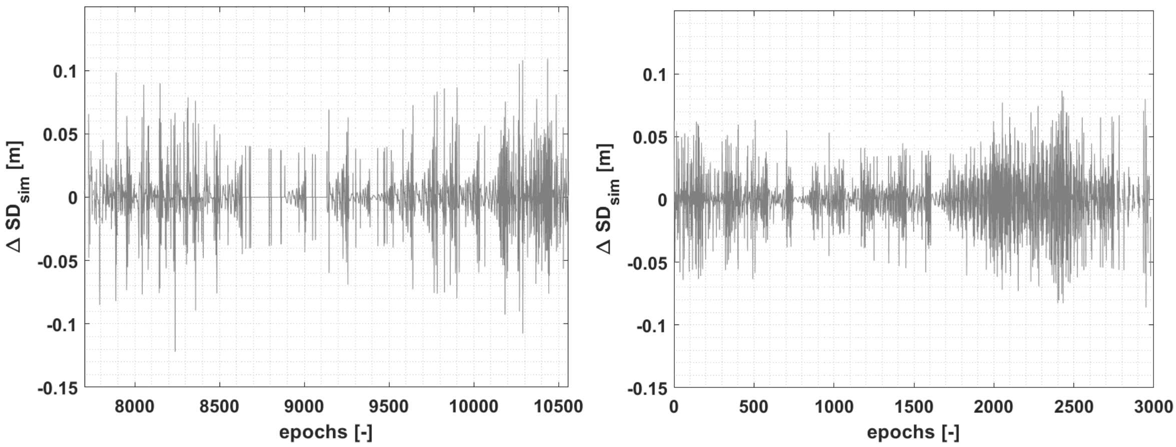

Figure 4.2: Example of the behaviour of GPS C1 ΔSD_{sim} from GPS PRN10 (left) and PRN24 (right) for a LEIAR25.R3 antenna during a robot calibration.

Figure 4.1 shows an example of how CCO (c) and CPV (d) values behave during a robot based antenna calibration, based on an estimated CPC pattern (Fig. 4.1 (a)) from a LEIAR25.R3 antenna, provided by the DLR using their anechoic chamber (cf. Section 6.5.1). The subfigure (b) of Fig. 4.1 depicts the actual AUT pose as the azimuth and zenith of the antenna's NM. Please note that the CPC pattern presented in subfigure (a) of Fig. 4.1 is calculated using Equation 3.2, and therefore, the CPC exhibit negative values.

When CCO and CPV are transformed into the antenna system for each epoch and satellite, the simulated ΔSD can be calculated with

$$\Delta\text{SD}^k_{sim} = \Delta(-\text{CCO}^k_{ant} + \text{CPV}^k_{ant}). \tag{4.2}$$

It is also possible to calculate simulated SD with

$$\text{SD}^k_{sim} = (-\text{CCO}^k_{ant} + \text{CPV}^k_{ant}). \tag{4.3}$$

It should be noted, that the constant parameter r is not considered in the simulation approach.

Figure 4.2 shows an example of how ΔSD_{sim} of the GPS C1 signal behave during a typical antenna calibration based on the DLR pattern for two different satellites.

The estimation of CPC is very challenging, due to a very poor pattern to noise ratio compared to the carrierphase, as it will be discussed in Section 4.2. In order to get a better understanding of the noise influence on the calibration results, Equation 4.2 can be extended by any kind of noise $\hat{\sigma}^k_{ant}$:

$$\Delta\text{SD}^k_{sim} = \Delta(-\text{CCO}^k_{ant} + \text{CPV}^k_{ant}) + \hat{\sigma}^k_{ant}, \tag{4.4}$$

whereas noise is directly added to the ΔSD_{sim} layer, so that no additional noise is added by time or single differencing. This approach was selected to ensure a better control over the amount of noise in the ΔSD_{sim}, even though it may not correspond to reality, as the observation noise is increased by the differencing techniques. Additionally, $\hat{\sigma}^k_{ant}$ is simulated for each satellite, to get independent values. A broad analysis of observation noise influence on the estimated pattern is presented in Section 4.3. The simulated

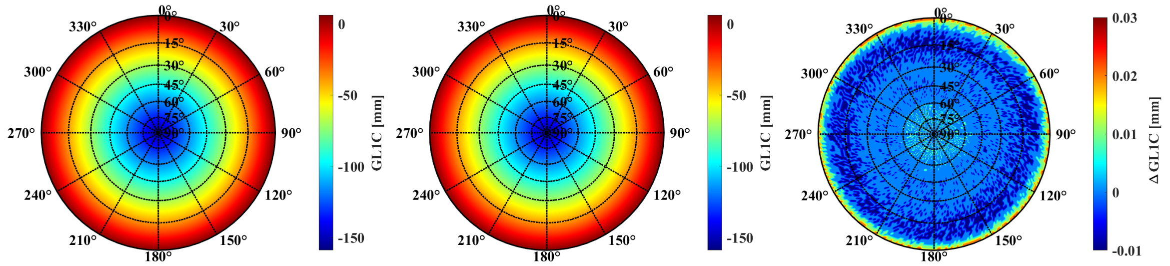

Figure 4.3: Example of a closed loop simulation for a LEIAR25.R3 antenna calibration. (Left) GPS L1 input pattern. (Middle) Estimated pattern with ΔSD_{sim} based on input pattern. (Right) Difference pattern.

observations, either with noise or pure pattern, can be used in the estimation approach to calculate a pattern, similar to real ΔSD. Thanks to perfect simulated observations, it is not necessary to add elevation masks or multipath maps. The advantage of the simulation approach is, that each simulated satellite signal only depends on the satellite geometry and the robot pose, consequently it is not degraded by multipath or the like. Therefore, it can be used to validate the estimation approach in a closed loop scenario.

Figure 4.3 shows an example of this scenario for a LEIAR25.R3 antenna. Here, the carrier signal GPS L1 is considered. The PCC values are estimated from a real calibration and are shown in the left subfigure. Based on this pattern, ΔSD_{sim} are computed and used as input for the estimation process to estimate another pattern (middle). By calculating the difference pattern between both (right), the accuracy of the estimation approach can be validated. Here, the hemispherical harmonics (HSH) approach is used (cf. Section 3.3.3). It should be noted that both patterns are estimated down to a negative elevation of five degrees, which are also included in the resulting ANTEX files.

It is visible, that still smaller differences exist, caused by the bilinear interpolation to compute ΔSD_{sim}. By doing so, some PCV information gets lost during the interpolation process, which impact the resulting pattern. Kröger (2025) shows in his work, that the closed loop with the HSH approach is valid and reached maximum differences at level

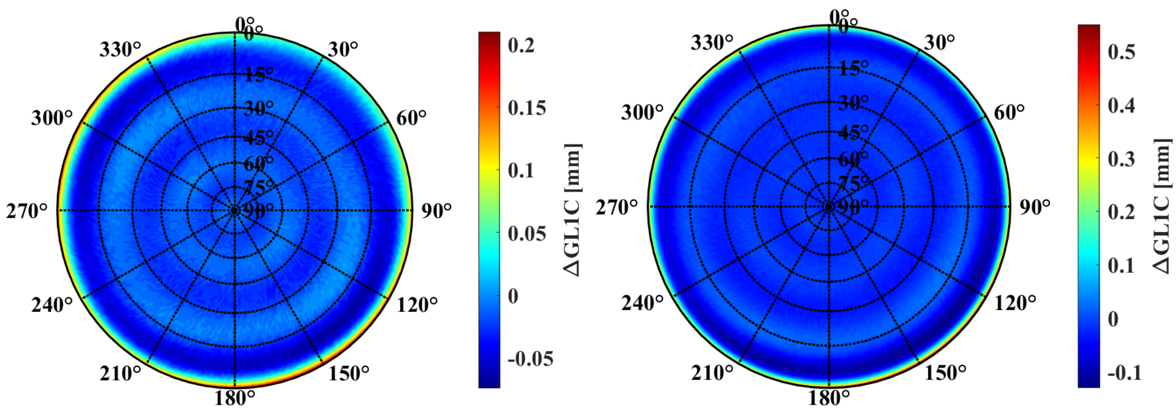

Figure 4.4: Closed loop differences with negative elevation obtained by extrapolating PCV from zero-degree elevation (left) and by mirroring PCV from positive elevations (right). Please note the different scales.

of the computation rounding accuracy, when estimating the pattern directly based on the coefficients and proofed, that the estimation process is internally consistent.

However, typically PCV from negative elevations are not listed in the ANTEX files for antennas, as previously mentioned. To determine these values, extrapolation techniques must be employed. Thus, PCV at zero-degree elevation is often extended to negative elevations (copying approach). Another approach is to mirror PCV from positive to negative elevations (mirroring approach). This is illustrated in Figure 4.4, where the left subfigure displays the closed loop differences using negative elevation derived from zero-degree PCV extrapolation, and the right subfigure presents the differences using mirrored PCV from positive elevations. Both approaches demonstrate similar differences at elevations ranging from approximately two degrees to the zenith, as shown in Figure 4.3. However, at very low elevations, the differences increase to 0.2 mm for the copying approach and 0.55 mm for the mirroring approach. Consequently, the copying approach is recommended.

In Section 4.3 the impact of different noise on the estimated CPC is carried out using the described simulation environment. The simulated patterns rely on the copying approach, despite its higher differences at low elevations compared to using a pattern estimated on a grid extending to minus five degrees. This choice is made for two reasons: firstly, the sub-millimeter differences have no significant impact on the results, because the added noise is predominant and secondly, ANTEX files typically do not provide PCV for negative elevations.

4.2 Noise Analysis of real Calibration Observables

Especially for GNSS codephase signals, the noise of the receiver-to-receiver single differences is very high compared to the magnitude of the CPC information. The amount of noise degrades the pattern estimation and leads to a worse repeatability. This section presents the actual ΔSD noise behaviour of different antennas and frequencies and describes the manufacturer's receiver default settings for three different GNSS receivers and their impact on the ΔSD. Additionally, an analysis is conducted on the impact of robot dynamics.

4.2.1 Noise Dependency on Signal Strength

Observation noise is a very crucial factor, when estimating CPC. Noisy ΔSD impact the calibration algorithms and consequently the resulting pattern. It can lead to worse repeatability and at the end to a wrong CPC. The challenge lies in managing relatively high noise levels compared to the magnitude of CPC information. Figure 4.5 illustrates this problem[1] and shows the code- and carrierphase ΔSD for a LEIAR25.R3 NONE (S/N: 9330001) antenna of GPS satellite PRN25 from a calibration carried out on the 27^{th} May 2024. The reference antenna and the AUT are each connected to a Javad

[1]Note: All figures shown in this section are created by using different techniques to eliminate problematic observations, like elevation masks (cf. Section 3.3.2), multipath maps (cf. Section 5.3) and further elimination techniques (Section 6.1.1).

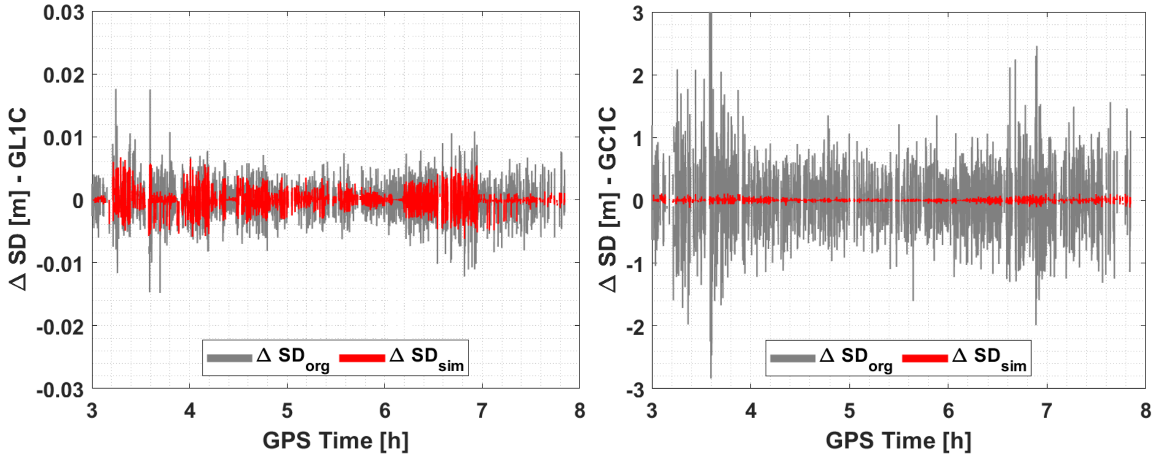

Figure 4.5: ΔSD (grey) and simulated ΔSD (red) from a calibration of an LEIAR25.R3 NONE (S/N: 9330001) for the GPS L1 (left) and C1 signal (right). The GPS satellite PRN25 is depicted. The calibration has been carried out with a Javad Delta TRE G3T receiver with default settings.

Delta TRE G3T, utilizing the manufacturer's default settings. The left figure shows the data for the GPS L1 carrierphase, whereas the right depicts the GPS C1 codephase signal. In order to visualize the pattern information within these signals, ΔSD_{sim} are additionally shown in red. As described in the previous section, ΔSD_{sim} contain only the pattern information ($\hat{\sigma}^k_{ant} = 0$). The carrierphase pattern is based on a previous calibration of this antenna and the codephase pattern was estimated in an anechoic chamber, by the DLR.

It is clearly visible, that the noise between code- and carrierphase differs roughly by a factor of 100. Instead of dealing with a noise at the centimeter or even millimeter level, which is usually achievable for the carrierphase, noise in the range of several decimeters to meters needs to be managed for the codephase signal. As a rule of thumb, it can be said that the noise is in the order of approximately one percent of the GNSS signal wavelengths/chiplengths. With a codephase chiplength of $\approx 293\,\text{m}$ and a carrierphase wavelength of $\approx 20\,\text{cm}$ the factor of 100 in the ΔSD between the two observation types is realistic. This holds also true after the two differencing steps to compute the ΔSD. Usually, the CPC values are slightly larger than the PCC values, however, a factor of 100 between CPC and PCC is very unrealistic.

When looking at Figure 4.5 and compare ΔSD_{sim} with the original ΔSD, it can be seen that the carrierphase ΔSD_{sim} are very well presented by the original observations, resulting in a very good pattern to noise ratio (PNR). When looking at the codephase, this ratio becomes very poor. Noise is dominating the CPC values. The challenge is now, to determine these small pattern information in this high noisy time series to estimate CPC accurately and reliably.

Obviously, the noise in the ΔSD does not behave as white noise (WN). The data follow more or less the robot movement, thus the signal is received at different points on the antenna hemisphere. Consequently, the signal strength between two consecutive observation epochs can vary quite a lot, explainable by the difference in the antenna's gain pattern. This is illustrated in Figure 4.6, which depicts the ΔSD for GPS satellite PRN11 from a calibration of an u-blox ANN-MB1 antenna, carried out in February 2024. The C1 signal is presented (left). The right figure shows the ΔSD distribution

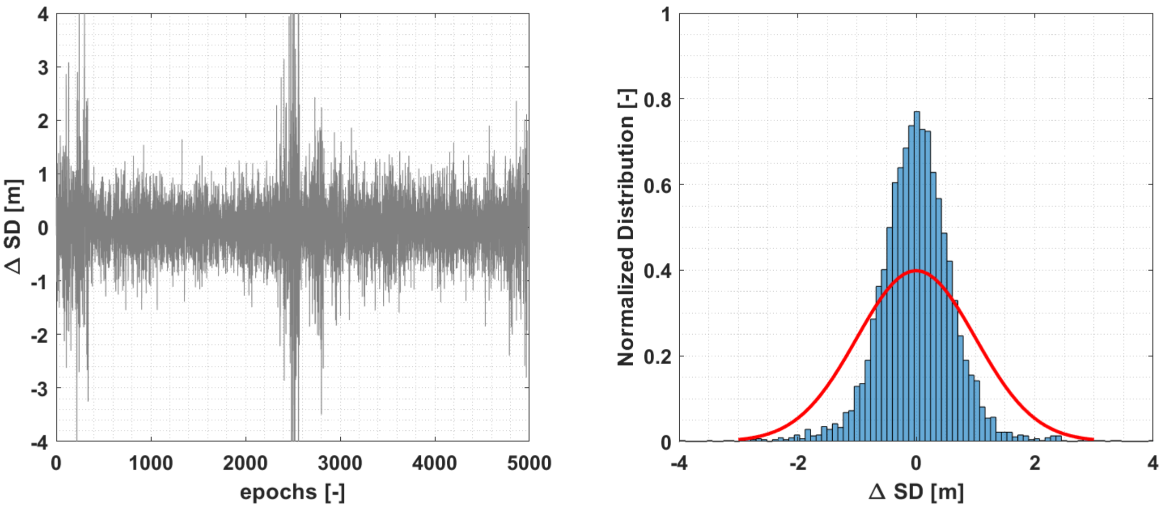

Figure 4.6: Example of the behaviour of GPS C1 ΔSD from GPS PRN11 (left) for u-blox ANN-MB1 antenna during a robot calibration. (Right) Distribution of the ΔSD in blue and standard normalized distribution in red.

in blue compared to a standard normal distribution in red. WN is defined as a normal distributed Gaussian noise with a specific standard deviation σ and mean value μ:

$$WN \sim N(\mu, \sigma^2). \tag{4.5}$$

Thus, if the ΔSD were affected by WN only, the blue data would align with the red curve. Clearly, this is not the case, indicating that the ΔSD is influenced by a different type of noise.

In order to analyse the noise behaviour, the signal strength and the antenna gain during a calibration is analysed w.r.t. the ΔSD. Figure 4.7 shows these observables with ΔSD in subfigure (a). Additionally, subfigure (b) depicts the azimuth and elevation changes in the antenna frame between consecutive epochs for GPS satellite PRN22. The differences in the C/N_0 and the antenna gain, provided by the DLR, between the sequential robot resting phases are presented in subfigure (c) and (d), respectively. The data is from the above-mentioned calibration for the u-blox ANN-MB1 antenna. As expected, the C/N_0 and the antenna gain are highly correlated. Significant variations are visible between 22 and 23 hours. During this time, the antenna's orientation changes rapidly, causing the satellite's elevation and azimuth in the antenna frame to vary significantly. Additionally, higher ΔSD occur during this time, which indicates a high correlation between the ΔSD noise and the signal strength variations.

Therefore, the hypothesis is proposed that the noise follows the behaviour of the signal strength. A commonly used C/N_0 noise model can be, for example:

$$\begin{aligned} \sigma_{Ref} &= \sqrt{a \cdot 10^{-\frac{C/N_0}{10}}}\ [\mathrm{m}] \\ \sigma_{AUT} &= \sqrt{b \cdot 10^{-\frac{C/N_0}{10}}}\ [\mathrm{m}] \end{aligned} \tag{4.6}$$

for the robot AUT and the reference station Ref. The coefficients a and b are antenna/receiver dependent and have to be estimated beforehand.

In applications, where the antenna is static, and the measurements are in equally time distances, the approach from de Bakker et al. (2009) can be used, which can be

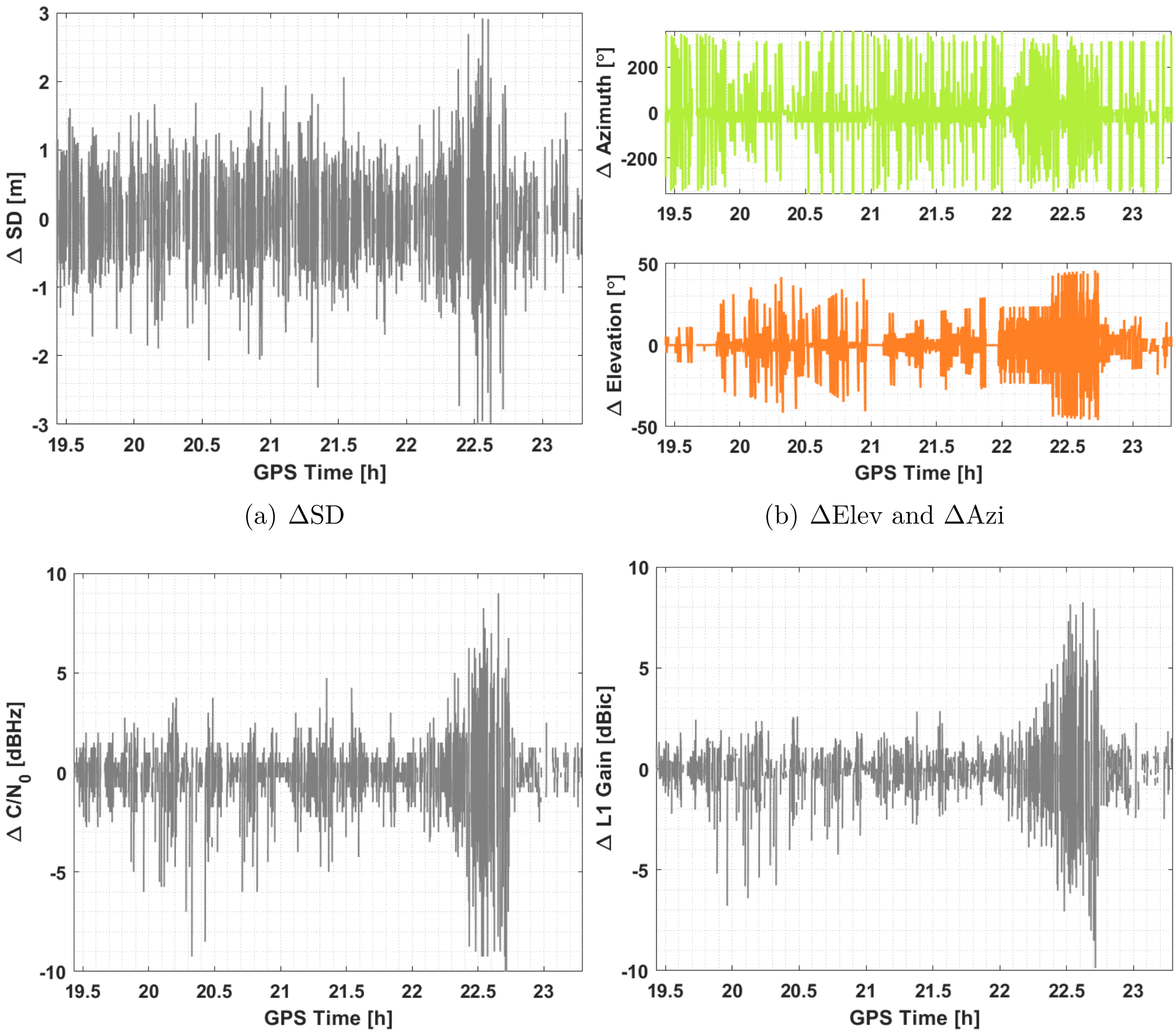

(a) ΔSD (b) ΔElev and ΔAzi

(c) $\Delta C/N_0$ (d) ΔGain

Figure 4.7: Example of the relation between C1 ΔSD (a) and the signal strength (c) and antenna gain (d) from GPS PRN22 for an u-blox ANN-MB1 antenna during a robot calibration. The azimuth and elevation changes in the antenna frame for this satellite is presented in (b).

summarized as follows. In a static measurement, the C/N_0 is slightly changing with time. This behaviour allows creating bins, including 120 consecutive epochs of the C/N_0 time series, from which the author estimated the standard deviations. Afterwards, the standard deviations are plotted against the mean C/N_0 values of the bins. The C/N_0 model is fitted through this data, to estimate the coefficient of the model.

This approach can not be used for this purpose, firstly because the antenna is rotating (high C/N_0 changes between epochs) and secondly the time periods between two robot resting phases are not constant. To get information about the ΔSD variances, an alternative approach is proposed. For this, the observations from the above-mentioned calibration using manufacturer's GNSS receiver settings (cf. Section 4.2.3) are considered. Due to the measurement setup with SD and time differencing, the noise of each station and epoch must be combined using variance propagation:

$$\bar{\sigma}^2_{C/N_0} = \sigma^2_{AUT}(t_{i+1}) + \sigma^2_{AUT}(t_i) + \sigma^2_{Ref}(t_{i+1}) + \sigma^2_{Ref}(t_i) \text{ [m]}. \tag{4.7}$$

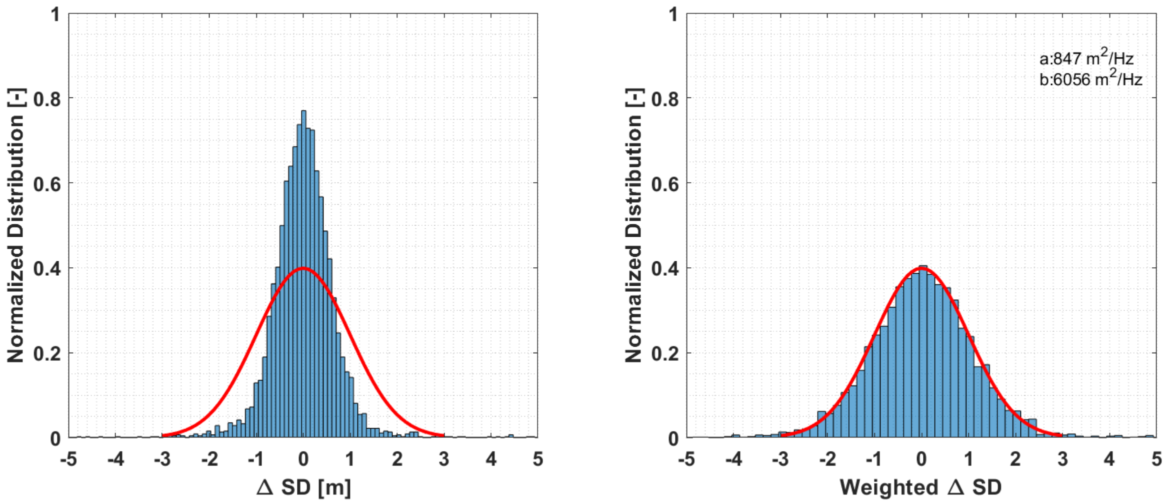

(a) PRN11

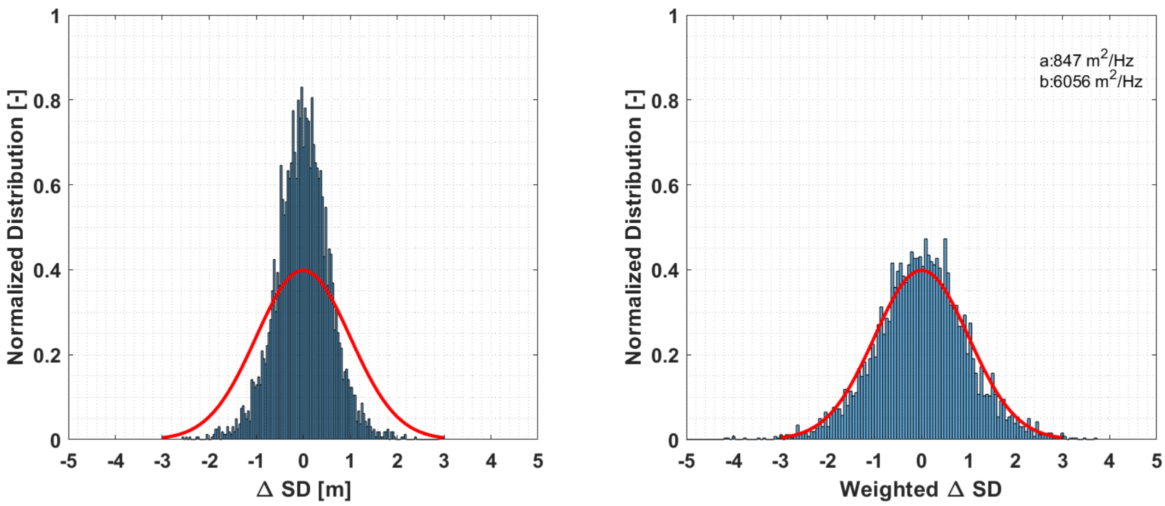

(b) PRN14

Figure 4.8: ΔSD distribution of the GPS C1 signal of satellite PRN11 (a) and PRN14 (b) for an u-blox ANN-MB1 antenna before (left) and after (right) C/N_0 weighting. The standard normal distribution is presented in red ($\sigma = 1\,\mathrm{m}$).

When Equation 4.6 is substituted into Equation 4.7, the coefficients a and b can be estimated using a least-squares adjustment. The design matrix $\boldsymbol{A}$ contains the partial derivatives of Equation 4.7 with respect to the two parameters:

$$\boldsymbol{A} = \begin{bmatrix} 10^{-0.1 \cdot C/N_0(AUT,t_{i+1})} + 10^{-0.1 \cdot C/N_0(AUT,t_i)} & 10^{-0.1 \cdot C/N_0(Ref,t_{i+1})} + 10^{-0.1 \cdot C/N_0(Ref,t_i)} \\ \vdots & \vdots \end{bmatrix} \tag{4.8}$$

The observation vector $\boldsymbol{l}$ consists of the epochwise variances, which are estimated using a moving window with a duration of 120 epochs over the ΔSD time series of the satellite. With

$$\boldsymbol{A}\boldsymbol{x} = \boldsymbol{l}, \tag{4.9}$$

the two coefficients can be estimated. They differentiate between the satellites slightly, however, by averaging them a good approximation for a and b can be achieved. For example, for an u-blox ANN_MB1 (S/N: 2133) antenna, the coefficients are: $a = 847\,\mathrm{m}^2/\,\mathrm{Hz}$ and $b = 6056\,\mathrm{m}^2/\,\mathrm{Hz}$.

The results can be seen in Figure 4.8 exemplarily for two different GPS satellites. The left subfigures show the actual distribution of the ΔSD of the GPS satellites PRN11 (a) and PRN14 (b) for the C1 signal. When dividing the ΔSD by $\bar{\sigma}_{C/N_0}$ (C/N_0 weighting), the ΔSD behaviour nearly conforms to a standard normal distribution for PRN11 (right). Thus, a good approximation of the actual noise during the antenna calibration is achieved using a C/N_0 dependent noise model. However, for PRN14, the ΔSD cannot be fully normalized to a standard normal distribution, indicating that the noise also depends on another source.

4.2.2 Observation Noise of different Frequencies and Antennas

Not only the observation type is responsible for the noise behaviour, also the used GNSS antenna can influence the ΔSD. Three different calibrations have been carried out to analyse the noise on the ΔSD. One calibration for a geodetic choke ring antenna on May, 25^{th} 2024, one for a geodetic rover antenna on June, 16^{th} 2024 and one calibration for a patch antenna on June, 13^{th} 2024 over a time period of 24-hours. Hereinafter, three antenna types are defined as categories 1 to 3 corresponding to the used antennas in this experiment:

- Category 1: Geodetic choke ring antennas - LEIAR25.R3 NONE (S/N: 9330001),
- Category 2: Geodetic rover antennas - NOV703GGG.R2 NONE (S/N:12420040),
- Category 3: Patch antennas - u-blox ANN-MB1 NONE (S/N:2133).

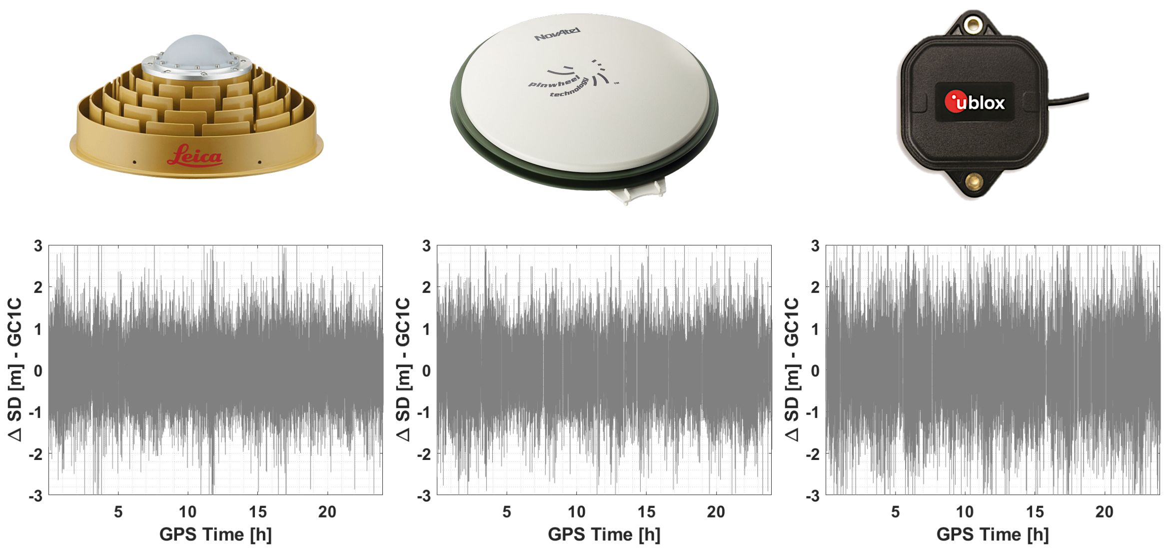

Figure 4.9: ΔSD from a calibration for a category 1 (left), category 2 (middle) and category 3 (right) antenna. The calibrations have been carried out with two Javad Delta TRE G3T receivers with manufacture's default settings. The GPS C1 signal from all visible satellites are plotted [Antenna pictures: Leica Geosystems AG (2024); Novatel (2011); U-Blox AG (2024)].

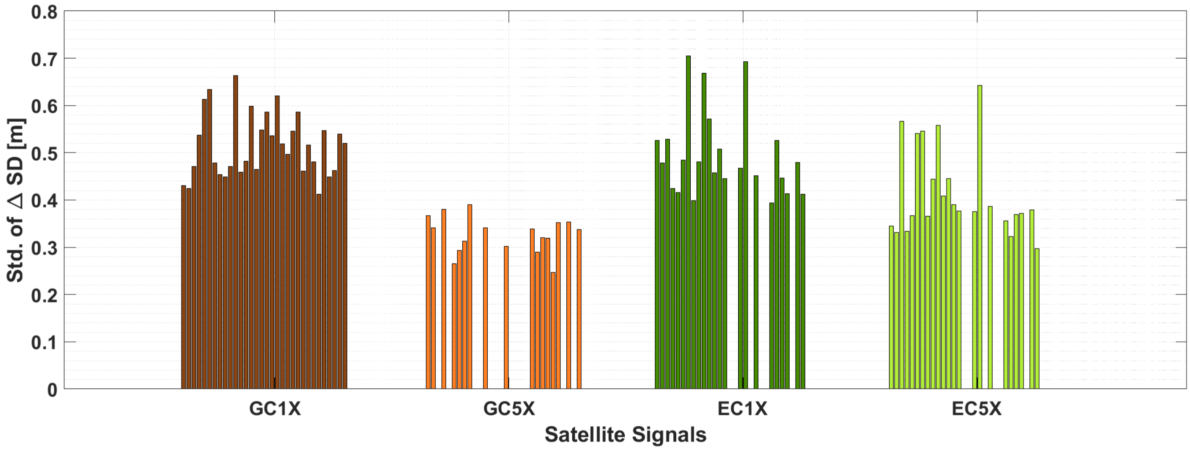

Figure 4.10: Standard deviations of all visible satellites for the C1 and C5 signal of GPS and Galileo for a 24-hour calibration of a category 2 antenna. The calibration has been carried out with a Javad Delta TRE G3T receiver with default settings.

The ΔSD of the three calibrations are shown in Figure 4.9, from category 1 (left) to category 3 (right). It should be noted, that the CPC pattern information is still included in the time series. Since the ΔSD pattern information is relatively small compared to the observations, the CPC are assumed to have no significant impact on this noise behaviour investigation. Two Javad Delta TRE G3T receiver were used with the manufacture's default settings to collect the data. The ΔSD of all visible satellites for the GPS C1 are presented. It can be seen, that the observables of the category 3 antenna are larger than observables of the other two antennas, however, the ΔSD of category 1 are slightly smaller than for category 2 antenna, visually. Additionally, the C/N_0 dependent noise behaviour of all antennas is observable. For a better comparison, the standard deviation σ_k over all visible satellites k are calculated and averaged w.r.t. the number of observations to get the weighted standard deviation σ_{ant} for each category and different frequencies:

$$\sigma_{ant} = \sqrt{\sum_{k=1}^{k_{max}} w_k \sigma_k^2}, \quad w_k = \frac{n_k}{n} \tag{4.10}$$

with n_k being the number of observations of satellite k, whereas n defines the total number of ΔSD. The results are shown in Table 4.1 for the C1 and C5 signals of GPS (GC1C, GC5X) and Galileo (EC1X, EC5X) for the three antennas. By comparing the different categories it is visible, that the standard deviation increases from category 1 to 3. The ΔSD of the choke ring antenna show the lowest standard deviation and consequently the lowest noise in the time series. Besides, σ_{ant} distinguishes between different satellite systems and frequencies. The σ_{ant} of both C5 signals are lower as the C1 signals, with a slightly worse performance for Galileo C5. The standard deviations

Table 4.1: Weighted averaged standard deviation of ΔSD from all visible satellites during a 24-hour calibration for different antennas. All values are in [m].

Category / Signal	GC1C	EC1X	GC5X	EC5X
1	0 476	0.433	0.334	0.340
2	0.515	0.486	0.323	0.414
3	0.620	0.600	0.445	0.552

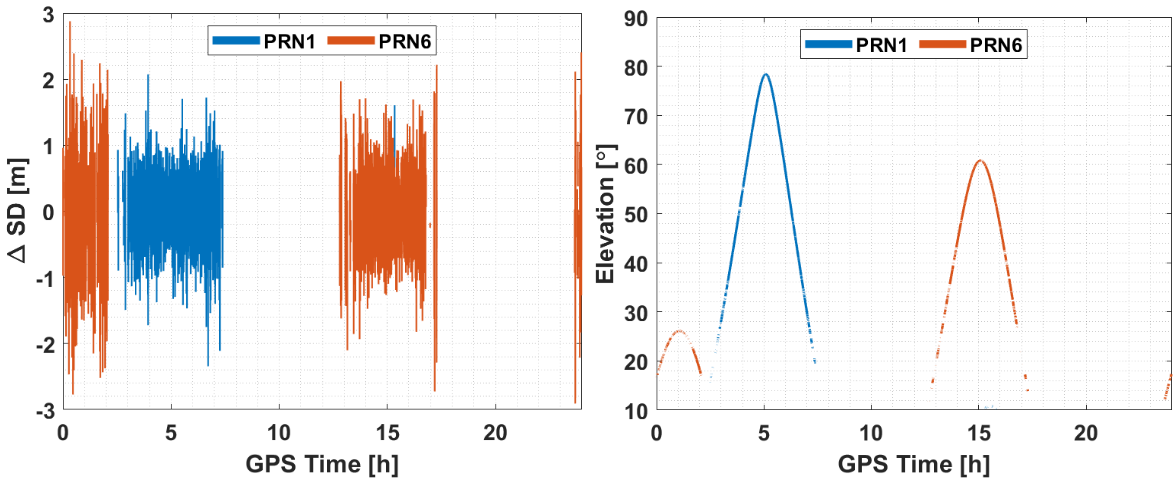

Figure 4.11: C1 ΔSD for GPS satellite PRN1 and 6 (left) and their corresponding topocentric elevation (right) for a category 2 antenna.

of the C1 signals of both system are very similar. The GPS C5 signal exhibits the smallest standard deviation. These signals are transmitted by the newest generations of GPS satellites, which utilize advanced technology, thereby reducing noise and benefiting the observable (Teunissen and Montenbruck, 2017). However, the number of satellites transmitting the GPS C5 signal is only about half of the entire GPS constellation.

This can be seen in Figure 4.10. Here, the standard deviation of each satellite is depicted for the analysed GNSS signals. The data is from the calibration of the category 2 antenna. Only 17 satellites transmitted the GPS C5 signal. The C1 signal of all GPS satellites has been received during the 24-hour calibration. This figure shows similar results to the weighted averaged standard deviation in Table 4.1. The challenge with the GPS C5 signal is to estimate a precise pattern, because only half of the observations are available compared to the C1 signal. An increase of the calibration duration can counteract this problem.

The standard deviation varies for each satellite across all GNSS signals, and these differences are highly correlated with the satellite's elevation in the topocentric frame. Figure 4.11 (a) shows the ΔSD of the GPS satellite PRN1 and PRN6 for the C1 signal together with their elevation in subfigure (b). It is evident, that higher noise occurs at low elevations. Thus, σ of satellite PRN1 (0.432 m) is significantly smaller than for PRN6 ($\sigma = 0.635$ m). Additionally, differences can also occur when more observations are eliminated using different elimination techniques[2].

A further comparison between the C1 and the C5 signal is presented in Figure 4.12 for the GPS satellite PRN10 and Galileo satellite PRN26 in a time window of about 3.5 hours with the same data used in Figure 4.10. The darker coloured data represent the C1 signal, whereas the brighter coloured data show the C5 signal. Obviously, the C5 signals show a less noisy time series than the C1 signal for both satellite systems. The data gaps occur because of different elimination techniques.

[2]Note: All figures shown in this section are created by using different techniques to eliminate problematic observations, like elevation masks (cf. Section 3.3.2), multipath maps (cf. Section 5.3) and further elimination techniques (Section 6.1.1).

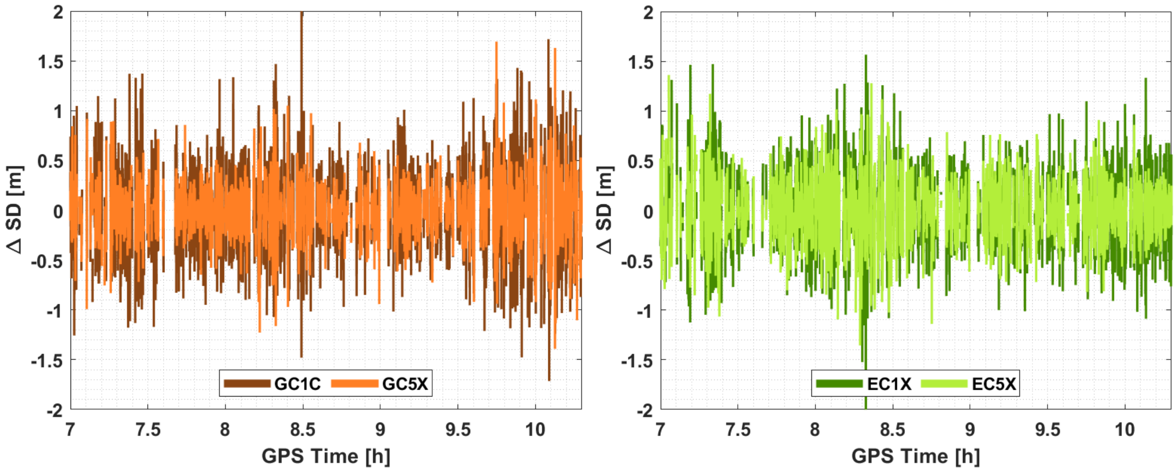

Figure 4.12: ΔSD of the GPS C1 and C5 signal of the satellite PRN10 from a category 2 antenna calibration (left) and Galileo C1 and C5 signal of the satellite PRN26 (right). The calibration has been carried out with a Javad Delta TRE G3T receiver with default settings.

In summary, the noise levels of different antenna types vary even when using the same GNSS receiver and settings. Patch antennas produce noisier data compared to a geodetic high-end choke ring antennas. Additionally, the C5 signal is less noisy than the C1 signal. A slight improvement in the weighted averaged standard deviation is achievable for Galileo signals compared to GPS for the C1 signal. The satellite elevation is the main factor responsible for the individual ΔSD standard deviations of the satellites.

4.2.3 Receiver with default Settings

So far, antenna calibrations have been carried out using default receiver settings as proposed by the manufacturer for estimating antenna's PCC and CPC. As discussed in Section 4.2.1, this works quite well for carrier phase calibrations, thanks to a very good PNR. However, this ratio gets worse for CPC. In general, default receiver settings are optimized from the manufacturers to ensure a stable receiver performance, mostly for static GNSS applications. However, they are not optimized for estimating CPC in an antenna calibration approach using a robot in the field. In this thesis, three different GNSS receivers have been analysed and used in different experiments. Two of the receivers are from the Javad company, the Javad Delta TRE G3T released in 2009 and the Javad DeltaS-3S released in 2021. The third used receiver type is the Septentrio PolaRx5TR, which is available since 2016 (cf. Figure 4.13 top row).

Each receiver employs a specific design that is proprietary to the manufacturer, however, some parameters can typically be modified by the user. The opportunities for changing and modifying the Javad receiver parameters are numerous. Here, we mainly focus on the tracking loop parameters, which are mostly responsible for the observation noise as described in Section 2.3.3. Modifications on the bandwidth of the DLL, which they call code lock loop (CLL), or PLL can be done, either for the general bandwidth or for weak and strong loops. Additionally, the order of the tracking loop filters can be defined. The CLL can be aided by the carrier loop, either with a 100 % aiding, partly or 0 %. The opportunity for modifying the predetection integration time or the correlator

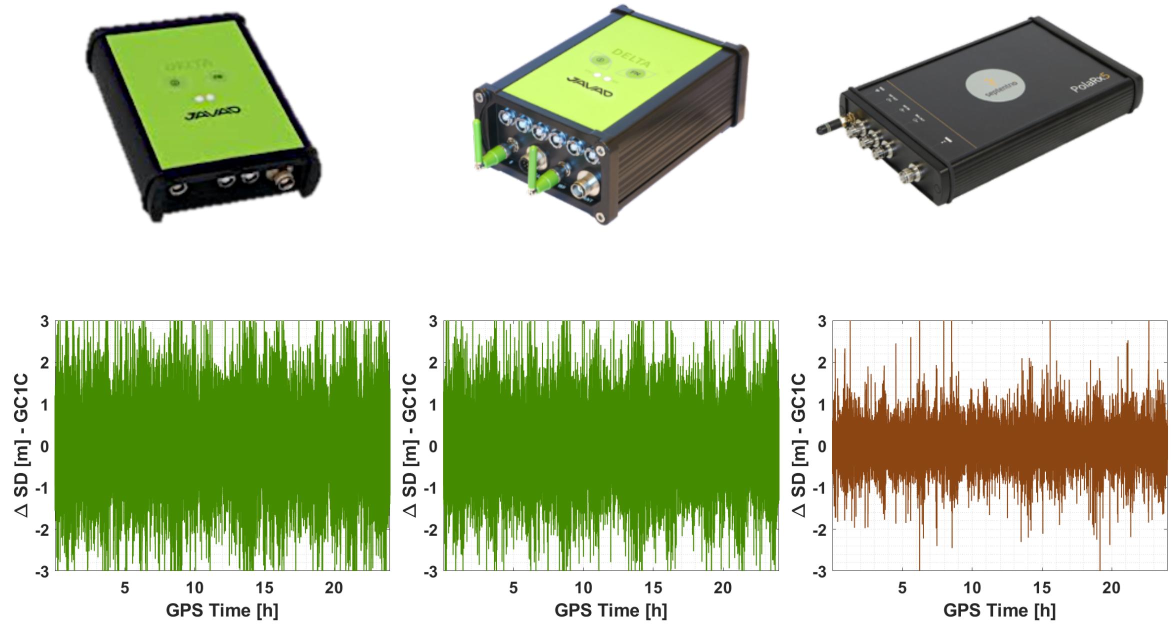

Figure 4.13: ΔSD from a calibration of an u-blox category 3 antenna for the GPS C1 signal with Javad Delta TRE G3T (left), Javad DeltaS-3S (middle) and Septentrio PolaRx5TR receiver (Right). The ΔSD of all visible satellites are plotted with the manufactures' default receiver settings [Receiver pictures: JAVAD GNSS (2024a), JAVAD GNSS (2024b), Septentrio (2024)].

spacing is not possible. Nevertheless, the Javad receiver has a great opportunity to optimize receiver settings for the calibration approach.

The options for adjusting the tracking loops for the Septentrio receiver are sparse. Directly, it is only possible to modify the bandwidth of the DLL and PLL and additionally change the predetection integration time. There are no information about the filter order or if the DLL is aided by the PLL, what makes optimization difficult. In addition, an *adaptive mode* can be activated. By turning this parameter on, the receiver dynamically changes the loop parameters for optimizing the performance in specific conditions (Septentrio, 2020).

In this thesis, several experiments have been carried out with default receiver settings. Later in Section 6.1.2, optimizations of the receiver tracking loops, especially the bandwidth of the DLL, are done. Therefore, using the terms *default settings* and

Table 4.2: Default settings for the tracking loops of the three receivers.

Loop	Settings	Delta TRE G3T (J)	DeltaS-3S (J)	PolaRx5TR (S)
DLL	Bandwidth [Hz]	3	3	0.25
	Filter Order	1	1	-
	Aiding [%]	100	100	-
	Int. Time [ms]	-	-	100
PLL	Bandwidth [Hz]	25	25	15
	Filter Order	3	3	-
	Aiding [%]	100	100	-
	Int. Time [ms]	-	-	10

optimized settings are distinguished in the tracking loops, only (cf. Section 2.3.3). In Table 4.2 the default tracking loop settings for the three receivers are listed. The Javad receivers are defined as (J) and Septentrio with (S).

The DLL bandwidth of the Septentrio receiver is with 0.25 Hz much smaller than the bandwidth of Javads' DLL default bandwidth of 3 Hz. In general, a smaller bandwidth leads to a less noisy time series (cf. Section 2.3.3). This is visible in Fig. 4.13. Here, the ΔSD for the GPS C1 signal is shown for all visible satellites for a calibration of a category 3 antenna. The antenna signal has been split via a GNSS splitter to feed the different receivers in a zero baseline approach. The same has been done for the reference antenna signal. Two identically constructed receivers define one receiver pair that is used to set up the ΔSD. The calibration was carried out on the 17^{th} February 2024. The data show the time period of 24-hours. It is clearly visible, that the ΔSD of the Septentrio receivers ($\sigma_{ant} = 0.2789\,m$) are less noisy, compared to the Javad receivers, whereas data from the Delta TRE G3T ($\sigma_{ant} = 0.6318\,m$) are a bit noisier than the DeltaS-3S ($\sigma_{ant} = 0.5789\,m$). Even though the default settings for the two Javad receivers are identical, the ΔSD differs in favour of the DeltaS-3S. This can be explained by the newer technology and receiver design for DeltaS-3S compared to the Delta TRE G3T, which have been released 12 years earlier. However, even the newer Javad receivers exhibit very large noise, that makes it very difficult to estimate CPC accuratly and precisely.

In order to better understand the difference in performances between the Javad and the Septentrio receiver, two static experiments have been carried out. The two receiver pairs have collected data for a category 2 antenna on two different days. The results are shown in Figure 4.14, exemplary for the GPS C1 signal from the PRN5 satellite. The data from the Javad Delta TRE G3T is presented in the left column, whereas the right column shows the data from the Septentrio PolaRx5TR receiver. For a better comparison, both receivers operated with a DLL bandwidth of 0.25 Hz. Each subfigure shows the results using a 1 Hz and a 10 Hz sampling rate for the Javad and 20 Hz for Septentrio, respectively. The first row depicts the ΔSD of both receivers with different sampling rates over the whole time period. The ΔSD of the Javad receiver, either with a 1 Hz or 10 Hz sampling, are very similar, with a bit less noisy time series for the 10 Hz data. The magnitude of the Septentrio ΔSD is highly decreased, compared to the Javad data. A 20 Hz sampling rate leads to a very small ΔSD magnitude of approximately 8 cm, which is very small for a double differentiated codephase signal.

The second row shows the SD of PRN5 as a zoom of the whole measurement duration. The Javad observations behave like expected. The 1 Hz data vary around zero, with the 10 Hz data varying between the 1 Hz sampling points. Here, SD are presented without the SD ambiguity.

The behaviour of the Septentrio SD differs. The 1 Hz data are very smooth, and the 20 Hz data follow a similar pattern. It can be assumed that the Septentrio receiver smooths the codephase with help of the carrierphase, which is of course beneficial for codephase based positioning or navigation applications, but disadvantageous for estimating CPC. Due to the codephase smoothing, important information about the codephase pattern gets lost. The last row of 4.14 shows a zooming of the ΔSD. Due to the codephase smoothing, the ΔSD of the Septentrio receiver achieves small noise or signal magnitude.

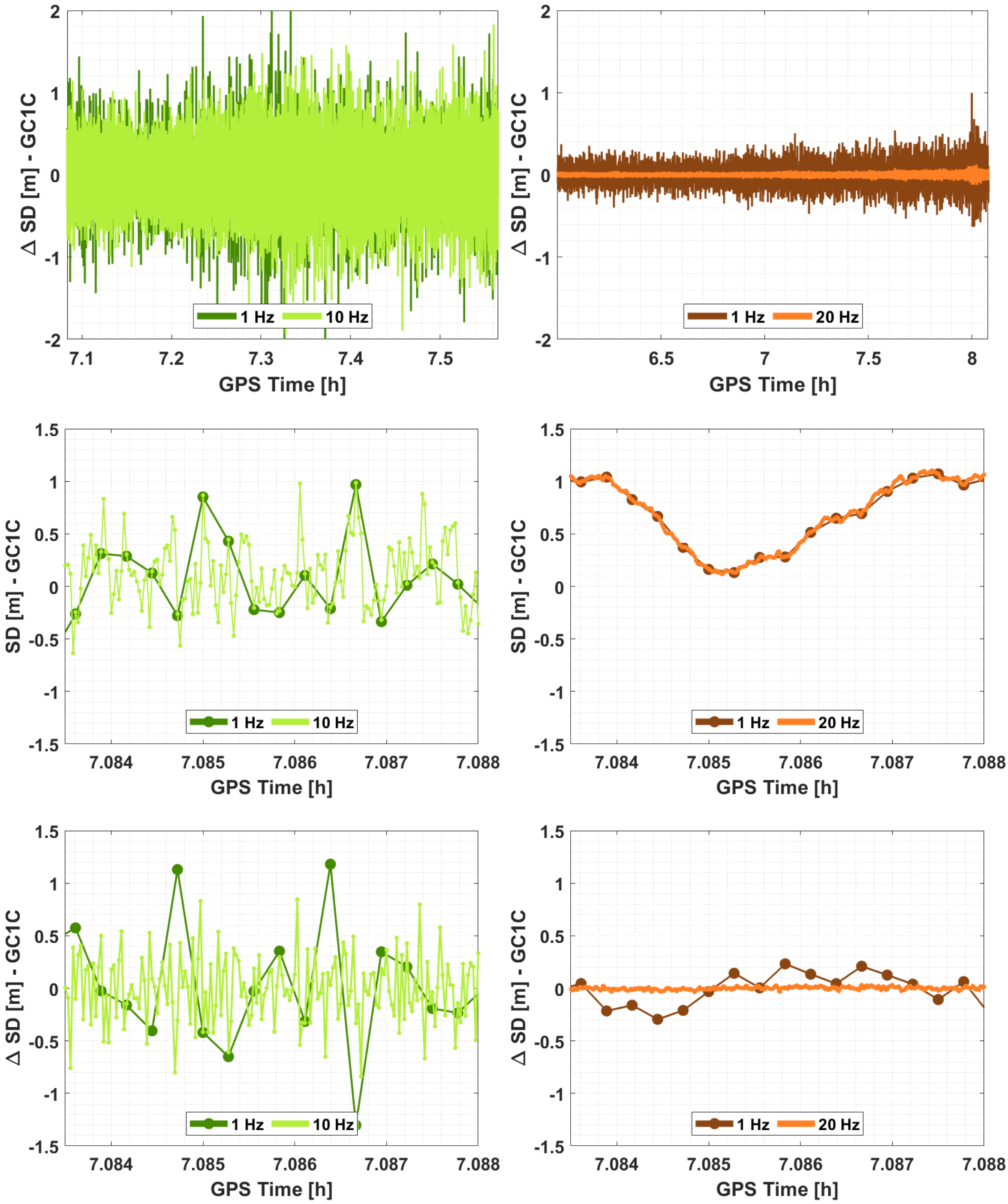

Figure 4.14: Static experiment for the GPS C1 signal for PRN5 satellite with a category 2 antenna with Javad Delta TRE G3T (left) and Septentrio PolaRx5TR receiver (right). Both receivers operate with a DLL bandwidth of 0.25 Hz. The experiments have been carried out on different days. The top row shows the ΔSD over the whole static time, the middle row depicts the SD in a zoom on a specific time span and the last row presents the corresponding ΔSD. 1 Hz and 10 Hz for Javad respectively 20 Hz for Septentrio are presented.

Closing Remarks The used receiver plays an important role for estimating CPC. However, the *default settings* are not optimized for codephase antenna calibrations. They need to be adapted in order to reduce the noise of the ΔSD by maintaining important pattern information. The optimization of the tracking loop parameters can be done, e.g.

with a software receiver, which allows studying the impact of different parameters in post-processing (cf. Section 4.4). Afterwards, the optimized settings are transferred to a hardware receiver (cf. Section 6.1.2). The Septentrio PolaRx5TR receiver cannot be used for CPC estimation because, firstly, its settings can only be modified to a limited extent (from an average user's perspective), and secondly, the code phase smoothing removes important pattern information, despite the ΔSD being less noisy.

4.2.4 Impact of Robot Dynamics

In Section 3.3.1 the mathematical robot model was introduced. The robot can maintain its pose during static phases with millimeter accuracy. However, the displacement between the ideal and actual FP must be considered for the calibration of carrierphase signals. For codephase signals, this offset is not significantly impactful, as the observation noise is the dominant factor. In this section, the dynamics of the robot during movements between static phases are investigated to assess their impact on the GNSS receiver, particularly in terms of whether a closed DLL can be maintained during a calibration.

On December, 13^{th} 2022, an experiment was conducted involving the standard calibration of a category 2 antenna, along with the installation of an IMU on the robot (cf. Figure 4.15). The IMU, namely LORD MicroStrain 3DM-GQ4-45, is installed on the upper part of module 5, ensuring that it experiences the same motion as the AUT around the FP, as the IMU and FP form a fixed system. Additionally, a GNSS splitter is installed on the other side of the module. This setup ensures that the antenna signal is connected not only to the GNSS receiver but also to the IMU, providing the GPS timestamp to the IMU. To this end, the IMU measurements are transferred to a nearby laptop for data storage.

Because of the fixed system between the FP and the IMU, the measured IMU angular rates, with a sampling rate of 100 Hz, can be directly applied to the FP. Additionally,

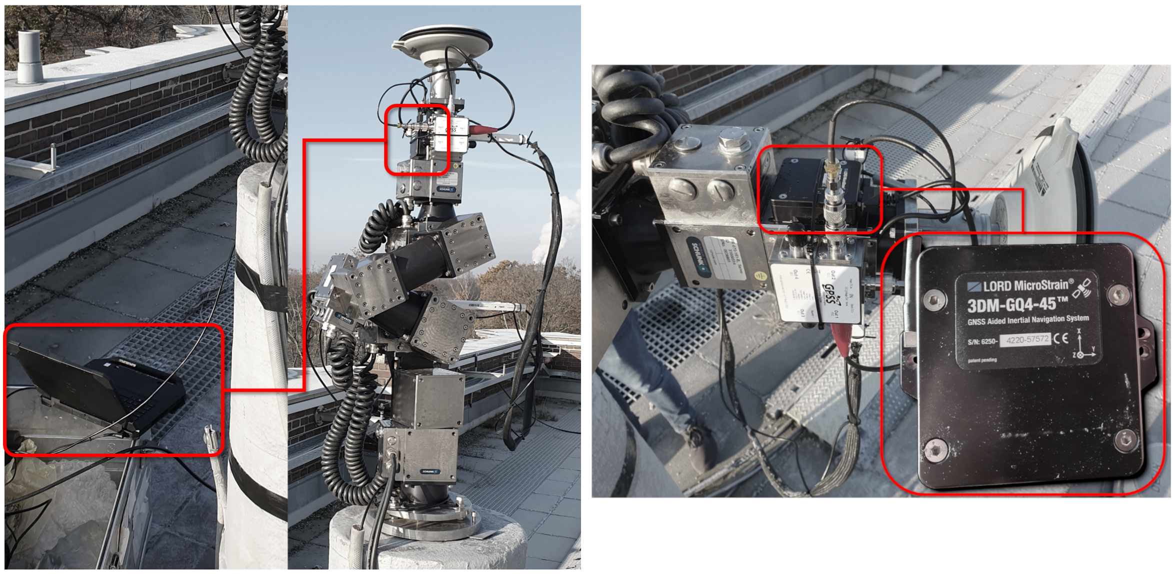

Figure 4.15: Experimental setup (left) with the definition of the IMU axis (right).

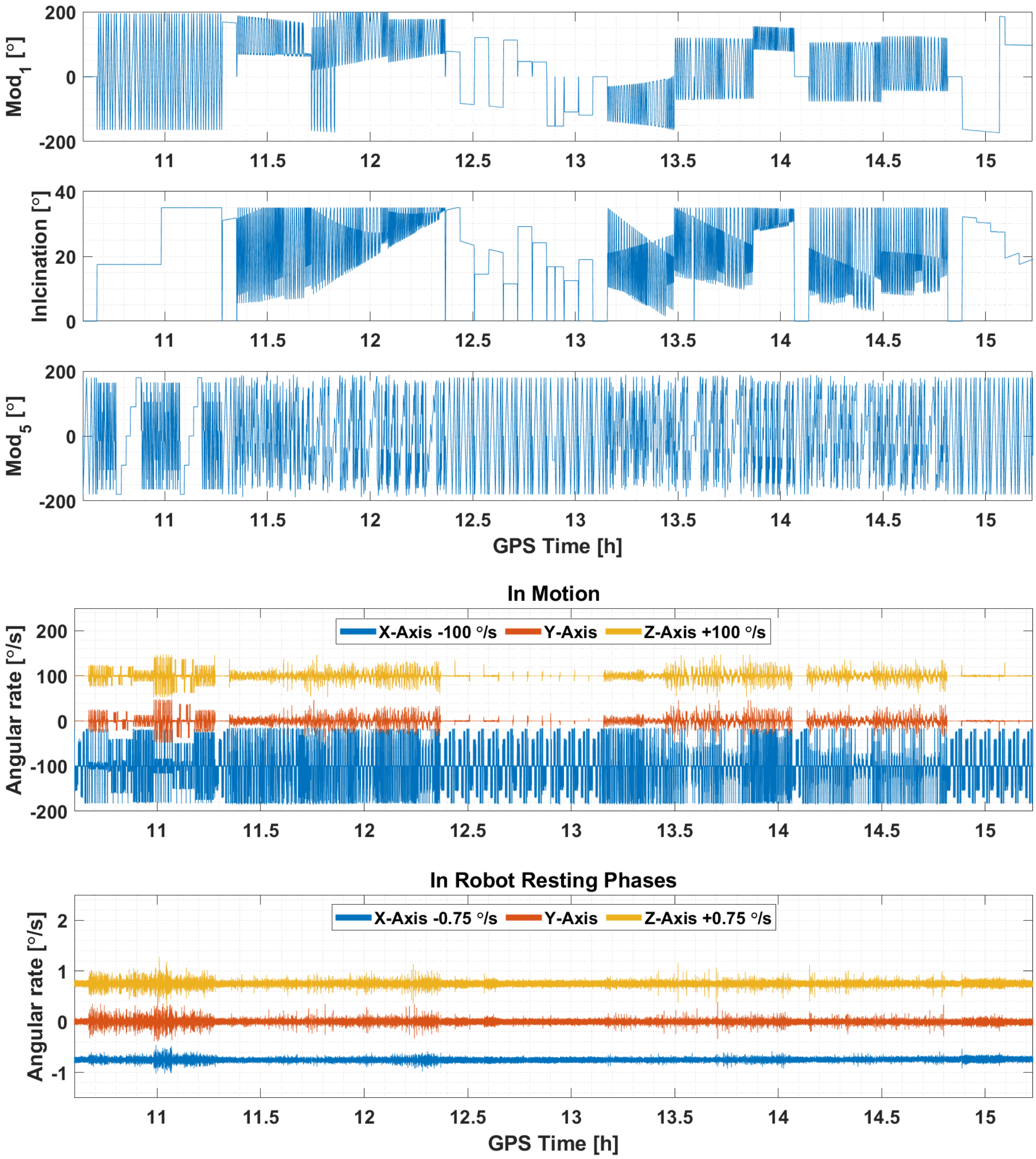

Figure 4.16: Robot module angles during a calibration (top) with the measured angular rates from the IMU (IMU) (bottom).

the IMU is positioned on the robot in a way that its axes align with the robot's axes. In the robot's initial position, the x-axis of the IMU points to the Up direction, the z-axis points towards North, and the y-axis points towards East. The transport rate and the Earth rotation rate can be neglected, as only the angular rates in the FP projected onto the satellite's LOS are needed. Consequently, no strapdown algorithm is required. At the end, an apparent velocity in the FP is calculated, caused by the PWU effect, which is described later in this section in more detail.

Figure 4.16 shows the measured angular rates of the three axes over a 5-hour calibration period. The two bottom subfigures indicate the angular rates during the robot's resting phases (bottom) and during robot motion (top). The top subfigure shows the corresponding angles of module 1 and module 5, as well as the inclination of the entire robot system, provided by the *gnp.ane* file (cf. Section 3.3.1). For visual clarity, an offset is introduced to the angular rates of two of the axes. It is visible, that most of the robot motions impact the x-axis of the IMU. Additionally, during the robot's resting phases, resonance effects occur in the z-axis and y-axis, primarily caused by the rotation of module 1, the lowest module of the robot. The separation of the 100 Hz IMU data into motion and resting phases is based on the GPS start and end times of the resting phases, as provided by the *gnp.ane* file.

To project the angular rates onto the LOS of the satellite, the azimuth α_{Ant} and elevation el_{Ant} of the satellite in the antenna frame are used (cf. Section 3.3.2). These angles define the transformation from the antenna frame, which is equivalent to the IMU frame, into the topocentric frame. The transformation of the angular rates $\boldsymbol{x}_{IMU}$ onto the LOS is accomplished by a three-dimensional rotation around the East axis $\boldsymbol{R}_E$, using $z_{ant} = 90° - el_{Ant}$, followed by a rotation around the North axis $\boldsymbol{R}_N$ with α_{Ant}:

$$\begin{aligned}\boldsymbol{x}_{LOS} &= \boldsymbol{R}_N(\alpha_{Ant})\boldsymbol{R}_E(z_{Ant})\boldsymbol{x}_{IMU} \\ &= \begin{bmatrix} 1 & 0 & 0 \\ 0 & \cos\alpha_{Ant} & -\sin\alpha_{Ant} \\ 0 & \sin\alpha_{Ant} & \cos\alpha_{Ant} \end{bmatrix} \begin{bmatrix} \cos z_{Ant} & 0 & \sin z_{Ant} \\ 0 & 1 & 0 \\ -\sin z_{Ant} & 0 & \cos z_{Ant} \end{bmatrix} \boldsymbol{x}_{IMU}.\end{aligned} \tag{4.11}$$

At this stage, the angular rates of the antenna at the FP, which is the robot's actual rotation point, are expressed in the satellite's LOS system.

In order to study the impact of the DLL tracking stability, Equation 2.34 can be used. In addition to the error caused by thermal noise, dynamic stress can also lead to tracking instabilities. The sum of both errors should not exceed D/2 chips, where D represents the correlator spacing. Here, the focus is on the dynamic stress, which can be calculated using the equation listed in Table 2.1 for a filter order of one and a bandwidth of 1 Hz.

This equation requires the relative LOS velocity between the satellite and the GNSS receiver. Due to the robot's rotation around the FP, there is effectively no velocity, as the geometric distance between the satellite and the antenna changes only due to their respective static positions. However, due to the rotating antenna, the carrierphase measurements are affected by the PWU effect (cf. Section 3.3.3). Consequently, an apparent change in the geometric distance between the satellite and antenna is observed. These range differences are used to calculate an apparent velocity due to the antenna rotation. Therefore, an angular rate change of 180°/s corresponds to a velocity of 10 cm/s, assuming a carrier wavelength of 20 cm. In Figure 4.17 the apparent LOS velocities calculated from the angular rates for the three IMU axes are presented, along with the elevation and azimuth of the GPS satellite PRN13 in the antenna frame. It is evident, that the apparent velocity reaches maximum values of about 4.5 cm/s to 5 cm/s.

By inserting 5 cm/s into the equations in Table 2.1, the dynamic stress error, due to the robot motion, can be calculated:

$$v = \frac{0.05\,[\text{m/s}]}{293.05\,[\text{m/chip}]} = 1.7 \cdot 10^{-4}\,[\text{chips/s}], \tag{4.12}$$

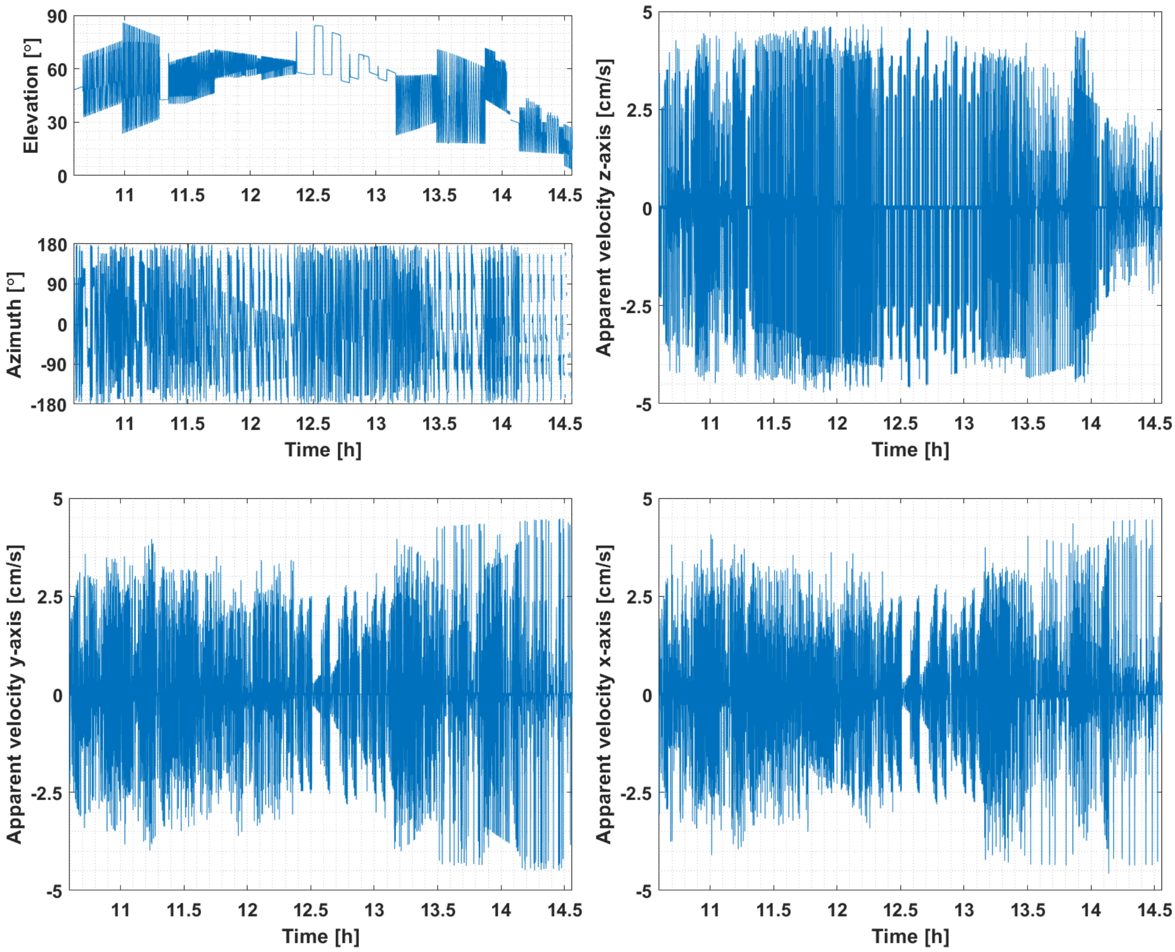

Figure 4.17: Robot module angles during a calibration (top) with the measured angular rates from the IMU (bottom).

resulting in

$$\frac{dR/dt}{\omega_0} = \frac{v}{w_0} = \frac{1.7 \cdot 10^{-4}\,[\text{chips/s}]}{4\,[\text{Hz}]} = 4.27 \cdot 10^{-5}\,[\text{chips}]. \tag{4.13}$$

As a result, the robot motion causes a dynamic stress error in the DLL of $4.27 \cdot 10^{-5}$ chips, which is significantly small compared to the dynamic stress error caused by the satellite velocity, which is 0.56 chips for a loop order of one and a bandwidth of 1 Hz. To this end, the DLL can ensure stable tracking during the antenna calibration, considering only the robot motion. The thermal noise error remains the most dominant error in the DLL.

4.3 Impact of Simulated Observation Noise on Calibration Outcomes

Concept

In this section, the influence of observation noise on the calibration results is investigated. Therefore, ΔSD_{sim} are computed and impacted with different noise type using the procedure described in the previous Section 4.1. The ΔSD_{sim} are used as input for the estimation process to estimate a pattern. The differences between the estimation outcome and the input pattern provide insights into the influence of noise. The workflow for this analysis is shown in Figure 4.18 and is briefly described here. Section 4.3.1 and 4.3.2 show the results, when using a white noise or a C/N_0 dependent noise behaviour, respectively. Section 4.3.3 describes, how different noise types impact the pattern behaviour illustrated as hemispherical harmonic coefficients. Thanks to the simulation approach, the outcomes of this analysis are valid for any observation type, GNSS system, or frequency. The process is as follows:

1. Availability of the antenna pattern to be analysed.
2. Computation of ΔSD_{sim}, containing only the CPC/PCC pattern information.
3. Add noise $\hat{\sigma}^k_{ant}$ to ΔSD_{sim}. In the workflow example, the gray data represents noise affected ΔSD_{sim}, whereas the red data shows the pure ΔSD_{sim}. They are presented together to visualize the small PNR. Hereinafter, the standard deviation of the noise is defined as noise factor.
4. Usage of noise affected ΔSD_{sim} as estimation inputs to estimate a pattern with unity weighting.
5. Calculation of a difference pattern between input and estimated pattern and derivation of comparison metric parameters (cf. Section 3.2.1).
6. Repetition of step 3 to 5 n-times (Monte-Carlo Simulation, e.g. n = 10000). This is necessary to get independent outcomes, because the simulated noise differs at each run. The comparison metric parameters of all runs are used to define three quantiles: 68 %, 95 % or 99.7 %, indicating the percentage of observations below each quantile.
7. Repetition of step 3 to 6 for different noise factors.

In Figure 4.18 the workflow is presented with a CPC pattern from a category 3 antenna, estimated by the DLR within an anechoic chamber for a 24 hour calibration. This example shows, that a Gaussian-distributed noise with a standard deviation of 2 m can maintain the original pattern, however with some deviations. 99.7 % of the maximum differences between input and estimated pattern from 10000 runs are below 0.33 m. The following analyses are based on this pattern. To validate the results, these analyses are also done with a different input pattern. The results can be found in the appendix (cf. Appendix A.1).

Thanks to a simulation based approach, the results can be adopted to other patterns. For this, relative values are used, considering the relation Rel_{NF} between the noise factor σ_f and the peak-to-peak difference of the input pattern P_{Peak} as well as the

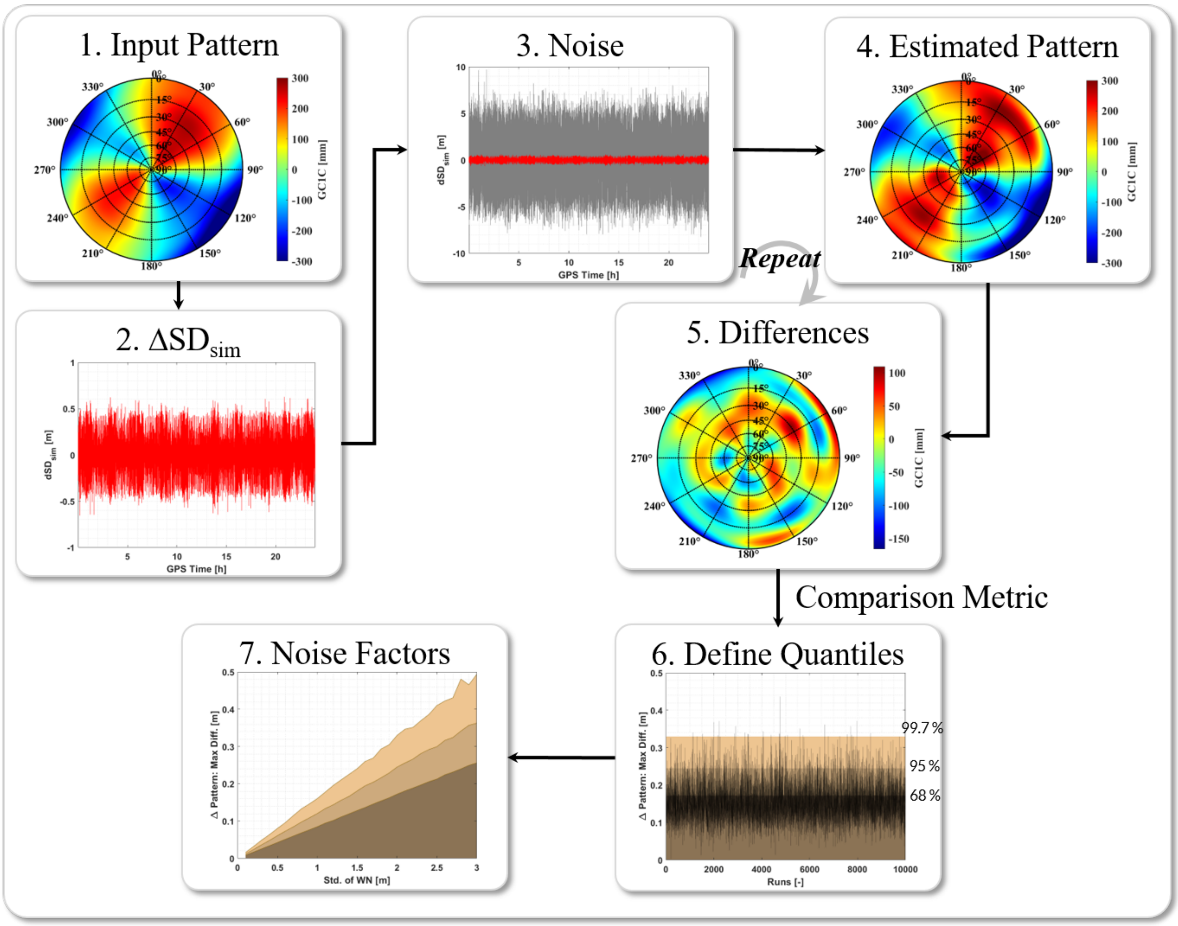

Figure 4.18: Workflow of noise simulation analysis.

quantile of the comparison metric parameter Q_{Para} to the peak-to-peak input pattern difference (Rel_{Para}):

$$\begin{aligned} Rel_{NF} &= \frac{\sigma_f}{P_{Peak}} \; [\%] \\ Rel_{Para} &= \frac{Q_{Para}}{P_{Peak}} \; [\%]. \end{aligned} \tag{4.14}$$

For example, the minimum CPC of the considered category 3 antenna is around -0.4 m, the maximum around 0.3 m. This leads to a pattern peak-to-peak of 0.7 m. The noise factor is related to this value. So, a noise factor of 0.7 m leads to $Rel_{NF} = 100\,\%$, a noise factor of 0.35 m to $Rel_{NF} = 50\,\%$. This relation is established for the comparison metric parameter, too. These two values allow investigating the impact of different noise factors on the estimation for any kind of input pattern. For example, Rel_{NF}= 100 % results in a Rel_{Para}= 16.1 % for the maximum pattern difference.

4.3.1 Impact of White Noise

White noise is defined as a normal distributed Gaussian noise with a specific standard deviation σ and mean value μ:

$$WN \sim N(\mu, \sigma^2), \tag{4.15}$$

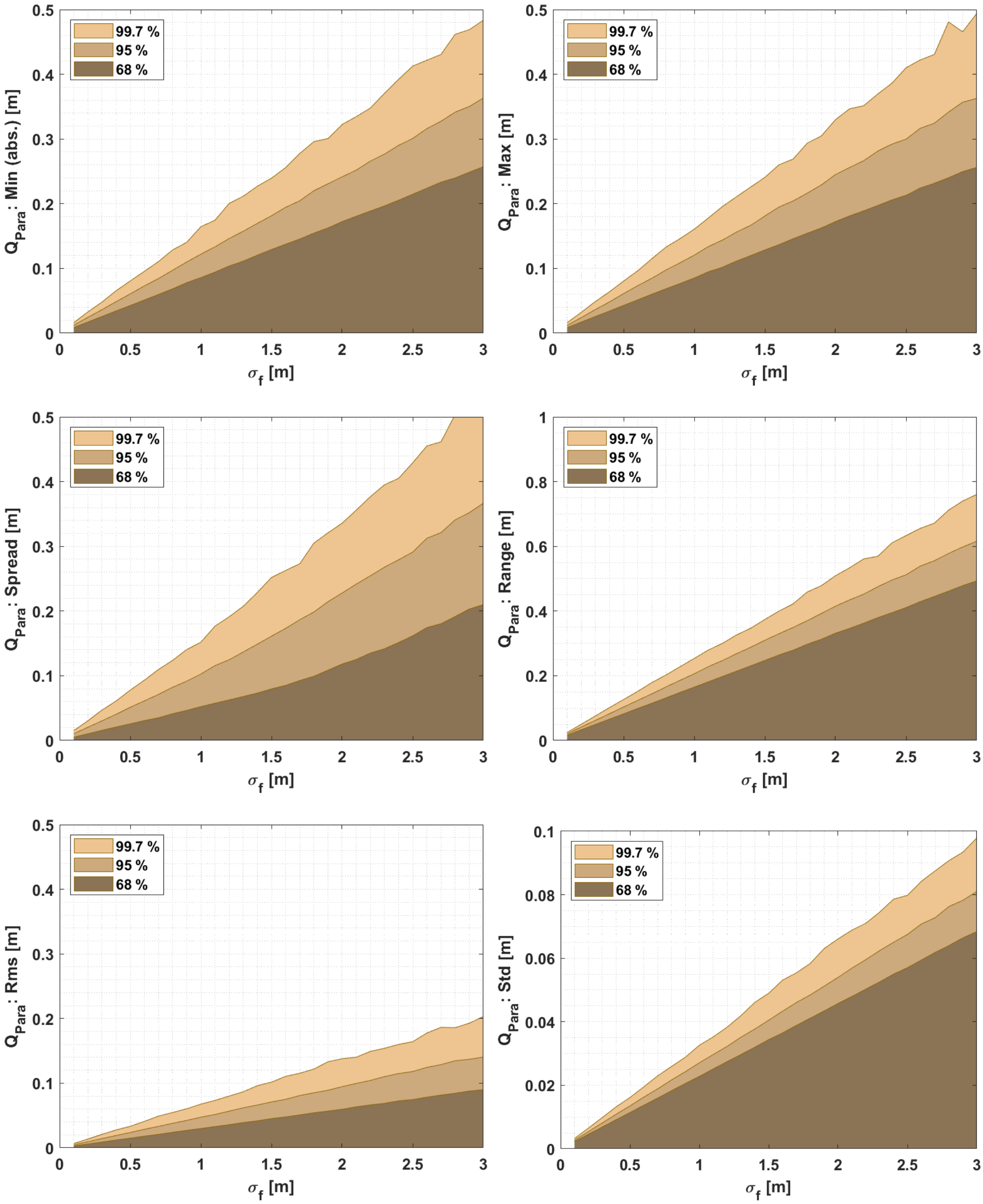

Figure 4.19: Results for absolute comparison metrics for the category 3 antenna, based on CPC provided by DLR with different noise factors. Note: Values only valid for this specific pattern (absolute).

where μ is assumed to be zero and σ equals the noise factor σ_f, which varies in this analysis between 0.1 m and 3.0 m. Additionally, 10000 runs are used to identify the three quantiles. The results are depicted in Figure 4.19 for six comparison metrics. Each of the subfigures consists of the x-axis showing the noise factor σ_f against the comparison metrics on the y-axis. The three quantiles are depicted from dark (lowest) to bright (highest). Here, absolute parameter values of the category 3 antenna are presented.

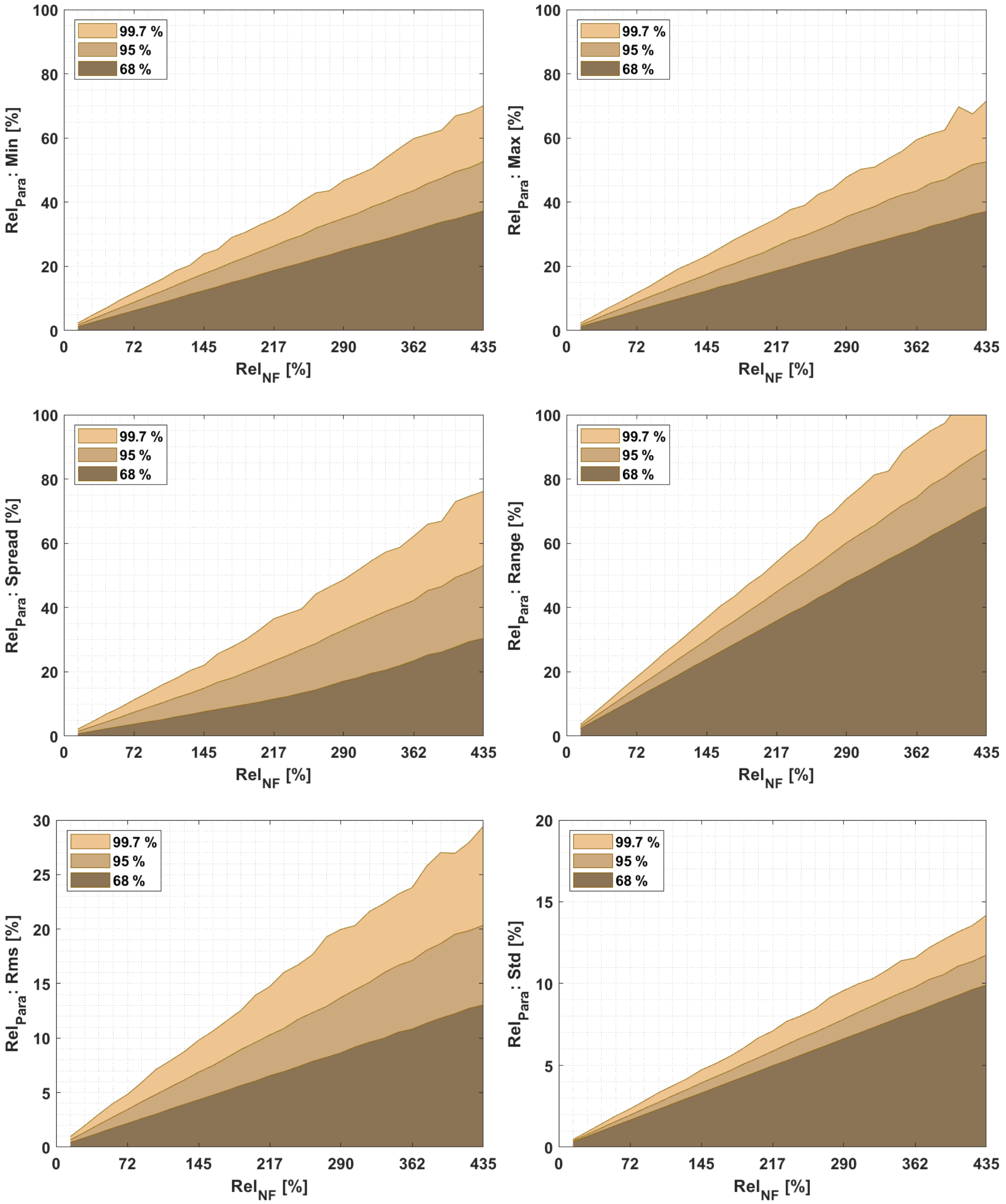

Figure 4.20: Results for relative comparison metrics with different noise factors. Note: Values valid for different patterns.

The first row shows the minimum and the maximum value of the difference patterns. It should be noted, that the minimum values are presented here as positive values. Additionally, the magnitude is very similar, so that WN noise does not introduce an offset. The second row shows the results for the spread and the range. Besides, the last row represents the RMS and the standard deviation of the difference pattern. It is obvious, that the quantiles of the comparison metrics increase, when adding more and more noise to the observations. For example, considering a P_{Peak} of 0.7 m for this

Table 4.3: Linear coefficients for relative comparison metrics for three different quantiles with a WN behaviour.

Comparison metric	Coefficient	Quantile 68 %	95 %	99.7 %
Min	β_0	0.0	-0.3	0.9
	β_1	11.7	8.3	6.2
Max	β_0	0.3	0.8	1.7
	β_1	11.7	8.2	6.1
Spread	β_0	34.2	18.7	13.3
	β_1	14.1	8.1	5.6
Range	β_0	0.0	-0.3	0.6
	β_1	6.1	4.9	4.0
Rms	β_0	0.7	0.4	-1.2
	β_1	33.2	21.0	14.9
Std	β_0	0.0	0.3	-0.4
	β_1	43.7	36.9	30.8

antenna, a σ_f of 3 m leads to a range error greater than the pattern itself. Additionally, the behaviour of the quantiles from each comparison metric is very close to linear[3].

Figure 4.19 showed the results for this very specific antenna. To get a better understanding of how WN influences other antenna patterns within the calibration using a robot in the field, these results are transformed to relative values, using Equation 4.14. The outcome can be seen in Figure 4.20. The subfigures are arranged similar to Figure 4.19, but with Rel_{NF} on the x-axis and Rel_{Para} on the y-axis. Needless to say, that the behaviour is not changed, so that the linearity is still present. Thus, the linear relation between Rel_{NF} and Rel_{Para} for each comparison metric and quantile is calculated by using a linear regression:

$$Rel_{NF} = \beta_0 + \beta_1 \cdot Rel_{Para}. \tag{4.16}$$

The estimated parameters β_0 and β_1 are summarized in Table 4.3. They can be used to assess the maximum allowable observation noise when a specific accuracy must be maintained, or vice versa. For example, when using a 99.7 % quantile and requiring the range error to be below 50 % ($\beta_0 = 0.6$, $\beta_1 = 4.0$), the allowable white noise can be calculated as follows:

$$Rel_{NF} = 0.6 + 4.0 \cdot 50\% = 200.6\%. \tag{4.17}$$

By rearranging Equation 4.16,

$$Rel_{Para} = \frac{-\beta_0 + Rel_{NF}}{\beta_1}, \tag{4.18}$$

the impact of a given noise on the comparison metrics can be studied. Table 4.4 gives an example of how a Rel_{NF} of 100 % impacts the 99.7 % quantiles of the six comparison metrics.

The same simulation is conducted using a different input pattern, as shown in Figure A.1 (cf. Annex A.1). The results are depicted in Figure A.2 and the estimated linear

[3]Fully linearity can be reached, when increasing the amount of runs to infinity.

Table 4.4: An example with a Rel_{NF} of 100 % impacts different comparison metrics with a quantile of 99.7 % with WN behaviour.

Comparison metric	Min	Max	Spread	Range	Rms	Std
Rel_{NF} of 100 % (99.7 % quantile)	16.1 %	16.1 %	15.5 %	25.3 %	16.6 %	3.5 %

coefficients in Table A.1. The coefficients of the comparison metric parameters show good agreement with those presented in Table 4.3, with differences averages of approximately 2%-3%. However, the β_0 coefficients for the spread differ significantly. This discrepancy can be explained by the magnitude of the patterns. In general, the spread provides information about the range differences between two patterns. Since the range of the category 3 antenna is about 0.7 m, and the range of the category 1 antenna is about 0.12 m, the β_0 coefficients exhibit these high deviations.

4.3.2 Impact of Signal Strength dependent Noise

Section 4.1 shows, that the actual noise behaviour of the ΔSD mostly depends on the received signal strength, thus, this section focuses on the impact of a C/N_0 dependent noise on the estimated antenna pattern. The analysis in the previous Section 4.3.1 is repeated, however, $\hat{\sigma}^k_{ant}$ in Equation 4.3 is replaced with $\sigma_{C/N0}$ using the estimated coefficients a and b for the u-blox antenna:

$$\begin{aligned}\sigma_{C/N_0} = &(\sigma_{AUT}(t_{i+1}) \cdot \sigma_{f,AUT}(t_{i+1}) - \sigma_{AUT}(t_i) \cdot \sigma_{f,AUT}(t_i)) - \\ &(\sigma_{Ref}(t_{i+1}) \cdot \sigma_{f,Ref}(t_{i+1}) - \sigma_{Ref}(t_i) \cdot \sigma_{f,Ref}(t_i))\end{aligned} \quad [\mathrm{m}], \tag{4.19}$$

where σ_{Ref} and σ_{AUT} are calculated with Equation 4.6. The noise factor σ_f is varied between 0.1 m and 2 m (Rel_{NF} = 290 %). It is reminded, that the noise factor is the standard deviation of the white noise. This step is necessary to get an actual noise carrier, instead of a weighting only. The comparison metrics are the same as those discussed in the previous section. The same input pattern is considered. However, the results of the absolute values are omitted. Additionally, a unity weighting is used for estimating the patterns.

The results of the relative comparison metrics are shown in Figure 4.21. The Rel_{Para} values are very similar between C/N_0 dependent noise and white noise, except for the RMS, which is lower for C/N_0 noise compared to WN. This is also evident in Table 4.5, where the 99.7 % quantile is presented for a Rel_{NF} of 100 % for both noise types, along with the difference between them. The C/N_0 dependent noise has slightly less impact

Table 4.5: An example with a Rel_{NF} of 100 % impacts different comparison metrics with a quantile of 99.7 % for a linear behaviour for WN and C/N_0 dependent noise.

Comparative Parameter	Min	Max	Spread	Range	Rms	Std
Rel_{NF} of 100 % (WN) (99.7 % quantile)	16.1 %	16.1 %	15.5 %	25.3 %	16.6 %	3.5 %
Rel_{NF} of 100 % (CN0) (99.7 % quantile)	15.3 %	15.3 %	13.8 %	24.4 %	3.7 %	2.2 %
Difference	0.8 %	0.8 %	1.7 %	0.9 %	12.9 %	1.3 %

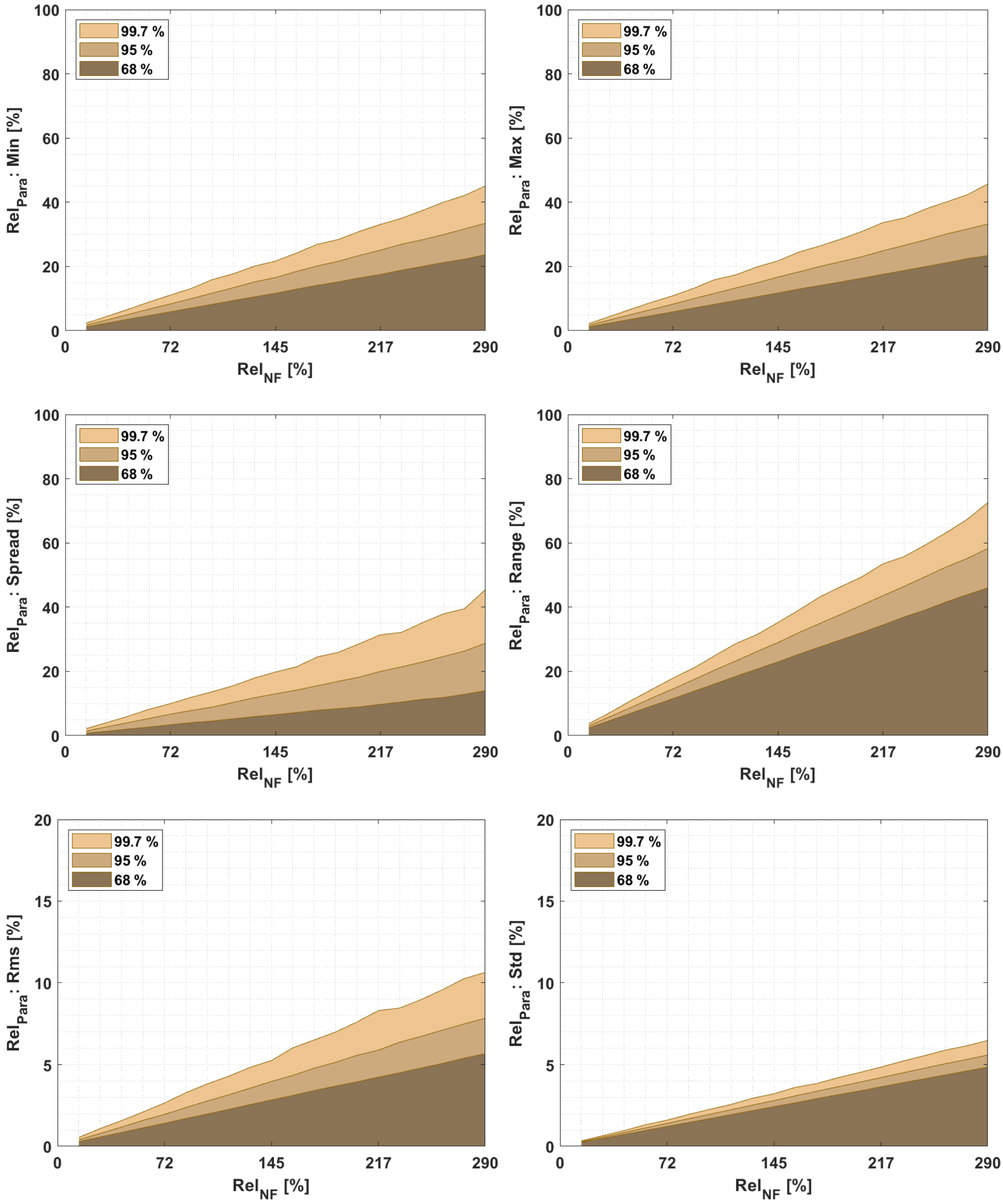

Figure 4.21: Comparison metric parameters as relative values with different noise factors for CN0 based noise.

on the estimated pattern for four of the comparison metrics, than a WN. However, for the RMS and standard deviation (Std) parameters, this impact is significantly reduced. The RMS decrease from 16.6 % to 3.7 %. Similarly, considering the values, the Std is also significantly reduced from 3.5 % to 2.2 %. This is even more evident when the difference is relatively compared to the Std of the WN, resulting in a relative decrease of 37 %. These results show, that a C/N_0 dependent noise has less impact on the

Table 4.6: Linear coefficients for relative comparison metrics of three different quantiles with C/N_0 dependent noise.

Comparison metric	Coefficient	Quantile 68 %	95 %	99.7 %
Min	β_0	0.0	-0.5	0.1
	β_1	12.3	8.7	6.5
Max	β_0	-0.5	0.1	1.5
	β_1	12.4	8.7	6.5
Spread	β_0	1.8	5.7	7.3
	β_1	21.6	10.4	6.7
Range	β_0	-0.2	-0.2	0.3
	β_1	6.3	5.0	4.1
Rms	β_0	-0.2	-0.2	-0.3
	β_1	51.3	36.8	27.1
Std	β_0	-0.3	-0.4	0.1
	β_1	59.9	51.8	44.7

estimated pattern and enables a more robust estimation of the pattern compared to a WN behaviour of the ΔSD.

Additionally, the comparison metrics for a C/N_0 dependent noise exhibit a linear behaviour, similar to WN. Thus, a linear regression is also possible using Equation 4.16. The estimated coefficients β_0 and β_1 are listed in Table 4.6. Similar to the WN analysis, the same approach is applied to another input pattern. The results and the estimated linear coefficients are presented in Figure A.3 and Table A.2, respectively. The differences in the coefficients are similar to those from the WN analysis, with slightly smaller differences. However, the β_0 of the spread parameter significantly differs, as already discussed in Section 4.3.1.

Closing remarks Observation noise has an impact on the estimated pattern. This holds true for a WN and for a C/N_0 dependent noise behaviour. For example, a WN with a standard deviation of 100 % of the peak-to-peak pattern difference leads to a $\approx$ 15 % error in the pattern estimation for minimum and maximum differences and even $\approx$ 25 % in the range. This analysis shows that the observation noise has to be decreased in order to get a precisely estimated pattern. The C/N_0 approach not only allows determining the noise impact on the pattern, it could also benefit the pattern estimation by weighting the observation in the least-squares adjustment, instead of using a unity weighting scheme. This is analysed in more detail in Section 6.4.

These noise investigations focus on comparison metrics, which enable a numerical comparison between two patterns. However, they only provide a limited assessment of the differences in the actual behaviour between the two patterns. Therefore, the hemispherical harmonic coefficients can be used to study the pattern behaviour, as discussed in the next section.

4.3.3 Pattern Behaviour

The actual pattern, used in the previous analyses, is shown in Figure 4.22. This pattern has a very prominent antisymmetric azimuthal behaviour, like a trefoil. This section focuses on how good this structure can be maintained, when the ΔSD are affected by noise. As in Section 4.2.1 already discussed, the actual noise behaviour of the ΔSD highly depends on the signal strength, thus, the Monte-Carlo simulation from the previous Section 4.3.2 is analysed with focus on the HSH coefficients.

The behaviour of an antenna pattern can be described by the HSH coefficients. With a degree and order of eight, 44 different coefficients exist for the parameters a_{nm} and b_{nm} with n as degree and m as order. In general, a_{10}, a_{11} and b_{11} give information about the PCO/CCO, whereas the other coefficients describe the pattern behaviour. In Figure 4.23 the differences between the original pattern coefficients and the coefficients from the noise affected patterns are presented for different noise factors σ_f. The left subfigures show the results for the a coefficients, whereas the b coefficients are depicted in the right. For clarity, only three different σ_f are shown: 1 m (a, b), 2 m (c, d) and 3 m (e, f). The x-axis shows the degree and order of the coefficients in ascending order. For example, 7,0 describing the results for $a_{7,0}/b_{7,0}$, the next data show the results for $a_{7,1}/b_{7,1}$ and so on, until $a_{7,7}/b_{7,7}$. Afterwards, $a_{8,0}/b_{8,0}$ is shown until $a_{8,8}/b_{8,8}$. Each coefficient shows the differences to the coefficient from the original pattern from the 10000 runs as a boxplot, whereas the box showing the 25 % and 75 % quantiles, the solid lines indicate the 2.7σ (99.3 %) quantiles and the dots represent the outliers.

For the a coefficients, higher variations are visible when the order is zero, and decrease when the order increases. For the b coefficients, the highest differences are evident for $b_{4,1}$ and $b_{5,1}$. However, for both, the C/N_0 dependent noise is more affecting the lower degree coefficients than the higher ones. Besides, higher noise increases the impact on the coefficients. This holds true for the a and b coefficients.

The interpretation of these differences can be difficult, therefore, the coefficient differences are used to calculate a difference pattern, which is shown in Figure 4.24 (right). The left subfigures show the actual patterns, when the noise affected ΔSD_{sim} are used as estimation inputs for the three noise figures, similar to Figure 4.23. A randomly chosen run, out of the 10000, for each σ_f is presented. A different run can show a different behaviour of the difference pattern. However, it is visible, that this prominent trefoil

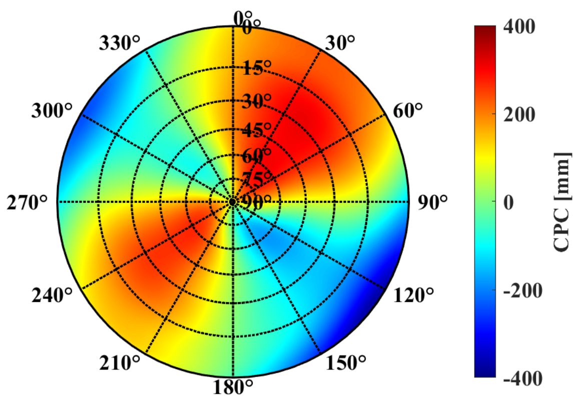

Figure 4.22: CPC pattern of the u-blox ANN-MB1 antenna (category 3), estimated in an anechoic chamber by the DLR.

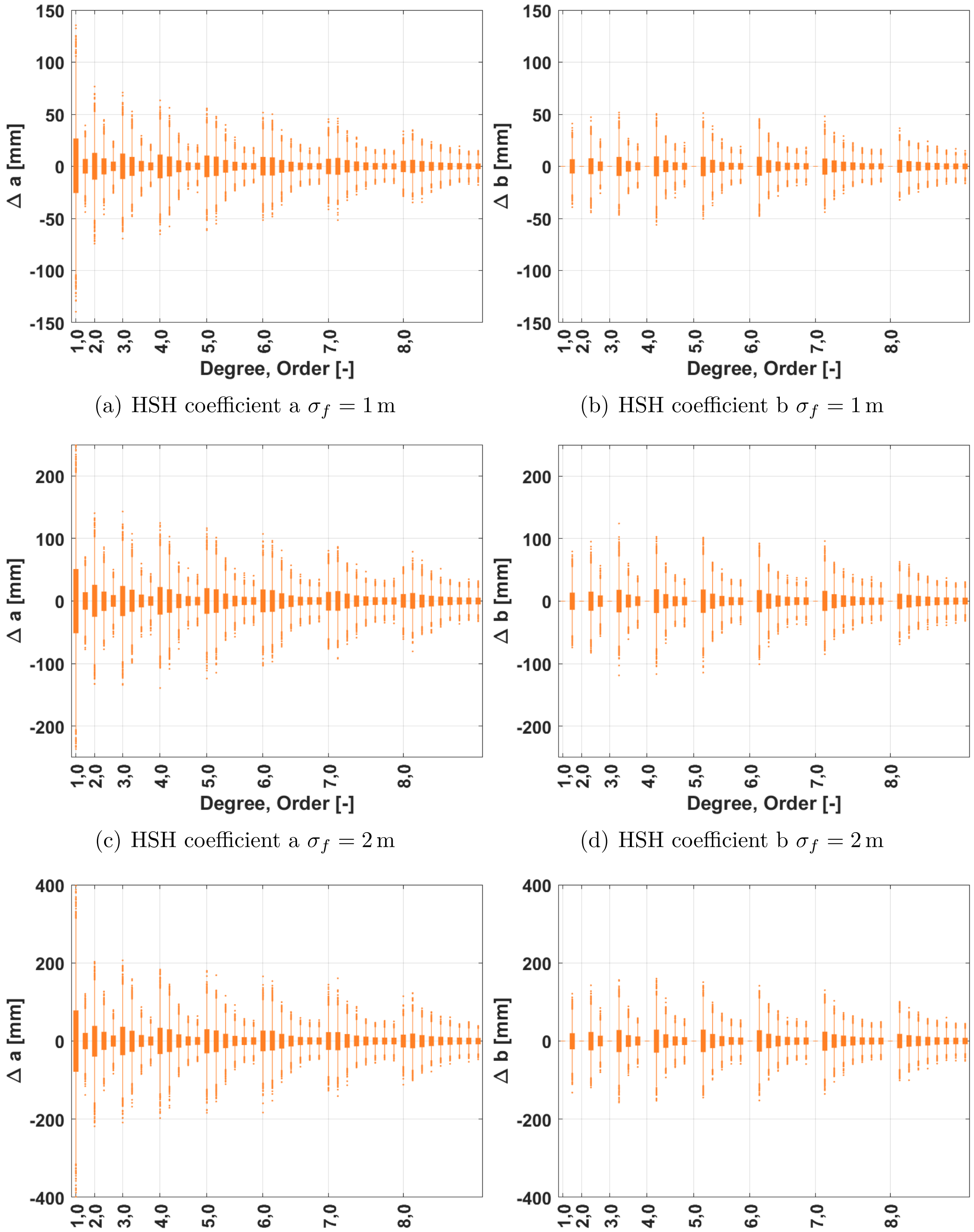

(a) HSH coefficient a $\sigma_f = 1\,\mathrm{m}$

(b) HSH coefficient b $\sigma_f = 1\,\mathrm{m}$

(c) HSH coefficient a $\sigma_f = 2\,\mathrm{m}$

(d) HSH coefficient b $\sigma_f = 2\,\mathrm{m}$

(e) HSH coefficient a $\sigma_f = 3\,\mathrm{m}$

(f) HSH coefficient b $\sigma_f = 3\,\mathrm{m}$

Figure 4.23: Differences of HSH coefficients a_{nm} (left) and b_{nm} (right), when $\sigma_f = 1\,\mathrm{m}$ (a, b), $\sigma_f = 2\,\mathrm{m}$ (c, d) and $\sigma_f = 3\,\mathrm{m}$ (e, f) is added. The x-axis shows degree and order of the coefficient starting from e.g. 7,0 to 7,7 with 7,1 ... 7,6 in between. Please note the different y-axis scales.

pattern can be maintained, even if a noise factor of 3 m is applied. As expected, the magnitude of the difference pattern increases with the amount of C/N_0 noise. Consequently, the magnitude of the estimated pattern differs from the original pattern, which

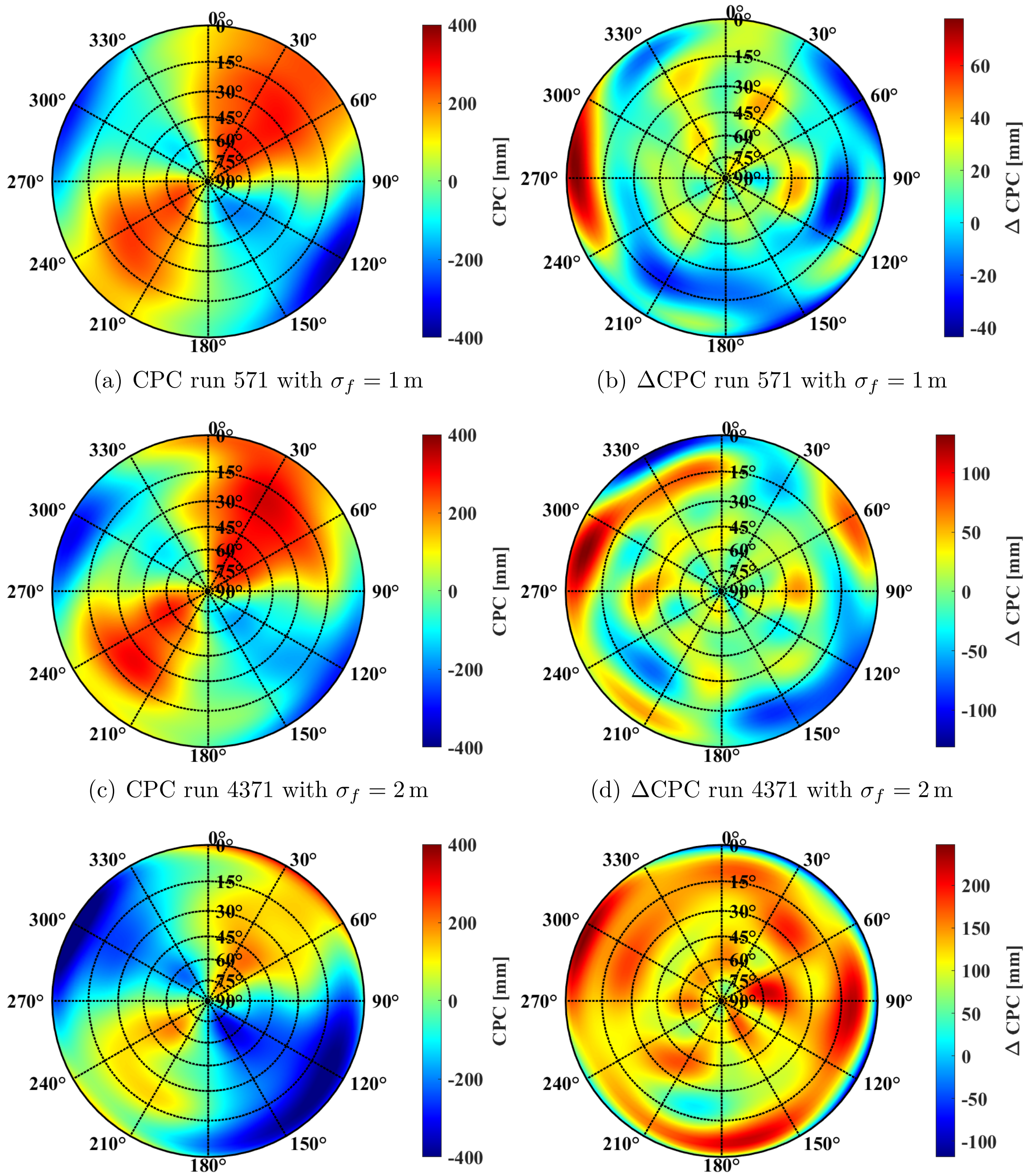

(a) CPC run 571 with $\sigma_f = 1\,\mathrm{m}$
(b) ΔCPC run 571 with $\sigma_f = 1\,\mathrm{m}$
(c) CPC run 4371 with $\sigma_f = 2\,\mathrm{m}$
(d) ΔCPC run 4371 with $\sigma_f = 2\,\mathrm{m}$
(e) CPC run 8228 with $\sigma_f = 3\,\mathrm{m}$
(f) Δ CPC run 8228 with $\sigma_f = 3\,\mathrm{m}$

Figure 4.24: CPC pattern (left) and their differences to the original pattern (right), when $\sigma_f = 1\,\mathrm{m}$ (a, b), $\sigma_f = 2\,\mathrm{m}$ (c, d) and $\sigma_f = 3\,\mathrm{m}$ (e, f) is added.

can be expressed by the comparison metrics described in the previous Section 4.3.2. Please note the different scales of ΔCPC in Figure 4.24.

4.4 Development of a digital Receiver Twin

The investigations in Section 4.2 have shown the actual noise of the estimation inputs (ΔSD) for three different hardware receivers, when using the manufacturer's default settings. A weak PNR exists for the codephase what makes the estimation of CPC challenging. In order to improve the estimation, the PNR has to be increased by reducing the observation noise in the ΔSD. This can be done by modifying the tracking loop parameter of the hardware receivers. However, optimizing hardware receiver settings for CPC estimation with a robot in the field can be very time-consuming, as each calibration allows only a single parameter value to be investigated. Thus, a software receiver (Sx3) developed by IFEN GmbH (2019) is used instead. It stores the IF data stream, which includes all satellite relevant information. This data stream can be modified in post-processing, allowing the investigation of different receiver settings without running further calibrations with the robot.

The Sx3 software receiver consists of two main components: a receiver front end, which is directly connected to an GNSS antenna and the receiver itself, a software installed on an average PC. In addition, the frontend can be fed with an external frequency standard. The raw data stream is received in the frontend and transferred via USB 3.0 to the PC and to the software, respectively. After the data is collected, the data stream can be used as input in the software, without using a real measure with the front end. This software receiver is a very powerful tool with over 170 changeable parameters, either for satellite acquisition or tracking loops. Based on the used parameter settings, the receiver creates different output files usable in different GNSS applications, e.g. RINEX files or SPP solutions. A very detailed description about each parameter and their relation to each other are listed in IFEN GmbH (2019). Besides, Pany (2010) describes the theoretical and mathematical background behind these parameters and the receiver itself.

Here, the focus lies on parameters for the tracking loops to analyse the codephase noise behaviour in the antenna calibration approach. Section 2.3.3 has shown that the bandwidth, filter order, correlator spacing, and predetection integration time are the primary factors affecting the receiver's noise performance, with the first two parameters having the most significant impact. On the other hand, the bandwidth and loop filter order (FO) can be modified in Javad receivers by the user. Therefore, both of them are analysed here to get more inside about their impact on ΔSD and the CPC antenna calibration outcomes, respectively. To this end, the insights gained are utilized to optimize the hardware receiver, aiming to achieve a less noisy observable while preserving the antenna pattern information (cf. Section 6.1.2).

To investigate changes in the receiver settings, a calibration has been carried out for a geodetic antenna (LEIAR25.R3) on the 30^{th} of May 2024. One calibration set (≈ 3 h and 20 min) was executed, while the software receiver's frontend and two hardware receivers (Javad Delta TRE G3T and Javad DeltaS-3S) were connected to the AUT in a zero baseline approach. Two identically constructed hardware receivers were connected to the reference antenna. All of them are connected to a rubidium frequency standard to ensure a common-clock setup. The software receiver provides RINEX files based on the measured data stream and the used receiver settings. These RINEX files are processed in the same way by the antenna algorithm, as real GNSS data. Thus, the ΔSD are generated using the software receiver outcomes for the AUT mounted on the robot and the Javad DeltaS-3S hardware receiver, which has been connected to the reference antenna. This receiver runs with a DLL bandwidth of 0.5 Hz and a loop FO of 1 with carrier aiding to minimize the observation noise on the reference station.

It is crucial that the software receiver delivers identical results when using the same data stream and settings to study changes in receiver parameters. This is achievable, when the receiver has fixed navigation data and a fixed position-velocity-time (PVT) solution. Thus, the data stream is processed several times in order to fix these data. More details about this fixing can be found in IFEN GmbH (2019). After the data are fixed, parameters can be changed and modified to investigate their impact on the ΔSD. To begin the research on codephase ΔSD, the receiver settings are first adjusted to ensure realistic behaviour in the carrierphase ΔSD and the estimation outcomes because of a better PNR. Those parameters are e.g. the carrierphase loop bandwidth, filter order or the usage of an external frequency standard. When the ΔSD, created by the software receiver, are aligned with the ractual ΔSD, a first stable parameter set is achieved. This set serves as a starting point for studying the impact of the DLL bandwidth and the loop FO on code phase ΔSD.

Breva et al. (2024) have demonstrated how different DLL parameters affect ΔSD observations and the resulting patterns, taking into account the repeatability for a category 2 antenna. The authors show that reducing the DLL bandwidth can significantly decrease the observation noise, while a filter order of 2 is required when no carrier aiding is used. A second-order unaided DLL results in similar ΔSD noise levels as a first-order aided DLL. This analysis is based on a comparison with Septentrio PolaRx5TR receivers, which are assumed to utilize codephase smoothing (cf. Section 4.2.3). Thus, ΔSD values were computed between a Septentrio receiver and the software receiver. The investigations in this section use a Javad DeltaS-3S as the reference receiver for computing ΔSD.

Further studies on the DLL and PLL bandwidth on different loop FOs in aided and unaided codephase loops are carried out. In order to compare the resulting ΔSD between the reference and the software receiver, the weighted averaged standard deviation over all visible satellites during the calibration is analysed, which can be calculated by Equation 4.10 and is denoted here as $\sigma_{\Delta SD}$. The standard deviation $\sigma_{\Delta SD}$ is calculated for different DLL bandwidths, varying between 0.1 Hz to 3 Hz for three different cases: (i) Unaided DLL with a loop FO of 1, (ii) Unaided DLL with a loop FO of 2 and (iii) Aided DLL with a loop FO of 1.

The results are presented in the top of Figure 4.25. In general, a smaller DLL bandwidth results in a less noisy ΔSD, visible in all three cases. As expected, the unaided first FO shows the noisiest ΔSD, due to the robot motion. As discussed in Section 2.3, first order filter loops are sensitive to velocity stress, which is clearly evident here. A tracking with a DLL B_n of 0.1 Hz is not possible for this case. It should be mentioned, that the figure is cut at a $\sigma_{\Delta SD}$ of 3 m, because of clarity. The maximum $\sigma_{\Delta SD}$ reached nearly 6 m for case (i) and 5 m for case (iii). An unaided DLL with a FO of 2 achieves similar results to an aided DLL. Even a smaller standard deviation is visible for particular DLL bandwidths, especially with bandwidth higher than 1 Hz. DLL bandwidths higher than 2 Hz lead to high variations of $\sigma_{\Delta SD}$ in all cases.

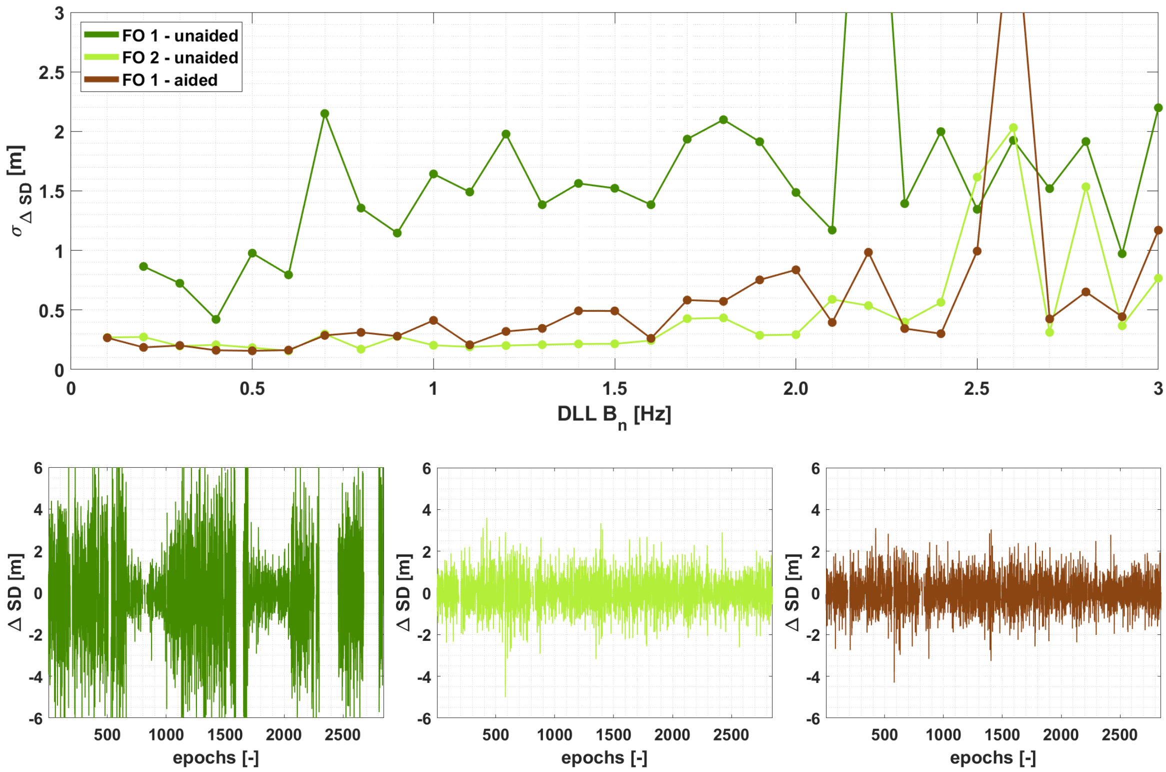

Figure 4.25: Impact of different DLL bandwidths on the observables indicated as weighted averaged $\sigma_{\Delta SD}$ over all visible satellites for an unaided DLL with filter order 1 (dark green), filter order 2 (bright green) and an aided DLL (brown). (Top) $\sigma_{\Delta SD}$ with different DLL bandwidth B_n. (Bottom) ΔSD with DLL bandwidth of 1 Hz for GPS satellite PRN16. Presented is the C1 signal for the three cases (same colors).

A DLL B_n of 0.5 Hz achieves the best ΔSD performance and the lowest noise for case (ii) and (iii). This is the reason why the reference antenna's receiver is operating with this bandwidth. Since the antenna is static, a smaller bandwidth can be chosen by simultaneously enabling a stable tracking of the satellite signals. Even if $\sigma_{\Delta SD}$ at a DLL bandwidth of 0.5 Hz achieves the best results, important pattern information of the AUT could get lost, due to the robot motion. Therefore, a bandwidth of 1 Hz is chosen for the receiver, which is connected to the AUT. This bandwidth is sufficient to track satellite signals within the robot antenna calibration, by also achieving a less noisy ΔSD ($\sigma_{\Delta SD} \approx 0.15\,\mathrm{m}$ - $0.2\,\mathrm{m}$) compared to the receiver default settings from Javad receiver (DLL B_n of 3 Hz in an aided DLL with a FO of 1 results in $\sigma_{\Delta SD} \approx 1.2\,\mathrm{m}$).

The bottom subfigures of Figure 4.25 show the ΔSD for the three cases, from case (i) left to case (iii) right. Here, a DLL bandwidth of 1 Hz is chosen. It is evident, that the unaided first loop order includes the dynamic velocity stress, caused by the robot motion. The other two cases show very similar results, even if $\sigma_{\Delta SD}$ is a bit smaller for the case (ii) with this DLL bandwidth.

When the DLL is aided by the carrier loop, also the PLL and phase wind up could impact the noise performance. Therefore, the PLL is varied from 5 Hz to 30 Hz for the different cases with a fixed DLL bandwidth of 1 Hz. The results are presented in Figure 4.26. Other than expected, the PLL bandwidth also impacts the unaided DLL performance. However, only small differences are visible for the second loop order DLL.

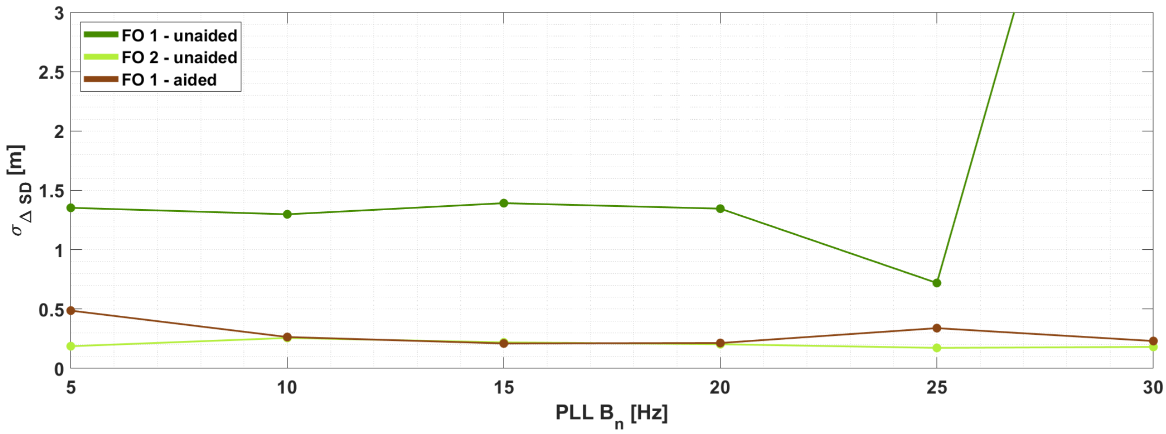

Figure 4.26: Weighted averaged $\sigma_{\Delta SD}$ over all visible satellites for an unaided DLL with filter order 1 (dark green), filter order 2 (bright green) and an aided DLL (brown) with different PLL bandwidth B_n with a fixed DLL bandwidth of 1 Hz.

The averaged standard deviation for an aided DLL is more or less similar for each PLL bandwidth, except for 5 Hz and 25 Hz. The higher variations for an unaided DLL with a FO of 1 can be explained by the velocity stress, caused by the robot motion.

Closing Remarks The software receiver is a powerful tool to analyse the impact of different tracking loop parameters on the antenna calibration observations in post-processing. A DLL bandwidth of 0.5 Hz shows the lowest weighted averaged standard deviations for a 2nd loop order unaided DLL and 1st loop order aided DLL. The bandwidth of the PLL has no significant impact on the codephase ΔSD. However, the results obtained are only valid for the software receiver, which might utilize different signal processing techniques compared to hardware receivers. Their designs depend on the manufacturer and are typically proprietary, inaccessible to the general user.

Nevertheless, the results of this analysis can be used to recommend certain tracking loop parameters to reduce observation noise. A DLL bandwidth of 0.5 Hz is sufficient for the receiver connected to the reference antenna. Since the antenna is static, a stable satellite tracking by achieving a less noisy observable should be guaranteed. The receiver connected to the AUT should operate with a DLL bandwidth of 1 Hz, to ensure a stable tracking and maintaining important pattern information. Besides, an unaided DLL with a FO of 2 leads to similar results as an aided DLL. For an accurate calibration, this should be approached with caution due to the lack of knowledge about the hardware receiver design. Therefore, a first loop order aided DLL is recommended. In Section 6.1.2, the recommended receiver settings, based on the software receiver results, are used in hardware receivers during an antenna calibration and show how these settings benefits the calibration repeatability.

5

Investigations on the Environment of the Antenna Calibration Robot at IfE

The surrounding of the calibration robot may degrade the received GNSS signals by multipath effects, caused by reflections on laboratory rooftop structures. This chapter investigates multipath effects in the robot environment and their impact during the antenna calibration algorithm. First, a digital twin of the scene is required. The geodetic surveying task of the rooftop to obtain the digital model is described in Section 5.1. The subsequent multipath analysis is done by using the MPLC in real calibration scenarios to find critical structures in the robot surrounding, based on the digital twin. This will be presented in Section 5.2. In addition, the benefits of time differencing for reducing multipath effects during the antenna calibration algorithm will be demonstrated and discussed. Section 5.3 briefly describes the development of multipath maps from the DLR and how they are behaving in different tilting and rotating scenarios of the robot.

5.1 Creation of a digital Robot Environment

In order to get a deeper understanding about the multipath environment of the robot, a digital twin of the GIH rooftop have been set up in the framework of the DFG Project (470510446): Understanding Multipath - Antenna - Receiver Interactions for Standardizable Calibration of Code Phase Variations of GNSS Receiving Antennas (MAESTRO). In Section 5.3 this digital model is used in DLRs' hybrid-simulative multipath estimation approach to create multipath maps for three different antenna categories, defined in Section 4.2.2. Additionally, it can be used for other experiments, including experiments that are not part of the robot antenna calibration. The final digital model is presented in Figure 5.1.

The robot is installed on pillar MSD7 and the reference antenna on pillar MSD8. Thus, the digital model in their surrounding area needs to be more detailed, compared to the wider surroundings. To do so, all structures that are larger than a carrierphase wavelength have to be modelled, because GNSS signal reflections on structures smaller than a wavelength are assumed to be non-existent. The basis of the digital twin is a practical survey with a Leica TS15 tacheometer, providing a distance accuracy of 1 mm+1.5 ppm and an angular accuracy of 0.3 mgon. The survey has been carried out in January 2022.

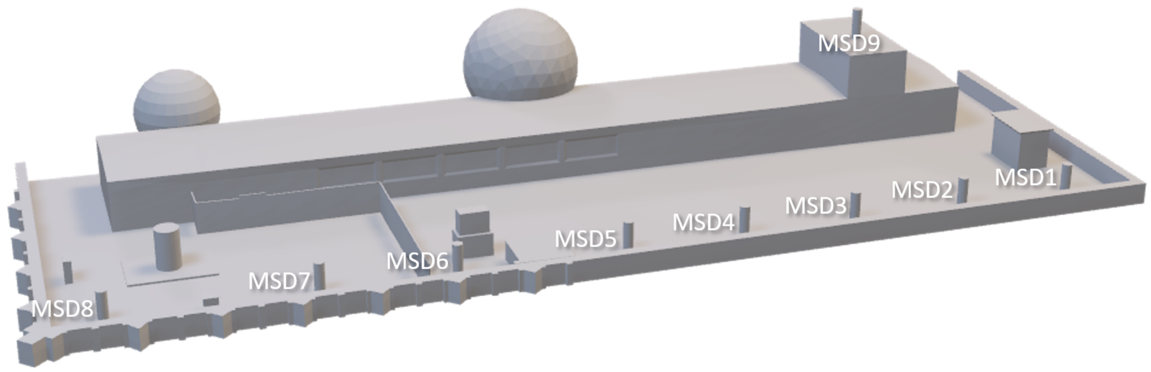

Figure 5.1: Digital twin of the robot environment on the laboratory rooftop of the GIH building.

Since, the pillar coordinates of the laboratory network have already been precisely determined (Koppmann, 2018), the tacheometer can directly be mounted on pillar MSD7 and MSD5. This allows the tacheometer coordinate system to be rotated into the pillar coordinate system (ETRS89) with the orientation unknown angle, which can be determined by additional measurements to stations with known coordinates. Here, circular prism are installed on pillar MSD1 and MSD9 and are measured from the tacheometer stations. In total, 334 points are observed in two phases to eliminate instrumental error sources. For the digital model, it is necessary to maintain the three-dimensional properties of specific structures on the rooftop. As a result, points are required at both the bottom and top of these structures, especially for those exhibiting orthogonal characteristics. Additional points are required for the curved roof of the building, as well as for the astronomic domes, which will later be modelled as spheres.

Figure 5.2 shows the measured points in blue in a topocentric North-East representation (left) and in an East-Up representation (right), where the robot station MSD7 defines the origin of this system. In order to create solid bodies for each structure,

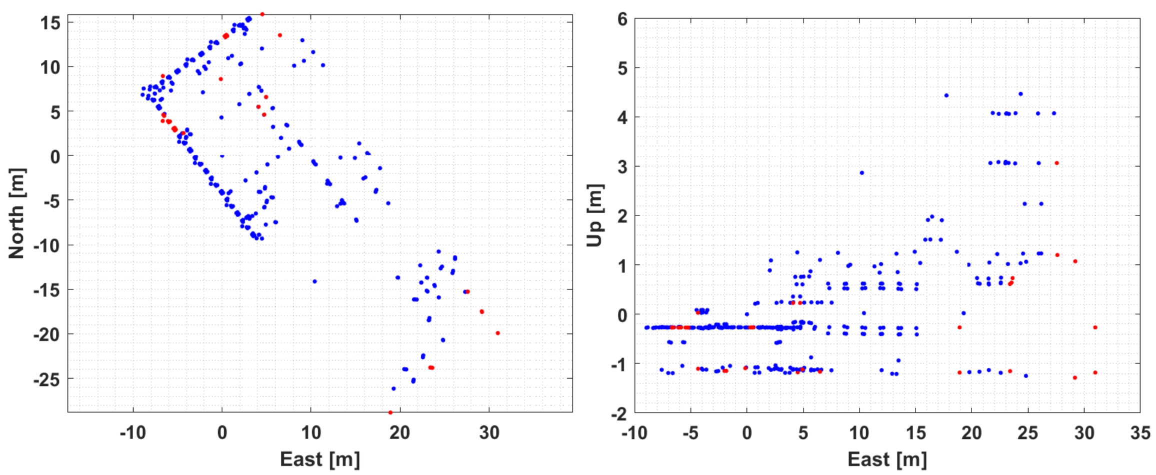

Figure 5.2: Measured points (blue) and calculated points (red) within the practical survey. (Left) Horizontal position of the points. (Right) Vertical position of the points.

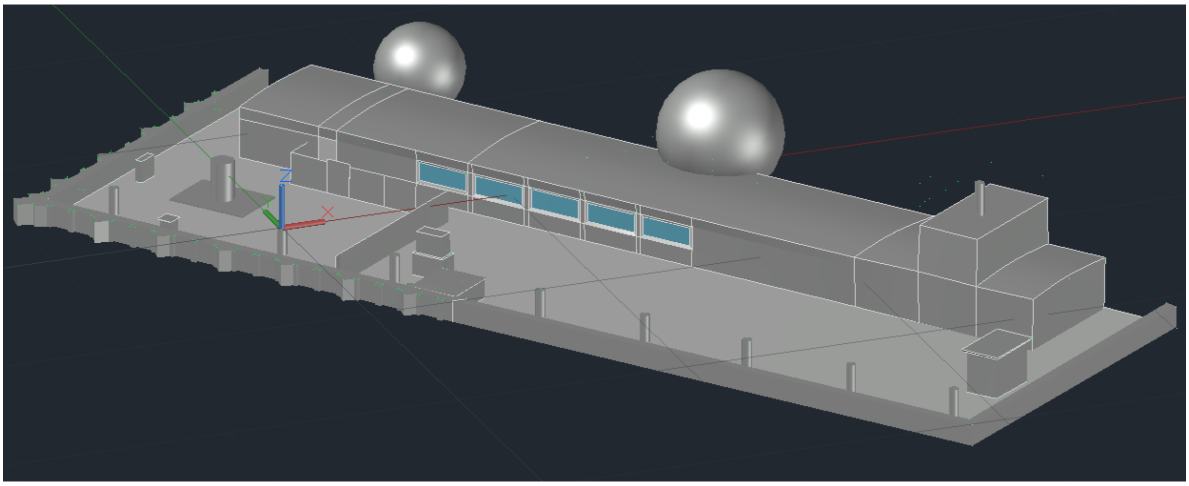

Figure 5.3: Digital twin of the robot environment on the laboratory rooftop of the GIH building in the AutoDesk software.

additional points are required (red dots). It was not possible to observe these points in the survey, due to visual blockage, thus, these points are calculated in post-processing using trigonometric functions, additional surveys by measuring tape and the assumption of structure orthogonality. With this strategy, the digital model may be continued, if needed, for further analysis or other experiments (e.g. extend the balustrade with this special triangular pattern).

The topocentric coordinates of all points, observed and calculated, are imported in the software *AutoCAD 2022* from the company Autodesk. On one hand, this software allows the creation of solid bodies; on the other hand, it can export these bodies in the commonly used STEP format. STEP stands for *Standard for the Exchange of Product Data* and is also known as the ISO 10303 (Pratt, 2001). As the name implies, it is a standardized format for describing three-dimensional models. Almost any modelling software can read this format, including the ray tracing software from DLR.

In order to create a solid body, the related points of a structure are linearly connected by 3D lines. A solid body can only be created, when the connected lines form a closed 3D dimensional space. For some structures, additional effort has to be done. For example, the fence, nearby the robot, was measured with one point on the top and one point on the ground for each fence pillar. By connecting these points, an area is created instead of a 3D body. Therefore, the fence is modelled as an area with a thickness of 5 cm[1]. This approach is also done for the ground, to create a solid body. The astronomic domes are modelled as spheres, whereas the center of the sphere and its radius are estimated beforehand, based on the measured points on the dome surface. The pillars are modelled as cylinders with a specific radius and height, which were measured by tape in the practical survey. The reference coordinates define the pillar's center.

Figure 5.3 shows all the created solid bodies for the robot environment. More detail modelling is done in the surrounding of the robot, thus the back of the rooftop is not considered. Nearby the robot pillar, another pillar is visible, which represents the new robot from IfE. Because no CAD model is available, by the time of writing this thesis,

[1]The metallic fence have been replaced with a non-metallic alternative.

the robot is approximated with a cylinder of 2 m height and 50 cm radius. The surface of the balustrade is extended downwards to the same height as the ground. Additionally, the smaller rectangular structures, like the rooftop building or the air ventilation shaft, are simply modelled by connecting the corner points. To this end, the final digital 3D-model is exported as a STEP file, which can be used for further multipath analysis or for creating multipath maps (cf. Section 5.3).

5.2 Multipath Analysis of Robot Surrounding

Multipath effects can impact GNSS observations and degrade the application results. During the antenna calibration at IfE, the robot is located in a challenging environment as presented in the previous section. This section focuses on how multipath effects act in the robot based antenna calibration. Therefore, the MPLC is used to find critical structures in the robot surrounding first and shows how an elevation mask can significantly reduce the number of multipath affected observations (Section 5.2.1). Section 5.2.2 investigates how different antennas are affected by multipath and how the multipath acts in tilting and rotating scenarios.

5.2.1 Using Multipath Linear-Combination to find Critical Structures

The laboratory rooftop of IfE has a lot of structures, that have the potential to reflect GNSS signals and create multipath effects within the receiver. As the digital model (cf. Section 5.1) already suggests, the robot has to deal with a challenging environment. In order to analyse the influence of the robot surrounding on the observations, the multipath linear combination, introduced in Section 2.4.3, is used. This LC helps to identify multipath-affected observations, with higher MPLC magnitudes indicating possible multipath effects. The MPLC is created using the GPS C1C, L1C, and L2W signals, and respectively, the C1X, L1X, and L5X signals for Galileo satellites. For this investigation, a calibration from a category 2 antenna (rover) is used, in particular the NOV703GGG.R2 NONE (S/N:12420040), which had been carried out between noon on the 15^{th} and midnight on the 17^{th} of July 2024 (DOY 197-199). Two Javad DeltaS-3S receiver were used, with optimized receiver settings (AUT: DLL bandwidth of 1 Hz, FO 1, aided; Reference: DLL bandwidth of 0.5 Hz, FO 1, aided).

In Figure 5.4 the absolute MPLC values for day of year (DOY) 197 (left) to DOY 199 (right) in a topocentric coordinate system are presented for all visible satellites and epochs over the days. The calibration on DOY 197 was conducted over 11 hours, while the calibration duration on the other two days was 24 hours. It should be noted that the antenna pose is not static and varying after each epoch. The top plots show the GPS MPLC and in the bottom figures the results for the Galileo MPLC are depicted. No additional elevation mask (or multipath map) is added. The location of the dots shows the actual satellite position and not the reflection points of the signal. The colour and size of the dots represent the amount of the calculated MPLC. The darker the colour, the higher the MPLC. Galileo signals are generally less noisy compared to GPS codephase signals, therefore, the plots show a brighter appearance. Nevertheless, there

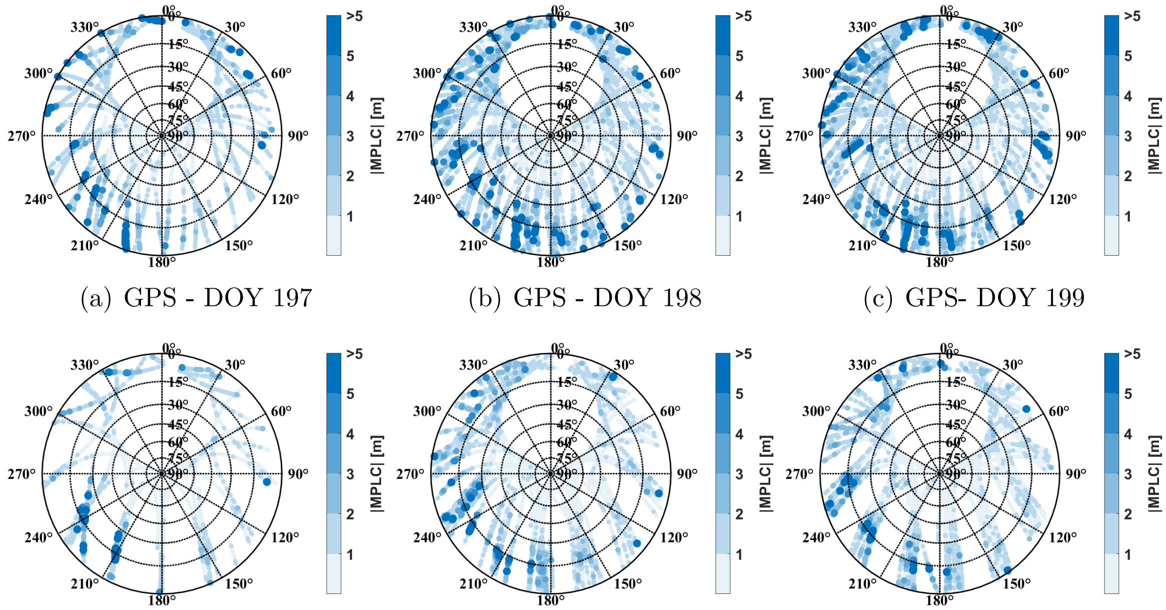

(a) GPS - DOY 197 (b) GPS - DOY 198 (c) GPS- DOY 199

(d) Galileo- DOY 197 (e) Galileo - DOY 198 (f) Galileo - DOY 199

Figure 5.4: Absolute MPLC values in topocentric frame for GPS with the signals C1C, L1C and L2W (top) and for Galileo with C1C, L1X and L5X (bottom) for a category 2 antenna. The data were observed within a calibration from DOY 197 (left) to DOY 199 (right). Please note that only 11 hours are used in DOY 197.

exist regions, where the MPLC reaches higher magnitudes. These areas are visible on every day and are located in the South and Western part. Some dots are also visible at 30° and 100° azimuth. Having a look on the GPS MPLC, these areas are more prominent, due to a higher MPLC magnitude. More multipath affected observations are located at lower elevations. Overall, Galileo and GPS show similar results and have higher MPLC values in specific areas. Comparing these results with Figure 5.3, where the topocentric coordinate system is depicted (Y axis pointed towards North), it can be seen, that the multipath affected region in the South and Western part could be caused by either horizontal reflections on the balustrade, which has a metallic surface, or by vertical reflection on the rooftop building. The areas around 30° and 100° azimuth are in the directions of the astronomic domes, where diffraction effects can occur. In addition, the building is located in this area, which can cause diffraction effects.

When transforming the topocentric satellite positions into the antenna frame and plotting them against the MPLC, it is evident that the multipath affected areas are mapped up to approximately 45° elevation across the entire azimuth range. This can be seen in Figure 5.5, especially on DOY 198 and 199, because the calibration was carried out over the entire day, instead of nearly eleven hours as on DOY 197. This behaviour is explainable by the tilting and the horizontal rotations of the robot.

The robot based antenna calibration at IfE uses time differenced observations, either in the ΔSD approach or in the ΔMPLC approach, proposed in this thesis. When two consecutive epochs are time differenced, multipath effects are cancelled out, when their magnitude is identical. However, due to different tilting and rotating scenarios of the robot, multipath effects act differently on the antenna at each epoch. Some remaining differential multipath is still included in the observations. Even if the satellite-reflector-

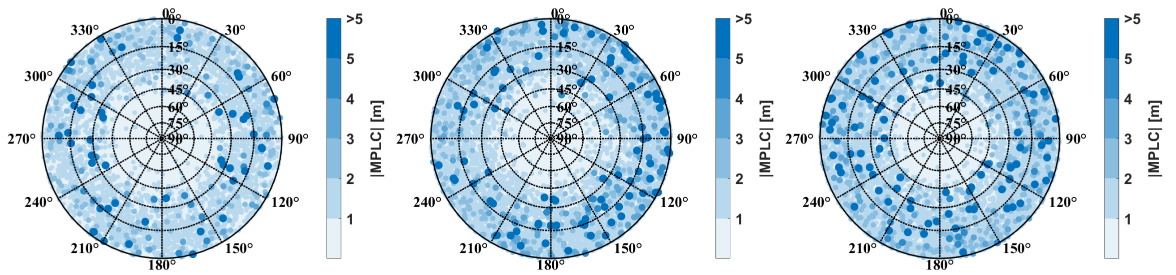

(a) GPS - DOY 197 (b) GPS - DOY 198 (c) GPS - DOY 199

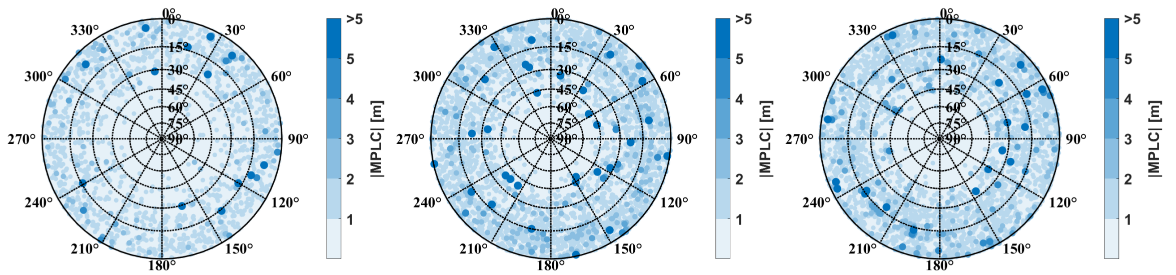

(d) Galileo - DOY 197 (e) Galileo - DOY 198 (f) Galileo - DOY 199

Figure 5.5: Absolute MPLC values in antenna frame for GPS with the signals C1C, L1C and L2W (top) and for Galileo with C1C, L1X and L5X (bottom) for a category 2 antenna. The data were observed within a calibration from DOY 197 (left) to DOY 199 (right). Please note that only 11 hours are used in DOY 197.

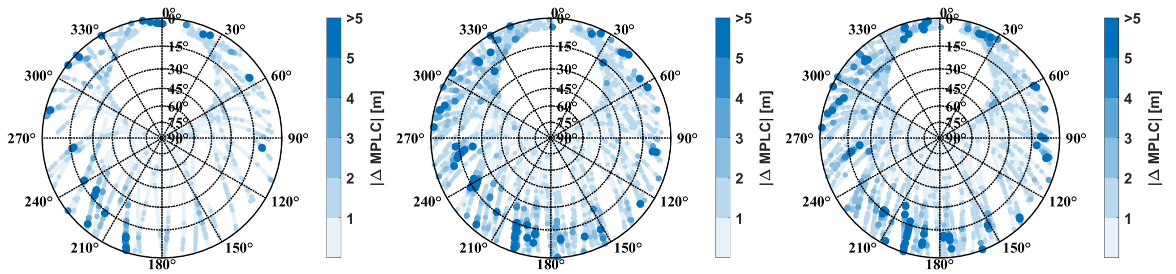

(a) Topo - DOY 197 (b) Topo - DOY 198 (c) Topo - DOY 199

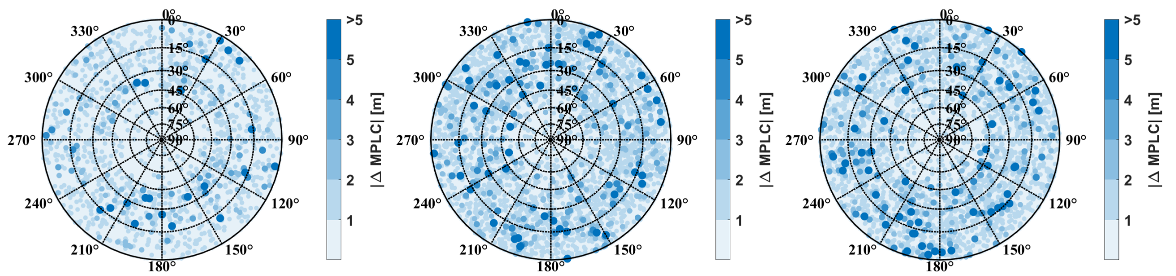

(d) Ant - DOY 197 (e) Ant - DOY 198 (f) Ant - DOY 199

Figure 5.6: Absolute ΔMPLC values in topocentric (top) and antenna frame (bottom) for GPS with the signals C1C, L1C and L2W (top) for a category 2 antenna. The data were observed within a calibration from DOY 197 (left) to DOY 199 (right). Please note that only 11 hours are used in DOY 197.

receiver geometry is not changing significantly between two robot poses, the receiving point of the antenna is changing and consequently the antenna gain. This will lead to additional multipath effects in the receiver. Therefore, the ΔMPLC are calculated for

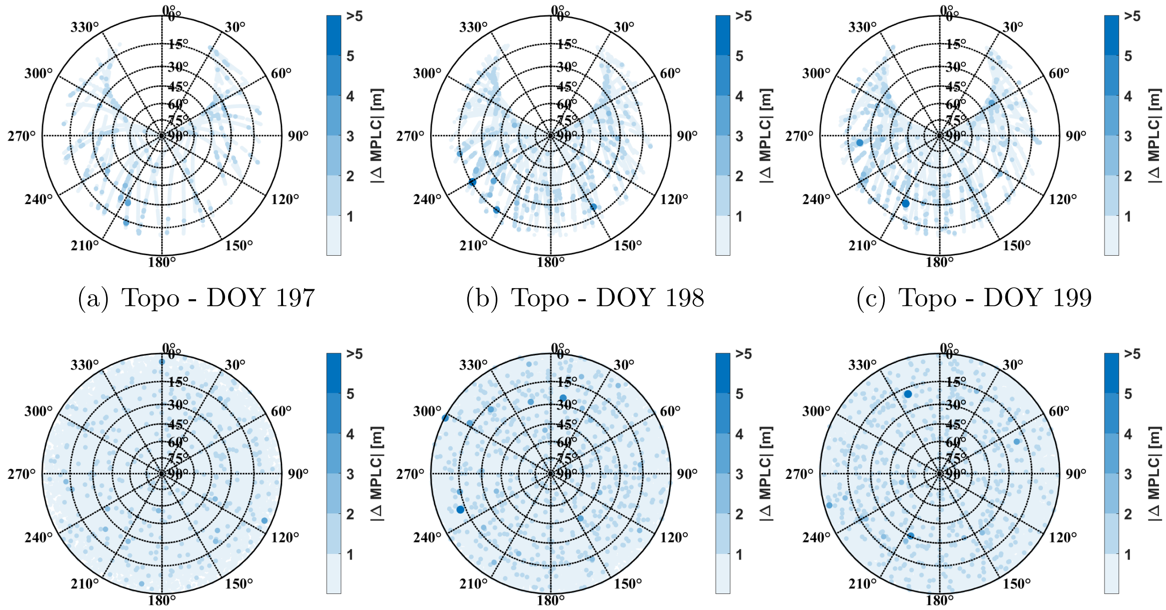

(a) Topo - DOY 197 (b) Topo - DOY 198 (c) Topo - DOY 199

(d) Ant - DOY 197 (e) Ant - DOY 198 (f) Ant - DOY 199

Figure 5.7: Absolute ΔMPLC values using a dynamic elevation mask in topocentric (top) and antenna frame (bottom) for GPS with the signals C1C, L1C and L2W (top) for a category 2 antenna. The data were observed within a calibration from DOY 197 (left) to DOY 199 (right). Please note that only 11 hours are used in DOY 197.

this experiment and the result is shown in Figure 5.6. For clarity, only the GPS data are presented here. The ΔMPLCs are related to the first satellite position. The top row shows the results in the topocentric system, while the bottom row presents the antenna system. By comparing the plots with the MPLC in Figure 5.4 (a-c) and 5.5 (a-c), the multipath effects are reduced. However, the critical regions in the South and Western and between 0° and 100° azimuth are still present, with high ΔMPLC magnitudes. This shows, that multipath on observations can not fully eliminate by time differencing. By transforming them into the antenna frame, still higher ΔMPLC are visible over the entire azimuth range for elevations up to 60°.

As Figure 5.4 already depicted, most of the multipath effects occur at low elevations. Almost every time differenced observation that includes low elevation measurements is affected by multipath. To avoid these observations, elevation masks are used in robot based antenna calibration, which are also applied in this experiment. Here, the dynamic elevation mask is used with a topocentric cut-off angle of 10° and a negative elevation mask of 5°. The results are visible in Figure 5.7, again for the GPS ΔMPLC and same structure as Figure 5.6. It is obvious, that the multipath effected observations are significantly reduced. However, some higher ΔMPLC values still remain in the South-West.

To summarize, multipath effects occur during the calibration process. They are mostly appearing from satellites in the West, which signals are either reflected on the rooftop building or the balustrade. Furthermore, the location of the astronomic domes can be critical. However, by using a time differencing approach in combination with a dynamic elevation mask, multipath affected observations can be significantly reduced.

Unfortunately, some small amount of multipath effects may still remain in the observations.

5.2.2 Multipath Impact on different Antenna Types and Tilting Scenarios

The investigations from previous Section 5.2.1 are based on a rover antenna, designed for effective multipath mitigation. This section focuses on the multipath impact on different antennas during a standard calibration. Therefore, one antenna of each category, defined in Section 4.2.2, is analysed. Due to the lack of the L2 signal for the u-blox antenna, the linear combination is calculated using the GPS C1C, L1C, and L5X signals. That is the reason why the results show fewer observations compared to the Novatel and Leica antenna, which is visible in Figure 5.8. Here, the total amount of ΔMPLC with and without adding a dynamic elevation mask (same mask used in Section 5.2.1) is presented for three different antennas. Each of the antennas has been calibrated for 24 hours. By adding a mask, the amount of usable observations decrease by approximately 40 % to 45 %. It is also visible, that the Novatel antenna received the most signals.

Figure 5.9 shows the results for each antenna with no additional elevation mask in (d) to (f) and with a dynamic elevation mask in (g) to (i) in a topocentric coordinate system. It is visible, that the multipath affected areas in the West as well as the direction of the astronomic domes are present for all antennas. By taking the number of observations into account, the u-blox antenna shows, in a percentage perspective, more multipath affected observations compared to the geodetic antennas. By adding an elevation mask, most of the multipath affected observations are eliminated, however still some higher ΔMPLC observations remains for all antennas, but most for the u-blox antenna. Typically, geodetic antennas are designed in a way, e.g. choke rings, that multipath effects can be reduced. The u-blox antenna is installed on a ground plate, to avoid ground reflected GNSS signals, but only up to a certain level.

Generally, GNSS antennas are designed in a way that the antenna gain, or the ratio between the RHCP and LHCP gain, is highest at high elevation in the antenna system,

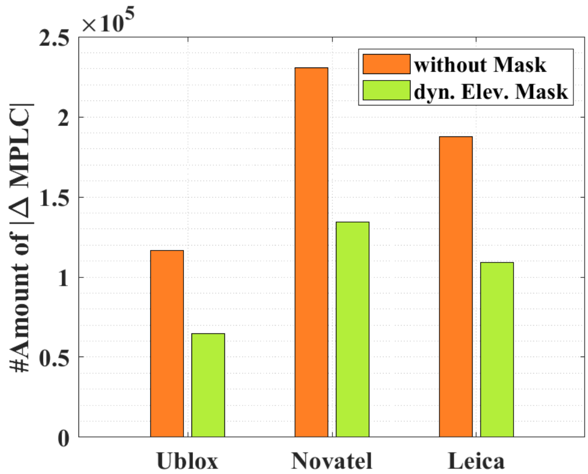

Figure 5.8: Amount of ΔMPLC with and without a dynamic elevation mask for three different antennas, calibrated over 24 hours.

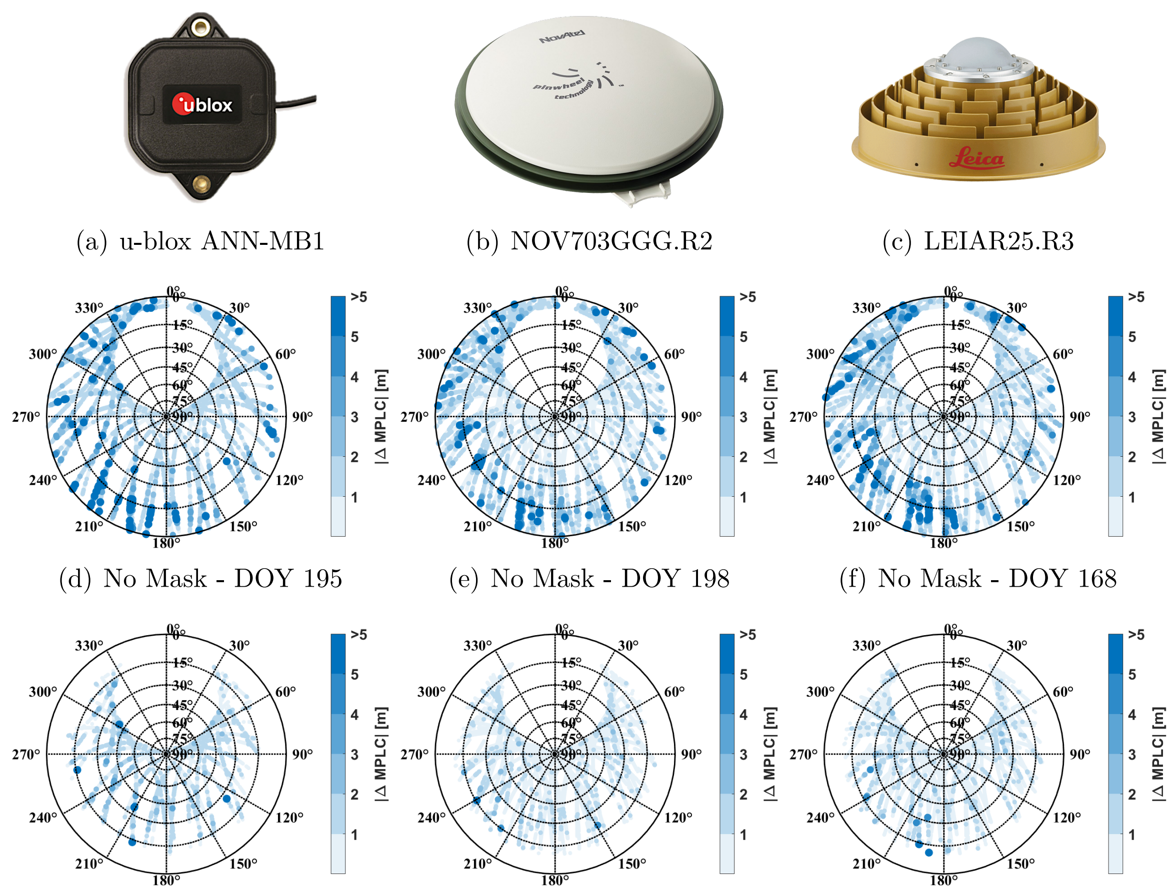

(a) u-blox ANN-MB1 (b) NOV703GGG.R2 (c) LEIAR25.R3

(d) No Mask - DOY 195 (e) No Mask - DOY 198 (f) No Mask - DOY 168

(g) Elev. Mask - DOY 195 (h) Elev. Mask - DOY 198 (i) Elev. Mask - DOY 168

Figure 5.9: Absolute ΔMPLC values in topocentric frame for GPS with the signals C1C, L1C and L2W for Novatel and Leica and L5X for u-blox antenna. Each column represents one antenna. The middle row shows the ΔMPLC without an elevation mask, the data in the last row are calculated using the dynamic elevation mask [Antenna pictures: U-Blox AG (2024), Novatel (2011), Leica Geosystems AG (2024)].

so that multipath arriving from below can be suppressed. This ratio determines among other factors the multipath susceptibility. Multipath effects are mostly LHCP polarized. Thus, they are more prominent at lower antenna elevations, due to worse antenna gain. Tilting the antenna can either reduce multipath effects when they are received in the upper part of the antenna hemisphere, or increase them when the incoming signal reaches the antenna at low elevations.

Figure 5.10 shows, how the MPLC acts in different tilting scenarios of the robot. No additional elevation mask is added for this investigation. Each row represents one antenna from (a) category 3 to (c) category 1. In the figures, the amount of multipath affected observations (left y-axis) is shown in different absolute MPLC intervals and different antenna inclinations during a calibration of 24 hours on the same days as listed in Figure 5.9. The grey area indicates the total amount of observations (right y-axis) within this specific inclination bin. For clarity, only GPS MPLC over 2 m are shown in four different intervals. The maximum inclination angle is different between the u-blox antenna with 42° and the other two antennas with a maximum tilting of 35°. The motion of the robot within the antenna calibration uses significant more poses at specific tilting angle, at 0°, 17° and 35°. For the u-blox antenna, more observations

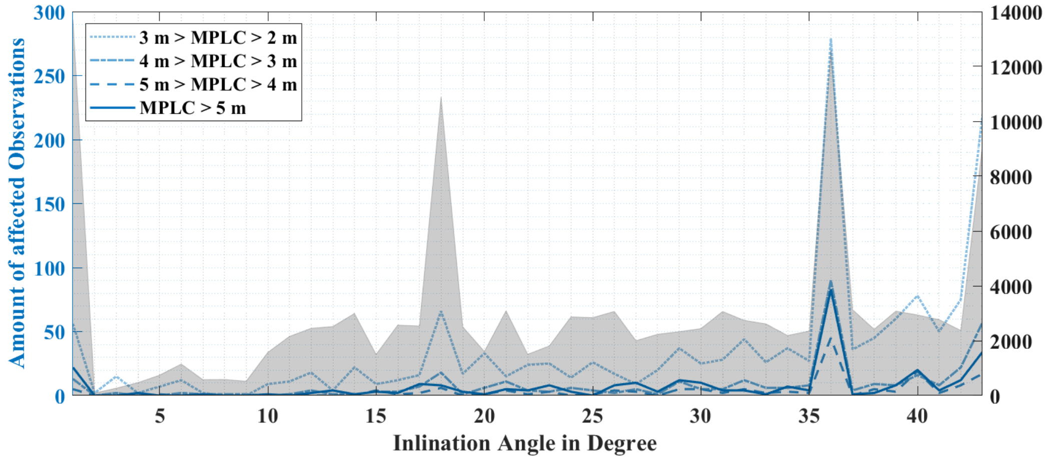

(a) Category 3 - u-blox

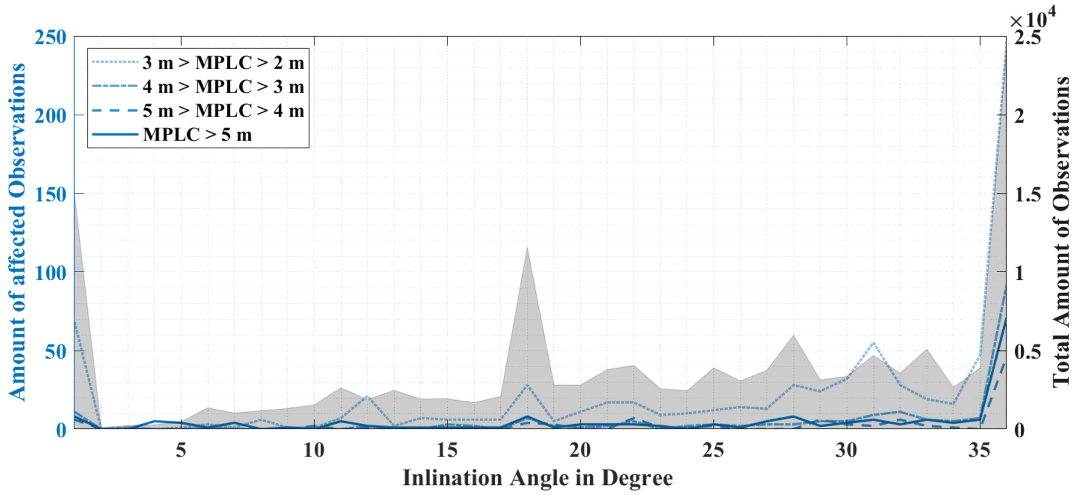

(b) Category 2 -Novatel

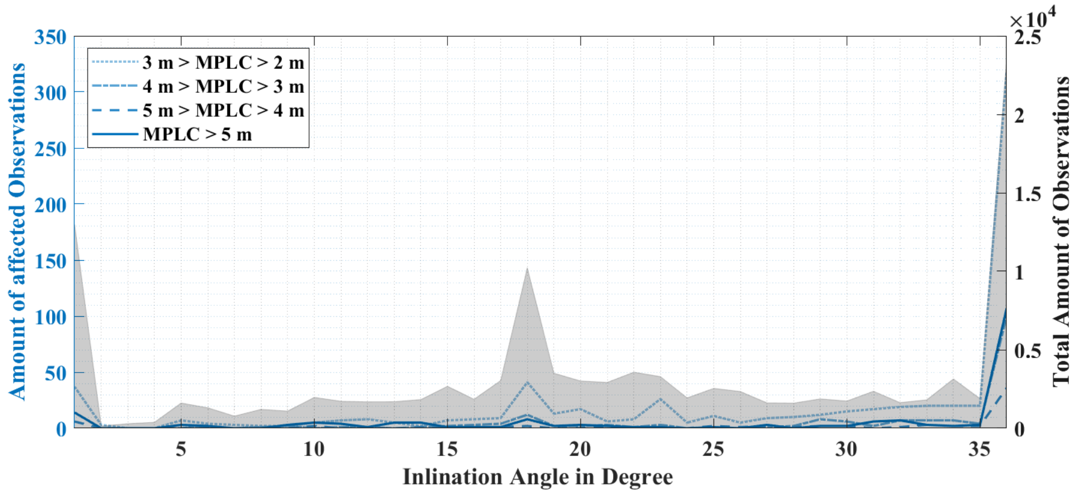

(c) Category 1 -Leica

Figure 5.10: Amount of multipath affected GPS observations versus the inclination of the robot for (a) category 3, (b) category 2 and (c) category 1 antenna. Different absolute MPLC intervals are presented. The grey area shows the total amount of observations within the specific inclination angle over a calibration of 24 hours.

are also collected at the maximum tilting angle of 42°. It should be noted, that the figures show the observations within particular inclination bins with a resolution of 1°. For example, the visual peak at 36° includes all the tilting angles between 35° (35° is included) and 36°. Having a look at the MPLC, a correlation between multipath affected observations and the total number of observations in the inclination bins is visible. It is also evident, that MPLC values between 2 m and 3 m increase with the antenna tilting. Greater MPLC, which are more related to multipath errors, are more prominent in the mentioned inclination bins. Comparing the MPLC with the total number of observations, each antenna exhibits similar behaviour, except that the u-blox antenna has relatively more multipath affected observations. Additionally, no dependency between higher MPLC values and the tilting angle is observed.

In addition to tilting scenarios, horizontal robot rotations are also performed. The satellite positions in the antenna frame are changing during these operations. Figure 5.11 shows how the ΔMPLC behave by azimuth and elevation changes between two consecutive epochs. The same data is used for the three different antennas. Here, GPS ΔMPLC are presented for all visible satellites above 2 m for clarity. It is evident that higher ΔMPLC values occur both with small antenna rotations or minimal changes in

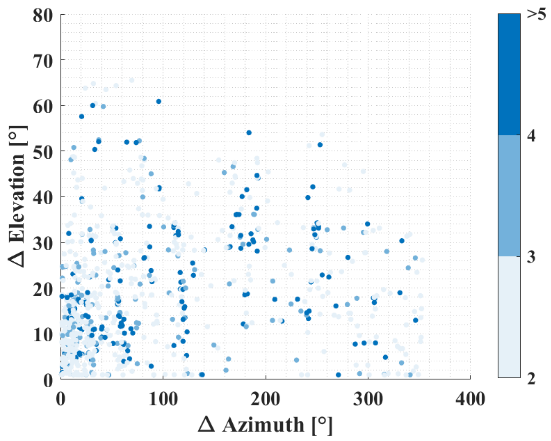

(a) Category 3 - u-blox

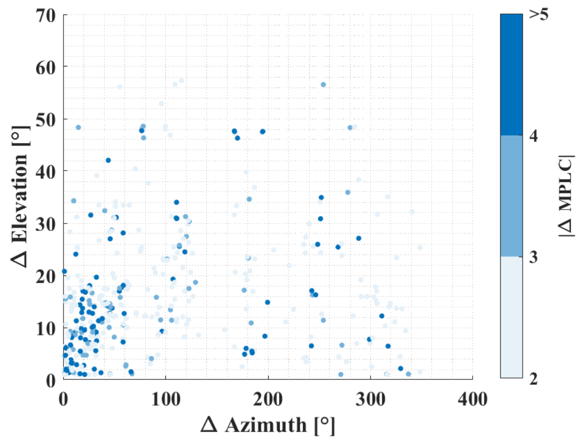

(b) Category 3 - Novatel

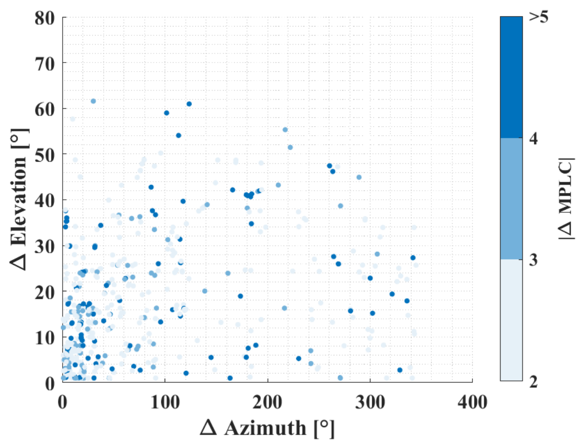

(c) Category 3 - Leica

Figure 5.11: GPS absolute ΔMPLC values versus elevation and azimuth changes of all visible satellite caused by the robot tilting and rotating for (a) category 3, (b) category 2 and (c) category 1 antenna. Only ΔMPLC over 2 m are presented for clarity.

satellite positions within the antenna system and with large changes. No dependency between changes and ΔMPLC can be determined. This holds true for each antenna.

This investigation shows, that multipath affected observations occur on category 3 antennas, as well as for category 2 and 1 antennas. However, when comparing the proportion of multipath affected observations to the total number of observations, category 3 antennas have a higher occurrence. No significant dependency between tilting or rotating scenarios and higher MPLC/ΔMPLC values is visible. Consequently, multipath effects are mostly related to the environment.

5.3 Multipath Maps from DLR

5.3.1 Multipath Map Development

Broad investigations have been made by the DLR to develop and generate multipath error maps, hereinafter abbreviated as multipath maps, which can be used in the antenna calibration. A brief overview about this process is given in this section. More details can be found in Addo and Caizzone (2023), Addo et al. (2024b) or Addo et al. (2024a). The basic idea is to characterize multipath errors by considering the electromagnetic antenna properties of the antenna itself and by installing them into a particular environment scene. The differences in the antenna behaviour between the standalone and installed scenarios represent the impact of the environment on the antenna, caused by multipath effects.

The foundation of the process is a specialized antenna, developed by Caizzone et al. (2021), which features dual-circular polarization to receive both LHCP and RHCP signals (cf. Figure 5.13). Each polarization has an individual antenna output port. To ensure optimal signal performance and maintain stable tracking, the antenna design must fulfil three requirements, as described in Addo et al. (2024b). Measuring the antenna's electromagnetic properties, e.g. the antenna gain or GDV, in an anechoic chamber is the first step of the algorithm (cf. Figure 5.12), which is described in Caizzone et al. (2019) in detail. From these measurements, so-called Huygens' boxes or near-field equivalent sources (NFS) are derived, describing the electromagnetic behaviour in the antennas' near field. The NFS are calculated for both standalone and installed scenarios. For the installed scenario, the digital model of the robot environment, as described in Section 5.1, is used. In addition, a CAD model of the antenna calibration robot is added to the scene, located on the pillar MSD7. With a 3D electromagnetic field and multi-

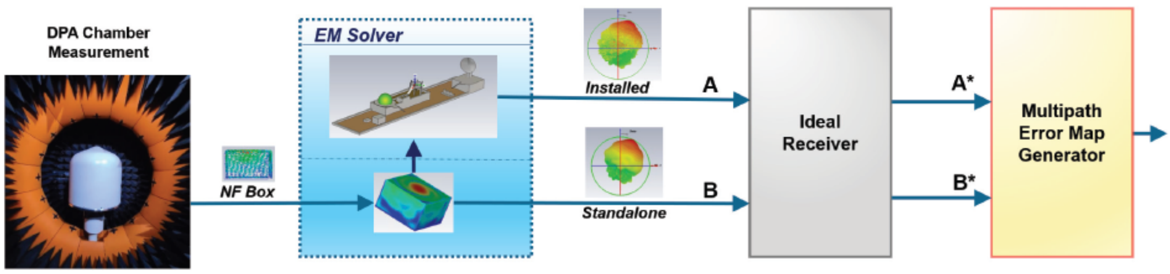

Figure 5.12: Scheme of *fullWaveIP* algorithm to generate multipath error maps (Addo et al., 2024b).

(a) No Tilt (b) Tilt

Figure 5.13: Experimental setup of DLR's antenna probe on the antenna calibration robot.

physics modelling and simulation tool, SIMULIA CST Studio Suite (Dassault-Systèmes, 2022), the distorted gain and phase behaviour of the antenna within the environment scene can be determined. The differences between the standalone and installed NFS show the multipath impact on the antennas' electromagnetic behaviour. The digital model includes different material conditions, like conductivity and relative permittivity properties, for particular structures on the laboratory rooftop.

Since, NFS are not good tangible observables for multipath analysis in GNSS applications, a particular software receiver (ideal receiver), established by Vergara et al. (2016), is used. It converts the input NFS into pseudorange errors for all azimuth and elevation angles. These errors for both, standalone and installed, scenario can easily be subtracted from each other, thanks to the grid and metric behaviour. The differences indicate the multipath error from a specific satellite signal direction. In order to generate a multipath map, a threshold is chosen, which defines either a GNSS signal from a specific direction is affected by multipath or not. When the difference pseudorange error exceeds the threshold, multipath impacts the signals and vice versa. The map is logically structured, so that false or '0' values indicate multipath affected locations, which should not be used in GNSS applications, and true or '1' for usable observations. A validation of the simulated maps has been done in the framework of the MAESTRO project on the robot environment at IfE with the antenna probe shown in Figure 5.13 (Addo et al., 2024a).

The above technique is a hybrid-simulative multipath estimation approach, abbreviated as *fullWaveIP*. Its main drawback is the big computing time, which takes about four hours to create one map (Addo et al., 2024a). Within the antenna calibration, the antenna pose is changing every couple of seconds and consequently the electromagnetic behaviour of the AUT. This leads to different NFS in the installed scenario. Considering the maximum robot tilting angle of 42°, 15162 different antenna poses are possible (1° resolution), which have to be covered by the same amount of maps. Obviously, the

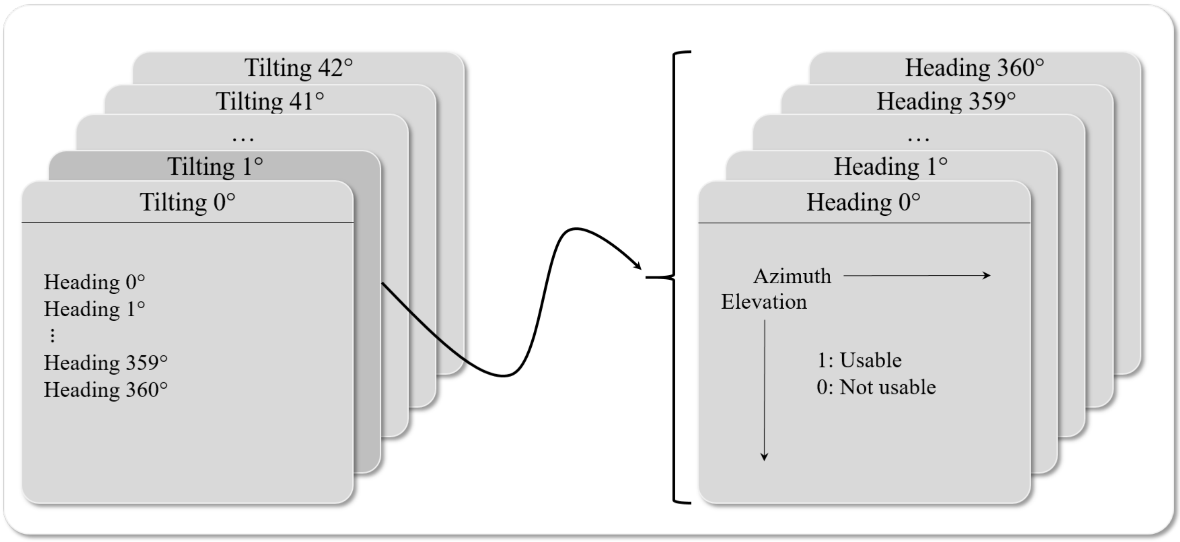

Figure 5.14: Basic structure of multipath maps.

fullWaveIP can not be used. Thus, Addo et al. (2024a) introduced a *fastIP* approach, which estimates a map within seconds. More details can be found in this contribution. This approach is used, to generate the required maps for the antenna calibration, based on different antenna categories. Therefore, one antenna of each category has been measured in the anechoic chamber to get the electromagnetic properties. The multipath maps are based on these chamber measurements and generated with three different thresholds (1 m, 1.5 m, 2 m).

5.3.2 Structure and Usage within the Antenna Calibration

In the framework of the MAESTRO project, DLR has calculated and provided multipath maps based on the principle described in the previous Section 5.3.1. These maps indicate, whether an incoming GNSS signal is contaminated by multipath or not. DLR calculated these maps for three different antennas with three different thresholds, where each antenna is a representative for one category, defined in Section 4.2.2. They are related to the FP during a calibration, which distinguishes between the antennas. For the u-blox antenna, the FP is located at a height of 0.9351 m above the pillar, for the Novatel antenna at 0.9755 m and 1.0774 m for the Leica antenna. The maps have to be calculated for each tilting and rotating scenario, because the multipath behaviour of the antenna is changing when the antenna is at a different pose. In total, 15162 different maps for one antenna and one threshold have been created. They are provided as a MATLAB file for including them into the antenna calibration algorithm at IfE.

The basic structure is shown in Figure 5.14. The first layer contains 43 different structures, which represent the robot tilting angles from 0° to 42° (maximum tilting during robot based antenna calibration) with a resolution of 1°. Each of these structures contains 361 different matrices for the heading angle (azimuth) or tilting directions of the robot. The matrices have a dimension of elevation×azimuth (91×361 for 1° resolution) and are filled with logical values. When the satellite signal is assumed to be contaminated by multipath, the particular elevation and azimuth bin is filled with '0'.

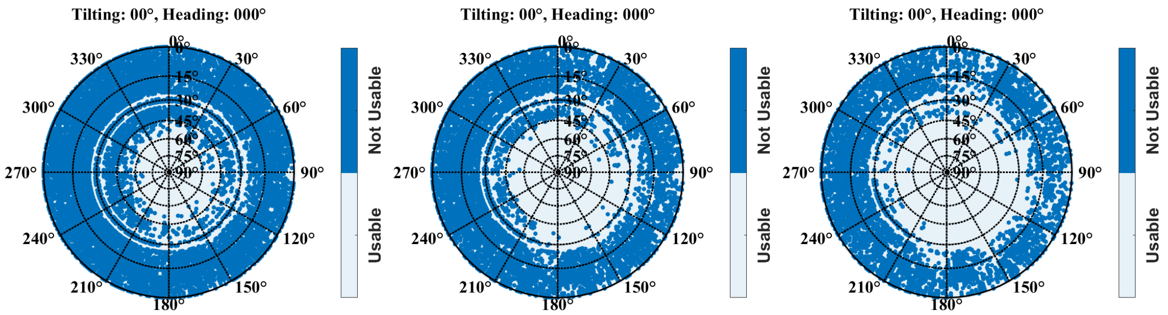

(a) Threshold 1 m (b) Threshold 1.5 m (c) Threshold 2 m

Figure 5.15: Multipath map for the Novatel antenna for three different thresholds: (a) 1 m (b) 1.5 m and (c) 2 m in a no tilting scenario and a heading of 0°.

On the other hand, a usable observation is defined as '1'. The given values are related to a topocentric coordinate system, where the FP marks the origin.

In the IfE antenna calibration, these maps are used to eliminate multipath affected observations before transforming them into the antenna system. The functions to set up the dynamic elevation mask (cf. Section 3.3.2) are extended by these maps. The first step is to find the robot pose at the considered epoch. The selection of the responsible map is based on the tilting and heading angle of the robot. Next, each visible satellite is checked and compared with the map to determine if the satellite's direction is affected by multipath. If so, this satellite observation is eliminated, otherwise it will be used for the estimation process. The maps can be used in combination with a topocentric or dynamic elevation mask.

An example of multipath maps are shown in Figure 5.15 in a topocentric coordinate system for the Novatel antenna with three different thresholds: (a) 1 m (b) 1.5 m and (c) 2 m. In this scenario, the robot is not tilted, and it is orientated towards north (heading angle is 0°). The blue dots represent multipath affected observations and the brighter dots usable observations. It is evident, by decreasing the selected threshold, also the number of usable observations is decreased. For a threshold of 1 m 76 % of the observations are usable, 83 % are usable, when choosing a threshold of 1.5 m and 87 % for a 2 m threshold. It is also visible, that more of the affected observations are located at the West (cf. Figure 5.15 (c)), which agrees with the investigations in Section 5.2.

Another example is presented in Figure 5.16, again for the Novatel antenna. A threshold of 2 m is chosen. The plots show, how the multipath maps behave in different tilting and heading scenarios. The left row depicts the maps for a non tilting scenario, but with different heading angles: (a) 0°, (d) 90°, (g) 180° and (j) 270°. In the middle row, a tilt of 17° is performed, whereas 35° tilt scenarios can be found in the last row. Considering the non tilting scenarios, it is evident, that they have a very similar behaviour. A different heading angle does not lead to more or less multipath affected areas, significantly, which is an indicator for an azimuthal symmetry gain behaviour of this antenna. However, a tilting of the antenna changes the multipath behaviour, significantly. Having a look at Figure 5.16 (b), where the antenna is tilting by 17° towards North direction, is can be seen, that the area of usable observations is shifted towards North. Because the antenna gain is usually strongest at high elevation, more low elevation observations are usable. However, higher elevation observations in the South

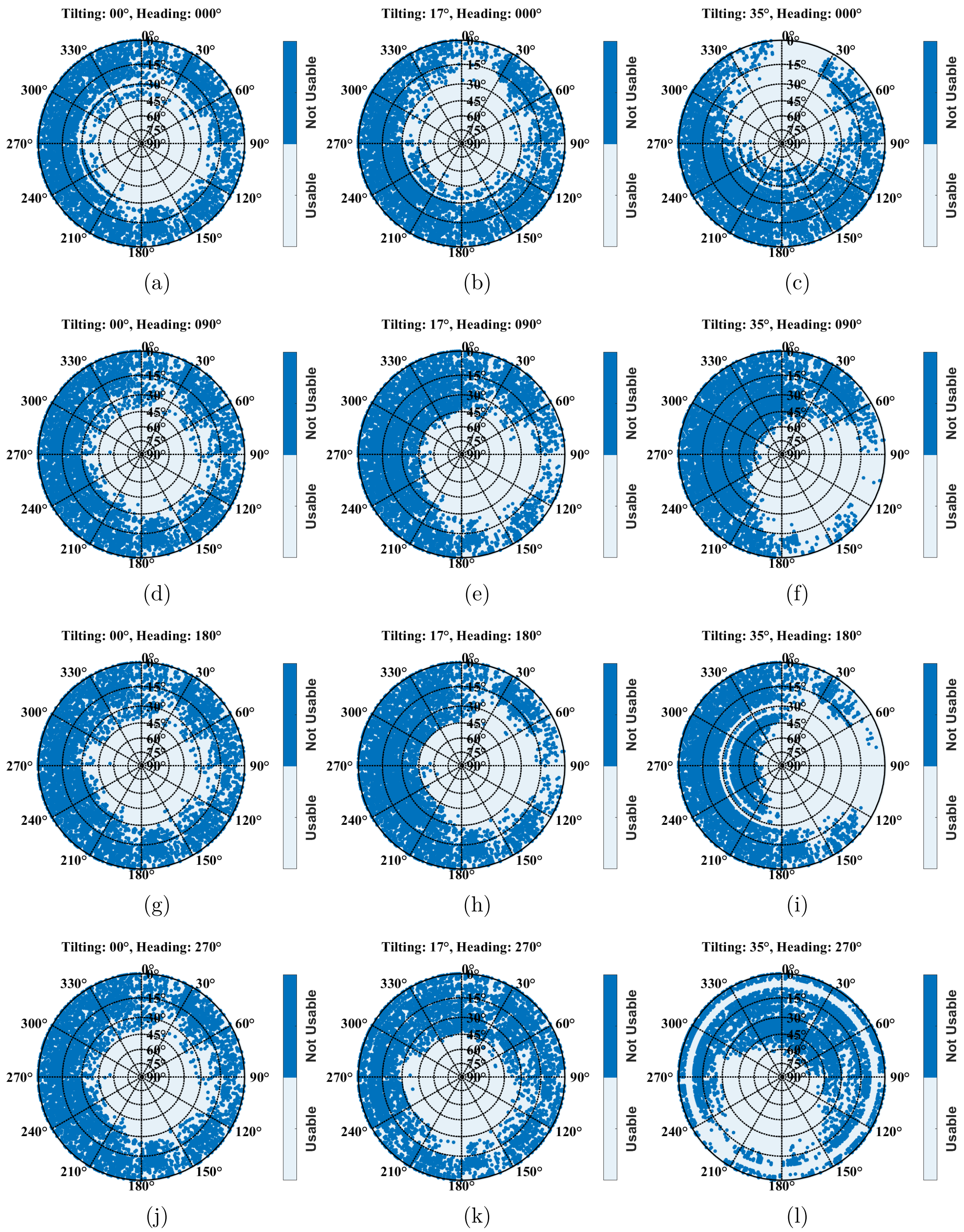

Figure 5.16: Multipath map for the Novatel antenna in different tilting and heading scenario with a threshold of 2 m.

are now marked as not usable, due to antenna gain loss in these areas. The number of usable observations is not significantly changing compared to a non tilting scenario. It decreases by only 59 usable observations (28645 → 28586). When the antenna is tilted to 35° towards North (Figure 5.16 (c)), this behaviour is reinforced. More low elevations areas in the North direction are now usable, at cost of higher elevation observations in the South. An additional loss of 82 usable observation has to be accepted.

When the antenna is tilted towards East in Figure 5.16 (c) and (d), the area of usable observations is shifted towards this direction as expected. However, more areas at higher elevations are affected by multipath. Also, the number of usable observations decreases more, compared to a heading of 0° (28410 → 28103 → 27602). As already investigated in Section 5.1, the rooftop building is located in the East direction relative to the robot position. Therefore, more satellite signals from the West may be vertical reflected on the building itself, which leads to more unusable observations from higher elevations in the West. In addition, not usable areas can be found in the North-Eastern Part. There, one of the astronomic domes is located, which can cause diffraction effects.

The multipath affected areas for a heading of 180° (Figure 5.16 (h) and (i)) do not perform as expected. The usable area is not shifted towards South, however, towards East. This indicates, that the vertical reflected GNSS signals from West located satellites are also influencing a Southern tilted antenna. In addition, low elevation observations in the South direction are visible. It can be assumed, that these signals are horizontally reflected on the balustrade of the rooftop, which is a highly potential reflection surface, made of metallic material. However, the number of usable observations is not changing significantly, compared to the non tilting scenario.

A tilting towards the West (Figure 5.16 (k) and (l)) even increase the number of usable observations from 28338 → 28338 → 29092, because vertical reflection on the rooftop building from GNSS signals may not reach the antenna any more. The usable area of observations is more shifted towards South-West.

To summarize, in non tilting scenarios no signifiant change can be seen in the multipath maps, which indicates a good azimuthal gain symmetry of the Novatel antenna. A tilting of the antenna shifts the area of usable observations, however, the direction of the shifting depends on the tilting direction and on the environment. Critical observation areas are mostly located in the West, due to vertical reflections on the Eastern located rooftop building or horizontal reflection on the balustrade. In addition, the North-Eastern part can be critical, due to diffraction effects on the astronomic dome. The maps show similar results as the investigations of the MPLC in the Section 5.2.1.

The previous multipath maps are valid for a category 2 antenna, Figure 5.17 shows the maps for the other two categories as well. The top row presents the results for the u-blox antenna (category 3) for three different tilting scenarios: (a) without tilting, (b) with a 17° tilting and (c) with 35° tilting. The same structure is used for the Leica antenna (category 1) in the bottom row. For a better comparison, the maps from the Novatel antenna (category 2) are also depicted in the middle row for these scenarios. The tilting direction of all plots is towards North (heading angle of 0°) with a threshold of 2 m. Considering the non tilting scenarios, it is visible, that the u-blox antenna provides the most usable observations with 29571 in total, whereas the Leica provides 29141 and the Novatel 28645 usable observations. It is also evident, that most of the multipath affected observations are located in the West for all the antennas. By tilting the antenna to 17°, the number of usable observations decreases, but most for the u-blox antenna with a loss of 473 observations (Leica 23 and Novatel 59). A tilting of 35° leads to 28860 usable observations for the u-blox antenna, 28504 for the Novatel and 28941 for the Leica antenna. The usable observation areas are very similar for each of

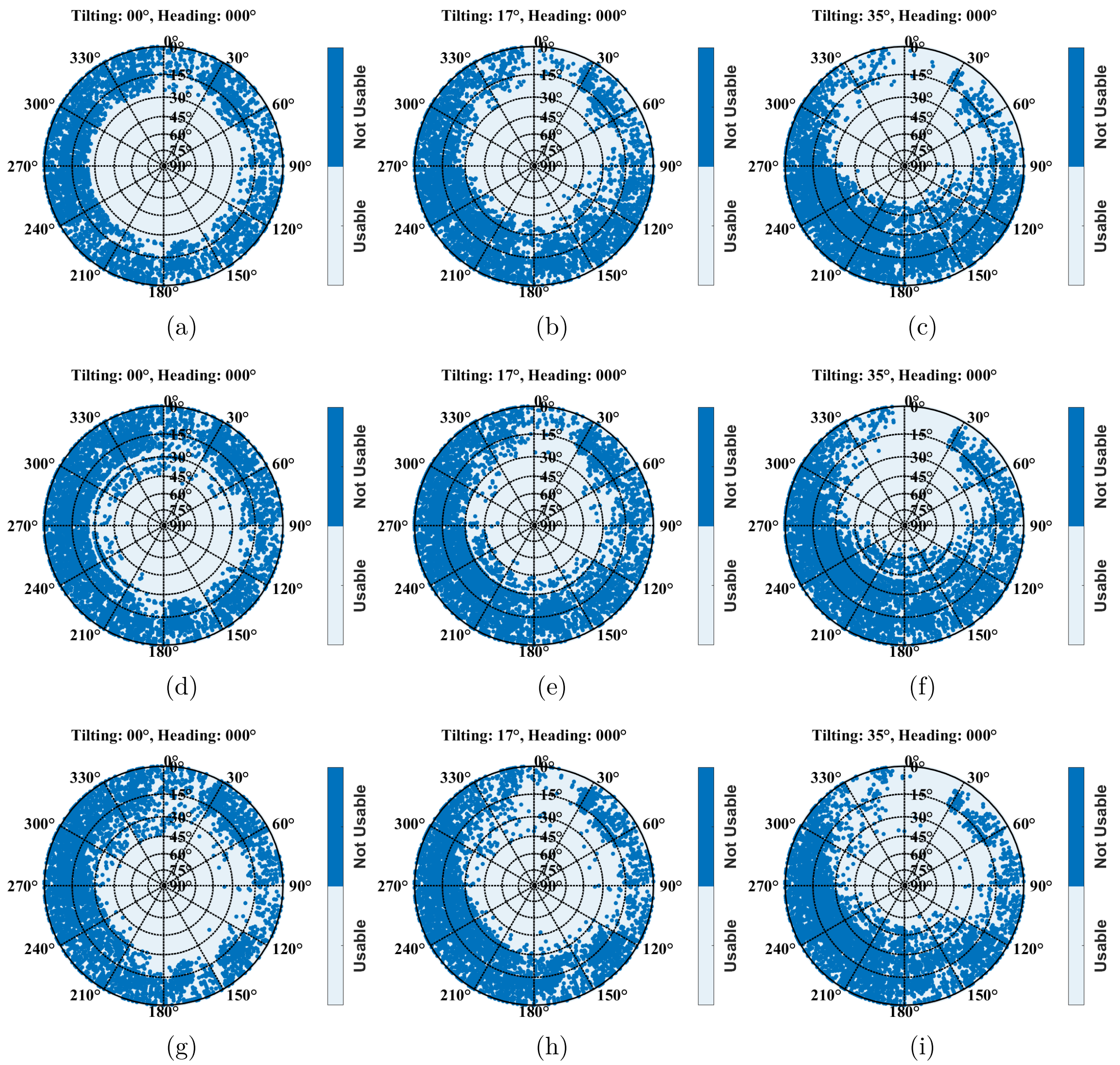

Figure 5.17: Multipath maps for three different antennas and tilting scenarios (2 m threshold). The top column represent the maps for the u-blox antenna, the second for Novatel and the last column for the Leica antenna. The tilting angle increase from left 0° to middle 17° and right 35° in North direction.

the antenna, however, with the better performance of the geodetic antennas in tilting scenarios. The overall loss of observations, due to tilting, is only 200 for the Leica and 141 for the Novatel antenna, which indicates a better multipath avoidance compared to the u-blox patch antenna, with a loss of 711 observations in total.

Each antenna is influenced by multipath affected observations, however, the geodetic antennas perform slightly better in tilting scenarios. The differences between the number of usable observations in different tilting or heading scenarios with different antennas are present, but relatively small. Approximately 80 % to 90 % of the observations can be used. Even if there are smaller differences between different antennas, the environment plays the major role on the behaviour of the multipath maps.

6

Estimation of Codephase Center Corrections

The previous chapters primarily focus on data acquisition and preprocessing for antenna calibration using a robot in the field with different methods and techniques, for example, to avoid multipath effects or reduce observation noise by optimizing the receiver settings. In this chapter, these preprocessed observations are used as inputs in the estimation process for estimating a CPC pattern.

Section 6.1 focuses on the elimination of problematic observations and how they impact the estimated CPC. Additionally, the hardware receiver settings are adjusted based on the proposed receiver tracking parameters from Section 4.4, determined with the software receiver. This allows the investigation of the CPC differences and repeatability compared to default receiver settings. Section 6.2 investigates the influence of the calibration duration on the estimation repeatability. In Section 6.3 the time differenced multipath linear combination, introduced in Section 3.3.3, is used as the input of the estimation approach. The resulting CPC, as well as their repeatability, are investigated. In Section 6.4, a signal strength dependent weighting is analysed, based on the study in Section 4.2. A validation of all the CPC, estimated using different methods, is carried out in Section 6.5. This is done by comparing them with CPC patterns estimated in an anechoic chamber and considering them in the observation and positioning domain.

6.1 Noise Reduction and Observation Elimination

When estimating CPC, observation noise is a crucial factor, because of a very poor pattern to noise ratio for codephase observations. Thus, for improving the repeatability of the calibration, the noise has to be reduced by maintaining the important pattern information. As the investigations in Chapter 5 already showed, multipath effects exist during the robot-based antenna calibration. However, by applying elevation masks and multipath maps, most of the multipath affected observations can be avoided. Section 6.1.1 shows, how these observations actual impact the estimated CPC. Additionally, some other techniques to avoid problematic observations are presented. Section 6.1.2 focuses on the optimization of the GNSS receiver settings, based on the studies in Chapter 4.

6.1.1 Elimination of problematic Observations

In the antenna calibration algorithm at IfE, several techniques are implemented to exclude observations that could affect the estimation of CPC. The majority of these problematic observations are due to multipath effects. However, by applying a dynamic elevation mask (DEM) in combination with a topocentric elevation mask (TEM) or multipath maps, almost all of these observations can be eliminated (cf. Chapter 5). Similar to other positioning approaches, like PPP, short satellite arcs can be eliminated to avoid e.g. short signal interruption, caused by obstacles in the robot surrounding or by the motion of the robot itself. Another crucial parameter is the time between robot resting phases. It is possible, that the robot stays in its pose for about 45 s, because the robot control software cannot provide the robot pose for the next phase. In this case, the robot restarts in its initial position and drives to the next resting pose. Consequently, the time gap in the ΔSD becomes large, which increases potential sources of errors. Therefore, observations separated by more than 6 seconds during the robot's resting phases are excluded from the estimation process. Additionally, an outlier detection is used, where each $\Delta SD > 4\,\mathrm{m}$ is eliminated, derived from the noise analysis in Figure 4.8, to ensure a stable estimation.

In Section 3.3.1 the *gnp.ane* file was introduced. Besides the robot module poses and their corrections, this file contains the start and end times of the phases during which the robot is at rest. The observations of the AUT and the reference antenna are aligned with these phases using their GPS timestamps. This alignment is achieved by identifying the start and end times of the robot's resting phase that include the observations. When using a 1 Hz sampling rate, it can happen that the observation is very close to the start or end of the resting phase. The hypothesis is that the tracking loop requires a certain amount of time to establish a locked state and can lose its tracking when the observations are close to the start of the resting phases. Figure 6.1 illustrates this time delay over the static robot phases for a standard calibration. It can be observed that there are several epochs very close to the beginning of these phases. Thus, the antenna calibration algorithm is able to eliminate all observations that fall below a chosen threshold, which will be 0.2 s for the following investigations.

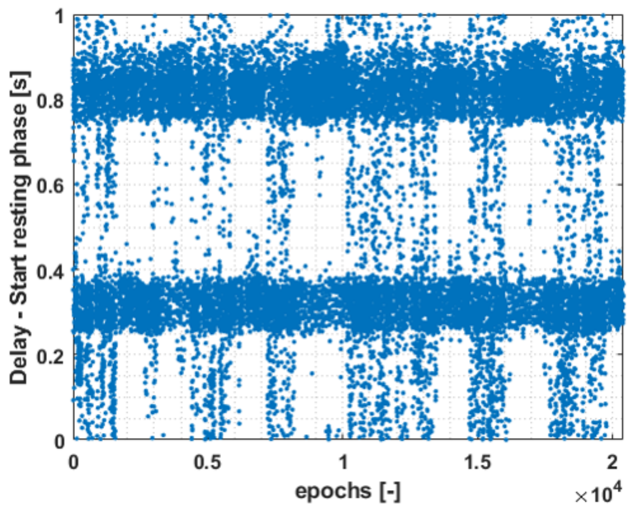

Figure 6.1: Delay between start of the robot resting phase and the actual observation.

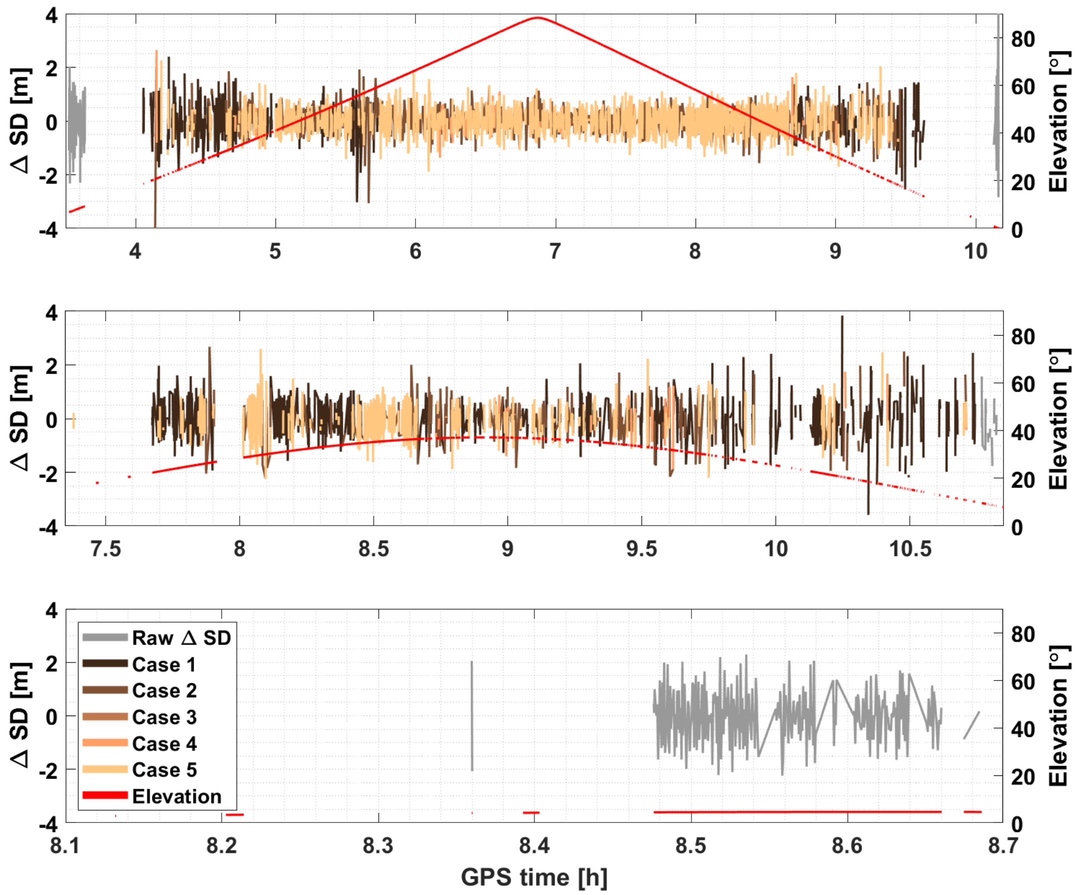

Figure 6.2: ΔSD after applying different strategies to eliminate problematic observations for GPS C1 signal and satellite PRN2 (top), PRN19 (middle) and PRN12 (bottom). Case 1: TEM (10°); Case 2: Case 1 + MP maps from DLR; Case 3: Case 2 + avoid ΔSD > 6 s; Case 4: Case 3 + avoid short satellite arcs < 20 epochs; Case 5: Case 4 + avoid static time delay < 0.2 s.

Figure 6.2 shows an example of the estimation inputs for three different GPS satellites, when using different elimination strategies. The calibration has been carried out on September, 20^{th} 2024 for a category 2 antenna with receiver default settings. The top subfigure presents the data for satellite PRN2, which has long visibility and high elevation over the calibration duration. The middle subfigure shows the ΔSD for a satellite (PRN19) in a mid to low elevation range, and the bottom subfigure is for a satellite with low elevation (PRN12). The elevation is depicted in red. Please note that elevation data is available even if there is no ΔSD data. This occurs especially at low elevation and is caused by the robot motion. ΔSD are only computed between consecutive epochs. If the robot tilts and rotates the antenna, making the satellite visible only every second epoch, then no ΔSD can be calculated. The raw ΔSD is shown in grey. This data would be used as estimation inputs if no TEM or other techniques are applied. However, a DEM is applied, but with a topocentric elevation

Table 6.1: Amount of ΔSD, when applying different elimination techniques.

Satellite	Raw ΔSD	Case 1	Case 2	Case 3	Case 4	Case 5
PRN2	4360	4185	3715	3161	3161	3014
PRN19	1894	1875	995	815	814	764
PRN12	266	0	0	0	0	0

cutoff angle of 0°. This is necessary to avoid satellite signal reaching the antenna from elevations less than 5° in the antenna system. Five different cases are defined:

1. Apply TEM (10°)
2. Apply TEM (10°) and MP maps from DLR
3. Apply TEM (10°), MP maps and avoid ΔSD > 6 s
4. Apply TEM (10°), MP maps and avoid ΔSD > 6 s and short satellite arcs < 20 epochs
5. Apply TEM (10°), MP maps and avoid ΔSD > 6 s, short satellite arcs < 20 epochs and static time delay < 0.2 s

It should be noted that the data from, for example, case 5 (beige) is also included in case 4 (orange). Therefore, the ΔSD after case 4 is represented by the combination of orange and beige ΔSD.

Obviously, the amount of observations decreases by applying more elimination techniques, as it is also visible in Table 6.1. By using a TEM, most of the observations at the end and the beginning of the observation arc are eliminated, as expected. For satellites at low elevations, all observations are eliminated, as shown in the bottom subfigure. When multipath maps are also used, observations even at higher elevations are removed, which can be seen, for example, around ≈ 5,6 h in the top subfigure (ΔSD in dark brown are eliminated when using case 2). For a satellite at low to mid elevation (middle subfigure), a significant number of observations (880) are affected by these maps, because even if the elevation is higher than the topocentric elevation mask, satellite signals can be affected by obstacles in the robot surrounding. Additionally, a higher

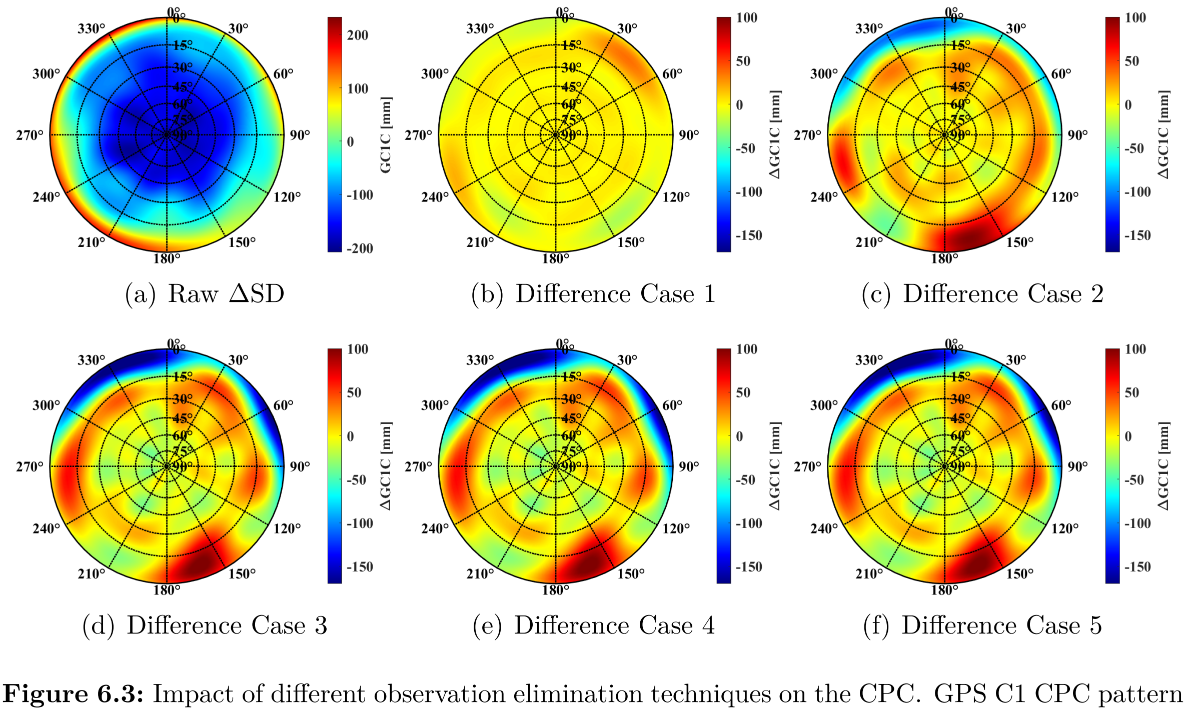

(a) Raw ΔSD (b) Difference Case 1 (c) Difference Case 2

(d) Difference Case 3 (e) Difference Case 4 (f) Difference Case 5

Figure 6.3: Impact of different observation elimination techniques on the CPC. GPS C1 CPC pattern with raw ΔSD are presented in (a), whereat the other plots show the differences to pattern (a) by applying different elimination techniques, defined as particular cases earlier.

number of observations are eliminated when avoiding all ΔSD generated between robot resting phases with a time gap higher than 6 s. The last two techniques are removing even more observations, so at the end 31 % of the observations are eliminated for PRN2, 60 % for PRN19 and 100 % for PRN12.

Figure 6.3 shows, how the different observation elimination techniques impact the GPS C1 CPC. The estimated pattern is based on the same calibration data as mentioned above, however for a calibration duration of 24 hours. Additionally, an outlier detection is used, where each $\Delta SD > 4\,m$ is eliminated, to ensure a stable estimation. Subfigure (a) shows the CPC pattern, when no additional observation elimination is applied. The following subfigures (b)-(f) show the difference pattern between (a) and the estimated pattern, when using different elimination techniques, as defined as particular cases earlier. When only a TEM with a cutoff of 10° is applied, the differences compared to a DEM with a topocentric cutoff angle of 0° reach up to 35 mm at low elevations. At higher elevations, these differences are minimal. Adding a multipath map increases the differences to up to 130 mm at low elevations. However, higher differences are observed at mid elevations. These differences become even higher when ΔSD with a time gap between epochs greater than 6 s are avoided. Further elimination techniques do not impact the estimated pattern, but they do reduce the number of observations.

This investigation demonstrates that problematic observations significantly impact the estimation of CPC, particularly signals from satellite at low elevations, which are often affected by multipath. To ensure accurate estimation of the antenna pattern, a DEM combined with a TEM (10° cutoff) and multipath maps should be used, and observations with time gaps greater than 6 s should be avoided. Short satellite arcs have no significant impact, as most of these signals have already been eliminated by other techniques. Furthermore, it does not matter whether the observation occurs at the beginning or end of the robot's resting phase. The tracking loops can maintain stable tracking even immediately after the robot has been at rest. However, these results should be taken with care, because the receivers operated with the manufacturer's default settings, which are not optimized for antenna calibration (cf. Section 4.4). GNSS signals received from low elevation satellites are generally noisier than those from the zenith due to multipath effects, among other factors. These noisy signals are reduced when a TEM or multipath maps are applied. As a result, the estimated pattern differences between raw ΔSD and case 2 are quite large. When the receiver settings are optimized to reduce the ΔSD noise, the impact of using this elimination technique is reduced compared to using default receiver settings. A detailed comparison between both scenarios is provided in the next section.

6.1.2 Noise Reduction by adapted Receiver Settings

The investigations in Section 4.4 have shown that a smaller DLL bandwidth in an aided DLL with a filter order of 1 results in a less noisy ΔSD in a software receiver. In this section, the proposed settings are adopted to hardware receivers. Thus, a calibration of a category 2 antenna (NOV703GGG.R2) has been carried out over four full days from September, 20^{th} to 23^{th} 2024. The AUT has been connected to a Javad Delta TRE G3T receiver, operating with default settings (cf. Table 4.2), and to a Javad DeltaS-3S receiver with a modified DLL bandwidth of 1 Hz. The reference antenna is

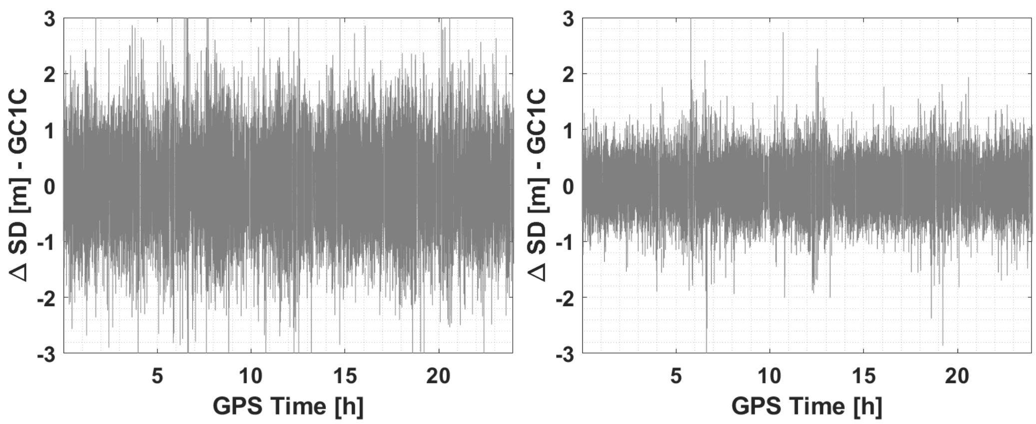

Figure 6.4: ΔSD of a 24-hour calibration for a category 2 antenna with default (left) and optimized receiver settings (right).

connected to two other receivers that are identical in construction to those connected to the AUT. However, the Javad DeltaS-3S operates with a DLL bandwidth of 0.5 Hz. Additionally, each of them are connected to an external frequency standard. This zero baseline approach allows for a direct comparison between the default and optimized receiver settings. The settings were selected based on the results from Section 4.4, where they are described in more detail. Here, the results for the category 2 antenna will be discussed, however, similar experiments have been carried out for the category 1 and 3 antennas. The estimated CPC for these antennas can be found in Figure 6.22 and 6.23 in Section 6.5.1, where they are compared to the CPC, estimated in an anechoic chamber. The estimation inputs are generated using case 4, defined in the previous Section 6.1.1.

Figure 6.4 shows the ΔSD for the GPS C1 signal on the first calibration day for all visible satellites, using both default and optimized receiver settings. It is evident, that the noise of the ΔSD can be decreased by optimizing the receiver settings. This gains clarity, when calculating the weighted averaged standard deviation based on Equation 4.10 over all satellites for both cases. It decreases from 0.530 m to 0.306 m, which corresponds to an improvement of 42 %.

The ΔSD from the four calibration days, hereinafter referred to as P1 to P4, are used to estimate the corresponding CPC pattern. The mean patterns for both default and optimized receiver settings for the GPS C1 and C5 signals, as well as the Galileo C1 and C5 signals, are presented in Figure 6.5. The overall behaviour of both receiver settings are very similar, however, the patterns with default settings show more deviations at the antenna's horizon. Additionally, a higher magnitude of the patterns using receiver default settings is evident. The patterns estimated with optimized receiver settings exhibit a smoother behaviour at low elevations, especially for the Galileo C1 and C5 signal.

The repeatability of the calibration is depicted in Figure 6.6 presented as a so called NOAZI presentation. For that, only the elevation dependent antenna pattern is considered. Usually, all CPC in one elevation bin are averaged to calculate the NOAZI. This presentation can be used for antennas that exhibit a more azimuthal pattern behaviour, rather than a pattern with significant azimuthal variations. The left subfigures show the results for the patterns estimated with default receiver settings, whereat the right

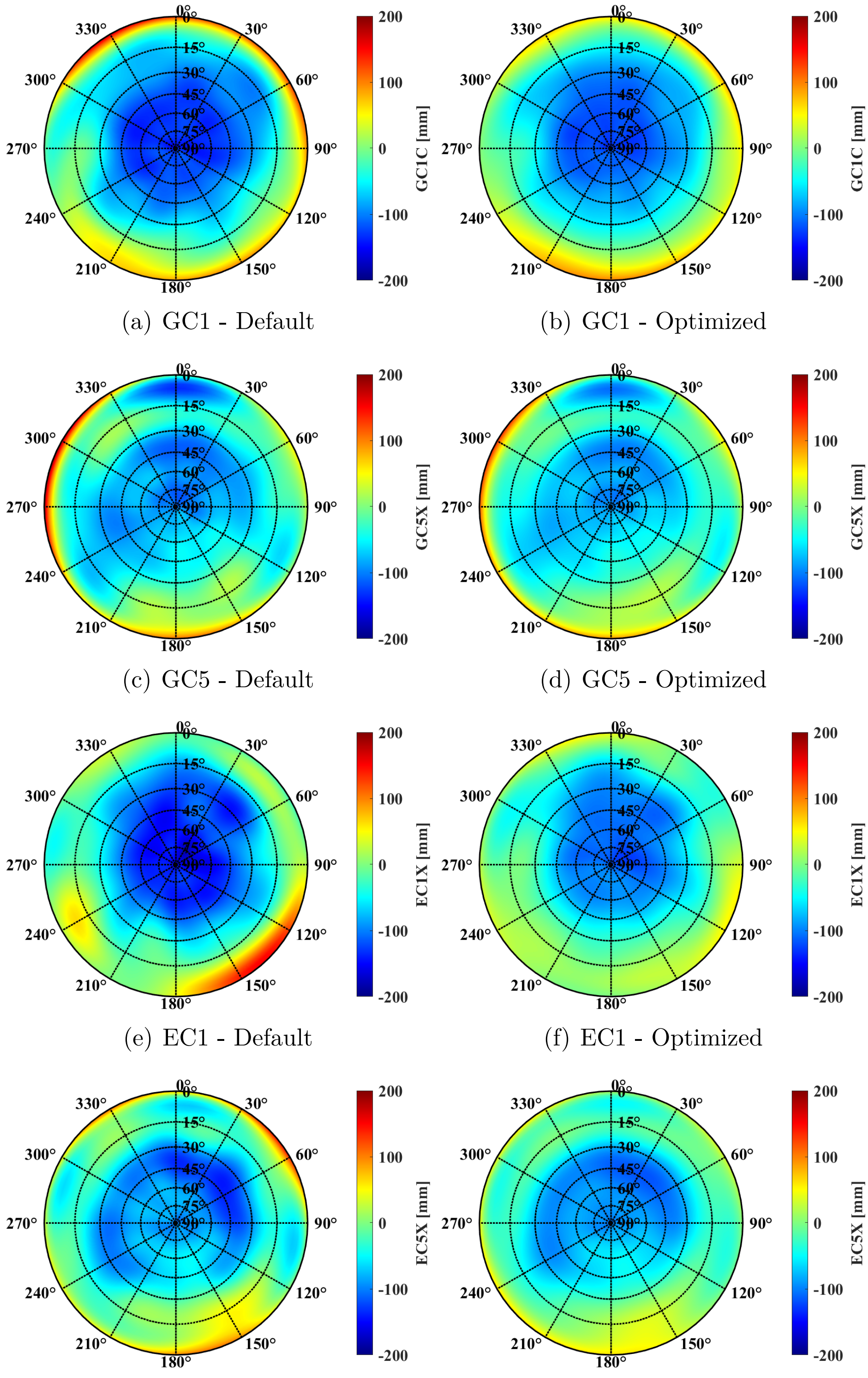

(a) GC1 - Default (b) GC1 - Optimized

(c) GC5 - Default (d) GC5 - Optimized

(e) EC1 - Default (f) EC1 - Optimized

(g) EC5 - Default (h) EC5 - Optimized

Figure 6.5: Estimated Mean CPC pattern for GPS C1 (a, b), C5 (c, d), Galileo C1 (e, f) and C5 (g, h) calibrated with default (left) and optimized (right) receiver settings. The pattern is calculated from four 24-hours calibrations on consecutive days for a category 2 antenna.

figures presented the results with optimized settings for the GPS and Galileo C1 and C5 signals. The NOAZI pattern is related to the NOAZI of the mean pattern, as depicted

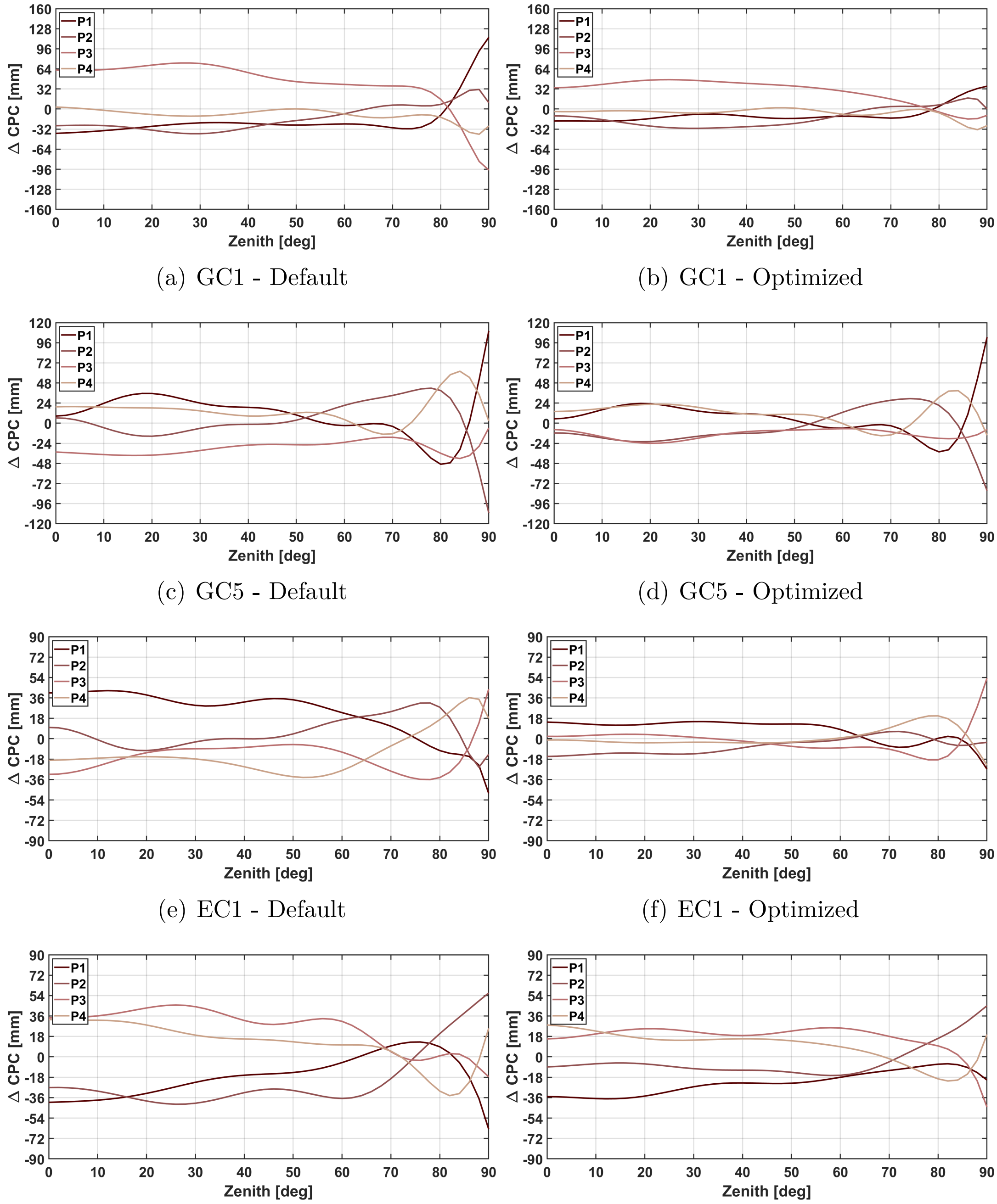

(a) GC1 - Default (b) GC1 - Optimized

(c) GC5 - Default (d) GC5 - Optimized

(e) EC1 - Default (f) EC1 - Optimized

(g) EC5 - Default (h) EC5 - Optimized

Figure 6.6: Comparison w.r.t to type mean CPC pattern for GPS C1 (a, b), C5 (c, d), Galileo C1 (e, f), C5 (g, h). The elevation dependent pattern (NOAZI) is presented, calibrated with default (left) and optimized (right) receiver settings. P1 to P4 are 24-hours calibrations on consecutive days for a category 2 antenna.

in Figure 6.5. The calibrations with optimized settings exhibit less scattering compared to the pattern estimated with default settings for all GNSS signals across all elevations.

In summary, by optimizing the receiver settings, a more repeatable pattern can be achieved. The pattern behaviour can be maintained with a smaller CPC magnitude, by reducing the DLL bandwidth for both the AUT receiver and the reference antenna receiver. The bandwidth of the reference receiver is set to 0.5 Hz, resulting in the best noise performance based on the investigations in Section 4.4. A bandwidth of 1 Hz is selected for the AUT, due to the dynamics of the robot motion. This bandwidth is a trade-off to ensure stable tracking while minimizing the noise of the observations.

6.2 Impact of the Calibration Duration on the Repeatability

The previous section presented the calibration results from a category 2 antenna using both default and optimized receiver settings during a calibration conducted over four consecutive days. Here, the same experiment with the same parameters is analysed, however, the four days are separated into 6-hours and 12-hours sets to analyse the impact of the calibration duration on the estimated CPC pattern. Thus, the ΔSD observed during these intervals are used to estimate the CPC. For clarity, only the GPS C1 signal is presented. In total, 16 different 6-hour sets are defined, with four sets for each calibration day: 0:00 to 6:00 GPS time, 6:00 to 12:00, 12:00 to 18:00 and 18:00 to midnight. For the 12-hour sets, two sets on each calibration day are defined: 0:00 to 12:00 and 12:00 to 24:00 GPS time.

In Figure 6.7 the repeatability of both approaches is depicted, whereas the top subfigures show the results of the 6-hour sets and in the bottom the results of the 12-hour sets are presented. On the other hand, the left subfigures present the NOAZI pattern differences to the calculated mean pattern estimated with default receiver settings and the right figures when using optimized settings. Similar to Figure 6.6, the different estimates scatter more, when using the default settings. It is evident, that this scattering

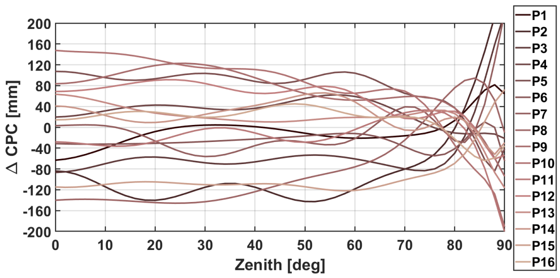

(a) 6 hours - Default

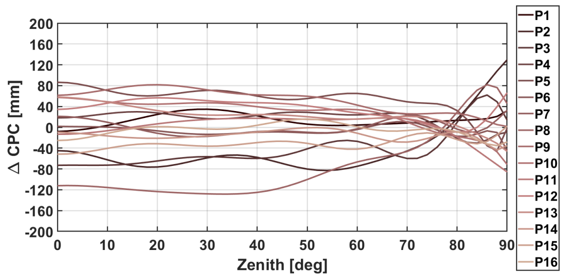

(b) 6 hours - Optimized

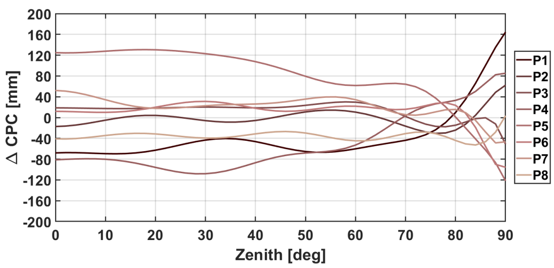

(c) 12 hours - Default

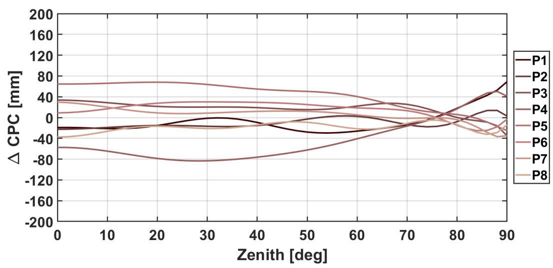

(d) 12 hours - Optimized

Figure 6.7: Comparison w.r.t to type mean CPC pattern for GPS C1. The elevation dependent pattern (NOAZI) is presented, calibrated with default (left) and optimized (right) receiver settings. All 6-hour calibration sets are presented in (a), (b) and 12-hour in (c), (d) extracted from P1 to P4.

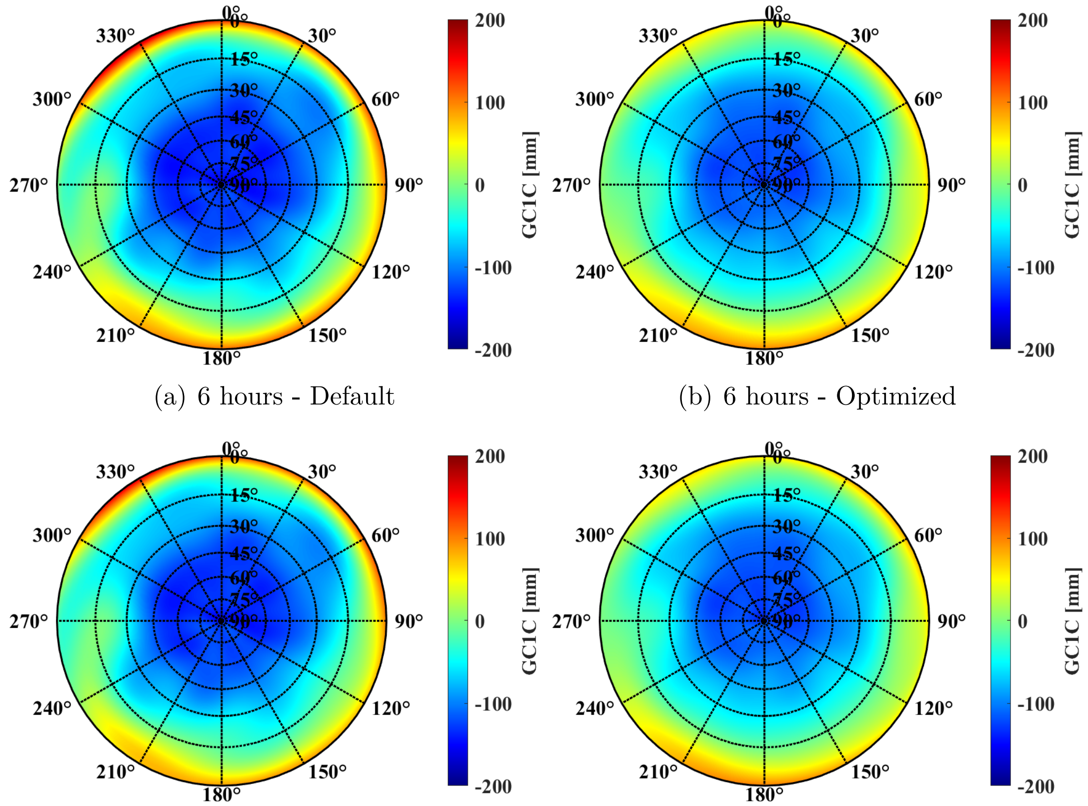

(a) 6 hours - Default
(b) 6 hours - Optimized
(c) 12 hours - Default
(d) 12 hours - Optimized

Figure 6.8: Estimated Mean CPC pattern for GPS C1 calibrated with default (left) and optimized (right) receiver settings. The pattern is calculated from all 6-hour calibration (a), (b) and 12-hour in (c), d) extracted from P1 to P4.

for both settings gets larger, when decreasing the calibration duration. By increasing the calibration duration, the repeatability is improved.

The NOAZI patterns in Figure 6.7 are presented w.r.t. the calculated mean pattern, which are presented in Figure 6.8. Even if the repeatability of the 6-hour sets are poor, the calculated mean pattern are almost identical to those from the 12-hour sets or the 24-hour sets (cf. Figure 6.5). Consequently, it does not make a difference, whether the NES (cf. Section 3.3.3) considers the entire calibration duration or averages the estimated CPC from individual time segments at the pattern layer, as expected due to the linearity of the adjustment problem. A similar difference between both receiver settings can be observed. The investigation shows, that a longer calibration duration stabilizes the estimated CPC.

This gets clearer, when the individual pattern, estimated with the 6-hour sets, are considered. Figure 6.9 shows the estimated CPC of the sets from three calibration days P2 (left) to P4 (right) when using optimized receiver settings. It is evident, that the CPC differs, especially the CPC depicted in (j). Additionally, no significant similarities can be seen between the same sets on different days. Therefore, the differences are not caused by the satellite constellation. The sidereal repetition of GPS satellites is assumed to have no impact on the CPC pattern, as only a marginal number of observation epochs differ over these three days. However, the receiving point on the antenna hemisphere differs,

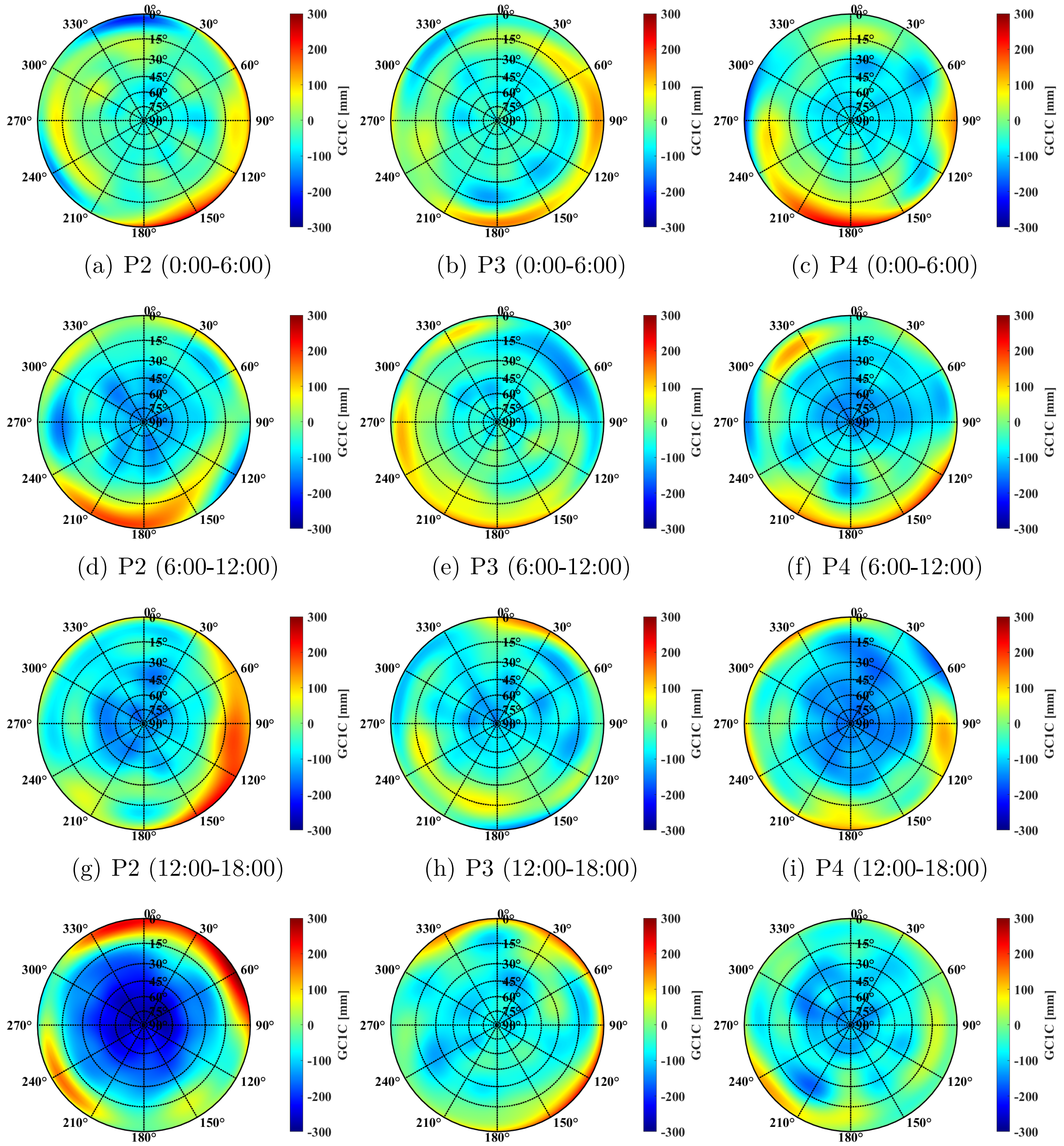

(a) P2 (0:00-6:00) (b) P3 (0:00-6:00) (c) P4 (0:00-6:00)

(d) P2 (6:00-12:00) (e) P3 (6:00-12:00) (f) P4 (6:00-12:00)

(g) P2 (12:00-18:00) (h) P3 (12:00-18:00) (i) P4 (12:00-18:00)

(j) P2 (18:00-24:00) (k) P3 (18:00-24:00) (l) P4 (18:00-24:00)

Figure 6.9: Estimated individual CPC pattern for GPS C1 calibrated with optimized receiver settings in 6-hour intervals extracted from P2 (left), P3 (middle) and P4 (right).

because the robot motion during each set is not the same. Consequently, the distribution on the antenna hemisphere differs as well, which results in different estimation outcomes.

To overcome this, the robot motion must have the same pose at the same satellite constellation. As mentioned in Chapter 3, the robot motion is controlled by the software from the *Geo++* company, which moves the robot as long as the standard deviation of their estimation approach achieves a particular value. The robot motion differs from set to set. This motion could be optimized to maximize the number of usable observations in order to improve the repeatability and accuracy of the estimated CPC pattern. A possible approach to achieve this is proposed here.

First, a detailed investigation into the relation between the robot poses, the estimated CPC, and the actual satellite constellation should be conducted. This involves determining which robot motions are necessary to obtain the most valuable pattern information from a specific satellite observable between two robot poses. Additionally, the robot motions should be adjusted for each visible satellite within these two phases to maximize the pattern information obtained from each satellite. Subsequently, this process should be repeated for a specific calibration duration, for example, 4 hours. Once the optimal robot poses are determined, the robot module angles can be calculated for each pose throughout the calibration period to set up the inputs for the robot control software. Given that these poses are optimized for a specific satellite constellation, the approach must either operate in real-time with the actual satellite constellation or in pre-processing using predictions of the constellation. A significant challenge is to estimate multi-GNSS, due to the optimization of poses for a particular GNSS. Another challenge lies in handling various types of antennas, as each antenna has its unique pattern, requiring different robot poses even with the same satellite constellation.

6.3 Alternative CPC Estimation based on Time differenced MPLC

When using ΔSD as estimation inputs, two differencing steps are performed, each increasing the noise of the GNSS observables. The use of ΔMPLC eliminates one of these differencing steps, thereby avoiding the corresponding noise increase. The method for calculating ΔMPLC within the antenna calibration algorithm has been introduced in Section 3.3.3. The MPLC can be calculated with Equation 3.38.

Because this LC is a combination of codephase and carrierphase observations, a differential PCC and PWU between the two carrierphase observations remains in the MPLC, which can be calculated with Equation 3.40 and Equation 3.41, respectively. These corrections are exemplarily presented for GPS satellite PRN18 in Figure 6.10 during a calibration of a category 2 antenna. It should be noted that the investigations in this section are based on the same calibrations used for the analyses in Section 6.1.2,

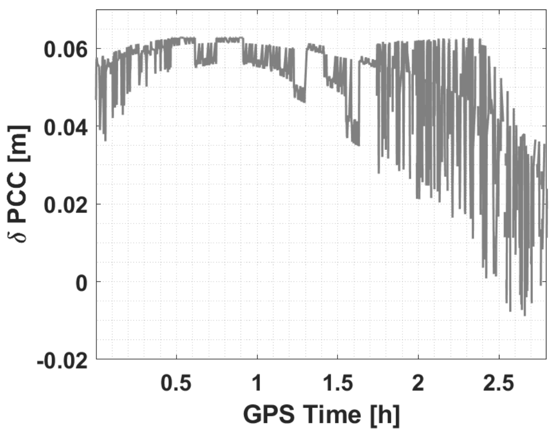

(a) Remaining PCC

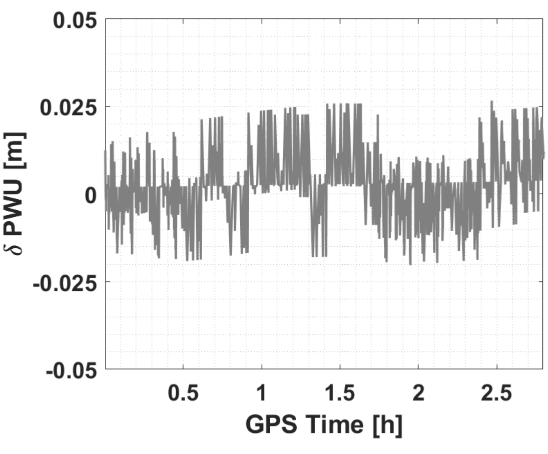

(b) Remaining PWU

Figure 6.10: Corrections applied to MPLC for GPS satellite PRN18.

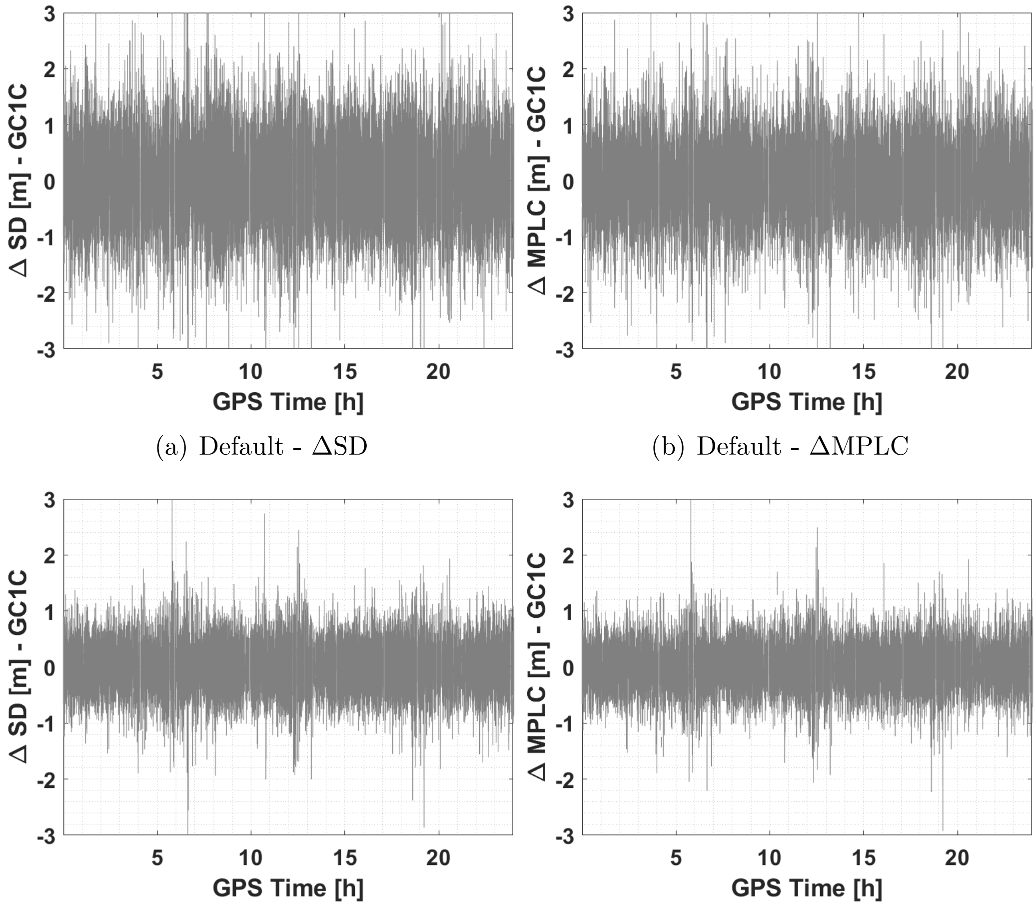

(a) Default - ΔSD (b) Default - ΔMPLC

(c) Optimized - ΔSD (d) Optimized - ΔMPLC

Figure 6.11: ΔSD (left) and ΔMPLC (right) of a 24-hour calibration for a category 2 antenna with default (top) and optimized receiver settings (bottom).

specifically the 24-hour calibrations for a category 2 antenna (NOV703GGG.R2) on September, 20^{th} to 23 th 2024. Compared to the codephase noise, even with optimized receiver settings, the magnitude of these corrections is relatively small with approximately 6 cm for δPCC and 2.5 cm for δPWU. Furthermore, the influence of these effects is further minimized by using time differenced MPLC as the observable. However, multipath effects are still included in the LC. The remaining multipath effects in the MPLC are assumed to be eliminated by applying the multipath maps, described in Section 5.3.

Figure 6.11 shows the ΔMPLC of the GPS C1 signal, calculated with the carrierphase observations L1 and L2 in the right subfigures with default (b) and optimized receiver settings (d). For comparison, the left subfigures show the same calibration data, when using ΔSD. In order to study the noise behaviour of the observables, the weighted averaged standard deviation (Equation 4.10) is calculated. The standard deviation is decreased for the ΔMPLC (σ_{ant}=0.447 m) compared to ΔSD (σ_{ant}=0.530 m) using default receiver settings. For optimized receiver settings, the standard deviation of ΔMPLC is σ_{ant}=0.271 m and for ΔSD σ_{ant}=0.306 m. The observations are preprocessed with case 4, defined in Section 6.1.1. A multipath map with a threshold of 1.5 m is applied to calculate the ΔMPLC. This demonstrates that ΔMPLC exhibits a smaller noise magnitude than ΔSD, especially when using default receiver settings.

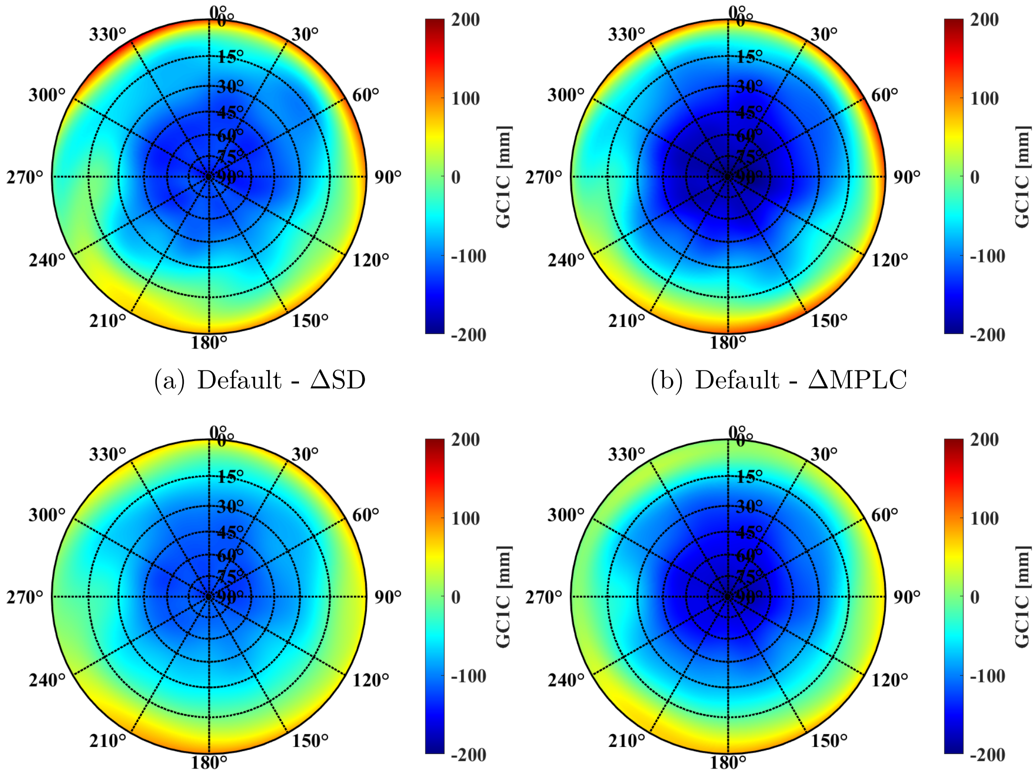

(a) Default - ΔSD (b) Default - ΔMPLC

(c) Optimized - ΔSD (d) Optimized - ΔMPLC

Figure 6.12: Estimated mean pattern of GPS C1, calibrated with default (top) and optimized (bottom) receiver settings with ΔSD as estimation inputs (left) and ΔMPLC (right) with multipath map threshold of 1.5 m.

The ΔMPLC is used to estimate the CPC pattern of the category 2 antenna of the four calibration days. The estimated mean pattern is shown in Figure 6.12 and 6.13 with default (b) and optimized settings (d). For comparison, the pattern estimated with ΔSD is shown in (a) and (c), respectively. For clarity, only the GPS C1 and the Galileo C1 signal is presented. The results for the GPS C5 and the Galileo C5 signals are depicted in Appendix A.2. Both C5 MPLC are calculated with the codephase signal C5 and the carrierphase signals L1 and L5.

When comparing the estimated pattern using ΔMPLC with the ΔSD pattern, it becomes evident that the pattern behaviour differs for the GPS C1 signal (cf. Figure 6.12). The CPC magnitude at the zenith down to elevations of approximately 15° to 30° is higher compared to the ΔSD pattern. This holds true for both default and optimized receiver settings. The reason are the differences in the estimated CCO. For example, the estimated CCO Up component using ΔMPLC as estimation inputs and optimized receiver settings is 18.1 cm, whereas the Up component using ΔSD is 12.5 cm. The difference of 5.6 cm corresponds to the differences in the estimated pattern. Please note, that the CCO is added with a negative sign in the CPC calculation (cf. Equation 3.2). Additionally, the CPC magnitude of particular regions at low elevations becomes smaller, when ΔMPLC are used as estimation inputs. This is evident, for example, with optimized receiver settings at an azimuth of approximately 180 deg as shown in Figure 6.12 (c, d). Similar results are evident for the Galileo C1 signal in Figure 6.13,

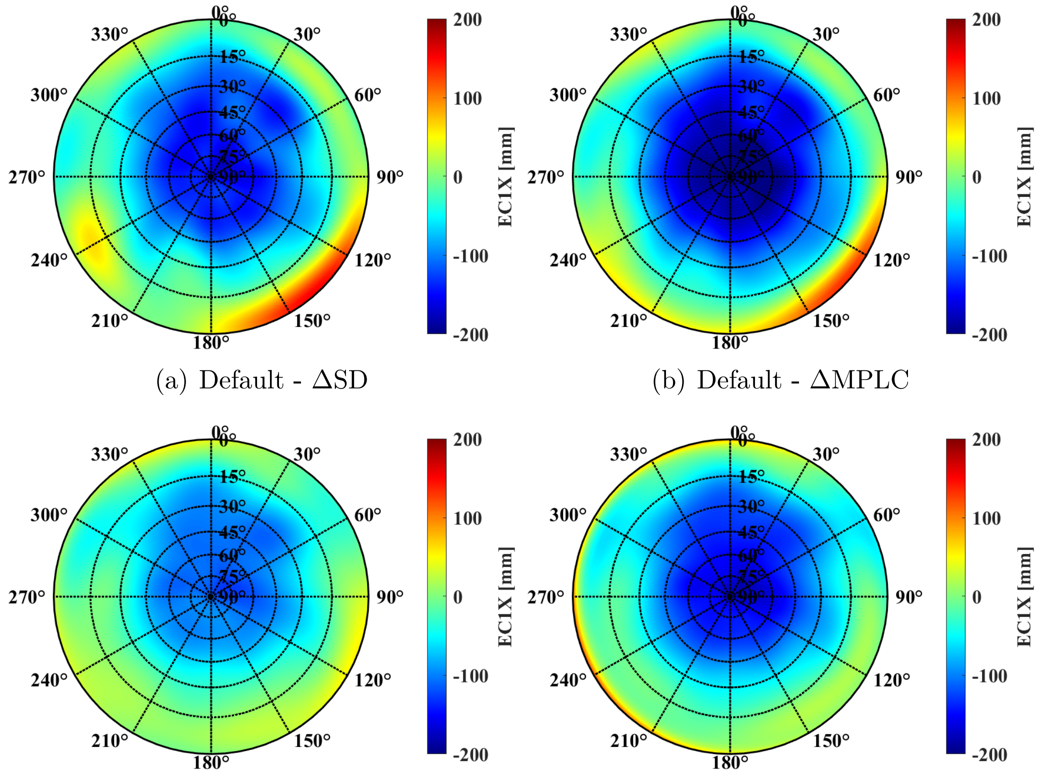

(a) Default - ΔSD (b) Default - ΔMPLC

(c) Optimized - ΔSD (d) Optimized - ΔMPLC

Figure 6.13: Estimated mean pattern of Galileo C1, calibrated with default (top) and optimized (bottom) receiver settings with ΔSD as estimation inputs (left) and ΔMPLC (right) with multipath map threshold of 1.5 m.

however, the differences in the pattern behaviour are smaller compared to the GPS C1 signal.

The repeatability of the four 24-hour calibrations are depicted in Figure 6.14 for the GPS C1 and in Figure 6.15 for the Galileo C1 signal. The structure is the same as depicted in the previous figures. The top row presents the results using default receiver settings, while the bottom subfigures show the repeatability with optimized receiver settings. The CPC pattern of the different calibrations P1 to P4 are presented as a NOAZI representation w.r.t. the mean pattern.

It is evident, that the repeatability is very similar between both approaches with a slightly better performance using the ΔSD approach for the GPS C1 signal with both, default and optimized receiver settings. An improvement by using the ΔMPLC is visible for the Galileo C1 signal, especially when using default receiver settings. Similar results are evident for the GPS C5 (cf. Figure A.4 and A.5) and Galileo C5 signal (cf. Figure A.6 and A.7) in Appendix A.2.

The patterns, estimated with ΔMPLC, are based on a multipath map with a threshold of 1.5 m. Figure 6.16 shows the patterns and their repeatability, when using ΔMPLC with different multipath map thresholds. For clarity, only the Galileo C1 signal is presented with optimized receiver settings. The mean patterns are presented in the left subfigures, with their corresponding NOAZI presentation in the right. The subfigures

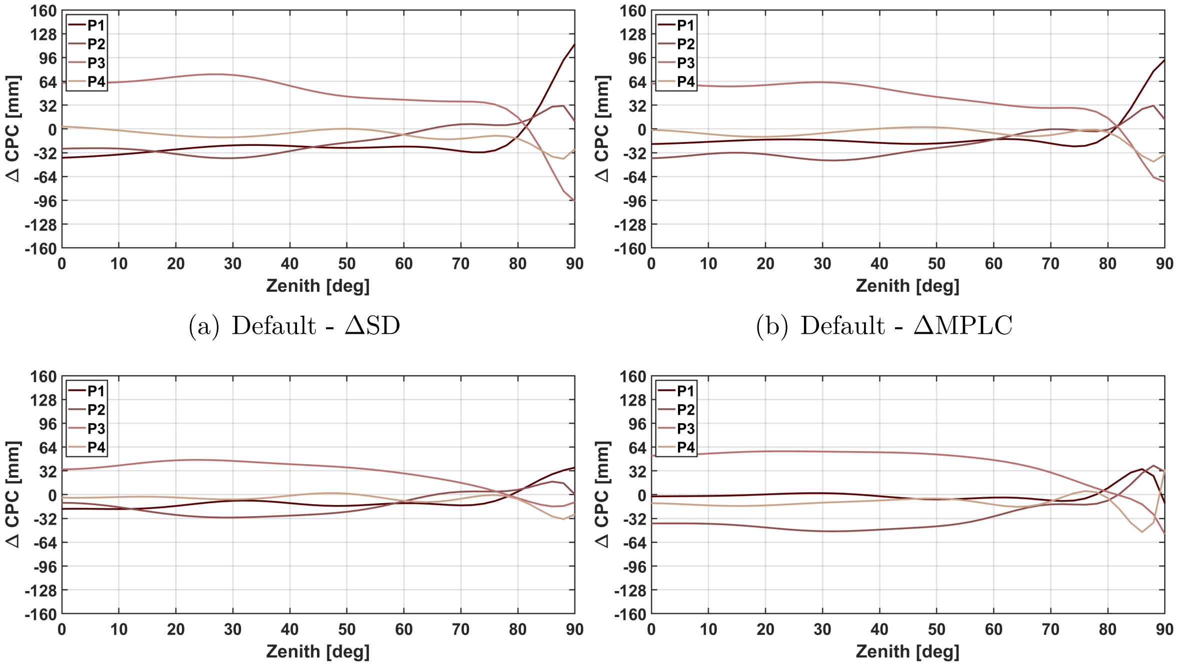

(a) Default - ΔSD (b) Default - ΔMPLC

(c) Optimized - ΔSD (d) Optimized - ΔMPLC

Figure 6.14: Comparison w.r.t to mean CPC pattern for GPS C1. The elevation dependent pattern (NOAZI) is presented, calibrated with default (top) and optimized (bottom) receiver settings with ΔSD as estimation inputs (left) and ΔMPLC (right) with multipath map threshold of 1.5 m.

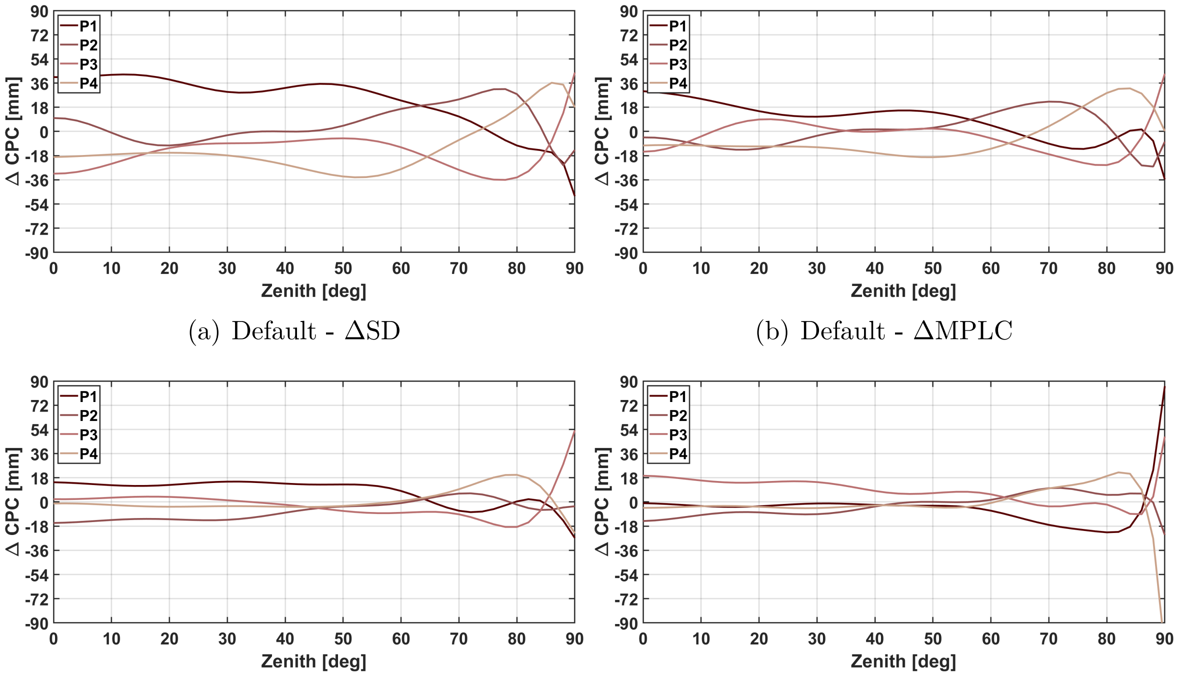

(a) Default - ΔSD (b) Default - ΔMPLC

(c) Optimized - ΔSD (d) Optimized - ΔMPLC

Figure 6.15: Comparison w.r.t to mean CPC pattern for Galileo C1. The elevation dependent pattern (NOAZI) is presented, calibrated with default (top) and optimized (bottom) receiver settings with ΔSD as estimation inputs (left) and ΔMPLC (right) with multipath map threshold of 1.5 m.

(a) and (b) depict the results with a multipath threshold of 1 m, (c) and (d) with 1.5 m and (e) and (f) with a 2 m multipath map threshold.

The estimated mean patterns are very similar for all three thresholds with only slight deviations noticeable, for example, at 300° azimuth. However, the repeatability improves when a higher multipath map threshold is selected. This can be explained by the number of observations. When the threshold is set very low, more observations are identified as being affected by multipath and are therefore eliminated during the antenna calibration process. Consequently, fewer observations are used in the estimation process, which degrades the CPC repeatability.

In summary, the ΔMPLC observables exhibit lower noise compared to ΔSD, especially when using default receiver settings. This leads to different CPC, where the magnitude of the CPC using ΔMPLC as estimation inputs exhibit a higher magnitude,

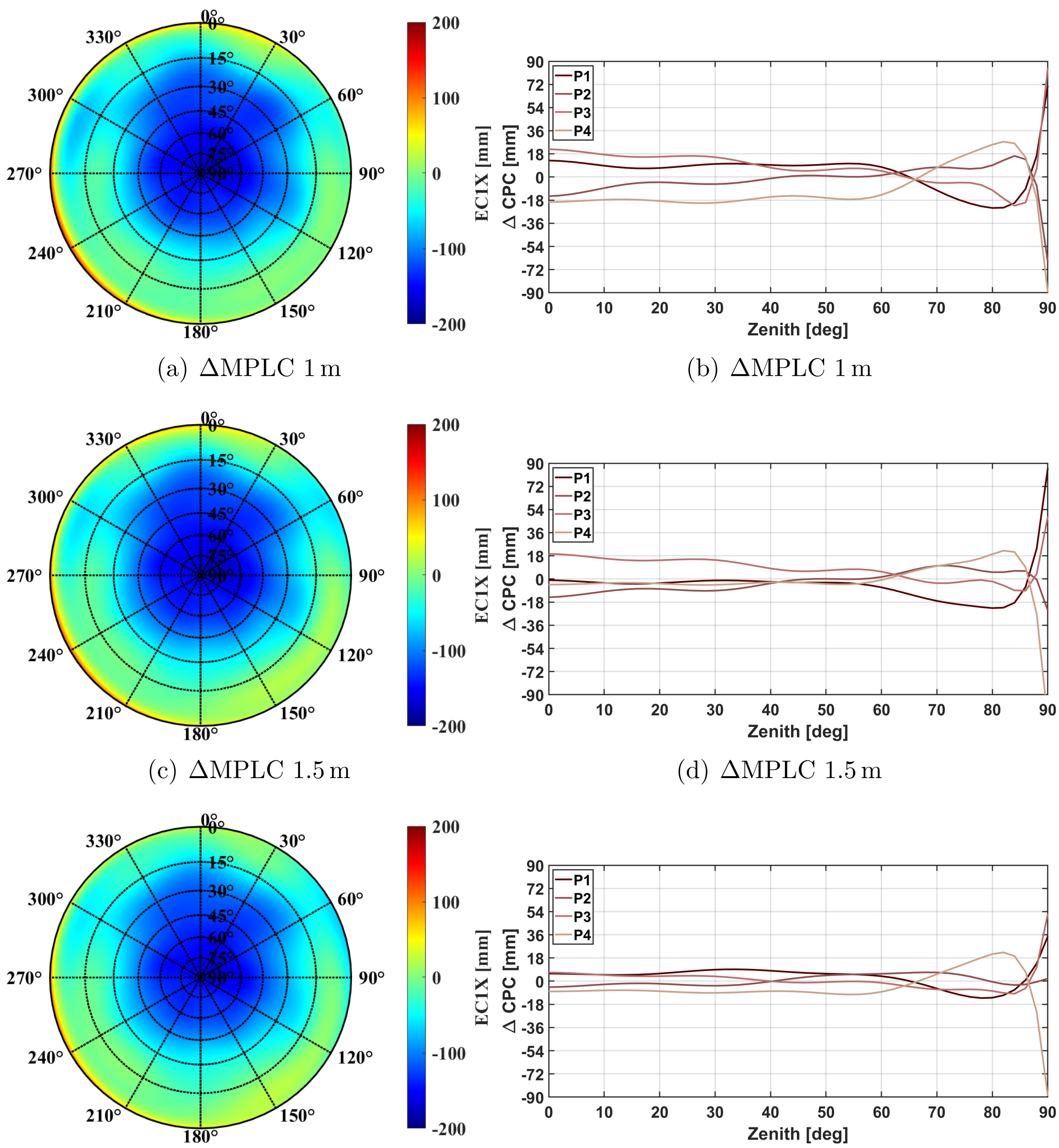

(a) ΔMPLC 1 m (b) ΔMPLC 1 m

(c) ΔMPLC 1.5 m (d) ΔMPLC 1.5 m

(e) ΔMPLC 2 m (f) ΔMPLC 2 m

Figure 6.16: Estimated mean pattern (left) and the corresponding NOAZI repeatability (right) of Galileo C1, calibrated with optimized receiver settings with ΔMPLC as estimation inputs. Multipath map thresholds of 1 m (a, b), 1.5 m (c, d) and 2 m (e, f) are applied.

mostly caused by the difference in the CCO. Even with reduced observation noise, the repeatability remains quite similar between both methods when a multipath map threshold of 1.5 m is used. However, this threshold also impacts the repeatability of the estimation. In Section 6.5, a validation of both approaches is carried out to assess the accuracy of the CPC using ΔSD and ΔMPLC.

6.4 CPC Estimation based on Signal Strength dependent Weighting

All previous CPC estimates in this thesis are based on a unit weighting. The analysis in Section 4.2.1 showed, that the noise behaviour of real calibration data are highly correlated with the signal strength. A modified model has been introduced, based on the approach from de Bakker et al. (2009), which effectively represents the ΔSD noise and can be calculated with Equation 4.6 and 4.7. To enhance understanding of the weighting approach, both equations are presented again here:

$$\bar{\sigma}^2_{C/N_0} = \sigma^2_{AUT}(t_{i+1}) + \sigma^2_{AUT}(t_i) + \sigma^2_{Ref}(t_{i+1}) + \sigma^2_{Ref}(t_i) \ [\mathrm{m}^2] \tag{6.1}$$

with

$$\begin{aligned} \sigma_{Ref} &= \sqrt{a \cdot 10^{-\frac{C/N_0}{10}}} \ [\mathrm{m}] \\ \sigma_{AUT} &= \sqrt{b \cdot 10^{-\frac{C/N_0}{10}}} \ [\mathrm{m}]. \end{aligned} \tag{6.2}$$

This model was used in Section 4.3 to study a C/N_0 dependent noise on the estimated antenna pattern in a simulation approach.

Another approach is to use the model in the estimation process described in Section 3.3.3 to weight the observations based on their signal strength. Observations with low signal strength are assigned lower weights in the weighting matrix P. Thus, $\bar{\sigma}^2_{C/N_0}$ are

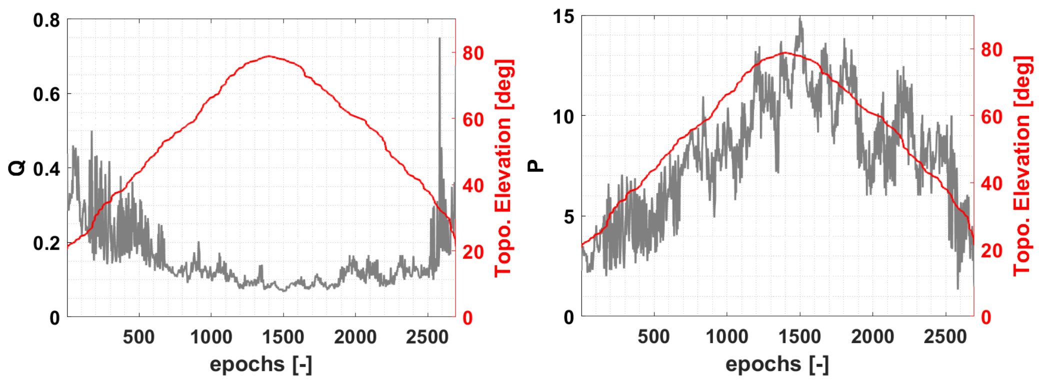

Figure 6.17: Example of the diagonal elements of the cofactor matrix Q (left) and weighting matrix P (right) for GPS satellite PRN1 during a calibration of a category 1 antenna using optimized receiver settings and a C/N_0 dependent weighting for the GPS C1 signal.

inserted in the cofactor matrix Q for each satellite k:

$$Q_k = \sigma_0^2 \cdot \begin{bmatrix} \bar{\sigma}^2_{C/N_0}(t_1) & 0 & \cdots & 0 \\ 0 & \bar{\sigma}^2_{C/N_0}(t_2) & \cdots & 0 \\ \vdots & \vdots & \ddots & \vdots \\ 0 & 0 & \cdots & \bar{\sigma}^2_{C/N_0}(t_n) \end{bmatrix} \tag{6.3}$$

and

$$P_k = inv(Q_k). \tag{6.4}$$

Figure 6.17 shows, exemplarily for the GPS C1 signal, how the cofactor and weighting matrix behave within a calibration of a category 1 antenna using a C/N_0 dependent weighting. It is evident that satellite signals near the horizon are down weighted. Additionally, some observations at higher elevations are also assigned lower weights due to the robot poses, where signals at low elevations in the antenna frame experience reduced signal strength, even if they are at a higher elevation in the topocentric frame.

This weighting matrix is used to estimate CPC for two different antennas, a category 1 (LEIAR25.R3) and a category 3 antenna (u-blox ANN-MB1). Each antenna has been calibrated over two full days on 15^{th} and 16^{th}, June 2024 for the category 1 antenna and on the 13^{th} and 14^{th}, July 2024 for the category 3 antenna, respectively. For the pattern estimation, ΔSD are used as estimation inputs.

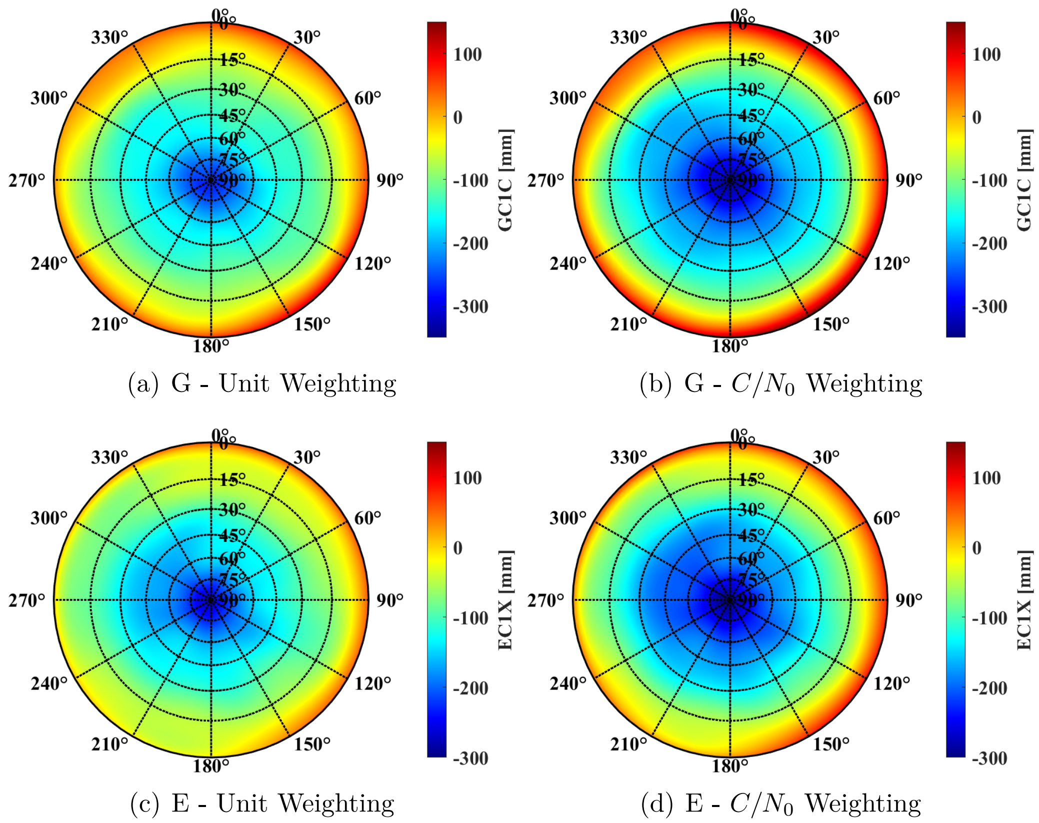

(a) G - Unit Weighting (b) G - C/N_0 Weighting

(c) E - Unit Weighting (d) E - C/N_0 Weighting

Figure 6.18: Mean CPC pattern of the category 1 antenna for GPS C1 (top) and Galileo C1 signal (bottom). Subfigure (a) and (c) presented the results using a unit weighting, whereas (b) and (d) shows the pattern when using a C/N_0 dependent weighting. Optimized receiver settings are used with a multipath map threshold of 2 m.

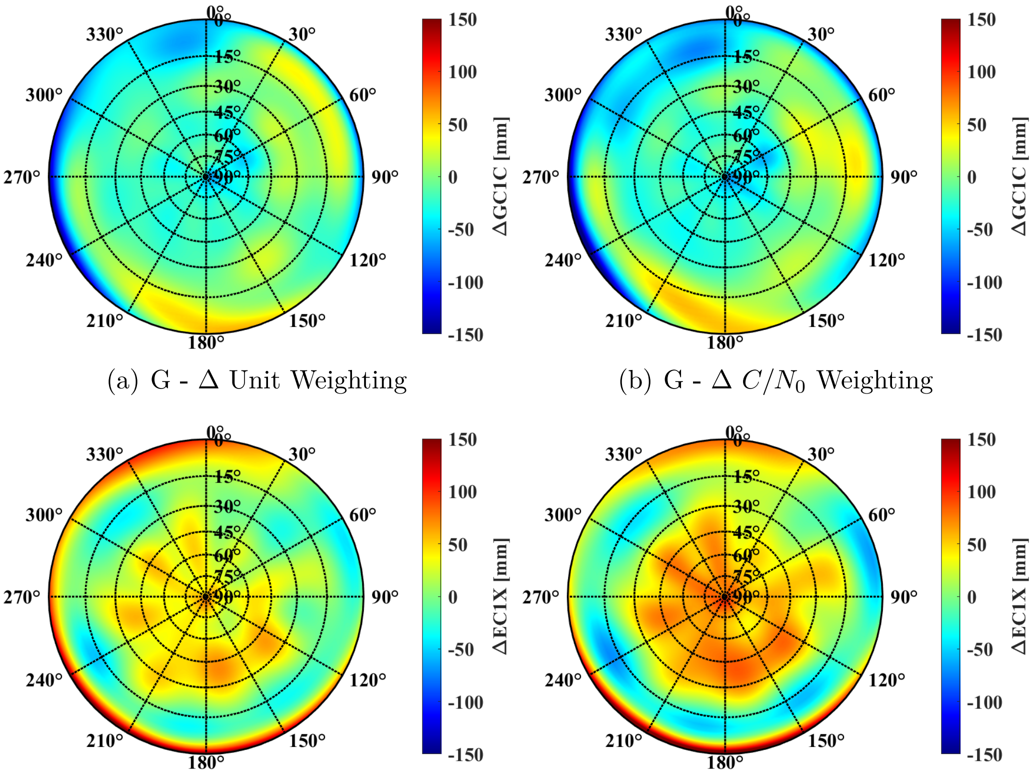

(a) G - Δ Unit Weighting

(b) G - Δ C/N_0 Weighting

(c) E - Δ Unit Weighting

(d) E - Δ C/N_0 Weighting

Figure 6.19: Differences between the CPC patterns estimated on two consecutive days of the category 1 antenna for GPS C1 (top) and Galileo C1 signal (bottom). Subfigure (a) and (c) presented the results using a unit weighting, whereas (b) and (d) shows the difference pattern when using a C/N_0 dependent weighting. Optimized receiver settings are used with a multipath map threshold of 2 m.

Figure 6.18 depicts the estimated CPC for the category 1 antenna, the GPS and Galileo C1 signal is exemplary shown, whereas the results for the C5 signal of both systems are presented in Figure A.8 in the Appendix A.2. The calibrations were carried out using optimized receiver settings. Subfigure (a) and (c) present the estimated mean pattern of the two calibration days when a unit weighting is applied in the estimation process, whereas subfigure (b) and (d) shows the mean pattern, when a signal strength dependent weighting is used. The data are preprocessed using the 4^{th} case to eliminate problematic observations (cf. Section 6.1.1) with a multipath map threshold of 2 m.

It is evident, that the CPC of both weighting methods exhibits azimuthal behaviour, primarily differing in their magnitude. Similar to the results when using ΔMPLC as estimation inputs (cf. Section 6.4) these differences are due to variations in the CCO. With unit weighting, the estimated CCO Up component is 26.3 cm for GPS C1 and 24.4 cm for Galileo C1. In contrast, with C/N_0 dependent weighting, the CCO Up component is 32.0 cm and 27.4 cm, respectively. These CCO differences are projected across all elevations, having the highest impact at zenith and decreasing as the elevation decreases. Additionally, differences at low elevations are visible, where the CPC with C/N_0 dependent weighting have a higher magnitude.

Because only two calibration days have been carried out, the CPC repeatability can be shown as the CPC differences between both days, which is presented in Figure 6.19 for the same signals and weighting methods as in Figure 6.18. It is visible, that the

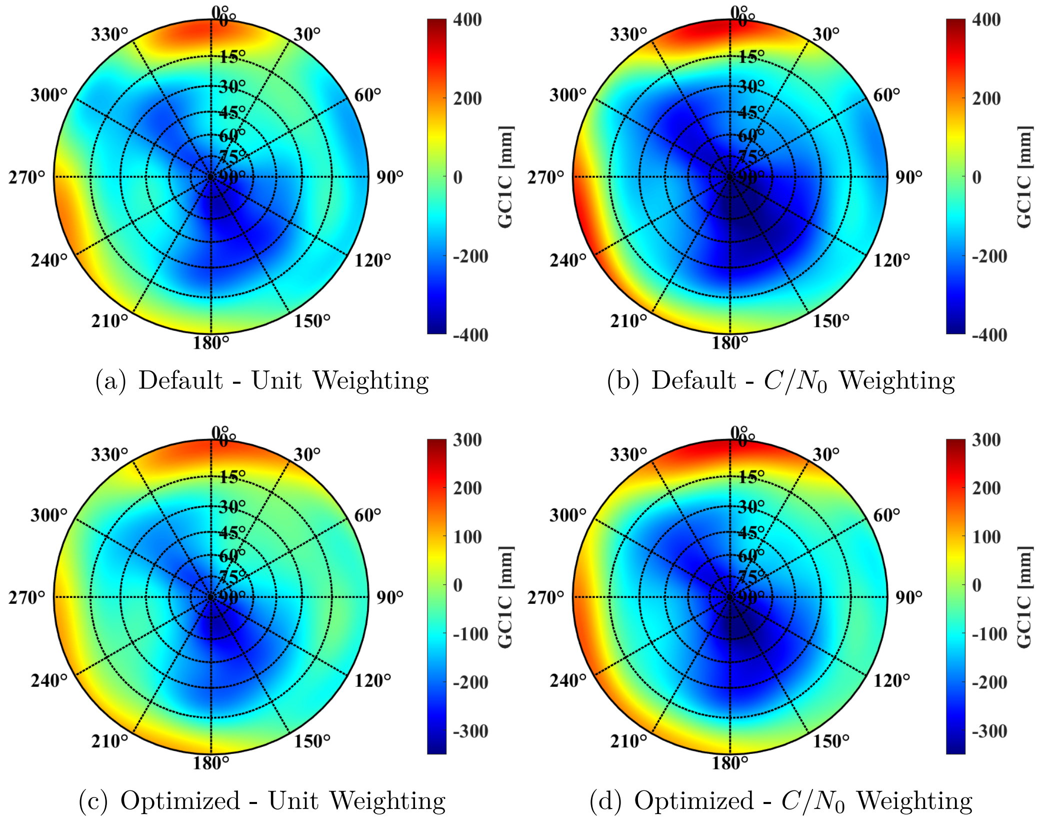

Figure 6.20: Mean CPC pattern of the category 3 antenna for the GPS C1 signal. Subfigure (a) and (c) presented the results when using a unit weighting, whereas (b) and (d) shows the pattern when using a C/N_0 dependent weighting. Default receiver settings are used for (a) and (b) and optimized receiver settings for (c) and (d). A multipath map threshold of 2 m is applied. Please note different scale between (a, b) and (c, d).

differences between a unit and a signal strength dependent weighting are very similar for the GPS C1 signal. For the Galileo signal, the differences are higher with a C/N_0 dependent weighting, especially at higher elevations. This is also visible in the RMS of the difference patterns. For the GPS C1 signal, the RMS increases from 3.4 cm to 3.9 cm, whereas the Galileo C1 signal worsens, with the RMS increasing from 4.5 cm to 6.4 cm, when using a C/N_0 dependent weighting.

The mean patterns of the category 3 antenna are presented in Figure 6.20. For clarity, only the GPS C1 signal is shown. The results for the other signals (GPS C5 and Galileo C1 and C5) can be found in Figure A.9, A.10 and A.11 in Appendix A.2. For this antenna, two receivers with default (a, b) and two receivers with optimized settings (c, d) have been used in a zero baseline approach. The left subfigures show the calculated mean pattern from two consecutive days when using a unit weighting, whereas the right subfigures present the mean CPC with a signal strength dependent weighting. Please note, that the scale between default and optimized receiver settings differ. The patterns show similar results as for the category 1 antenna in Figure 6.18. The behaviour with both weighting methods is similar, however, the magnitude of the pattern estimated with C/N_0 dependent weighting is higher compared to unit weighting. The differences between the default and optimized settings resemble the results for the category 2 antenna described in Section 6.1. The CPC behaviour gets smoother, and the repeatability improves, which can be seen in Figure 6.21. Here, the difference patterns

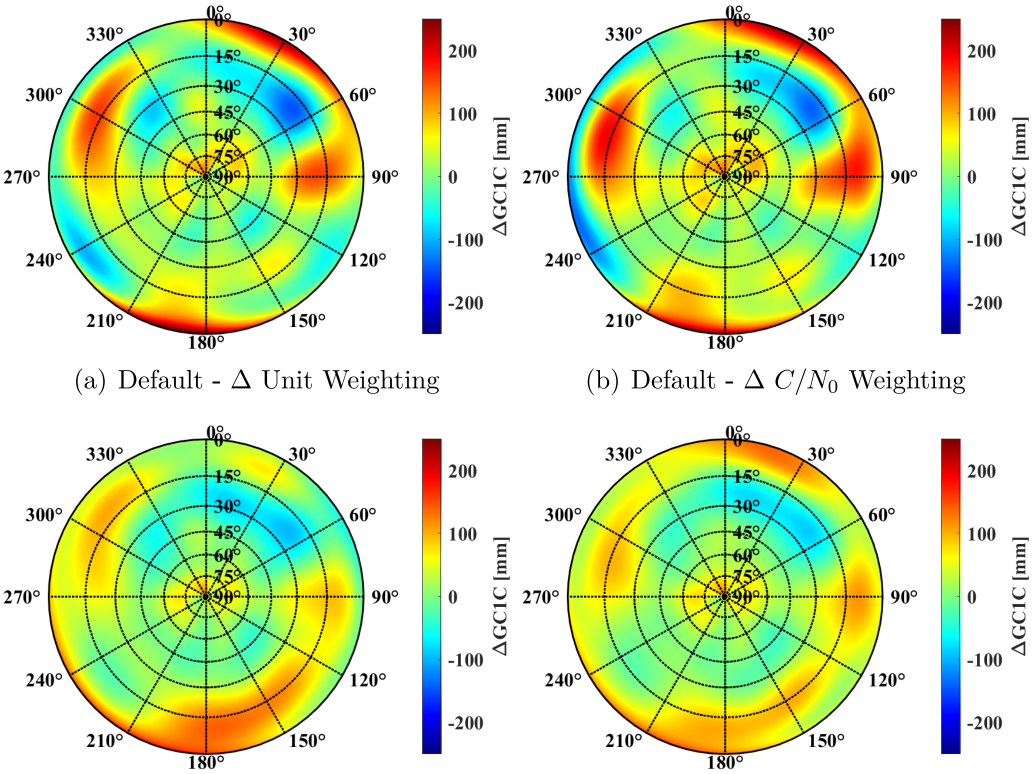

(a) Default - Δ Unit Weighting (b) Default - Δ C/N_0 Weighting

(c) Optimized - Δ Unit Weighting (d) Optimized - Δ C/N_0 Weighting

Figure 6.21: Differences between the CPC patterns estimated on two consecutive days of the category 3 antenna for GPS C1. Subfigure (a) and (c) presented the results when using a unit weighting, whereas (b) and (d) shows the pattern when using a C/N_0 dependent weighting. Default receiver settings are used for (a) and (b) and optimized receiver settings for (c) and (d). A multipath map threshold of 2 m is applied.

between the two calibration days are shown. The differences are higher for the CPC estimated with default receiver settings to optimized receiver settings, as expected.

In summary, a signal strength dependent weighing model results in differences in the estimated pattern compared to unit weighting, primarily due to the estimated CCO. Generally, the CCO Up component is larger with C/N_0 weighting, similar to the outcomes when using ΔMPLC as estimation inputs. However, the repeatability gets worse, when using a C/N_0 dependent weighting instead of a unit weighting. A validation of the estimated pattern is carried out in the next section for the category 1 and 2 antenna.

6.5 Validation

Different methods for estimating CPC using the robot-based antenna calibration algorithm at IfE have been discussed in the previous sections. Here, a validation of these patterns are carried out. Section 6.5.1 provides a comparison and discussion of the CPC estimated by IfE with those estimated in an anechoic chamber by the DLR. In Section 6.5.2 the CPC are applied in a SPP approach to study their impact in the positioning domain. To this end, a validation in the observation domain is performed with single differences.

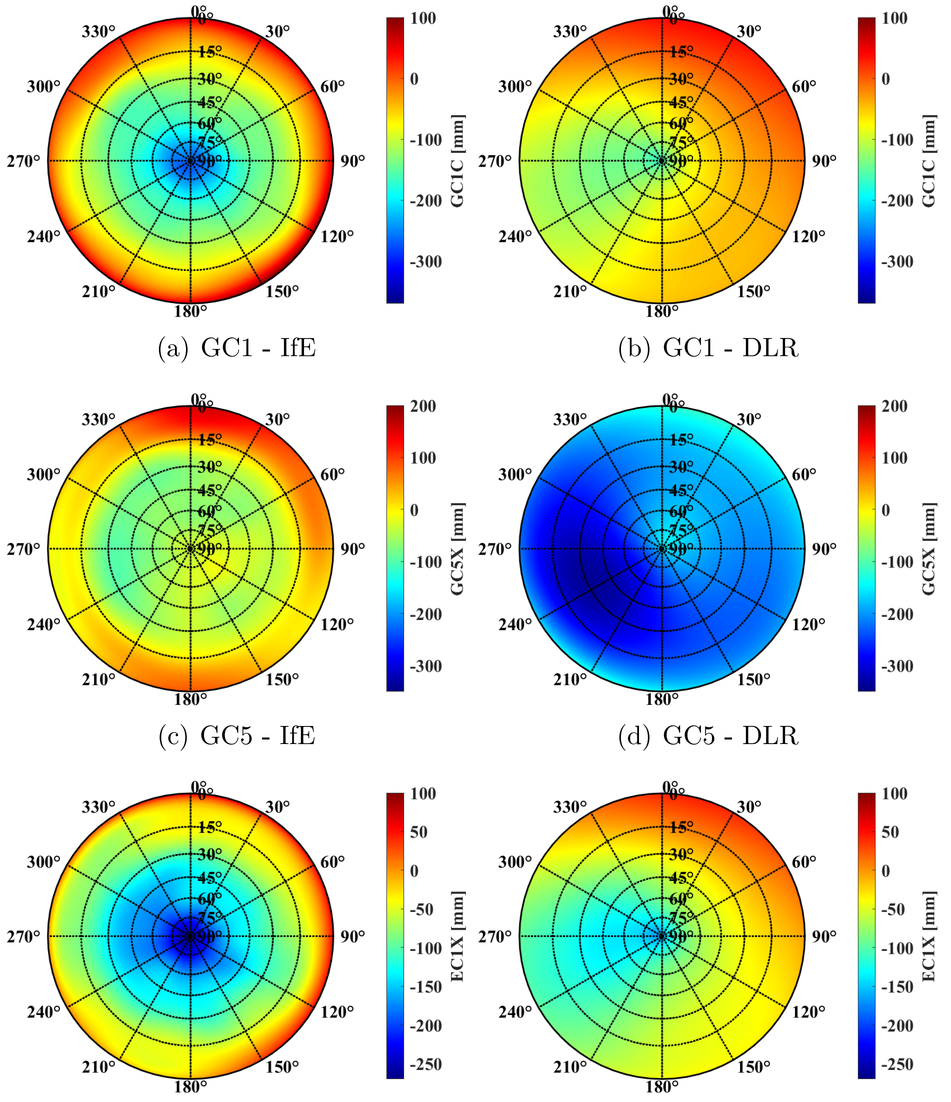

(a) GC1 - IfE (b) GC1 - DLR

(c) GC5 - IfE (d) GC5 - DLR

(e) EC1 - IfE (f) EC1 - DLR

Figure 6.22: Estimated Mean CPC pattern for GPS C1 (a) and C5 (c) and Galileo C1 (e) calibrated at IfE with optimized receiver settings and calibrated in an anechoic chamber by DLR (b, d, f) for a category 1 antenna.

6.5.1 Comparison to Results from anechoic Chamber

Beside the estimation of absolute CPC using a robot in the field, these corrections can also be determined within an anechoic chamber using synthetically generated GNSS signals. The MAESTRO project is a cooperation between IfE and DLR, which studies the impact of multipath-antenna-receiver interactions for receiving antennas on the CPC, estimated with the robot at IfE. For this purpose, the antennas analysed in this thesis have been calibrated using both approaches. Since the identical antennas are used, a direct comparison between the two methods can be performed.

The approach for estimating CPC within an anechoic chamber at the DLR can be found in Caizzone et al. (2019) and will not be discussed here. The category 1 and category 3 antenna, namely LEIAR25.R3 NONE (S/N: 9330001) and u-blox ANN-MB1 NONE (S/N:2133), have been calibrated with a specific holder, which approximates

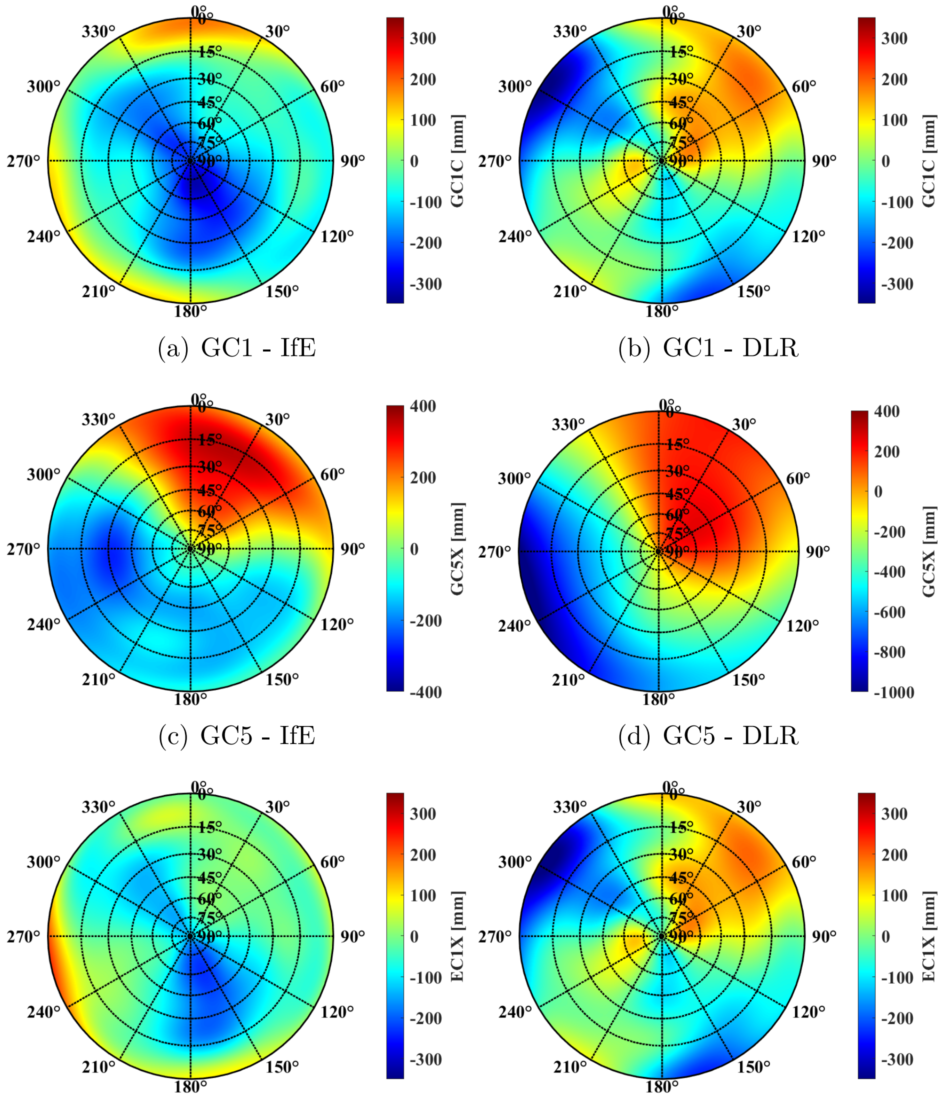

(a) GC1 - IfE (b) GC1 - DLR

(c) GC5 - IfE (d) GC5 - DLR

(e) EC1 - IfE (f) EC1 - DLR

Figure 6.23: Estimated Mean CPC pattern for GPS C1 (a) and C5 (c) and Galileo C1 (e) calibrated at IfE with optimized receiver settings and calibrated in an anechoic chamber by DLR (b, d, f) for a category 3 antenna.

the near field of the robot. The estimated CPC are presented in the right column of Figure 6.22 and Figure 6.23 for the category 1 and category 3 antenna, respectively. Three different GNSS signals are shown: The GPS C1 signal in the top subfigures, the GPS C5 signal in the middle and the Galileo C1 signal in the bottom subfigures. For comparison, the CPC estimated with the robot in the field, with optimized receiver settings, ΔSD as estimation inputs and a unit weighting scheme, are depicted in the left columns.

The estimated CPC for both, robot-based and anechoic chamber, significantly differ for the category 1 antenna in Figure 6.22. The CPC estimated at IfE exhibit azimuthal behaviour, whereas the CPC estimated at DLR shows deviations in the South-Western antenna hemisphere. Furthermore, the magnitude of both approaches differs, which is mainly caused by the estimated CCO. The CCO obtained using the anechoic chamber approach is very similar to the carrier PCO of the considered GNSS signal, while the

CCO estimated using the robot-based approach is significantly higher. For example, the CCO for the GPS C1 signal is approximately 12 cm higher compared to the estimation performed within the anechoic chamber. The highest differences are visible for the GPS C5 signal. The DLR pattern exhibits only negative CPC with lower values at the region in South-West.

More similarities between both estimation approaches are evident for the category 3 antenna in Figure 6.23. The GPS and Galileo C1 signals exhibit a very prominent trefoil pattern, with negative CPC in the North-West and South-East and higher values in the North-East and South-Western antenna. This pattern behaviour is typical for this kind of patch antennas. The GPS C5 signal has higher CPC in the North-Eastern part of the antenna. However, the CPC magnitude between both approaches for all considered GNSS signals differs. This becomes very clear when comparing the GPS C5 signal. The pattern behaviour shows a good agreement, however, the magnitude differs, especially in the South-Eastern part of the antenna. The CPC estimated at IfE reaches values up to -200 mm in this region, while the CPC estimated at DLR extends up to -1000 mm. Please note the different scale in the figure for the GPS C5 signal.

This comparison shows that there are significant differences between the two estimation approaches. Without a ground truth for the CPC of these antennas, which is currently not existing, it is not possible to determine which CPC estimation is correct. The differences between both approaches could be explained either by the differences in estimation methods or by the noisy observations present only in the robot-based antenna calibration, due to the use of real GNSS signals. Furthermore, the robot itself can influence the antenna's near field. The measurements in the anechoic chamber using a specific holder, which approximate this near field, but it represents only a portion of the entire robot system. Differences may occur due to the interaction between the robot and the antenna. To counteract this issue, the entire robot-antenna system could be calibrated together in the anechoic chamber.

Since there is no ground truth for the CPC of these antennas, it is very difficult to optimize the robot-based antenna calibration approach in terms of accuracy. The different methods and strategies proposed in this thesis are primarily focusing on optimizing the repeatability of the estimated patterns, by reducing the observation noise. The next section compares the CPC estimated using different methods, as well as the CPC obtained in an anechoic chamber, in both the positioning and observation domains. This comparison aims to study the improvements in these domains achieved by correcting the observations using the CPC.

6.5.2 Positioning and Observation Domain

To validate the estimated pattern using the different methods described in the previous chapters, a static experiment has been carried out on the measurement rooftop of the GIH from 28^{th} to 29^{th}, September 2024. In this experiment, the category 1 antenna was installed on the robot (MSD7) at its initial antenna calibration pose (cf. Figure 6.24 right). The category 2 antenna was mounted on the pillar MSD4 using a height adapter placed on a tripod (cf. Figure 6.24 left). Both antennas are each connected to a Javad DeltaS-3S receiver, using optimized receiver settings (DLL B_n of 0.5 Hz). Additionally,

Figure 6.24: Measurement configuration for validation with category 2 antenna on pillar MSD4 (left) and category 1 antenna mounted on the robot (right).

both receivers are linked to an external frequency standard (Rubidium FS725) with a stability of $2 \cdot 10^{-11}$ @1 s

Since the estimated coordinates in an absolute positioning approach are based on the coordinate frame of the satellite coordinates, the reference coordinates of the pillars must also be in the same coordinate frame for comparison with the estimated coordinates. Koppmann (2018) estimates the pillar coordinates in the ETRS89, realized by the ETRF2000, whereas the satellite coordinates are in the ITRF2020. Thus, a software from the Royal Observatory of Belgium is used to transform the pillar coordinates into the required frame (Bruyninx, 2023). First, the transformation from ETRF2000 to ITRF2020 is performed at the epoch of December, 1^{st} 2016, to which the pillar coordinates are referenced. With the ITRF2020 station velocity of [-0.0155, 0.0164, 0.0097] m/yr at epoch 2015.0 from the IGS station PTBB, maintained by the

Table 6.2: Reference pillar coordinates in different coordinate frames.

Station	ECEF X [m]	ECEF Y [m]	ECEF Z [m]
ETRF2000, epoch 1.12.2016			
MSD4	3845229.1021	658129.3828	5029184.7804
MSD7	3845219.8138	658117.2357	5029193.3845
ITRF2020, epoch 1.12.2016			
MSD4	3845228.6346	658129.7967	5029185.1013
MSD7	3845219.3463	658117.6496	5029193.7054
ITRF2020, epoch 27.09.2024			
MSD4	3845228.5134	658129.9250	5029185.1772
MSD7	3845219.2251	658117.7779	5029193.7813

Physikalisch-Technische Bundesanstalt (PTB), the ITRF2020 coordinates from epoch 2016 are transformed to the date of the experiment[1]. The different coordinates of the pillar MSD7 (category 1 antenna) and MSD4 (category 2 antenna) are listed in Table 6.2.

Positioning Domain

A single point positioning (SPP) approach is used to validate the CPC, estimated with different methods, in the coordinate domain. An elevation mask of 3° is applied to the GNSS observations, whereas the GPS C1 signal is processed. Additionally, a signal strength dependent weighting is used in the epochwise least-squares adjustment process. The observations are corrected for the tropospheric effect with the Vienna Mapping Function (re3data.org, 2020), for the ionospheric effect with the IONEX TEC maps provided by the IGS and by relativistic effects. Additionally, the satellite's PCO is assumed to be identical to the satellite's CCO describing the distance from the satellite's center of mass to the transmitting antenna. To this end, final orbits and clock products from Center for Orbit Determination in Europe (CODE) are used.

Figure 6.25 and 6.26 show the estimated topocentric coordinates w.r.t. the reference ITRF2020 coordinates listed in Table 6.2 at epoch 27.09.2024 for the category 1 and category 2 antenna, respectively. Here, no CPC have been applied. As expected, the East component exhibits the smallest variations, while the largest variations are observed in the Up component. To enable a better comparison of the coordinates when applying CPC, estimated with different methods, the mean coordinates of the epochwise coordinates over the 48-hour measurement period are calculated and presented in red in the figures. These topocentric coordinates are:

$$MSD4_{w/o,CPC} = \begin{bmatrix} 0.172 \\ 0.054 \\ -0.103 \end{bmatrix} \text{ [m]}, \; MSD7_{w/o,CPC} = \begin{bmatrix} 0.074 \\ -0.019 \\ 0.661 \end{bmatrix} \text{ [m]} \tag{6.5}$$

The SPP approach is repeated for both stations using the same settings as described above. However, an additional correction is applied, considering the estimated CPC with different methods. Since the CPC is typically not known for GNSS antennas, the carrier PCO is often used in codephase GNSS application in place of the CCO. Thus, the first SPP is calculated using the phase PCO as a CPC correction. Further SPP solutions have been calculated using the estimated CPC, previously described in this thesis:

- CPC estimated with ΔSD and a unit weighting (cf. Section 6.1.2)
- CPC estimated with ΔMPLC and a unit weighting (cf. Section 6.3)
- CPC estimated with ΔSD and a signal strength dependent weighting (cf. Section 6.4).

All patterns are estimated using optimized receiver settings. Additionally, another SPP solution has been calculated using the CPC provided by the DLR (cf. Section 6.5.1).

[1] It is assumed that the station velocity at PTB is the same as that on the laboratory rooftop of the GIH building.

For each epochwise coordinate solution, the topocentric mean coordinates w.r.t. to the reference coordinates are calculated and presented in Figure 6.27 for station MSD7 (left) and MSD4 (right). By applying CPC it is evident, that mostly the Up component is affected. In case of the category 1 antenna, which was installed on the robot in its initial calibration pose, the consideration of CPC improves the estimated coordinates. The most accurate topocentric position is achieved, when using CPC estimated with ΔMPLC and unit weighting. Nevertheless, each estimation method developed in this thesis improves the coordinate solution compared to the solutions where no CPC is applied or only the carrier PCO is considered. Additionally, a slight improvement is observed in the East component. The results using the DLR CPC still offers an improvement over not applying a CPC, but results in a worse positioning solution compared to using only the carrier PCO. Because the Leica antenna exhibits a very azimuthal CPC behaviour, the coordinate improvement is mostly prominent in the Up component, which magnitude corresponds to the estimated CCO. For example, the CCO estimated with ΔMPLC and unit weighting is approximately 42 cm, whereas the phase PCO is only approximately 16 cm. This difference of 26 cm can be seen in the Up components of both cases.

In contrast, the estimated coordinates for the Novatel antenna show opposite results (cf. Figure 6.27 right). When a CPC is considered, the Up component worsens, even when only the carrier PCO is applied. However, improvements in the North and East components are achieved when using CPC with ΔSD or ΔMPLC.

In general, incorporating CPC into an SPP results in an estimated position with a lower topocentric height, primarily due to the CCO. However, the impact of CPC in an absolute codephase GNSS application is relatively small, as other error sources, such as codephase noise or multipath effects, dominate. The Novatel antenna has been installed on the pillar at a height of approximately 23 cm. In contrast, the Leica antenna on the robot is located at a height of approximately 92 cm. The Novatel antenna is closer to potential reflective surfaces, such as the ground or the balustrade, and is more

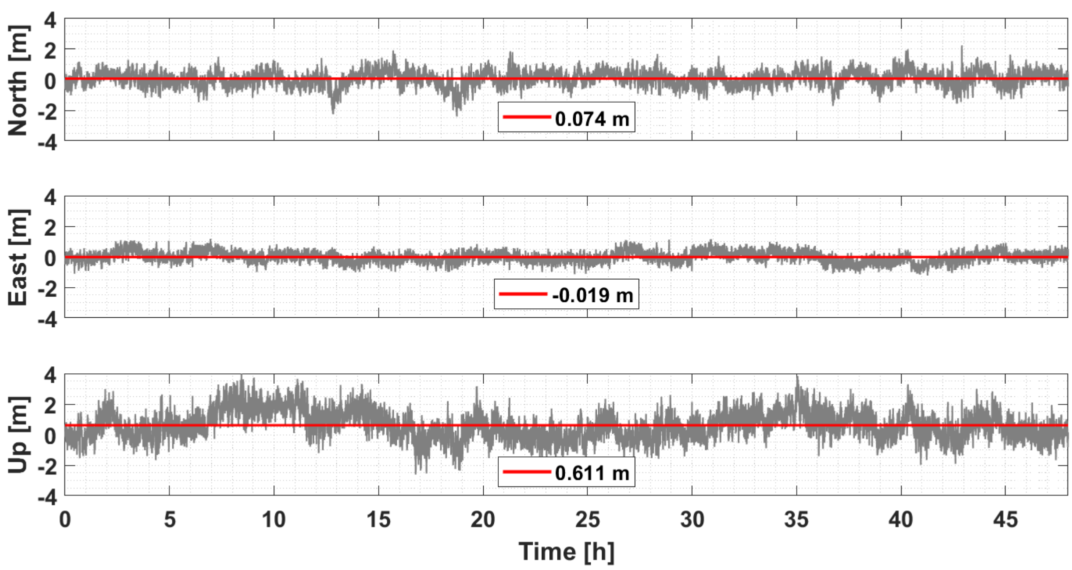

Figure 6.25: Estimated topocentric coordinates w.r.t the reference ITRF2020 coordinates at epoch 27.09.2024 (MSD7) for the category 1 antenna with no additional CPC. The mean value is presented in red.

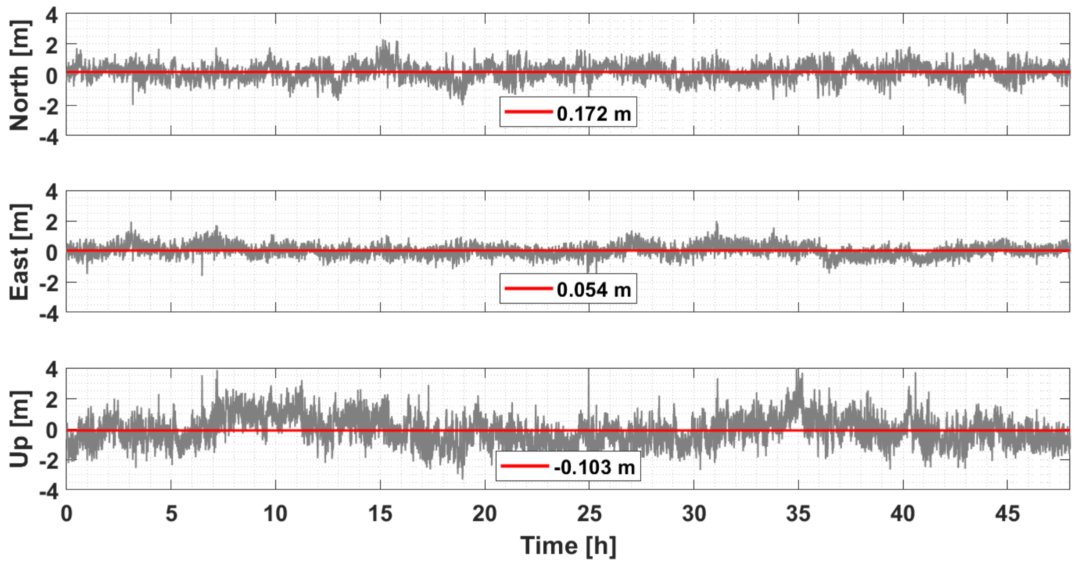

Figure 6.26: Estimated topocentric coordinates w.r.t the reference ITRF2020 coordinates at epoch 27.09.2024 (MSD4) for the category 2 antenna with no additional CPC. The mean value is presented in red.

affected by vertical reflections from the rooftop building compared to the Leica antenna. As a result, the estimated coordinates could be less accurate, as the multipath effects dominate over the CPC impact. Since the estimated Up component, without accounting for any pattern information, is lower than the reference height, incorporating a CPC further worsens this height estimate.

Observation Domain

Besides the SPP, the measurement configuration allows calculating SD in order to study the impact of CPC in the observation domain. The SD are calculated between the Leica antenna, installed on the robot, and the Novatel antenna on pillar MSD4. In

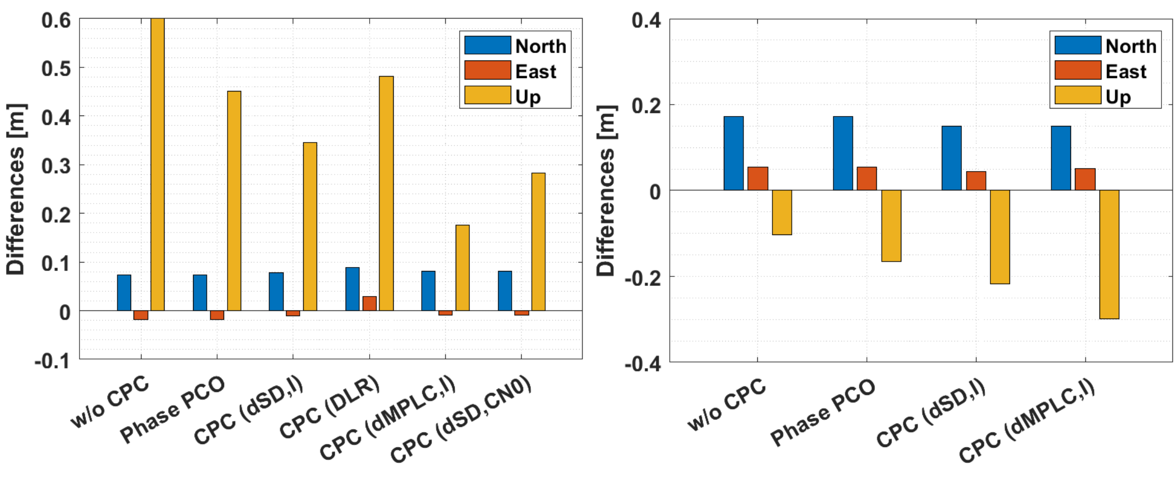

Figure 6.27: Estimated mean topocentric coordinates w.r.t the reference ITRF2020 coordinates at epoch 27.09.2024 for the category 1 (left) and category 2 antenna (right) by applying different CPC pattern.

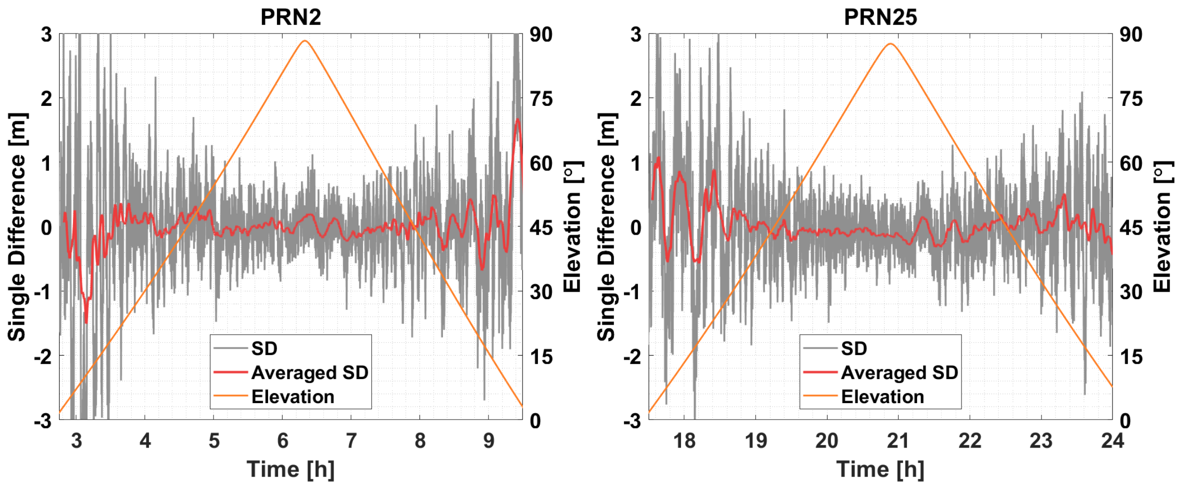

Figure 6.28: Single differences of GPS satellite PRN2 (left) and PRN25 (right) in grey, with their moving average single differences in red.

this analysis, the GPS C1 signal is studied, as illustrated in Figure 6.28 exemplary for the GPS satellite PRN2 (left) and PRN25 (right). The same corrections are applied to the SD as those used in the SPP analyses, except that no cutoff angle is applied.

The SD without any CPC are presented in gray in Figure 6.28 after removing the SD ambiguity caused by the differential receiver clock error between the two stations. Thanks to the common-clock setup with an external frequency standard, no additional drifts between the clocks occur. The ambiguity can be determined by calculating the median of the SD for each satellite observation arc.

Since CPC exhibits long periodic trends within the observation domain, an averaged SD is calculated to eliminate high-frequency noise in the time series. Thus, a moving average is calculated with a timing window of ten minutes, which is depicted in red in the figure for both satellites. This benefits the analysis of CPC in the SD.

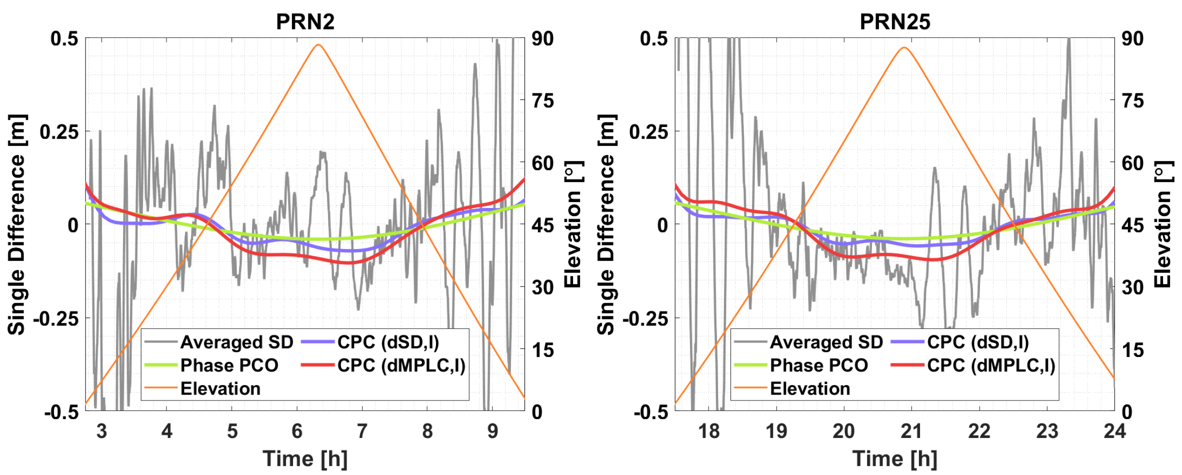

Figure 6.29: Moving average single differences of GPS satellite PRN2 (left) and PRN25 (right) in grey, with different CPC.

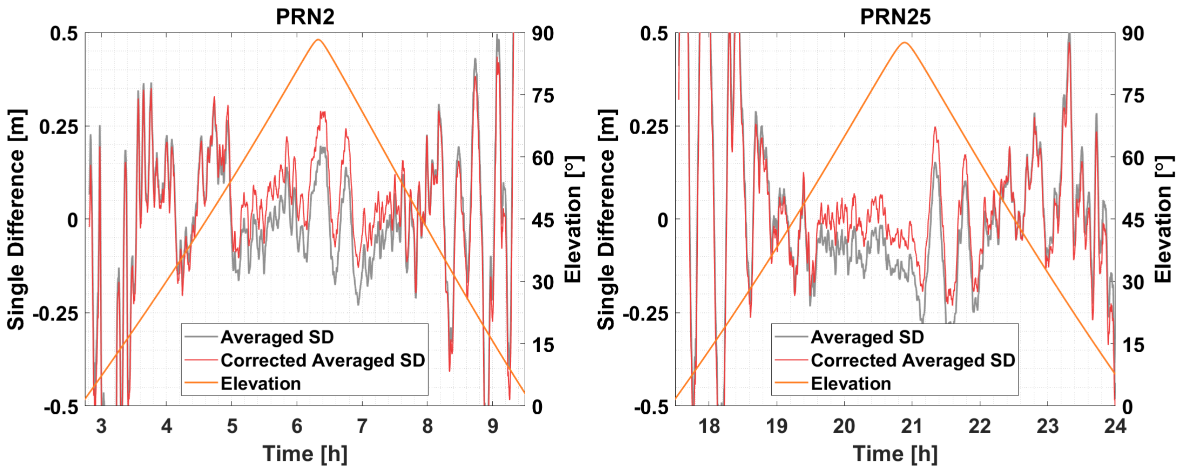

Figure 6.30: Moving average single differences of GPS satellite PRN2 (left) and PRN25 (right) in grey, and by applying CPC in red.

The averaged SD of both satellites are depicted in Figure 6.29 in gray as a zoomed-in view of Figure 6.28. Furthermore, the differential CPC between both antennas is depicted, estimated using different methods. This representation shows not the correction itself, but its actual effect. Additionally, an offset, calculated as the median of the CPC, is removed from the CPC. This offset would have been eliminated with the SD ambiguity when CPC is applied to the observations. Thus, this adjustment is made for better comparison.

It is evident, that all considered CPC represent the long periodic trend within the SD time series, with the best alignment achieved using the ΔMPLC approach. The phase PCO patterns still reflect this trend, although not as accurately as the CPC pattern, using both the ΔMPLC and ΔSD methods.

When a CPC pattern is applied as a correction to the SD, the long periodic trend can be removed, visible in Figure 6.30. Here, the averaged SD are presented in gray, while the SD corrected by the CPC are depicted in red. The CPC were estimated using the ΔMPLC as estimation inputs. After applying the CPC, the SD fluctuates more close to zero, which indicates that the trend has been removed.

7 Summary and Outlook

In absolute robot-based multi-GNSS multi-frequency antenna calibration, observation noise is the most significant factor impacting the accurate and precise estimation of the CPC pattern. In this thesis, the noise behaviour of codephase GNSS signals during antenna calibration has been thoroughly investigated by analysing the actual observation noise from different GNSS receivers and antennas, and by using a Monte-Carlo simulation to study the impact of varying noise levels on the estimated CPC pattern. The acquired knowledge has been utilized to develop a digital receiver twin for optimizing the GNSS receiver tracking loops during robot-based antenna calibration. These settings have been adapted to GNSS hardware receivers. By employing optimized receiver settings in the robot-based calibration of codephase signals and by eliminating problematic observations, mostly caused by multipath, the observation noise is significantly reduced, leading to a more repeatable and accurate CPC pattern.

The theoretical and mathematical fundamentals form the foundation of the investigations conducted in this thesis. The modulation of analog radio frequency signals for transmitting GNSS data from the satellite to the user is described, along with the basics of GNSS antennas and the primary components of GNSS receivers. A more detailed explanation of the loop filter and tracking loops is provided, as these are the most critical components for noise reduction, with the selected bandwidth and filter order having the largest impact on noise performance.

The GNSS observation equation is presented along with a brief overview of the error sources that must be considered in absolute antenna calibration. A detailed definition of multipath effects is provided, as they are not eliminated by the time differencing approach used in the calibration algorithm. Additionally, observation differences are described, as receiver-to-receiver single differences serve as inputs for CPC estimation. Furthermore, commonly used linear combinations are outlined.

Since the observation quality during antenna calibration using a robot in the field is investigated in this thesis, a detailed description of the absolute antenna calibration algorithm at IfE is provided. The calibration robot and its mathematical model are described in detail. Furthermore, the ΔMPLC is introduced and proposed as an input for the estimation process. In contrast to ΔSD, the ΔMPLC avoids one differencing step, reducing the added noise on the observations by a factor of $\sqrt{2}$. The observation noise, represented as the weighted average standard deviation σ_{ant} over all visible satellites during the calibration period, decreases when using ΔMPLC instead of ΔSD as the observable. For instance, for a geodetic rover antenna, an improvement of 16 %

with default receiver settings and 11 % with optimized receiver settings for the GPS codephase signal C1 is achieved.

Multipath effects still remain in the ΔMPLC. However, using multipath maps generated by the DLR can eliminate observations affected by multipath. These maps are implemented in the antenna calibration algorithm at IfE to exclude these observations, preventing their use in the estimation process. Approximately 10 % to 20 % of observations are excluded using these maps.

They are based on a digital twin of the robot's surroundings, created in a CAD environment using measurements from a practical survey conducted in January 2022. This model is also used to identify critical structures in the robot environment based on the MPLC. Most multipath effects are caused by signals from satellites at low elevations (15°-20°) in the southwest direction, which are suspected to reflect off the metallic balustrade of the rooftop. Additionally, the two astronomical domes are identified as critical structures, located at azimuths of approximately 30° and 100°, respectively, and are considered to cause diffraction effects.

The investigations show that by transforming these observations into the antenna system, the multipath affected observations are projected up to 45° elevation in the antenna system. Since time differenced observations are used as observables in the estimation process, multipath affected observations are reduced, but still remain. Applying dynamic elevation masks helps to avoid almost all multipath effects. This demonstrates that using time differenced observations in combination with a dynamic elevation mask, with a negative elevation angle of 5° and a topocentric cutoff angle of 10°, can significantly reduce multipath effects. The results are consistent with the findings achieved using the multipath maps. Additionally, the tilting angle of the AUT and the changes in elevation and azimuth between two static epochs have no significant impact on multipath effects. Consequently, it is the environment, or more specifically, the satellite-reflector-receiver geometry, that causes multipath effects rather than the robot's pose.

A detailed noise investigation is conducted during the antenna calibration for three different GNSS antennas, classified as categories 1 to 3, using the manufacturer's default receiver settings. The noise levels varied among the different types of antennas, with the patch antenna (category 3) producing noisier observations compared to the high-end geodetic choke ring antenna (category 1). Additionally, Galileo signals were generally less noisy than GPS signals. The noise in the ΔSD observable does not behave like white noise. Using an adapted approach from de Bakker et al. (2009), the observations can be normalized, suggesting that the noise behaviour depends on the satellite's signal strength.

Furthermore, three different GNSS receivers are analysed in terms of their noise behaviour using default receiver settings. The two Javad receivers perform similarly, while the Septentrio receiver is significantly less noisy. The analysis suggests that the Septentrio receiver is likely using codephase smoothing with the help of the carrierphase. Additionally, there are limited opportunities to adjust the tracking loops in this receiver. Thus, the Javad receivers are used for optimization.

A Monte-Carlo simulation is performed to study the impact of observation noise on the estimated CPC. This simulation is conducted within a simulation environment integrated into the antenna calibration algorithm, which allows for simulating ΔSD with computational accuracy based on existing patterns. Two parameters, Rel_{NF} and Rel_{Para}, are defined to relate the added noise to the peak-to-peak pattern magnitude and to the parameters of the comparison metrics. As the noise increases, the comparison parameters increase linearly. A Rel_{NF} of 100 % degrades the estimated CPC by approximately 16 % for minimum, maximum, spread, and RMS, 25 % for the range, and 3.5 % for the standard deviation when white noise is added. When C/N_0 dependent noise is added, similar degradation is observed, except for significant improvements in the RMS and standard deviation.

Thanks to the linear behaviour, a linear regression is performed to calculate β_0 and β_1 for each comparison metric parameter. This allows for calculating either the noise threshold, ensuring the error remains below a chosen threshold, or the degradation of the CPC pattern for a specific noise magnitude. A validation with a different input pattern is conducted, producing similar results for the coefficients, with differences in the range of 2 %-3 %, except for the spread, which describes the range differences between two patterns. Even with very high observation noise, the pattern behaviour can be maintained. However, it exhibits a different magnitude, which is already described by the comparison metrics.

The Monte Carlo simulation indicates that the codephase observation noise must be reduced to estimate a more precise and accurate CPC. To achieve this, a software receiver is utilized during antenna calibration, allowing adjustments to receiver settings in post-processing. The best performance is achieved with a DLL bandwidth of 0.5 Hz and a filter loop order of 1 with carrier aiding, or 2 without carrier aiding. Due to limited knowledge about the hardware receiver's components, it is proposed to use a DLL bandwidth of 1 Hz and a filter loop order of 1 with carrier aiding for the AUT, and a DLL bandwidth of 0.5 Hz and a filter loop order of 1 with carrier aiding for the reference antenna. This configuration ensures stable tracking despite dynamic stress, significantly reduces noise, and maintains important pattern information in the observables.

The acquired knowledge is applied to Javad hardware receivers during the calibration of a category 2 antenna. The average weighted standard deviation over all visible satellites for the ΔSD decreases from 0.530 m, using default settings, to 0.306 m, with optimized settings, for the GPS C1 signal, corresponding to an improvement of 42 %. The estimated CPC becomes smoother, especially at lower elevations in the antenna frame. The repeatability over four calibration days improves when using optimized receiver settings. Additionally, strategies to eliminate problematic observations are employed to remove multipath affected observations. Applying a topocentric/dynamic elevation mask modifies the estimated CPC. Furthermore, using multipath maps also impacts the estimated CPC. Small differences still occur when ΔSD calculated between two robot resting phases exceed 6 seconds. Additional elimination techniques, such as avoiding short satellite arcs or observations acquired immediately after the robot comes to rest, have no significant impact on the estimated CPC.

The four calibration days allow for the investigation of the impact of calibration duration on the estimated CPC and its repeatability. The repeatability decreases as the calibration duration is reduced. Nevertheless, it does not matter whether the estimated CPC is combined in the pattern domain or the observations are combined in the NES to calculate the mean CPC. However, the total duration of the calibration is crucial. The CPC from the 6-hour calibrations varies significantly, even if the satellite-reflector-antenna geometry remains unchanged (sidereal repetition), but the robot poses do. Thus, it is recommended to extend the calibration duration to at least one full day.

The proposed ΔMPLC is used to estimate the CPC. The pattern behaviour is similar when using ΔSD as estimation inputs. However, using ΔMPLC results in a larger CPC magnitude due to differences in the estimated CCO. The repeatability is significantly improved, and applying a multipath map threshold of 2 m provides the most repeatable CPC estimation. Instead of using unity weighting, the observations can be weighted based on the C/N_0 model proposed in this thesis. The results are similar to those obtained using ΔMPLC. However, the repeatability is worse compared to using unity weighting.

The estimated CPC are validated in both the positioning and observation domains for the category 1 and category 2 antennas. A SPP is calculated by incorporating CPC estimated using different methods and comparing them to results obtained without adding a CPC or by using the carrierphase PCO as a correction. For the category 1 antenna, the best accuracy is achieved with the ΔMPLC approach, resulting in differences in the Up component of approximately 18 cm, while using no CPC corrections leads to an Up component deviation of 60 cm from the reference height. Applying CPC to the SPP for the category 2 antenna results in worse accuracy. Even adding the carrierphase PCO degrades the estimated position, which can be explained by the dominance of multipath effects, which are more prominent at this antenna than at the category 1 antenna.

In SD, a long-period trend is visible, which is well represented by the estimated CPC pattern of both antennas. The best alignment is achieved when using CPC estimated with the ΔMPLC approach.

The CPC estimated using a robot in the field significantly differs from the results obtained in an anechoic chamber. These differences may arise from variations in the estimation approaches or from not considering the robot itself as a reflective element in the anechoic chamber.

Outlook To improve the repeatability of CPC estimation using a robot in the field, the robot's motion should be optimized by considering the environment and the actual satellite constellation during the calibration to increase the number of usable observations. A possible approach for this optimization is proposed in this thesis.

To enable a more accurate comparison with the anechoic chamber, the entire robot-antenna system could be calibrated within the chamber, as the antenna's near field affects the estimated CPC.

The receiver optimization in this thesis relies on the software receiver's results. However, the hardware receiver might employ different filtering techniques, among other variations. Therefore, the optimized tracking loop settings could be further enhanced if details about the hardware receiver's design were available. This information is proprietary to the manufacturer, presenting a challenge.

A
Appendix

A.1 Impact of Simulated Observation Noise on Calibration Outcomes

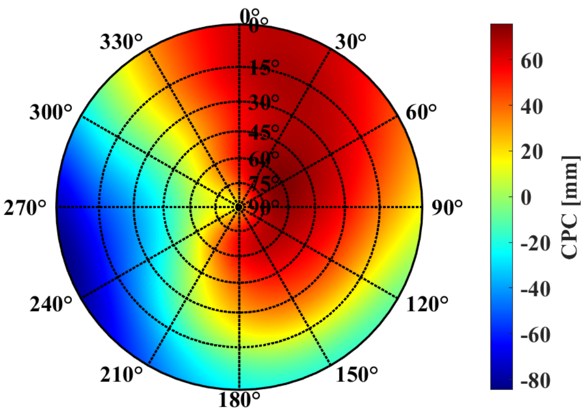

Figure A.1: CPC pattern of a category 1 antenna provided by DLR.

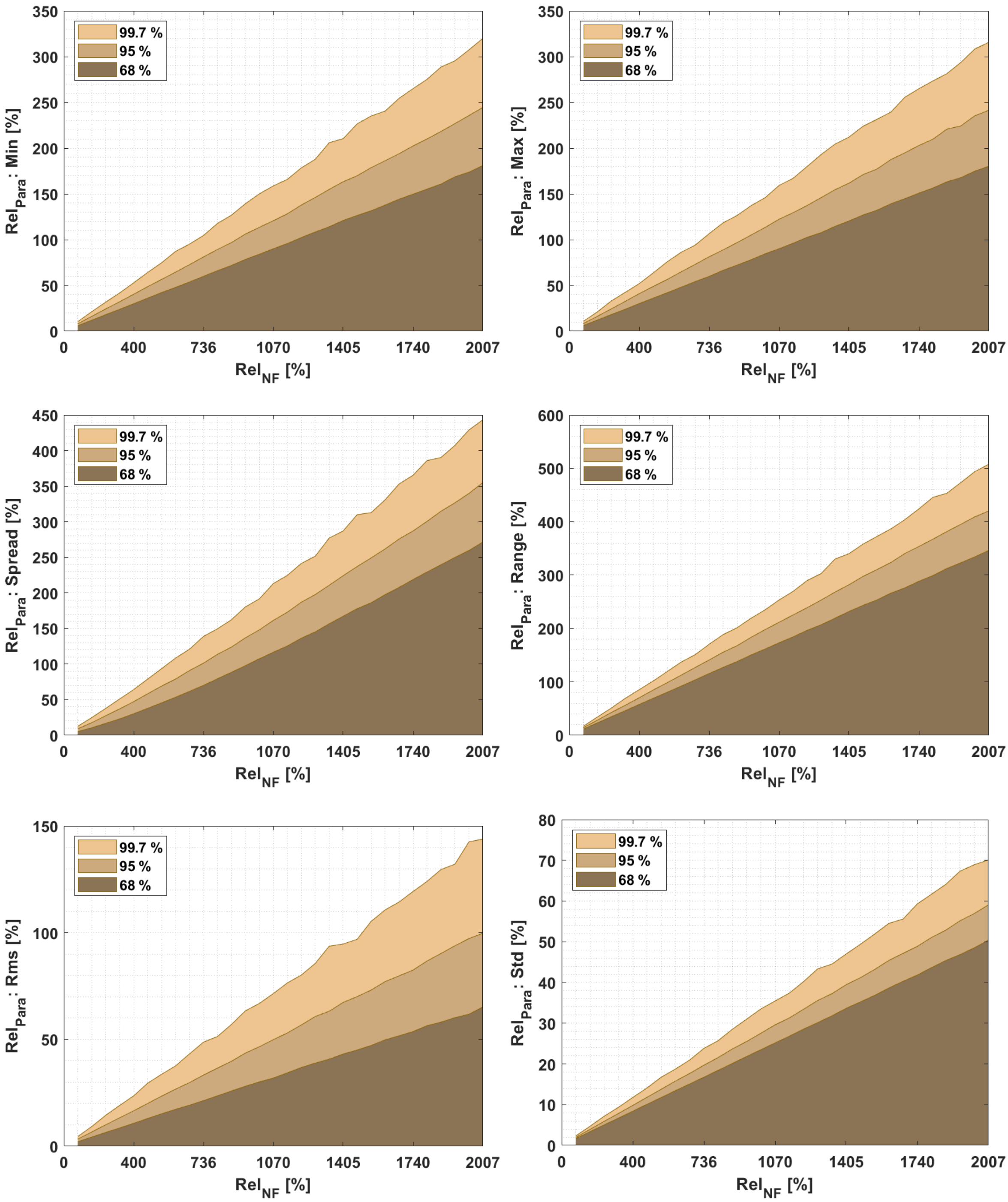

Figure A.2: Results for relative comparison metrics for the category 1 antenna with additional WN, based on input pattern in Figure A.1 with different noise factors. Because the noise factor is varying up to 3 m and P_{Peak} is 149.44 mm, $\mathrm{Rel}_{\mathrm{NF}}$ is varying to 2007 %.

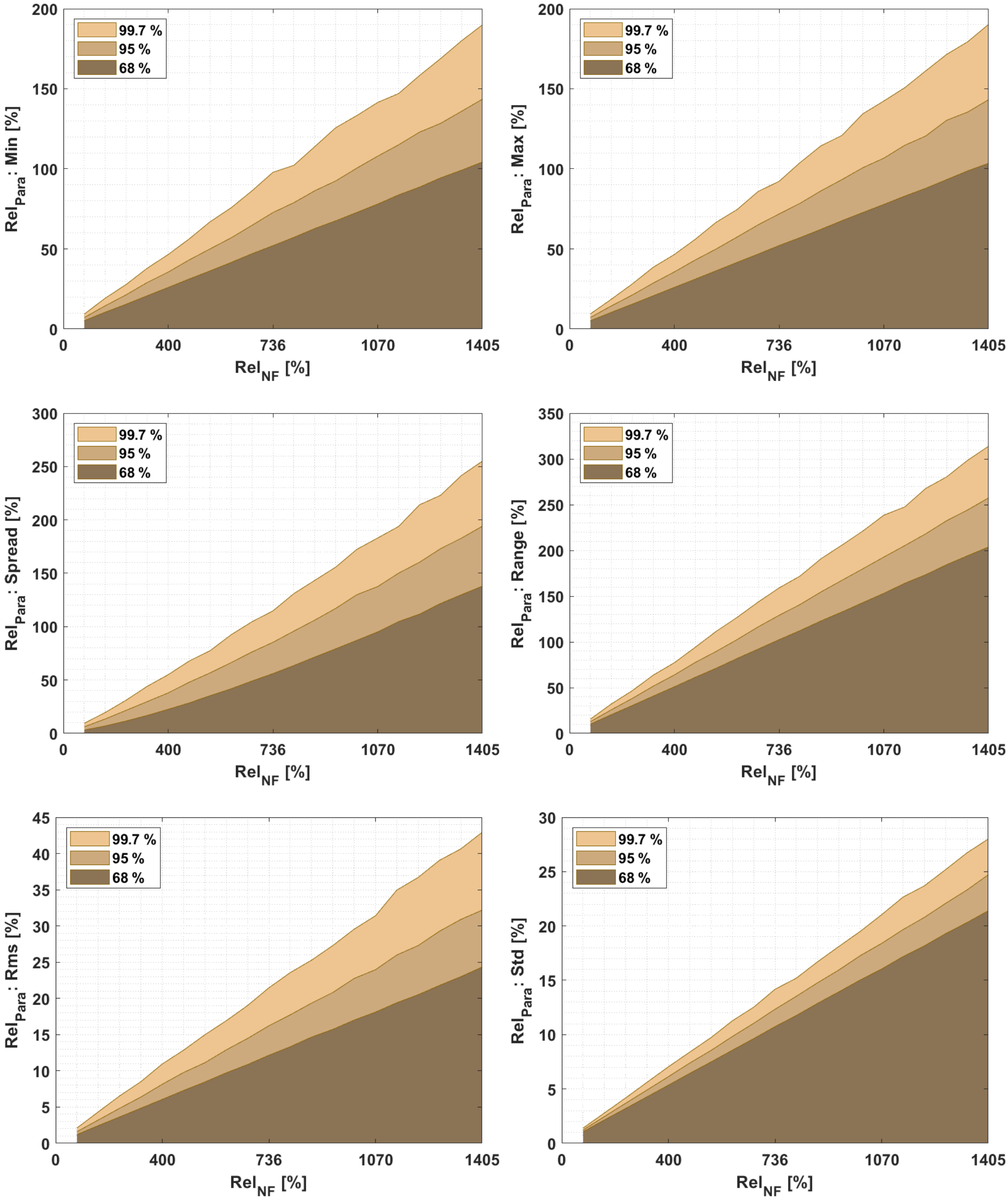

Figure A.3: Results for relative comparison metrics for the category 1 antenna with additional C/N_0 noise, based on input pattern in Figure A.1 with different noise factors. Because the noise factor is varying up to 2 m and P_{Peak} is 149.44 mm, $\mathrm{Rel}_{\mathrm{NF}}$ is varying to 1405 %.

Table A.1: Linear coefficients for relative comparison metrics for three different quantiles with a WN behaviour of a category 1 antenna and with differences to the category 3 antenna in Table 4.3 in the brackets.

Comparison metric	Coefficient	Quantile 68 %	95 %	99.7 %
Min	β_0	1.4 (1.3)	2.4 (2.8)	5.8 (4.9)
	β_1	11.1 (0.5)	8.3 (0.0)	6.3 (0.2)
Max	β_0	0.0 (0.3)	0.9 (1.7)	-7.5 (9.2)
	β_1	11.1 (0.5)	8.3 (0.0)	6.3 (0.2)
Spread	β_0	138.0 (103.8)	86.1 (67.4)	57.5 (44.2)
	β_1	7.0 (7.0)	5.5 (2.5)	4.5 (1.1)
Range	β_0	0.4 (0.4)	1.3 (1.5)	2.7 (2.1)
	β_1	5.8 (0.3)	4.7 (0.1)	3.9 (0.0)
Rms	β_0	0.5 (0.2)	1.3 (0.9)	-0.6 (0.6)
	β_1	31.1 (2.0)	20.0 (1.1)	14.1 (0.8)
Std	β_0	0.5 (0.5)	1.7 (1.4)	2.8 (3.2)
	β_1	39.9 (3.9)	34.0 (2.9)	28.3 (2.5)

Table A.2: Linear coefficients for relative comparison metrics for three different quantiles with a C/N_0 noise behaviour of a category 1 antenna and with differences to the category 3 antenna in Table 4.6 in the brackets.

Comparison metric	Coefficient	Quantile 68 %	95 %	99.7 %
Min	β_0	2.0 (2.0)	-0.1 (0.4)	-2.2 (2.2)
	β_1	12.8 (0.5)	9.3 (0.6)	7.1 (0.6)
Max	β_0	-1.0 (0.5)	-0.5 (0.6)	3.6 (2.1)
	β_1	12.9 (0.5)	9.4 (0.7)	7.0 (0.6)
Spread	β_0	120.1 (118.2)	73.8 (68.2)	49.6 (42.3)
	β_1	9.1 (12.5)	6.7 (3.8)	5.2 (1.6)
Range	β_0	0.1 (0.3)	0.2 (0.4)	-3.4 (3.7)
	β_1	6.6 (0.3)	5.2 (0.2)	4.3 (0.2)
Rms	β_0	-0.5 (0.4)	1.6 (1.8)	2.4 (2.7)
	β_1	55.2 (3.9)	41.4 (4.6)	3.2 (4.1)
Std	β_0	-0.5 (0.2)	0.3 (0.6)	0.8 (0.7)
	β_1	62,5 (2.7)	54.4 (2.6)	47,7 (3.1)

A.2 CPC Estimation with alternative Methods

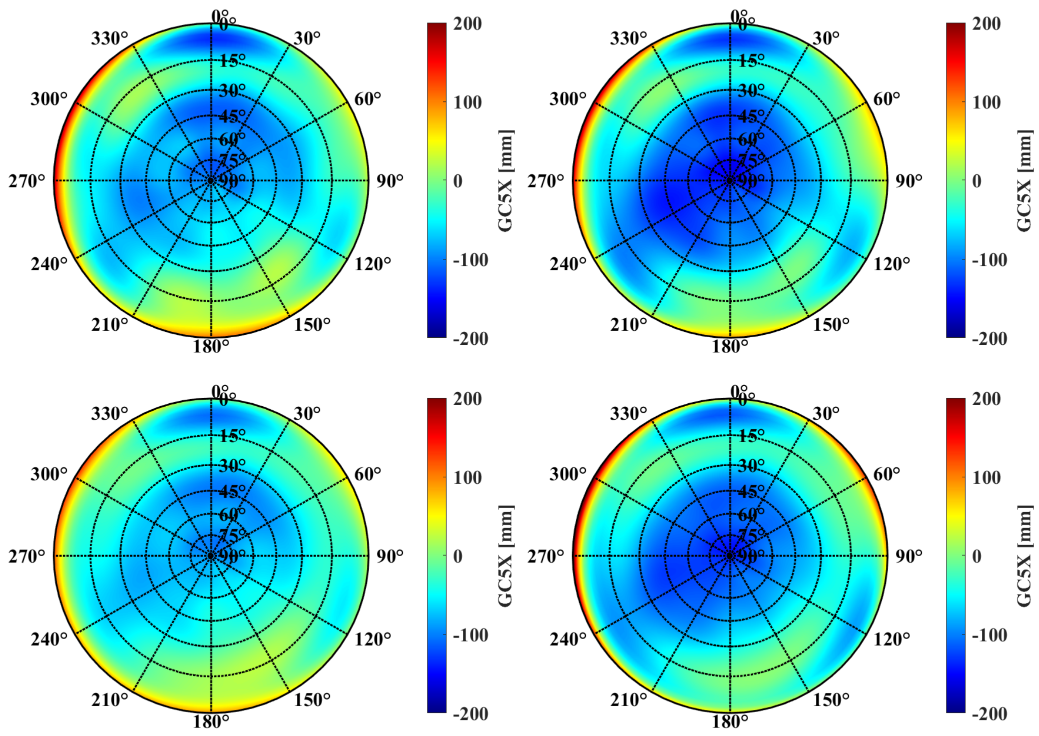

Figure A.4: Estimated mean pattern of GPS C5, calibrated with default (top) and optimized (bottom) receiver settings with ΔSD as estimation inputs (left) and ΔMPLC (right) with multipath map threshold of 1.5 m.

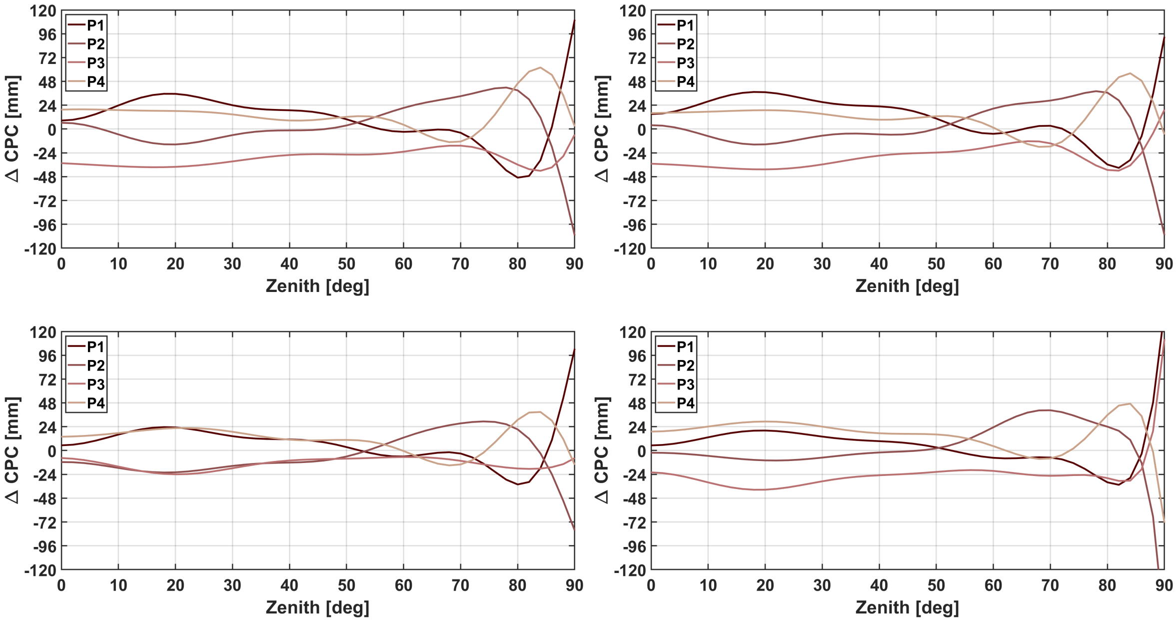

Figure A.5: Comparison w.r.t to type mean CPC pattern for GPS C5. The elevation dependent pattern (NOAZI) is presented, calibrated with default (top) and optimized (bottom) receiver settings with ΔSD as estimation inputs (left) and ΔMPLC (right) with multipath map threshold of 1.5 m.

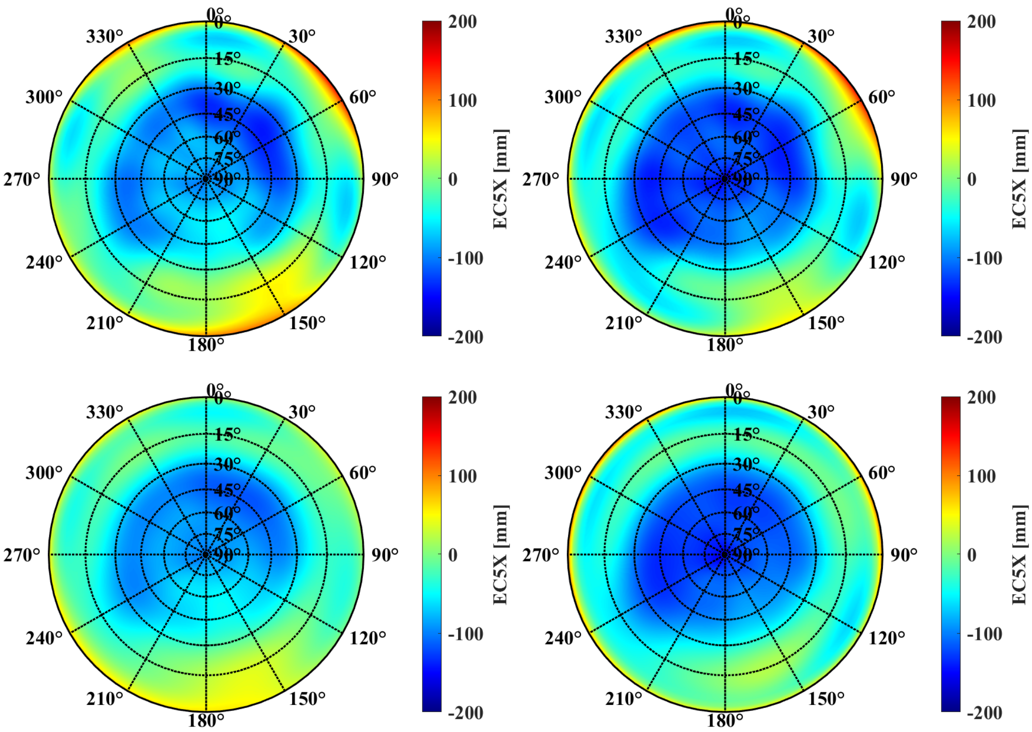

Figure A.6: Estimated mean pattern of Galileo C5, calibrated with default (top) and optimized (bottom) receiver settings with ΔSD as estimation inputs (left) and ΔMPLC (right) with multipath map threshold of 1.5 m.

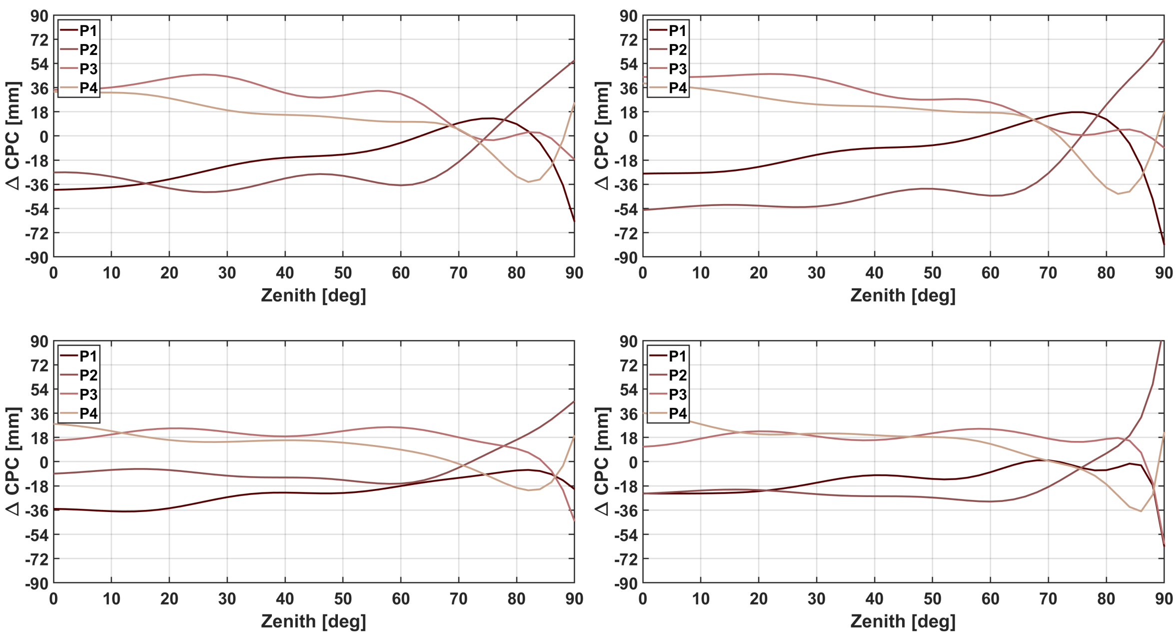

Figure A.7: Comparison w.r.t to type mean CPC pattern for Galileo C5. The elevation dependent pattern (NOAZI) is presented, calibrated with default (top) and optimized (bottom) receiver settings with ΔSD as estimation inputs (left) and ΔMPLC (right) with multipath map threshold of 1.5 m.

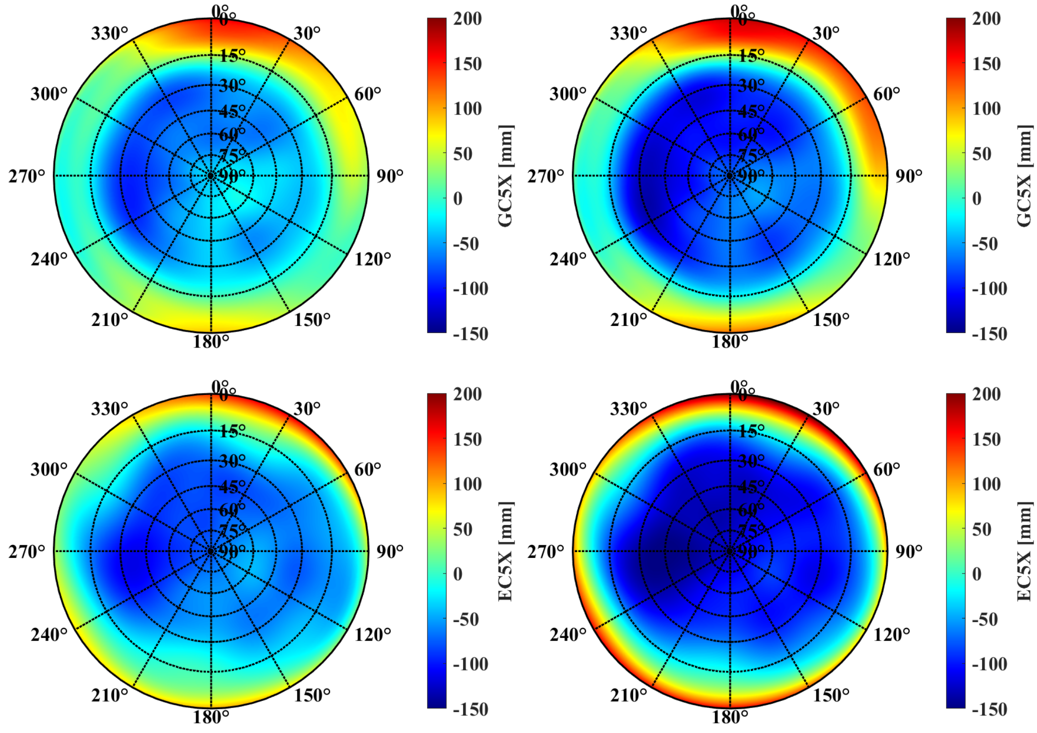

Figure A.8: Mean CPC pattern of the category 1 antenna for GPS C5 (top) and Galileo C5 signal (bottom). The left subfigures presented the results using a unity weighting, whereas the right subfigures show the pattern when using a C/N_0 dependent weighting. Optimized receiver settings are used with a multipath map threshold of 2 m.

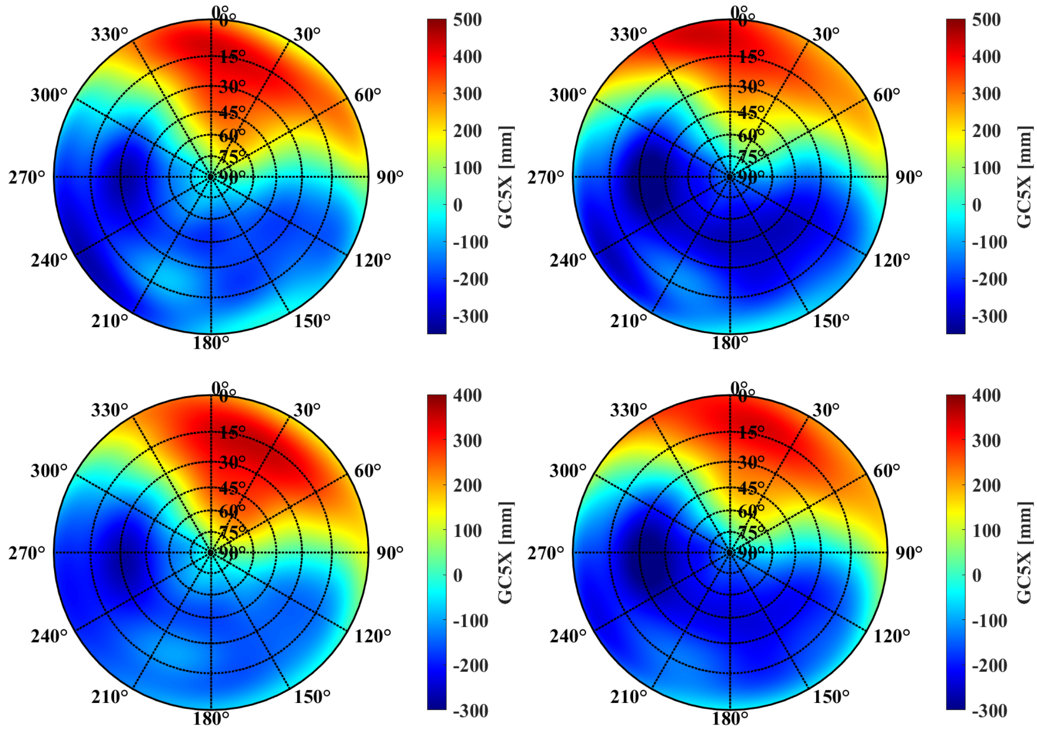

Figure A.9: Mean CPC pattern of the category 3 antenna for the GPS C5 signal. The left subfigures present the results when using a unity weighting, whereas the right subfigures show the pattern when using a C/N_0 dependent weighting with default (top) and optimized receiver settings (bottom). A multipath map threshold of 2 m is applied. Please note different scale between.

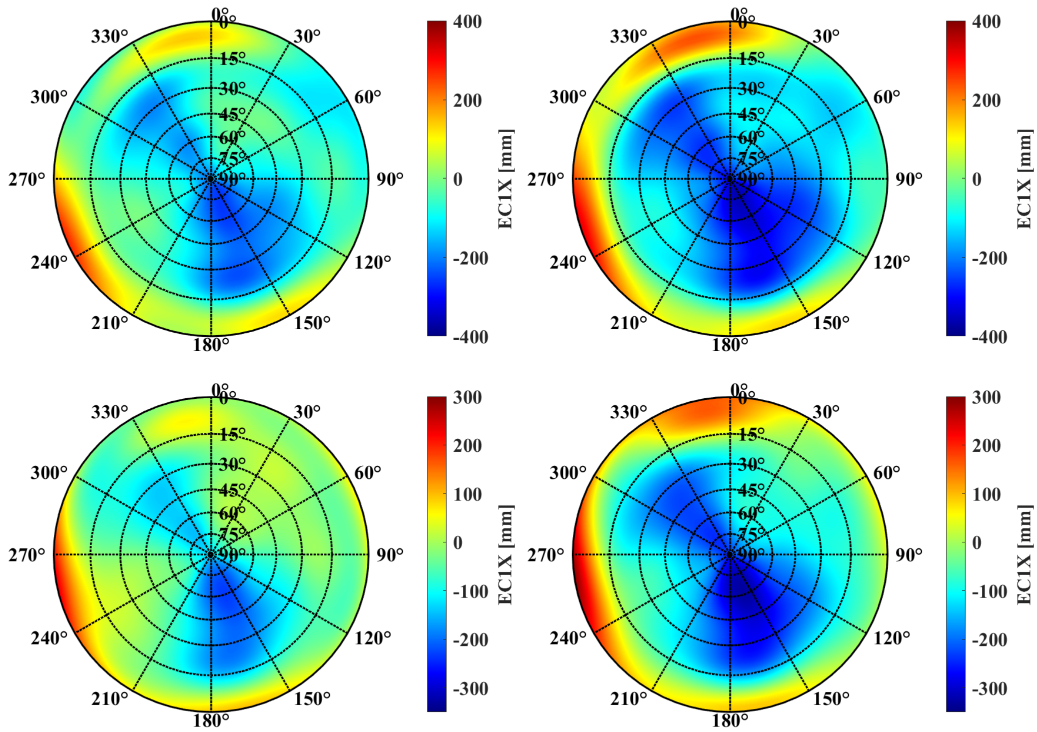

Figure A.10: Mean CPC pattern of the category 3 antenna for the Galileo C1 signal. The left subfigures present the results when using a unity weighting, whereas the right subfigures show the pattern when using a C/N_0 dependent weighting with default (top) and optimized receiver settings (bottom). A multipath map threshold of 2 m is applied. Please note different scale between.

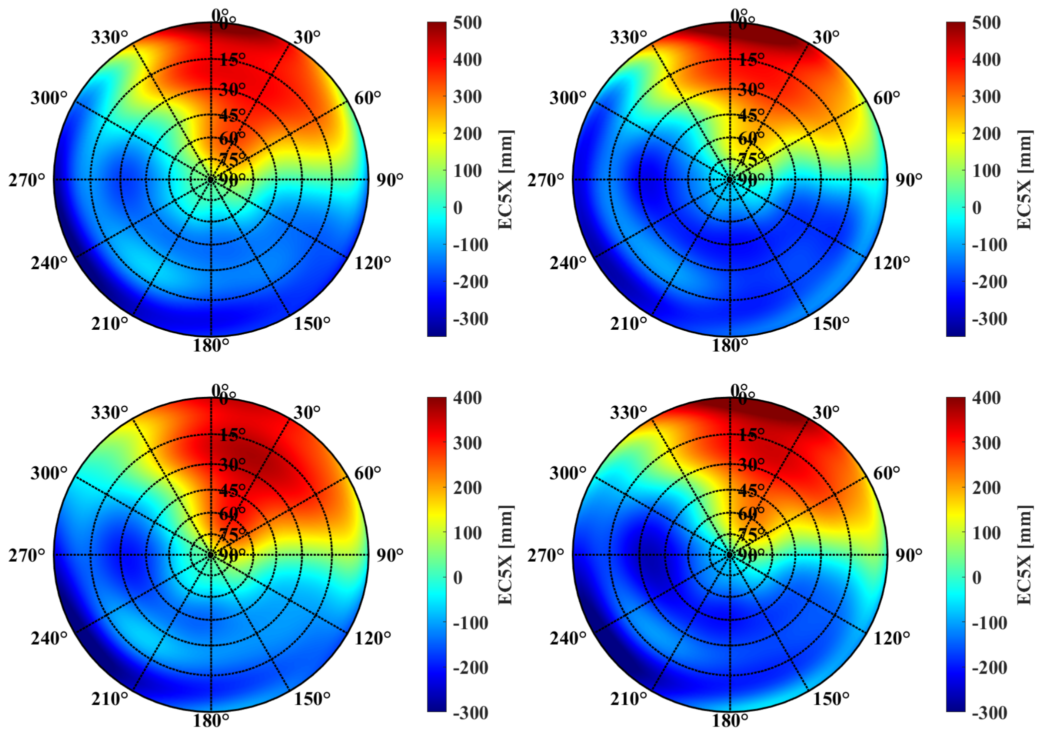

Figure A.11: Mean CPC pattern of the category 3 antenna for the Galileo C5 signal. The left subfigures present the results when using a unity weighting, whereas the right subfigures show the pattern when using a C/N_0 dependent weighting with default (top) and optimized receiver settings (bottom). A multipath map threshold of 2 m is applied. Please note different scale between.

Bibliography

Addo, E. O., Breva, Y., Kröger, J., Kersten, T., Schön, S., and Caizzone, S. (2024a). Minimal-Cost Generation of Multipath Error Maps from Antenna Installed Performance Analyses. Internal Report.

Addo, E. O. and Caizzone, S. (2023). Characterizing GNSS Multipath in Challenging Installation Scenario using Combined Simulation-Measurements of Dual-Polarization Antennas. In *Proceedings of the 2023 International Technical Meeting of The Institute of Navigation*, pages 799–807.

Addo, E. O., Elmarissi, W., and Caizzone, S. (2024b). Digital Twin-Enabled Characterization of GNSS Multipath in Challenging Reference Stations Using a Dual-Polarized Probe. *NAVIGATION: Journal of the Institute of Navigation*, 71(2).

Baasch, K.-N., Icking, L., Ruwisch, F., and Schön, S. (2022). Coordinate frames and transformations in GNSS ray-tracing for autonomous driving in urban areas. *Remote Sensing*, 15(1):180.

Becker, M., Zeimetz, P., and Schönemann, E. (2010). Anechoic Chamber calibrations of phase center variations for new and existing GNSS signals and potential impacts in IGS processing. In *Presentation at the IGS Workshop 2010 and Vertical Rates Symposium, June 28 - July 2, Newcastle upon Tyne, United Kingdom of Great Britain*.

Bedford, L., Brown, N., and Walford, J. (2009). New 3D four constellation high performance wideband choke ring antenna. In *Proceedings of the 2009 International Technical Meeting of The Institute of Navigation*, pages 829–835.

Beer, S. (2022). *Bestimmung richtungsabhängiger Codeverzögerungen von GNSS-Satellitenantennen*. PhD thesis, Technische Universität Dresden.

Beer, S., Wanninger, L., and Heßelbarth, A. (2019). Galileo and GLONASS group delay variations. *GPS Solutions*, 24(1).

Beer, S., Wanninger, L., and Heßelbarth, A. (2021). Estimation of absolute GNSS satellite antenna group delay variations based on those of absolute receiver antenna group delays. *GPS solutions*, 25(110):10.

Betz, J. W. (2001). Binary offset carrier modulations for radionavigation. *Navigation*, 48(4):227–246.

Beyerle, G. (2008). Carrier phase wind-up in GPS reflectometry. *GPS Solutions*.

Bilich, A., Mader, G., and Geoghegan, C. (2018). 6-axis robot for absolute antenna calibration at the US National Geodetic Survey. In *Presentation at the IGS Workshop 2018, October 29 - November 2, Wuhan, China*. Poster.

Böder, V., Menge, F., Seeber, G., Wübbena, G., and Schmitz, M. (2001). How to Deal With Station Dependent Errors, New Developments of the Absolute Field Calibration of PCV and Phase-Multipath With a Precise Robot. In *Proceedings of the 14th International Technical Meeting of the Satellite Division of The Institute of Navigation (ION GPS 2001), September 11 - 14, Salt Lake City, UT, USA*, pages 2166–2176. Institute of Navigation (ION), IEEE.

Braasch, M. S. (2017). Chapter 15. Multipath. In Montenbruck, O. and Teunissen, P., editors, *Springer Handbook of Global Navigation Satellite Systems*. Springer Nature.

Breuer, B., Campbell, J., Görres, B., Hawig, J., and Wohlleben, R. (1995). Kalibrierung von GPS-Antennen für hochgenaue geodätische Anwendungen. *SPN-Zeitschrift für satellitengestützte Positionierung, Navigation und Kommunikation*, 2:49–59.

Breva, Y., Kröger, J., Kersten, T., and Schön, S. (2019a). Validation of Phase Center Corrections for new GNSS-Signals obtained with absolute antenna calibration in the field. *Geophysical Research*

Abstracts 21 (2019). Poster.

Breva, Y., Kröger, J., Kersten, T., and Schön, S. (2022). Estimation and Validation of Codephase Center Correction using the Empirical Mode Decomposition. In Freymueller, J. T. and Sánchez, L., editors, *Geodesy for a Sustainable Earth: Proceedings of the 2021 Scientific Assembly of the International Association of Geodesy, Beijing, China, June 28–July 2, 2021*, pages 333–343. Springer.

Breva, Y., Kröger, J., Kersten, T., and Schön, S. (2024). On the Impact of GNSS Receiver Settings on the Estimation of Codephase Center. In Freymueller, J. T. and Sánchez, L., editors, *Gravity, Positioning and Reference Frames: Proceedings of the IAG Commission 4: Positioning and Applications, Potsdam, Germany, September 5-8, 2022*, volume 156, page 101. Springer Nature.

Breva, Y., Kröger, J., Kersten, T., and Schön, S. (2019b). Estimation and validation of receiver antenna codephase variations for multi GNSS signals. *7th International Colloquium on Scientific and Fundamental Aspects of GNSS*. Poster.

Bruyninx, C. (2023). ETRF/ITRF Coordinate Transformation Tool. Royal Observatory of Belgium. https://epncb.oma.be/_productsservices/coord_trans [Accessed: (27.11.2024)].

Caizzone, S., Circiu, M.-S., Elmarissi, W., Enneking, C., Felux, M., and Yinusa, K. (2017). Effect of antenna pattern uniformity on the pseudorange tracking error. In *Proceedings of the 30th International Technical Meeting of the Satellite Division of the Institute of Navigation (ION GNSS+ 2017)*, pages 3460–3470.

Caizzone, S., Circiu, M.-S., Elmarissi, W., Enneking, C., Felux, M., and Yinusa, K. (2019). Antenna influence on Global Navigation Satellite System pseudorange performance for future aeronautics multifrequency standardization. *Navigation*, 66(1):99–116.

Caizzone, S., Circiu, M.-S., Elmarissi, W., Enneking, C., Rippl, M., and Sgammini, M. (2022). The Role of Antennas on GNSS Pseudorange and Multipath Errors and Their Impact on DFMC Multipath Models for Avionics. *NAVIGATION: Journal of the Institute of Navigation*, 69(3).

Caizzone, S., Tripathi, V., and Hehenberger, S. (2021). Investigating GNSS Multipath in Aeronautic Applications Through Antenna Installed Performance. In *2021 15th European Conference on Antennas and Propagation (EuCAP)*, pages 1–5. IEEE.

Dach, R., Lutz, S., Walser, P., and Fridez, P., editors (2015). *Bernese GNSS Software Version 5.2*. University of Bern, Bern Open Publishing. doi: 10.7892/boris.72297.

Dassault-Systèmes (2022). CST studio suite: Electromagnetic field simulation software. https://www.3ds.com/fileadmin/PRODUCTS-SERVICES/SIMULIA/PRODUCTS/CST/SIMULIA-CST-Studio-Suite-Brochure.pdf [Accessed: (10.10.2024)].

de Bakker, P. F., van der Marel, H., and Tiberius, C. C. (2009). Geometry-free undifferenced, single and double differenced analysis of single frequency GPS, EGNOS and GIOVE-A/B measurements. *GPS solutions*, 13:305–314.

Dilßner, F. (2007). *Zum Einfluss des Antennenumfeldes auf die hochpräzise GNSS-Positionsbestimmung*. PhD thesis, Wissenschaftliche Arbeiten der Fachrichtung Geodäsie und Geoinformatik der Leibniz Universität Hannover, Nr. 271.

Gurtner, W., Beutler, G., and Rothacher, M. (1989). Combination of GPS Observations Made with Different Receiver Types. In *Proceedings of the 5th International Geodetic Symposium on Satellite Positioning*, pages 362–374.

Görres, B., Campbell, J., Becker, M., and Siemes, M. (2006). Absolute calibration of GPS antennas: laboratory results and comparison with field and robot techniques. *GPS Solutions*, 10(2):136–145.

Harris, M., Miltner, M., Murphy, T., Raghuvanshi, A., and van Graas, F. (2017). Bounding GPS L1 antenna group delay variation for GNSS landing system integrity. In *Proceedings of the 2017 International Technical Meeting of the Institute of Navigation*, pages 591–605.

Hegarty, C. J., Ligler, G. T., Alexander, K., Chesto, L., Moses, H., Wichgers, J. M., Enge, P., Erlandson, B., Van Dierendonck, A., Azoulai, L., et al. (2015). RTCA SC-159: 30 Years of Aviation GPS

Standards. In *Proceedings of the 28th International Technical Meeting of the Satellite Division of the Institute of Navigation (ION GNSS+ 2015)*, pages 877–896.

Hu, Z., Zhao, Q., Chen, G., Wang, G., Dai, Z., and Li, T. (2015). First Results of Field Absolute Calibration of the GPS Receiver Antenna at Wuhan University. *Sensors*, 15(11):28717–28731.

Häberling, S. (2016). *Theoretical and Practical Aspects of High-Rate GNSS Geodetic Observations*. PhD thesis, Geodätisch-geophysikalische Arbeiten der Schweiz, Band 95.

Icking, L., Kersten, T., and Schön, S. (2020). Evaluating the Urban Trench Model For Improved GNSS Positioning in Urban Areas. In *2020 IEEE/ION Position, Location and Navigation Symposium (PLANS)*, pages 631–638. IEEE.

Icking, L., Ruwisch, F., and Schön, S. (2022). Multipath Characterization Using Ray-Tracing in Urban Trenches. In *Geodesy for a Sustainable Earth: Proceedings of the 2021 Scientific Assembly of the International Association of Geodesy, Beijing, China, June 28–July 2, 2021*, pages 359–365. Springer.

IFEN GmbH (2019). *SX3 Navigation Software Receiver - User Manual*.

International GNSS Service (2010). Antex 1.4 format description. https://files.igs.org/pub/data/format/antex14.txt [Accessed: (10.10.2024)].

International GNSS Service (2024). RINEX format description. Technical report, International GNSS Service. https://igs.org/wg/rinex/#documents-formats [Accessed: (07.11.2024)].

JAVAD GNSS (2024a). JAVAD Delta TRE. https://www.javad.com/jgnss/products/receivers/delta-3.html [Accessed: (10.10.2024)].

JAVAD GNSS (2024b). JAVAD DeltaS-3S. https://www.javad.com/jgnss/products/receivers/deltas-3s.html [Accessed: (10.10.2024)].

Kalyanaraman, S. K., Braasch, M. S., and Kelly, J. M. (2006). Code tracking architecture influence on GPS carrier multipath. *IEEE transactions on Aerospace and Electronic Systems*, 42(2):548–561.

Kaplan, E. D. and Hegarty, C. J. (2017). *Understanding GPS/GNSS Principles and Applications*. GNSS Technology and Application Series. Artech house, third edition.

Kersten, T. (2014). *Bestimmung von Codephasen-Variationen bei GNSS-Empfangsantennen und deren Einfluss auf die Positionerung, Navigation und Zeitübertragen*. PhD thesis, Wissenschaftliche Arbeiten der Fachrichtung Geodäsie und Geoinformatik der Leibniz Universität Hannover, Nr. 315.

Kersten, T., Bilich, A., Sutyagin, I., and Schön, S. (2024a). A Global Collaboration to Enhance GNSS Receiver Antenna Calibration: The IGS Antenna Ring Campaign. Technical report, Copernicus Meetings.

Kersten, T., Kröger, J., and Schön, S. (2022). Comparison concept and quality metrics for GNSS antenna calibrations: Cause and effect on regional GNSS networks. *Journal of geodesy*, 96(7):48.

Kersten, T. and Schön, S. (2017). GPS Code Phase Variations (CPV) for GNSS Receiver Antennas and Their Effect on Geodetic Parameters and Ambiguity Resolution. *Journal of Geodesy*, 91(6):579–596.

Kersten, T., Sutyagin, I., Bilich, A., and Schön, S. (2024b). Uniting Global Efforts to Calibrate GNSS Antennas: Models, analyses and pilot results. *Bern: IGS*.

Klobuchar, J. A. (1987). Ionospheric time-delay algorithm for single-frequency GPS users. *IEEE Transactions on aerospace and electronic systems*, 3:325–331.

Koppmann, V. (2018). Bestimmung neuer ITRF14 und ETRS89 Referenzkoordinaten für das GNSS-Labornetzwerk des Institut für Erdmessung. Bachelor's thesis, Leibniz Universität Hannover.

Kröger, J., Breva, Y., Kersten, T., and Schön, S. (2019). Phase Center Corrections for new GNSS-Signals. In *Geophysical Research Abstracts 21*, number 21 in Geophysical Research Abstracts. Presentation.

Kröger, J., Kersten, T., Breva, Y., and Schön, S. (2021). Multi-frequency multi-GNSS receiver antenna calibration at IfE: Concept-calibration results-validation. *Advances in Space Research*, 68(12):4932–4947.

Kröger, J., Kersten, T., Breva, Y., and Schön, S. (2022). On the potential of image similarity metrics for comparing phase center corrections. In Freymueller, J. T. and Sánchez, L., editors, *Geodesy for a Sustainable Earth: Proceedings of the 2021 Scientific Assembly of the International Association of Geodesy, Beijing, China, June 28–July 2, 2021*, pages 345–357. Springer.

Kröger, J. (2025). *Estimation and Validation of multi-GNSS multi-Frequency Phase Center Corrections and their Impact on Geodetic Parameters*. PhD thesis, Leibniz Universität Hannover. Submitted.

Kröger, J., Breva, Y., Kersten, T., and Schön, S. (2024). Recent Antenna Calibration Developments at IFE. In *IGS 2024 Symposium*, Bern, Switzerland.

Langley, R. B., Teunissen, P. J., and Montenbruck, O. (2017). Chapter 1. Introduction to GNSS. In Montenbruck, O. and Teunissen, P., editors, *Springer Handbook of Global Navigation Satellite Systems*. Springer Nature.

Leica Geosystems AG (2024). Leica AR25 GNSS Antenna. https://leica-geosystems.com/products/gnss-reference-networks/antennas/leica-ar25 [Accessed: (10.10.2024)].

Leistner, H. (2000). Roboterkalibrierung - Funktionales Modell. Technical report, Geodätisches Institut Hannover (GIH), Leibniz Universität Hannover. Interner Bericht für Institut für Erdmessung.

Mader, G. (1999). GPS Antenna Calibration at the National Geodetic Survey. *GPS Solutions*, 3(1):50–58.

Mader, G., Bilich, A., and Geoghegan, C. (2012). Absolute GNSS Antenna Calibration at the National Geodetic Survey. In *Presentation at the European Geophysical Union General Assembly 2012*, volume 14 of *Geophysical Research Abstracts #EGU2012-3080*. Poster, URL: http://meetingorganizer.copernicus.org/EGU2012/EGU2012-3080.pdf [Accessed: (03.12.2024)].

Mader, G. L. and MacKay, J. R. (1996). Calibration of GPS Antennas. In Neilan, R., Scoy, P. V., and Zumberge, J., editors, *Presentation at the IGS Analysis Center Workshop, March 19-21, Silver Spring, MD*. International GPS Service, JPL Publication 96-26, Jet Propulsion Laboratory, Pasadena, California.

Maqsood, M., Gao, S., and Montenbruck, O. (2017). Chapter 17. Antennas. In Montenbruck, O. and Teunissen, P., editors, *Springer Handbook of Global Navigation Satellite Systems*. Springer Nature.

Marut, G., Hadas, T., and Nosek, J. (2024). Intercomparison of multi-GNSS signals characteristics acquired by a low-cost receiver connected to various low-cost antennas. *GPS Solutions*, 28(2):82.

Meiser, V. (2009). Kalibrierung des GNSS-Antennenkalibrierroboters des Institut für Erdmessung mittels Lasertracking. Technical report, Geodätisches Institut Hannover (GIH), Leibniz Universität Hannover. Interner Bericht für Institut für Erdmessung.

Melbourne, W. G. (1985). The Case for Ranging in GPS-Based Geodetic Systems. In Goad, C. C., editor, *Proceedings of the First International Symposium on Precise Positioning with the Global Positioning System, April 15-19, Rockville, MD, USA*, volume 1, pages 373–386. International Union of Geodesy and Geophysics, International Association of Geodesy, U.S. Department of Defense and U.S. Department of Commerce.

Menge, F. (2003). *Zur Kalibrierung der Phasenzentrumsvariationen von GPS-Antennen für die hochpräzise Positionsbestimming*. PhD thesis, Wissenschaftliche Ar- beiten der Fachrichtung Geodäsie und Geoinformatik der Leibniz Universität Hannover, Nr. 247.

Menge, F., Seeber, G., Völksen, C., Wübbena, G., and Schmitz, M. (1998). Results of the absolute field calibration of GPS antenna PCV. In *Proceedings of the 11th International Technical Meeting of the Satellite Division of The Institute of Navigation (ION GPS 1998), September 15 - 18, Nashville, TN, USA*, pages 31–38. Institute of Navigation, IEEE.

Misra, P. and Enge, P. (2006). *Global Positioning System: Signals, Measurements, and Performance*. Ganga-Jamuna Press, Lincoln, Massachusetts, second edition.

Murphy, T., Geren, P., and Pankaskie, T. (2007). GPS Antenna Group Delay Variation Induced Errors in a GNSS Based Precision Approach and Landing Systems. In *Proceedings of the 20th International Technical Meeting of the Satellite Division of The Institute of Navigation (ION GNSS 2007), September 25 - 28, Fort Worth, TX, USA*, pages 2974–2989. Institute if Navigation (ION), IEEE.

Novatel (2011). GPS-703-GGG. Product Sheet, Novatel.

Paffenholz, J. A., Bielenberg, O., Neuner, H., Schön, S., and Kutterer, H. (2007). Neukalibrierung des IfE-Roboters mittels Lasertracking. In *Geodätische Woche 2007, 26.09., Leipzig, Deutschland*.

Pany, T. (2010). *Navigation Signal Processing for GNSS Software Receivers*. Artech House, Norwood, USA.

Pratt, M. J. (2001). Introduction to ISO 10303—the STEP standard for product data exchange. *Journal of Computing and Information Science in Engineering*, 1(1):102–103.

Raghuvanshi, A. and van Graas, F. (2016). Impact of antenna group delay variations on protection levels. In *2016 IEEE/ION Position, Location and Navigation Symposium (PLANS)*, pages 857–862. IEEE.

Rao, B. R., Kunysz, W., Fante, R. L., and McDonals, K. (2013). *GPS/GNSS Antennas*. Artech House, Norwood, USA.

re3data.org (2020). VMF Data Server. Registry of Research Data Repositories. editing status 2020-12-14.

Riddell, A., Moore, M., and Hu, G. (2015). Geoscience Australia's GNSS antenna calibration facility: Initial results. In *Proceedings of the International Global Navigation Satellite Systems Society IGNSS Symposium*, volume 14, page 16.

Rothacher, M. and Mader, G. (2002). Receiver and satellite antenna phase center offsets and variations. In *Position Paper of the" Antenna Session"*.

Rothacher, M., Schaer, S., Mervat, L., and Beutler, G. (1995). Determination of Antenna Phase Center Variations using GPS Data. In *Presentation at the IGS Workshop - Special Topics and new Directions, May 15 - 18, Potsdam, Germany*, page 16.

Schaper, A., Ruwisch, F., and Schön, S. (2022). Diffraction Modeling for Improved 3DMA GNSS Urban Navigation. In *Proceedings of the 35th International Technical Meeting of the Satellite Division of the Institute of Navigation (ION GNSS+ 2022)*, pages 1902–1916.

Schmid, R., Mader, G., and Herring, T. (2005). From relative to absolute antenna phase center corrections. In *In: Meindl M.(Ed.) Proceedings of the IGS Workshop and Symposium 2004, Bern, Astronomical Institute, University of Bern*, pages 209–219.

Schmid, R., Steigenberger, P., Gendt, G., Ge, M., and Rothacher, M. (2007). Generation of a consistent absolute phase-center correction model for GPS receiver and satellite antennas. *Journal of Geodesy*, 81(12):781–798.

Schmitz, M., Wübbena, G., and Boettcher, G. (2002). Tests of phase center variations of various GPS antennas, and some results. *GPS solutions*, 6(1-2):18–27.

Schmolke, A., Wanninger, L., and Frevert, V. (2015). Erste GNSS-Antennenkalibrierungen im Feldverfahren auf neuen Signalfrequenzen (First GNSS antenna calibrations in the field for new frequencies). *zfv – Zeitschrift für Geodäsie, Geoinformation und Landmanagement*, 140(5):283–289.

Schön, S. and Kersten, T. (2013). On adequate Comparison of Antenna Phase Center Variations. In *Presentation at the American Geophysical Union, Annual Fall Meeting 2013, December 09.-13., San Francisco, CA, USA*, Geophysical Abstracts #G13B-0950.

Schupler, B. (2001). The response of GPS antennas - how design, environment and frequency affect what you see. *Physics and Chemistry of the Earth, Part A: Solid Earth and Geodesy*, 26(6-8):605–611.

Seeber, G. and Böder, V. (2002). Entwicklung und Erprobung eines Verfahrens zur hochpräzisen Kalibrierung von GPS Antennenaufstellungen - Schlussbericht zum BMBF/DLR Vorhaben 50NA9809/8. Technical report, Institut für Erdmessung.

Seeber, G., Menge, F., Völksen, C., Wübbena, G., and Schmitz, M. (1997). Precise GPS Positioning Improvements by Reducing Antenna and Site Dependent Effects. In *Scientific Assembly of the International Association of Geodesy IAG97, September 03-09., Rio de Janeiro, Brasil.*

Septentrio (2020). PolaRx5TR - User Manual. Product Sheet, Septentrio. https://www.gnss-imu.com/down/upload/20220923/1663940754.pdf [Accessed: (27.12.2024)].

Septentrio (2024). Septentrio PolaRx5TR. https://www.septentrio.com/en/products/gnss-receivers/gnss-reference-receivers/polarx-5tr [Accessed: (10.10.2024)].

Sims, M. L. (1985). Phase center variation in the geodetic TI4100 GPS receiver system's conical spiral antenna. In *Proc 1st International Symposium on Precise Positioning with the Global Positioning System, Rockville*, pages 227–244.

Sutyagin, I. and Tatarnikov, D. (2020). Absolute robotic GNSS antenna calibrations in open field environment. *GPS Solutions*, 24(4):92.

Teunissen, P. J. and Montenbruck, O. (2017). *Springer Handbook of Global Navigation Satellite Systems*. GNSS Technology and Application Series. Springer Nature, first edition.

Tsui, J. B.-Y. (1995). Digital Techniques for Wideband Receivers. *Artech House*.

Tupek, A., Zrinjski, M., Švaco, M., and Barković, Đ. (2023). GNSS Receiver Antenna Absolute Field Calibration System Development: Testing and Preliminary Results. *Remote sensing*, 15(18):4622.

U-Blox AG (2024). ANN-MB1 L1/L5 multi-band high precision GNSS antenna. Product Sheet, U-Blox AG. https://content.u-blox.com/sites/default/files/ANN-MB1_DataSheet_UBX-21005551.pdf [Accessed: (10.10.2024)].

Van Nee, R. D. (1993). Spread-spectrum code and carrier synchronization errors caused by multipath and interference. *IEEE transactions on aerospace and electronic systems*, 29(4):1359–1365.

Vergara, M., Sgammini, M., Thoelert, S., Enneking, C., Zhu, Y., and Antreich, F. (2016). Tracking Error Modeling in Presence of Satellite Imperfections. *Navigation: Journal of The Institute of Navigation*, 63(1):3–13.

Vizemuller, P. (1995). RF Design Guide: Systems, Circuits and Equations. *Artech House*.

Wanninger, L. and Beer, S. (2015). BeiDou satellite-induced code pseudorange variations: diagnosis and therapy. *GPS solutions*, 19:639–648.

Wanninger, L., Sumaya, H., and Beer, S. (2017). Group delay variations of GPS transmitting and receiving antennas. *Journal of Geodesy*, 91(9):1099–1116.

Willi, D. (2019). *GNSS receiver synchronisation and antenna calibration.* PhD thesis, ETH Zurich, ETH NO. 25854.

Willi, D., Lutz, S., Brockmann, E., and Rothacher, M. (2019). Absolute field calibration for multi-GNSS receiver antennas at ETH zurich. *GPS Solutions*, 24(1).

Wu, J., Wu, S., Hajj, G., Bertiger, W., and Lichten, S. (1993). Effects of antenna orientation on GPS carrier phase. *Manuscripta geodaetica*, 18:91–98.

Wübbena, G. (1985). Software Developments for Geodetic Positioning with GPS using TI 4100 Code and Carrier Measurments. In Goad, C. C., editor, *Proceedings of the First International Symposium on Precise Positioning with the Global Positioning System, April 15-19, Rockville, MD, USA*, volume 1, pages 403–412. International Union of Geodesy and Geophysics, International Association of Geodesy, U.S. Department of Defense and U.S. Department of Commerce.

Wübbena, G., Menge, F., Schmitz, M., Seeber, G., and Völksen, C. (1996). A New Approach for Field Calibration of Absolute Antenna Phase Center Variations. In *Proceedings of the 9th International Technical Meeting of the Satellite Division of The Institute of Navigation (ION GPS 1996), September 17-20, Kansas City, MO*, pages 1205–1214. Institute of Navigation (ION), IEEE.

Wübbena, G., Schmitz, M., Menge, F., Böder, V., and Seeber, G. (2000). Automated Absolute Field Calibration of GPS Antennas in Real-Time. In *Proceedings of the 13th International Technical Meeting of the Satellite Division of The Institute of Navigation (ION GPS 2000), September 19-22, Salt Lake City, UT, USA*, pages 2512–2522. Institute of Navigation (ION).

Wübbena, G., Schmitz, M., and Propp, M. (2008). Antenna group delay calibration with the geo++ robot-extensions to code observable. In *IGS Analysis Workshop, Poster, June*, pages 2–6.

Wübbena, G., Schmitz, M., and Warneke, A. (2019). Geo++ Absolute Multi Frequency GNSS Antenna Calibration. In *Presentation at the EUREF Analysis Center (AC) Workshop, October 16 - 17, Warsaw, Poland*. URL: http://www.geopp.com/pdf/gpp_cal125_euref19_p.pdf.

Zeimetz, P. (2010). *Zur Entwicklung und Bewertung der absoluten GNSS-Antennenkalibrierung im HF-Labor*. PhD thesis, Universität Bonn, In: Schriftenreihe / Institut für Geodäsie und Geoinformation, 21.

Zhou, R., Hu, Z., Zhao, Q., Chen, G., and Tao, J. (2023). Absolute field calibration of receiver antenna phase center models for GPS/BDS-3 signals. *Journal of Geodesy*, 97(9):83.

List of Tables

List of Figures

Acronym

ADC	analog-to-digital conversion
AGC	automatic gain control
ANTEX	antenna exchange format
ARP	antenna reference point
AUT	antenna under test
BDS	Beidou
BMBF	Bundesministerium für Bildung, Wissenschaft, Forschung und Technologie
BOC	binary offset carrier
BPF	band pass filter
BPSK	binary phase shift keying
C/A	coarse-acquisition
CCO	codephase center offset
CDMA	code division multiple access
CLL	code lock loop
CMC	code-minus-carrier
C/N_0	carrier to noise density
CPC	codephase center corrections
ΔCPC	difference pattern
CODE	Center for Orbit Determination in Europe
CPV	codephase center variations
DD	double differences
DEM	dynamic elevation mask
DLL	delay lock loop
DLR	Deutsches Zentrum für Luft- und Raumfahrt
DOY	day of year
ΔSD	time differenced receiver-to-receiver single differences
$\Delta\mathbf{SD}_{sim}$	simulated time differenced receiver-to-receiver single differences
ΔMPLC	time differenced multipath linear combination
DSSS	discret sequence spread spectrum
ECEF	Earth-centered Earth-fixed
EM	east marker

EMD	empirical mode decomposition
FP	fixed point in space
FO	loop filter order
FDMA	frequency division multiple access
FLL	frequency lock loop
GDV	group delay variations
GIH	Geodetic Institute Hannover
GLONASS	GLObalnaja NAwigazionnaja Sputnikowaja Sistema
GNSS	Global Navigation Satellite System
GPS	Global Positioning System
HSH	hemispherical harmonics
ID	integrate and dump process
IfE	Institut für Erdmessung
IF	intermediate frequency
IGS	International GNSS Service
IMU	IMUinertial measurement unit
LC	linear combinations
LHCP	left-handed circularily polarized
LNA	low noise amplifier
LC	linear combination
LO	local oscillator
LOS	line-of-sight
LPF	low pass filter
MW	Melbourne-Wübbena
NCO	numerical controlled oscillator
NFS	near-field equivalent sources
NGS	National Geodetic Survey
NES	normal equation system
NM	north marker
NL	narrow lane
NLOS	non-line-of-sight
MAESTRO	DFG Project (470510446): Understanding Multipath - Antenna - Receiver Interactions for Standardizable Calibration of Code Phase Variations of GNSS Receiving Antennas
MPLC	multipath linear combination
PNR	pattern to noise ratio
PCO	phase center offset

PCC phase center corrections

ΔPCC difference pattern

PCV phase center variations

PLL phase lock loop

PPP precise point positioning

PRN pseudo random noise

PSD power spectral density

PVT position-velocity-time

PWU phase-wind up

PTB Physikalisch-Technische Bundesanstalt

OXCO oven-compensated crystal oscillator

QPSK quadrature phase shift keying

QZSS Quasi-Zenith Satellite System

RHCP right-handed circularily polarized

RINEX receiver independent exchange format

RF radio frequency

RMS root mean square

RTK real time kinematic

SBAS Satellite Based Augmentation System

SD single differences

SPP single point positioning

Std standard deviation

TXCO temperature-compensated crystal oscillator

TD triple differences

TEM topocentric elevation mask

VGA variable gain amplifier

WL wide lane

WN white noise

XPD cross-polar discrimation indicator

Acknowledgement

I would like to thank Prof. Steffen Schön for the opportunity to engage in my PhD at the Institut für Erdmessung. I greatly appreciate the encouraging discussions and support throughout my doctoral studies. Additionally, I would like to thank Prof. Gregor Möller from TU Vienna and Dr. Hamza Alkhatib for reviewing my thesis and providing valuable feedback.

I would like to thank all the colleagues at the Institut für Erdmessung I have met over the past years, especially those in the Positioning and Navigation group. In particular, I want to express my gratitude to Dr. Tobias Kersten for introducing me to GNSS antenna calibration with the robot in the field and for his continuous support during my experiments and analyses. Additionally, I would like to thank my good friend and colleague Thomas Maschke for his invaluable assistance with the calibration robot in various experiments. Special thanks goes to one of my best friends and colleagues, Dr. Johannes Kröger, for countless discussions, his support throughout my work, and many hours spent together after work. I extend my heartfelt gratitude to my best friend, Dr. Annike Knabe, for proofreading my thesis, for her constant mental support and numerous hours of discussion after work.

Finally, I am deeply grateful to my friends and family for their constant support and love.

Wissenschaftliche Arbeiten der Fachrichtung Geodäsie und Geoinformatik der Leibniz Universität Hannover

(Eine vollständige Liste der Wiss. Arb. ist beim Geodätischen Institut, Nienburger Str. 1, 30167 Hannover erhältlich.)

Nr. 380	PETERS, Torben:	Learning Multi-View 2D to 3D Label Transfer for Semi-Supervised Semantic Segmentation of Point Clouds (Diss. 2022)
Nr. 381	WASSINK, Martin:	Kommunal- und Regionalentwicklung durch Kooperation und Teilung von Verantwortung in ländlichen Räumen - eine multiperspektivische Untersuchung an Beispielen aus dem Raum Steinwald/Fichtelgebirge (Diss. 2022)
Nr. 382	GOLDSCHMIDT, Jürgen:	Die Berücksichtigung künftiger Entwicklungen bei der Verkehrswertermittlung (Diss 2022)
Nr. 383	KRUSE, Christian:	Impact maps from bomb craters detected in aerial wartime images using marked point processes (Diss. 2023)
Nr. 384	ZOURLIDOU, Stefania:	Traffic Regulation Recognition from GPS Data (Diss. 2023)
Nr. 385	SLEDZ, Artuom:	Thermal anomaly detection based on information fusion from optical and infrared images (Diss. 2023)
Nr. 386	WITTICH, Dennis:	Deep Domain Adaptation for the Pixel-wise Classification of Aerial and Satellite Images (Diss. 2023)
Nr. 387	SINGH, Vishwa Vijay:	Lunar Laser Ranging - Improved Modelling and Parameter Estimation (Diss. 2023)
Nr. 388	HARTMANN, Jens:	Hochgenaue 3D-Erfassung von Großstrukturen durch kinematisches terrestrisches Laserscanning (Diss. 2023)
Nr. 389	ZHUGE, Xia:	Characterizing slope instability kinematics by integrating multi-sensor satellite remote sensing observations (Diss. 2023)
Nr. 390	DOROZYNSKI, Mareike Marianne:	Image Classification and Retrieval in the Context of Silk Heritage using Deep Learning (Diss. 2023)
Nr. 391	KNABE, Annike:	New Concepts for Gravity Field Recovery using Satellites (Diss. 2023)
Nr. 392	KALIA, Andre:	Landslide activity detection based on nationwide Sentinel-1 PSI datasets (Diss. 2023)
Nr. 393	BROCKMEYER, Marco:	Modellierung von Bodenbewegungen anhand heterogener Messverfahren am Beispiel der niedersächsischen Landesfläche (Diss. 2023)
Nr. 394	ZHANG, Mingyue:	Characteristics and Benefits of Differential Lunar Laser Ranging (Diss. 2023)
Nr. 395	DENNIG, Dirk:	Entwicklung eines kinematischen Profilvermessungssystems am Beispiel Kranbahnvermessung (Diss. 2024)
Nr. 396	FUEST, Stefan:	Nudging travelers to societally favorable routes by means of cartographic symbolization (Diss. 2024)
Nr. 397	MOFTIZADEH, Rozhin:	Advanced Particle Filtering for Vehicle Navigation based on Collaborative Information (Diss. 2024)
Nr. 398	VASSILEVA, Magdalena Stefanova:	Satellite Radar Interferometry for Geohazards: from ground deformation to processes understanding (Diss. 2024)
Nr. 399	MALINOVSKAYA, Anna:	Statistical Process Monitoring of Networks (Diss. 2024)
Nr. 400	BANNERT, Jörn:	Der Einfluss von Straßenverkehrslärm und Umgehungsstraßen auf Grundstücks-werte in Ortslagen - Bestimmung mittels Expertenbefragung nach der Delphi-Methode (Diss. 2024)
Nr. 401	AXMANN: Jeldrik:	Maximum consensus localization using LiDAR (Diss. 2024)
Nr. 402	TENNSTEDT, Benjamin:	Concept and Evaluation of a Hybridization Scheme for Atom Interferometers and Inertial Measurement Units (Diss. 2024)
Nr. 403	HAKE, Frederic:	Schadenserkennung an Bauwerken mittels maschinellem Lernens (Diss. 2025)
Nr. 404	KARIMIDOONA, Ali:	On Integrity Prediction for Network-RTK Positioning in Urban Environments (Diss. 2025)
Nr. 405	ORTEGA, Mabel:	Domain Adaptation for Deforestation Detection in Remote Sensing: Addressing Class Imbalance and Performance Estimation (Diss. 2025)
Nr. 406	KUPRIYANOV, Alexey:	Investigation of Optical Accelerometry and Novel Satellite Formations for Future Gravimetry Missions (Diss. 2025)
Nr. 407	BREVA, Yannick:	On the Observation Quality of Robot-based GNSS Antenna Calibration for Determining Codephase Corrections (Diss. 2025)